SWINBURNE
UNIVERSITY OF
TECHNOLOGY

Valentin Ivannikov

PhD Thesis

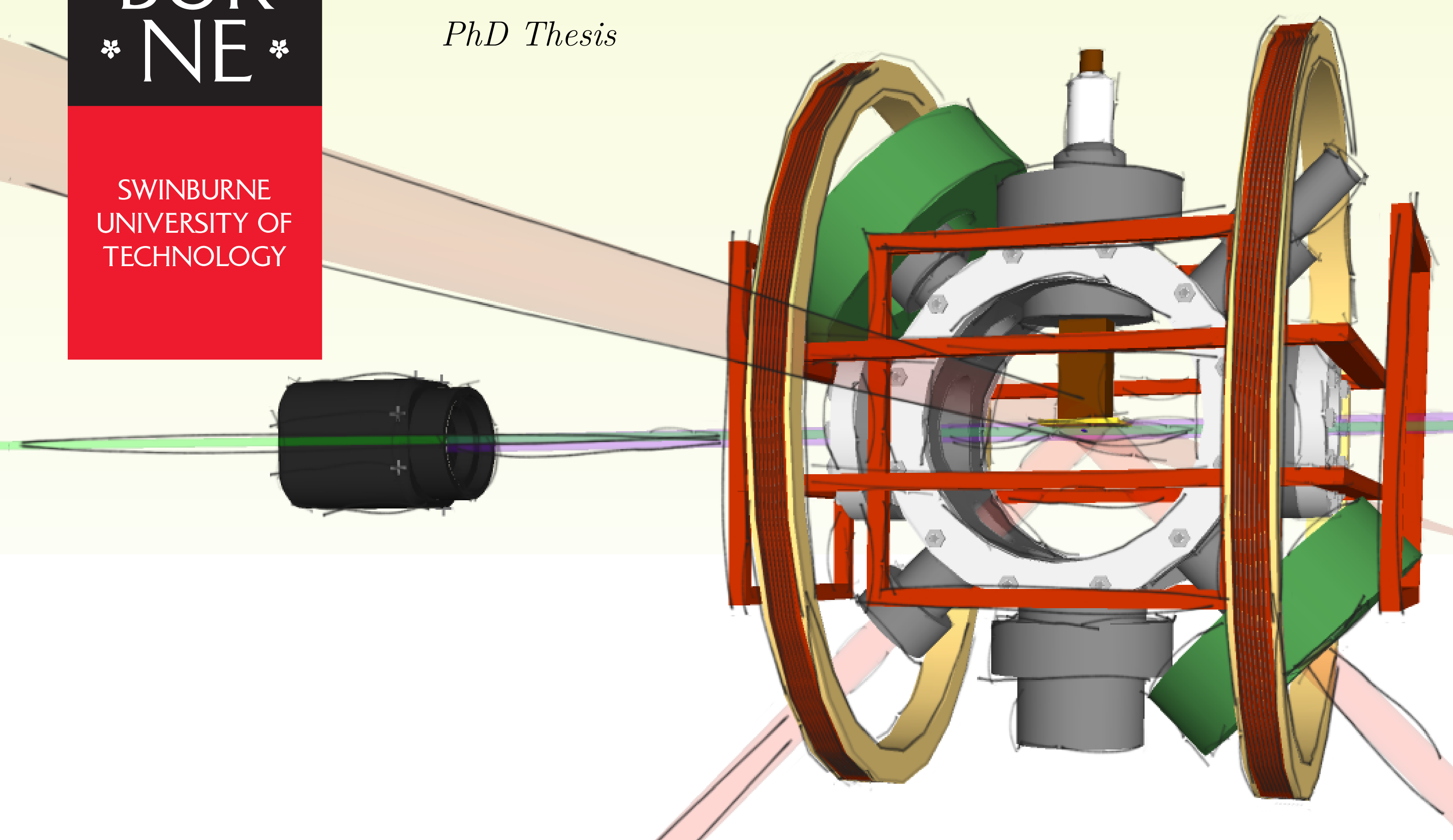

Analysis of a trapped atom clock with losses

Centre for Atom Optics and Ultrafast Spectroscopy
Swinburne University of Technology

Supervisory Panel

Prof. Andrei Sidorov
Dr. Brenton Hall
Prof. Sergey Pulkin
Prof. Russell McLean
Prof. Peter Hannaford

Melbourne, Australia
August 2013

Abstract

We present a number of analytical means for the analysis of the evolution of an atom clock, emphasizing the role of many-body processes in the population and coherence loss. A master equation with one-body and two-body losses included is presented for a thermal cloud ensemble, suitable for modelling atom clock evolution. Approximate solutions for the coupled rate equations with one-body and two-body losses are obtained for the case of Ramsey free evolution, and their validity is analyzed. An approach is suggested to combine the analytical trap-induced fringe envelope function with a numerically evaluated many-body envelope function.

A set of Ramsey and spin echo models is offered with analytical solutions for the off-resonant and on-resonant regimes with one-body population loss and phenomenological dephasing. Their detuning spectra are presented and the difference between them and the standard Ramsey model is shown: the Rabi pedestal in the present model has no spectral ripples due to the $\pi/2$-pulse duration equal to a quarter of a Rabi oscillation, even off resonance, in contrast to the Ramsey method where the $\pi/2$-pulse duration is not corrected off resonance and causes spectral ripples.

An interferometric fringe in long evolution experiments is typically measured with a visibility decay primarily due to phase diffusion, phase instability, trapping effects and many-body losses. It constitutes a problem to extract parameters from a fringe obtained in the time domain because of the growing uncertainty of the fringe amplitude and phase. This visibility loss can be compensated for systems with unequal state population losses, as the one we have, by tailoring the pulse durations. Methods are suggested for the one-body and many-body cases.

A comprehensive set of experiments is conducted on the characterization of the stability of the trapped atom clock: with condensate and thermal cloud ensembles, with phase-domain Ramsey and spin echo interferometries, with synchronization from a rubidium frequency standard and from an oven-controlled quartz oscillator. The types of noise present in the system are identified by means of an Allan deviation analysis. Despite the 50 times different cloud densities of the condensate and the thermal clouds, an equality of the phase stability in the Ramsey interferometry with BEC and thermal clouds is demonstrated. The spin echo interferometry has shown a slightly superior stability with the thermal clouds as compared to the BEC.

Acknowledgements

During the years of work on this thesis there have been so many people without whom the work would not have been completed successfully that I have reservations to state it has all been on my own and would like to express my gratitude to those who have made it happen together with me.

At the time I joined Swinburne in 2009 the atom chip group had reached a good level of development and the carrier of all the knowledge was one of my predecessors, Russell Anderson. Russ was completing his thesis and was infectious with his attitude to research; he was setting the standard. Much of the later group activity was based on his achievements. A year later, perhaps for something good in the past, I was awarded Shannon Whitlock, my dearest postdoc who was on a short visit from Amsterdam to shine in the group again as years before my arrival when he was a graduate student at Swinburne. It was a very practical time; Shannon was a living example of how research should be done. It is him to whom I am most indebted for sharing knowledge, help and support. And for the revitalizing buzz.

I greatly appreciate my participation in the world scale research and the visits to the best scientific schools and laboratories during my studies, owing to the care of my supervisors and the opportunities we have had at Swinburne. It was an unforgettable experience to attend the lectures of Nobel prize winners during ICAP 2010 in Cairns. A particular imprint was left by École de Physique des Houches: an amazing syllabus that makes your brain burn and shows what the community expects from you when the PhD is over. We have also had adorable Physics courses and invited talks at CAOUS and I wish to thank Peter Hannaford and Russell McLean for arranging such a brilliant research program.

I extend my thanks to the supervisors: Andrei Sidorov for coordinating research, Peter Hannaford for the help in strategical questions, Russell McLean for his support throughout the studies, Brenton Hall for helping out in the laboratory, and Sergey Pulkin (Сергей Пулькин) for discussions and his suggestion in 2008 to join Swinburne. And I particularly thank all the supervisory team for participating in thesis discussions and proof-reading. Separate thanks to our theoretical group at Swinburne, especially to Bogdan Opanchuk for the involved consultations and

Laura Rosales Zárate (now I am crossing continents with your handmade coffee cup!).

On the other side of the thesis there were many friends, far away from Australia, but so close to my heart. I thank my old group mate Olya (Оля Харькова) for her kindness and moral support, my warm ever-supporting Manoj Nambiar and Nandula Ramanarasimha (I keep your McDonald's note next to me, Ramu!), Artem (Артём Трифонов), Yavor (Явор Коларов). Thank you guys for your kindness and flamboyant personalities.

I express my limitless gratitude to Amy (宇羊) for her heartly warmth and support during my hard times. And most of all I am thankful to my parents for their infinite patience.

Declaration

I, Valentin Ivannikov, hereby certify that this thesis:

- contains no material which has been accepted for the award of any other degree or diploma, except where due reference is made in the text of the thesis;
- to the best of my knowledge contains no material previously published or written by another person except where due reference is made in the text of the thesis; and
- where the work is based on joint research or publications, discloses the relative contribution of the respective workers or authors.

21 August, 2013
Valentin Ivannikov

Иванников

Contents

List of figures

Chapter 1

Introduction

A long time after the discoveries of stimulated emission and the laser, implementation of high-precision spectroscopy methods for laser line stabilization [1] and a series of revolutionary cooling methods for neutral particles [2–7], Bose-Einstein condensation was finally obtained [8, 9], seventy years after its theoretical prediction by Bose and Einstein [10–15]. The development of Doppler-free spectroscopy has first enabled the direct observation of the fine structure [16] and then allowed to access single hyperfine structure components [17, 18] which became the basic tool in the state preparation of cold atoms. The technological breakthroughs in cold atomic beams over almost a century has led to new incarnations of NMR techniques; Rabi and Ramsey inteferometers [19–21] and the subsequent implementation of atomic clocks [22–24], magnetometers [25], and high-precision measurements [26] of gravity [27], gravity gradients [28] and rotations by atomic gyroscopes [29], and the photon recoil of an atom [30, 31].

With the development of atom chips [32, 33] it became possible to create microtraps with well defined magnetic field potentials and high field gradients, suitable for magnetic trapping of neutral atoms [34–38]. Since their invention atom chips have become a universal test bed for fundamental experiments [39–44] and a variety of applications [45–54]. Trapping has drastically increased the interrogation time; the atoms have become available in experiments for minutes before they are lost from the trap. Neutral atom traps suffer from inhomogeneous potential profiles which cause ensemble spin dephasing. Moving in the trap, thermal atoms occupy energy levels according to the Maxwell-Boltzmann statistical distribution. They traverse the trap in different directions changing their orientations with respect to the quantizing field and, as a consequence, they are excited by a mixture of the atomic polarizations σ^+, σ^- and π. Eventually, the ensemble acquires a motionally averaged ensemble spin [55]. At the same time the interrogating field has a finite frequency stability that is well approximated by a normal distribution around the clock resonance. These trapping effects limit the ensemble coherence time, one by inducing atomic dephasing and the other by introducing reference frequency fluctuations.

However, the coherence has in a thermal cloud recently been shown to extend over a surprisingly long time owing to the formation of spin waves in the atomic sample, the identical spin rotation effect (ISRE) [56]. ISRE makes the ensemble spin dephasing negligible by bringing into the interaction atoms of an ensemble that are divided into slow and fast velocity classes. The interaction of the corresponding collective spins of the slow and fast classes keeps them in mutual precession. If the ISRE conditions are fulfilled, the mutual precession is tight, and the total ensemble spin stays focused over substantial periods of time. In experiments with the Ramsey method of separated oscillatory fields [20] the projective detection reveals high visibility [56–58].

As to a fundametal limitation, we pay dedicated attention to the phase diffusion and the sources of noise perturbing the system. An extensive frequency stability analysis is presented for all experimental cases.

The Ramsey visibility function also depends on the many-body collisional processes. Cold atomic collisions induce both atomic number loss and mean-field energy level shift. Since the hyperfine ground states of ^{87}Rb have spherically symmetric wavefunctions, the collisional shift of the transition frequency is well described by the s-wave scattering lengths [59] that can be measured in Ramsey experiments. The atom number losses gradually destroy ensemble phase, such a phase loss accompanies the Ramsey free evolution resulting in a fringe visibility envelope. This is different from the collisional shift that does not affect the fringe visibility. This brings us to the Liouville–von Neumann equation with a loss term that is used to model the ensemble dynamics. Its classical version with exponential decays of populations is equivalent to the master equation describing one-body losses. In a physical system this loss term accounts for vacuum limitations, i.e., for finite pressure causing hot background gas particles to collide with the cold trapped atoms and to transfer a momentum large enough to escape from the trap. However, in high density clouds the rate of two-particle collisions is high and additional channels of population decay should appear in the formalism in addition to one-body losses. For the atom clock states of ^{87}Rb these channels are the intra-state and inter-state two-body collisions that add three additional terms to the corresponding coupled rate equations. They also add terms to the off-diagonal elements of the density operator that govern the phase evolution. In this thesis we present a version of the master equation with the relevant many-body loss terms included in the model. This equation (Eq. 3.60) should be used for the appropriate modelling of lossy evolution in Ramsey interferometry instead of its one-body counterpart (Eq. 3.13). In condensates three-body recombination, leading to Rb_2 molecule formation, is also present [60–63], but it plays a minor role in thermal ensembles because of the much smaller atomic densities and the small value of the three-body relaxation rate [64, 65]. According to the known many-body population relaxation constants and typical experimental conditions this model is of particular value for systems with very long coherence times. In thermal clouds, routinely used in atomic frequency standards, the dominant loss processes are one-body and two-body collisions.

Atoms with a magnetic moment are susceptible to the ubiquitous magnetic field noise that perturbs energy levels in interferometry. The states involved in interferometry can be decoupled from the ambient magnetic field noise by utilizing the nonlinearity of the Zeeman effect. At the "magic" field the atomic transition becomes insensitive to the magnetic noise up to the first order in magnetic field centred around the "magic" value. The second-order contribution is already much smaller than can be observed in our experiments, amounting to units of mHz. In dedicated experiments magnetic shielding is also used to reduce the noise reaching the atoms.

The high density ensembles constantly interact losing bits of phase information in collisional events. In Ramsey free-evolution collisions lead to phase diffusion and ensemble spin dephasing. This diffusion can be alleviated by employing a spin echo [66], as we do in this thesis, or a more advanced dynamic decoupling technique [67–69].

In the Bose-Einstein condensate regime the clouds have orders of magnitude higher density than thermal clouds. In two-state interferometry experiments the two modes of the condensate produce collective oscillations if the state scattering lengths are different [70]. In this work we study the phase stability of condensate interferometry and relate it to the stability of conventional thermal atom interferometry.

We offer a set of Ramsey and spin echo models for the off-resonant and on-resonant regimes with one-body population loss and phenomenological dephasing. Their detuning spectra are given and the difference between them and the standard Ramsey model is shown: the Rabi pedestal in the present model has no spectral ripples due to each $\pi/2$-pulse duration being equal to a quarter of a Rabi oscillation, even off resonance, in contrast to the Ramsey method where the $\pi/2$-pulse duration is not corrected off resonance and causes spectral ripples.

An interferometric fringe in long evolution experiments is typically measured with a visibility decay primarily due to phase diffusion, phase instability, trapping effects and many-body losses. It constitutes a problem to extract parameters from a fringe obtained in the time domain because of the growing uncertainty of the fringe amplitude and phase. This visibility loss can be compensated for systems with unequal state population losses, as the one we have, by tailoring the pulse durations. Methods are suggested for the one-body and many-body cases.

1.1 Thesis structure

In this thesis we present a set of analytical means and models for a wide range of interferometry experiments and provide an extensive study of the atom clock phase stability with the determination of the types of noise present in the experiment. We also present a many-body master equation with one-body and two-body losses included; this master equation is appropriate for the modelling of the evolution of the atom clock. As a generalization, a third-level extension of the loss term of the master equation is offered.

In Chapter 1 we reviewed the main achievements in the fields of lasers and cold atoms that made it possible to reach the current stage of development and to conduct the present study.

In Chapter 2 we present the main figures on the apparatus construction, its characteristic parameters and describe measurements of coupling strengths. This chapter describes the optical excitation schemes used in the experiment with corresponding data of the absorption, saturated absorption and polarization spectra identifying the D_2-line transitions of a natural mixture of isotopes ^{85}Rb and ^{87}Rb.

In Chapter 3 a set of off-resonant and on-resonant Ramsey and spin echo type models is presented. Analytical solutions are given for the case of one-body losses and a numerical solution of the many-body model including one-body and two-body losses is presented. All the models incorporate a phenomenological dephasing. The many-body master equation is given in Eq. 3.60 and it is demonstrated that the Ramsey fringe envelope function departs from an exponential or hyperbolic secant (sech) shapes.

In Chapter 4 we present phase stability measurements and identify the types of noise. The analysis is performed for all relevant experimental cases: with thermal atoms, with a BEC, in phase-domain Ramsey and spin echo interferometries, with an oven-controlled quartz oscillator and a rubidium frequency standard. The fractional frequency used in the analysis is taken both corrected and uncorrected for atom number fluctuations, where relevant.

In Chapter 5 concluding remarks and a brief summary of the thesis are presented.

In the Appendices we provide a list of relevant ^{87}Rb hyperfine transition frequencies (Appendix A), a detailed vacuum system bakeout schedule (Appendix B), and summarize the laser cooling lower temperature limits for each of the cooling methods used in our experiments (Appendix C).

Chapter 2

Experimental apparatus

In the present chapter we discuss the details of the implementation of the experimental apparatus. The apparatus description can be split into several aspects: laser sources, field configuration, physical apparatus geometry, electronics, operation and quantum state preparation sequence. The optical sources, based on custom coated laser diodes in combination with commercial laser heads, provide a linewidth in the order of a few hundred kHz. This allows us to build laser sources suitable for high precision optical spectroscopy of the hyperfine split magnetic levels of ^{87}Rb. The trap fields are created by a number of coil pairs ranging in response time to suit the needs of the control sequence. We provide an accurate description of the physical layout, including the atom chip, that establishes the relations between the other elements of the setup. Overall, the apparatus allows us to conduct high precision experiments based on Ramsey or spin echo inteferometry such as an atom clock or a radiation shift interferometric sensor. The key system parameters are provided as well as the exact models of the equipment.

The purpose of the complete system [71] is to prepare a ^{87}Rb Bose-Einstein condensate (BEC) or a thermal atomic cloud in the stretched $|1, -1\rangle$ state[1]. The preparation starts from the magneto-optical trapping (MOT) of a rubidium vapour. Then the atoms are transferred to the atom chip based microtrap and undergo sub-Doppler cooling and subsequent optical pumping to the $|1, -1\rangle$ state. From there the atoms are transferred to the magnetic trap. In this final stage the magnetic field can be set to a “magic” value that protects the clock transition from ambient magnetic noise, significantly extending the lifetime.

We describe the methods used for detection, including microwave adiabatic population transfer followed by Stern-Gerlach separation of the states and dual state imaging [72]. Finally, we outline the data post-processing methods that reduce the number counting uncertainty to the shot-noise level.

---

[1] The system was also used to obtain a condensate in the $|2, +2\rangle$ state [71].

2.1 Optical system

Four independent diode lasers are used to cool and trap in the MOT, to cool below the Doppler limit by polarization-gradient cooling (PGC), repopulate states (RP, repump), optically pump (OP) and image (IMG) ^{87}Rb atoms. Optical transitions of the D_2 line fine-structure doublet component, $5^2S_{1/2} \rightarrow 5^2P_{3/2}$, are used (Fig. 2.1). The lasers are first coarsely tuned by tilting the external cavity grating and monitoring the laser spectra with an optical spectrum analyzer with sub-nanometer resolution. Then the grating piezo actuator voltage is periodically modulated and scans across a few-GHz range, roughly the scale of the frequency hops induced by returned diffraction modes from the grating. When the Rb absorption resonances overlap with the scanned range, slowly shifted by the coarse grating tuning, the vapour produces a fluorescent trace in the rubidium cell[2]. The blinking trace is monitored by an infrared viewer, its intensity is facilitated by a Peltier element that is driven by 1.5 A to provide +60°C temperature. Once the

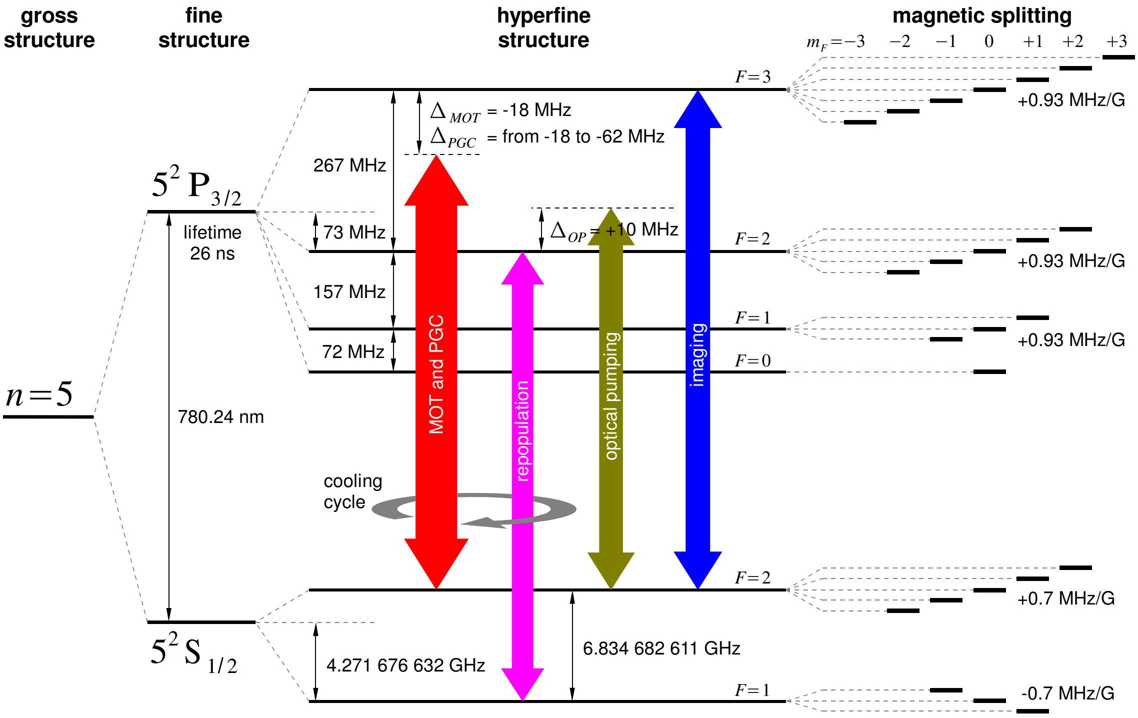

Figure 2.1: Diagram of ^{87}Rb energy levels. The two-level laser excitations are shown with level designations as they are seen in the saturated absorption spectrum (Fig. 2.7), without light polarizations taken into account. $5^2P_{3/2}$ has a lifetime $\tau \approx 26$ ns. Linear Zeeman splitting adequate for a weak magnetic field, like B_{Earth}, is shown for the Zeeman sublevels. The ground state $F = 1$ and $F = 2$ magnetically split levels in the "magic" B-field of 3.228 G are given in Appendix A.

---

[2] Toptica CE RB 50 Rb-gas cell with the natural abundance of isotopes ^{85}Rb (72.2%) and ^{87}Rb (27.8%); windows are 2-mm thick with optical quality, length 5 cm, diameter 26 mm. Four identical vapour cells are used in the apparatus (Figs. 2.2 to 2.5), placed on a Peltier oven heated to +60°C to enhance fluorescence.

trace is found, further tuning continues with precision methods by adjusting the bias and ramp voltages of the piezo to correspondingly shift and zoom the laser frequencies onto the atomic resonances. In this way a single zero crossing needs to be located inside a single piezo ramp for the locking electronics to find the right error signal minimum and lock onto it. The PID controller should be adjusted so that the locking is tight to minimize laser linewidth and stable enough to operate in the lab noise environment. The laser sources are mounted on a pneumatically damped optical table isolated from the vacuum chamber with the atom chip. The optical signals are decoupled by single-mode polarization maintaining (PM) fibers which provide nearly ideal Gaussian spatial mode intensity profiles.

2.1.1 MOT laser source

The MOT laser is locked to the cycling transition $5^2\mathrm{S}_{1/2}(F_g = 2) \rightarrow 5^2\mathrm{P}_{3/2}(F_e = 3)$ and is used for two purposes: magneto-optical trapping (MOT) with detuning $\Delta_{MOT} = -18$ MHz and polarization-gradient cooling (PGC) with detuning Δ_{PGC} ramped from -18 MHz to -62 MHz (Fig. 2.1). The laser head (Fig. 2.2) is a commercial Toptica DLX110, a nominally 800 mW laser diode with an anti-reflection (AR) coated front facet placed in a closed thermally stabilized housing. It has an external cavity in Littrow configuration with the grating mounted on a piezo actuator. The high-quality AR-coating in combination with the external grating provides a linewidth of the order of a few hundred kHz, suitable for optical spectroscopy of the excited levels. The zeroth order diffraction beam from the grating, of nearly the same power as the laser diode output, passes through the -60 dB optical isolator and propagates to the polarizing splitter PS1, where 4% of the power is split off to the spectroscopy and locking circuit. The $\lambda/2$-waveplate regulates the polarization so that PS4 transmits all power to AOM2[3], the double-pass acousto-optical Bragg frequency shifter (acousto-optical modulator, AOM). The one-pass AOM efficiency is routinely measured to be 80%. Approximately 64% of the power returns back to PS4 after the double-pass with 90°-rotated polarization at the $\lambda/4$-waveplate and $+70.2$ MHz shift as measured by a frequency counter[4].

Unlike the imaging source, the double-pass AOM is not used for frequency shifting of the power beam, because the loss would amount to 36%, or 70 mW. Instead, the AOM is placed in the low-power (circa 8 mW) spectroscopy part to *lock* the laser onto a different transition. Hence, the minus sign appears in the

---

[3] An acousto-optic Bragg cell ISOMET 1205C with a deflector driver ISOMET D301B.

[4] Thurlby Thandar Instruments TF830.

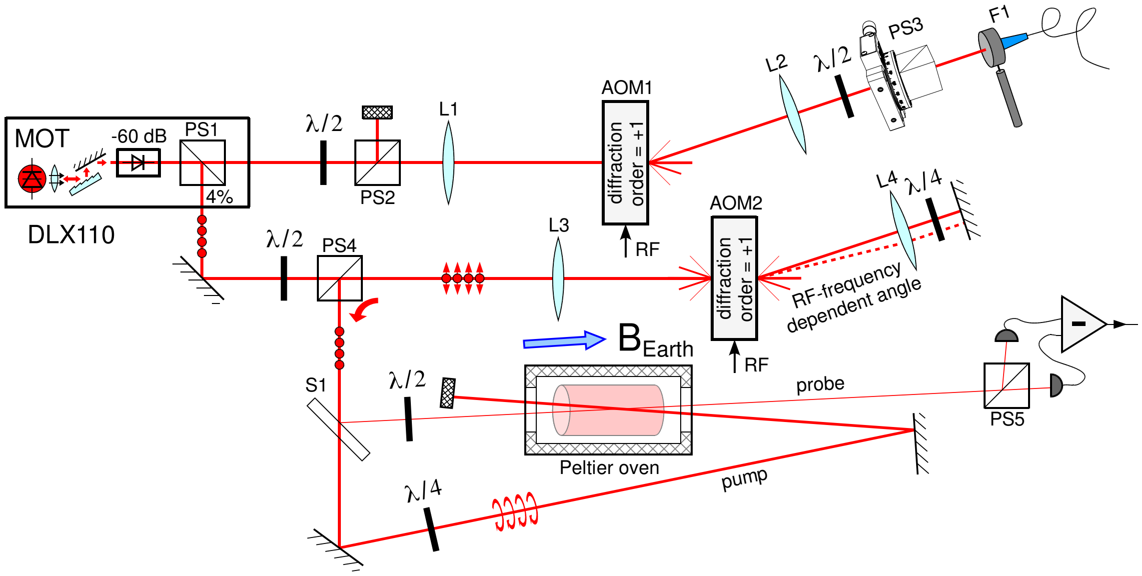

Figure 2.2: MOT-laser source principal schematics, top view. The diode laser with a sub-MHz linewidth is locked to the cycling transition $5^2S_{1/2}(F_g = 2) \rightarrow 5^2P_{3/2}(F_e = 3)$ having a strong polarization resonance, but operates at a detuned wavelength: $\Delta_{MOT} = -18$ MHz and $\Delta_{PGC} =$ from -18 to -62 MHz. Optical power after PS1 at the 96% port is 450 mW, power at the fiber output is 200 mW, frequency scanning range 7 GHz. Mirror-MOT beam diameters at the cloud are 3 cm. PS3 is installed on a rotary mount to filter off a linearly polarized light at different angles. Legend:

L – lenses with focal lengths of 40 cm;
S – 4/96 non-polarizing glass-slab beam splitter;
F – fiber coupler with a lens in its construction;
RF – radiofrequency signals;
PS – 50/50 polarizing beam splitter cubes, except PS1 with 4/96 splitting ratio;
AOM – acousto-optical modulators.

MOT detuning Δ_{MOT} calculated for Fig. 2.2 as:

$$\Delta_{MOT} = f_1 - 2\underbrace{f_2}_{var}$$

where f_1 and f_2 are the AOM1- and AOM2-driver frequencies, resulting in $\Delta_{MOT} = 122.4 - 2 \times 70.2 = -18$ MHz. The same formula is valid for the Δ_{PGC} calculation. The beam returned from the double-pass AOM is completely reflected by PS4 to the polarization spectroscopy in a vapour cell [73, 74] where an error signal is generated and read from the balanced polarimeter (PS5, the two photodiodes and the subtractor [75]). The vapour cell is placed on a Peltier element heated by a 1.5 A current to +60°C to enhance fluorescence. The balanced polarimeter signal is modulated by the Toptica SC110 scan control and fed to the Toptica PID110 regulator for laser stabilization. The piezo actuator and scan control span a 7 GHz frequency range.

Doppler-free polarization spectroscopy [73, 74] utilizes the birefringent property of Rb vapour to change the linear polarization of the probe to elliptical polarization: the *Faraday rotation* induces rotations of opposite sign in the vapour for the σ^+ and σ^- components [76, 77].

The remaining 96% of the power from PS1, normally constituting 450 mW to give 200 mW at the fiber output, is attenuated by the $\lambda/2$-waveplate and PS2 pair, enters AOM1[5] and is shifted by +122.4 MHz. This AOM1 is driven by a fixed-frequency RF-signal to preserve beam position for further coupling to the fiber[6]. Δ_{MOT} is controlled via computer by varying AOM2 RF-frequency.

The light intensity entering the spectroscopy block at PS4 is attenuated by the half-wave plate and PS4. The pair of lenses L1 and L2 with focal lengths of 40 cm are installed to achieve the maximal 80% AOM-transmission efficiency for the relevant diffraction order by increasing the beam intensity at the lens foci where the AOM is placed. L3 and L4 are of the same focal lengths. L4 additionally achieves independence of the returning beam position due to the angle-to-displacement conversion at L4 and the perpendicular reflection after it. Undesirable ellipticity in the light polarization is removed before the PM-fiber coupling by a $\lambda/2$-waveplate in combination with PS3 installed on a rotary mount. By simultaneously changing the angle of the $\lambda/2$-waveplate and PS3 a transmission maximum of linear polarization can be found with zero ellipticity.

2.1.2 Repumping source

The population of atoms pumped to the short-lived $5^2P_{3/2}$ level with lifetime $\tau \approx 26$ ns is lost to the dark state $5^2S_{1/2}(F_g = 1)$ via spontaneous emission in the cooling cycle (Fig. 2.1). The repump[7] returns atoms to the respective process[8] by exciting to an optical state with short lifetime and redistributing them back to the ground state, where they can only reside in $F_g = 2$, because from $F_g = 1$ they are continuously excited to $5^2P_{3/2}$. The repump laser (see Fig. 2.3) is locked to the saturated-absorption peak of the $F_g = 1 \rightarrow F_e = 2$ transition. $F_e = 2$ has been chosen in favour of the alternative $F_e = 1$, because its Clebsch-Gordan coefficients are larger by approximately an order of magnitude and repumping occurs correspondingly faster. The saturated-absorption inset in Figure 2.7 is taken with the spectroscopy arrangement of this laser source. Doppler-free saturated absorption spectroscopy [78] on counter-propagating beams [17, 18] is performed with peak-locking rather than locking to a polarization resonance that could bring the laser

---

[5] An acousto-optic Bragg cell ISOMET 1206C with a deflector driver ISOMET D323B-788.

[6] Fiber OZ Optics PMJ-A3A-3AF-800-5/125-3-5-1, coupler HPUC-23AF-800-P-6.2AS-11.

[7] Repopulation pumping.

[8] Repumping is also used during optical pumping and imaging in some cases. For example, imaging of $|1, -1\rangle$ is often performed with the MW-RF two-photon pulse and the repumping light in the absence of the MW adiabatic passage.

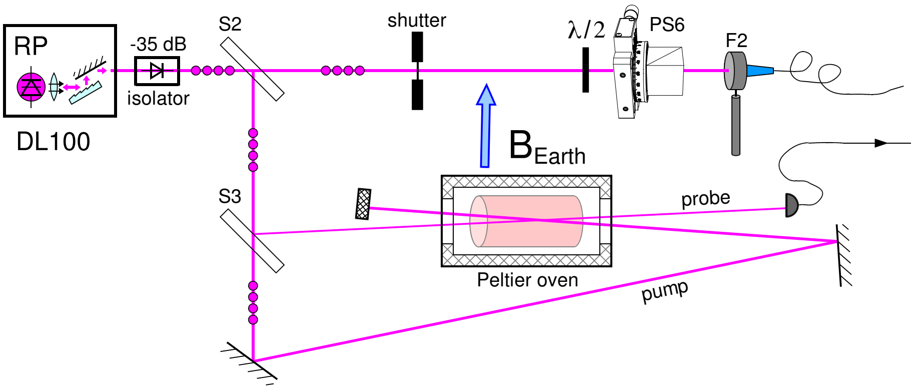

Figure 2.3: Repumping laser source principal schematics, top view. The diode laser with a sub-MHz linewidth is locked to the cycling transition $5^2\mathrm{S}_{1/2}(F_g = 1) \rightarrow 5^2\mathrm{P}_{3/2}(F_e = 2)$ with a weak saturated-absorption resonance. Optical power at DL100 ouput is 35 mW, at the fiber output is 11 mW; frequency scanning range is 1 GHz. Beam diameter at the cloud is 3.5 mm with power 0.1 mW. PS6 is installed on a rotary mount to filter off linearly polarized light at different angles. Beam shutter is controlled from a computer and has a 0.1 ms smooth transient measured by the beam-power drop. Legend:
S – 4/96 non-polarizing glass-slab beam splitters;
F – fiber coupler with a lens in its construction;
PS – 50/50 polarizing beam splitter cube.

slightly off-resonance at zero-crossing. Such a scheme makes the spectroscopy arrangement trivial, removes AOMs and polarizing optics (cubes and waveplates) at the cost of a low-contrast resonance used for error signal generation.

The laser is a Toptica DL100, an external cavity diode laser with the grating in Littrow configuration and a direction-correcting mirror [79] which gives 35 mW of optical power. The diode laser is custom AR-coated to achieve a sub-MHz linewidth. A saw-tooth voltage is applied to the grating piezo actuator by the Toptica SC100 scan control. The generated spectrum is read out by the photodiode, passes through an integrating amplifier, and is fed to a Toptica Lock-in Regulator LIR100 for laser frequency stabilization. To derive the zero-crossing signal required for the lock-in electronics, the photodiode response is differentiated. The main power of the frequency stabilized laser emanates from S2 to the beam shutter[9], passes through a polarization cleaner consisting of a $\lambda/2$-waveplate and PS6, and enters the PM-fiber[10]. Optical power at the fiber delivery end amounts to 11 mW. The RP beam of diameter equal 3.5 mm coaxially overlapped with an optical pump of 2 mW of a diameter 6 mm at the cloud is 0.1 mW.

The photon scattering rate (Eq. 2.2) induced by the MOT light is not high for $\Delta_{MOT} = -18$ MHz to the $F_g = 1$ and $F_g = 2$. Hence resonant repopulation requires a weaker beam intensity than that of the MOT beam; empirically, repopulation no

---

[9] All the four shutters in the apparatus are Uniblitz LS6T2, complemented with shared three-channel shutter drivers Uniblitz UMM-D3. See Figs. 2.3 and 2.6.

[10] Fiber OZ Optics PMJ-3AF-3AF-633-4/125-3-5-1, coupler HPUC-23AF-800-P-6.2AS-11.

longer limits MOT-loading when its optical power reaches 5% of that of the MOT[11]. For a MOT beam fiber output of 200 mW, the repopulation beam is only 7 mW at PS17 (Fig. 2.6) where they are mixed with identical beam diameters of 3 cm in the vacuum. When working in combination with optical pumping, this power is also sufficient because optical pumping is resonant, has the same beam diameter at the cloud location and a commensurate power of 3 mW at the fiber output. A small imbalance in the optical intensities of the repump and optical pump is usually compensated by adjusting the laser pulse durations. In the case when repopulation facilitates imaging, its intensity is higher than that of the imaging beams (see Section 2.1.5).

2.1.3 Optical pumping source

Optical pumping follows the sub-Doppler polarization gradient cooling (PGC) stage, after which the atoms are distributed over all the magnetic states from $m_F = -2$ to $m_F = +2$. For BEC preparation in a stretched state[12] the atoms are localized to $|F = 1, m_F = -1\rangle$ by optical pumping with σ^- light [80–83] and a small π-polarization component to let the population relax to $F_g = 1$ magnetic levels instead of getting completely trapped in the maximally stretched $|F = 2, m_F = -2\rangle$. Optical pumping is performed in two stages. In the first stage it is performed simultaneously with a σ^--polarized repumping pulse of 1.5-ms duration to prevent rapid population loss to the dark state $F_g = 1$. In the second stage, the slowly decaying intensity tail, residually penetrating through the closing mechanical beam shutter (Fig. 2.6), extends over the 1.5-ms period for a few hundred nanoseconds. The optimal overlap of the two stages is found experimentally. Optical pumping is off-resonant in MOT; the optimal optical pumping is found at a detuning of $\Delta_{OP} = +10$ MHz [72].

The optical pumping source (Fig. 2.4) is a home-made external cavity laser diode having a similar design and characteristics to a Toptica DL100. It is equipped with a custom AR-coated laser diode that provides a sub-MHz linewidth in the Littrow cavity. The laser head output is 40 mW, and the PM-fiber[13] output power amounts to 3 mW. Laser locking to an atomic transition and stabilization is done by a Moglabs Diode Laser Controller. The source employs a polarization spectroscopy [73, 74] signal for side-locking on the $5^2\mathrm{S}_{1/2}(F_g = 2) \rightarrow 5^2\mathrm{P}_{3/2}(F_e = 3)$ transition, similar to the MOT and imaging lasers, but operates at $5^2\mathrm{S}_{1/2}(F_g = 2) \rightarrow 5^2\mathrm{P}_{3/2}(F_e = 2)$ detuned by Δ_{OP} from it. To control detuning, the scheme comprises a double-pass

---

[11] This includes differences in the beam diameters and intensities at the cloud.

[12] In the next chapters we discuss that the stretched states have the benefit of population trapping that results in lower collisional losses.

[13] Fiber OZ Optics PMJ-A3A-3AF-800-5/125-3-5-1, coupler HPUC-2,A3A-800-P-6.2AS-11.

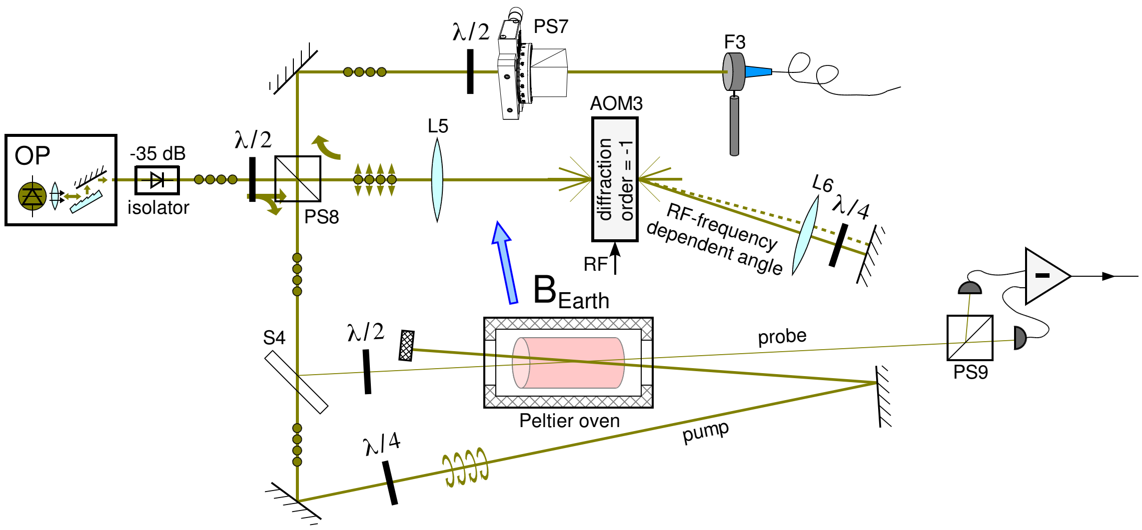

Figure 2.4: Optical pumping laser source principal schematics, top view. The diode laser with a sub-MHz linewidth is locked to the cycling transition $5^2\mathrm{S}_{1/2}(F_g = 2) \rightarrow 5^2\mathrm{P}_{3/2}(F_e = 3)$ having a strong polarization resonance, so that the double-passed beam through the AOM operates at around the next transition $5^2\mathrm{S}_{1/2}(F_g = 2) \rightarrow 5^2\mathrm{P}_{3/2}(F_e = 2)$ at a detuning of $\Delta_{OP} = +10$ MHz from it. Optical power at the ouput of the laser cavity is 40 mW, at the fiber output maximally 3 mW; frequency scanning range is 3 GHz. Beam diameter at the cloud is 6 mm with power 2 mW. PS7 is installed on a rotary mount to filter off linearly polarized light at different angles. Legend:
L – lenses with focal lengths of 40 cm;
S – 4/96 non-polarizing glass-slab beam splitter;
F – fiber coupler with a lens in its construction;
RF – radiofrequency signal;
PS – 50/50 polarizing beam splitter cubes;
AOM – acousto-optical modulator.

AOM shifting the frequency by −257 MHz. The laser is locked to the cycling transition $5^2\mathrm{S}_{1/2}(F_g = 2) \rightarrow 5^2\mathrm{P}_{3/2}(F_e = 3)$ which has a stronger polarization resonance for locking; it is 267 MHz offset from the $5^2\mathrm{S}_{1/2}(F_g = 2) \rightarrow 5^2\mathrm{P}_{3/2}(F_e = 2)$ line around which the optical pump should operate. The $F_g = 2 \rightarrow F_e = 3$ transition could be used for optical pumping, but it would lead to cloud heating due to spontaneous emission of the population trapped in the cooling cycle. The sub-Doppler cooled sample would raise the temperature to the Doppler-cooling limit instead. The detuning Δ_{OP} from $F_g = 2 \rightarrow F_g = 2$ transition depends on the AOM3 driving RF-frequency f_3 according to the relation:

$$\Delta_{OP} = 267\ \mathrm{MHz} - \underbrace{2f_3}_{var}$$

The signal from the −35 dB optical isolator is split on the $\lambda/2$-waveplate and PS8 into a 4% spectoscopy beam and the rest for frequency shifting in the double-pass AOM3 by −257 MHz to provide a detuning of +10 MHz from the optical pump resonance (Fig. 2.1). Detuning control is done via computer; the deflection angle varies with the set RF-frequency, but after normal incidence on the mirror the reflected beam restores the direction after passing AOM3 a second time. The double-pass returns 64% of the entering optical power, rotated by 90° in polarization, back to PS8, from where it is passed to the polarization cleaner and PM-fiber coupling.

2.1.4 Imaging laser source

Imaging should fill the quantum wells of the CCD camera, optimally collecting 40 000 electron counts in the brightest parts of the image. The imaging pulse duration is chosen from the recoil limit to be 100 μs which should satisfactorily saturate the atomic transition by a 1.6 mW imaging beam with 8 mm diameter at the cloud position.

The laser source is a Toptica DL100 with a Littrow-mounted diffraction grating. The laser diode was replaced with a custom AR-coated one that allows sub-MHz linewidths to be achieved. The diffraction grating is piezo-actuated and locked by a Moglabs Diode Laser Controller; its output gives an optical power of 45 mW and a 9-GHz scanning range. The imaging source (Fig. 2.5) is locked to the $5^2\mathrm{S}_{1/2}(F_g = 2) \to 5^2\mathrm{P}_{3/2}(F_e = 3)$ transition (Figs. 2.1 and 2.7).

Imaging detuning Δ_{IMG} is be determined from the following relation:

$$\Delta_{IMG} = 2\underbrace{f_5}_{var} - f_4$$

where f_4 and f_5 are the AOM4- and AOM5-driver frequencies. In zero-field imaging is expected to be resonant, but due to imperfect cancellation of magnetic fields under varying experimental conditions[14] and side-locking, some detuning may be present. To tune to resonance, we measure the absorption versus detuning Δ_{IMG} to find the maximum. To fine-tune the laser line around the resonance, AOM4[15] and AOM5[16] are used: AOM5 for varying the frequency, and AOM4 for bringing it back to zero detuning. The double-pass configuration preserves the beam position from AOM5 back to PS11 during the computer controlled variation of the AOM5 frequency. The AOMs have a central frequency at around 100 MHz; one double-pass would not suffice to operate near the 6-MHz-wide resonance with high efficiency. The AOM4 RF-frequency is fixed to preserve the beam position entering the fiber[17].

The 45 mW beam passes through a moderate isolation of −35 dB and is split

---

[14] E.g. it is unrealistic to recalibrate the imaging in accordince to a different time-of-flight where the atoms are photographed in a magnetic field dependent on the distance from atom chip.

[15] AOM4 is an IntraAction ATM-1501A2 with a home-made deflector driver.

[16] AOM5 is an IntraAction ATM-801A2, accompanied by a home-made deflector driver.

[17] Fiber OZ Optics PMJ-3AF-3AF-633-4/125-3-5-1, coupler HPUC-23AF-800-P-6.2AS-11.

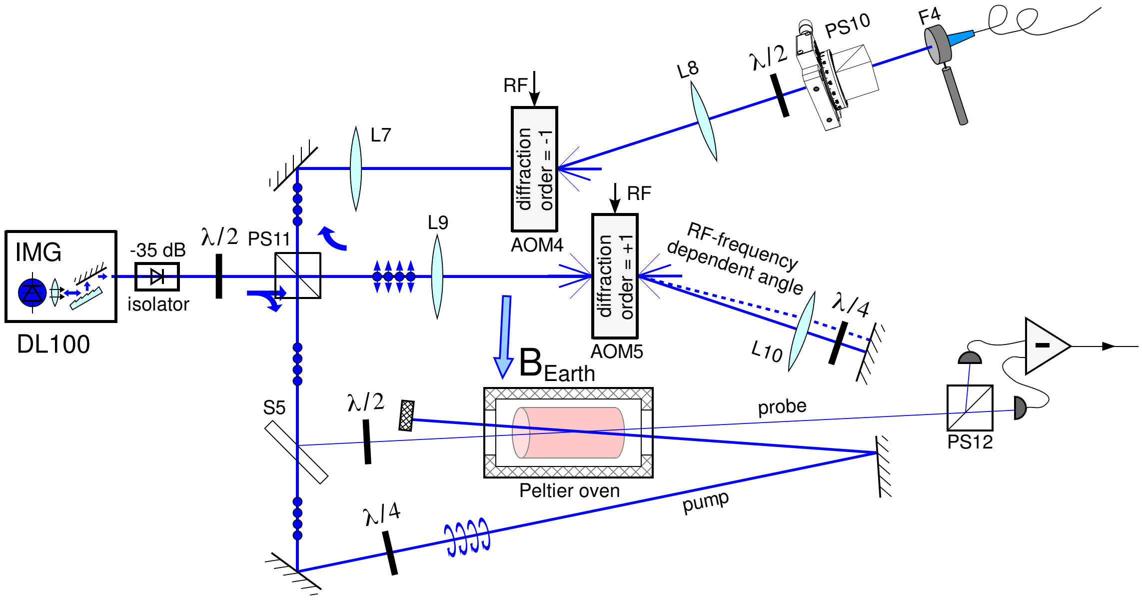

Figure 2.5: Imaging laser source principal schematics, top view. The diode laser with a sub-MHz linewidth is locked to the cycling transition $5^2\mathrm{S}_{1/2}(F_g = 2) \rightarrow 5^2\mathrm{P}_{3/2}(F_e = 3)$ having a strong polarization resonance, with fine adjustment of detuning Δ_{IMG}. Optical power at the ouput of DL100 is 45 mW, at the fiber output maximally 3 mW; frequency scanning range is 9 GHz. Beam diameter at the cloud is 8 mm with power attenuated to 1.6 mW for a 100 μs imaging pulse yielding optimal 40 000 CCD counts per pixel. PS10 is installed on a rotary mount to filter off linearly polarized light at different angles. Legend:
L – lenses with focal lengths of 40 cm;
S – 4/96 non-polarizing glass-slab beam splitter;
F – fiber coupler with a lens in its construction;
RF – radiofrequency signals;
PS – 50/50 polarizing beam splitter cubes;
AOM – acousto-optical modulators.

into two pathways by a $\lambda/2$-plate and PS11 so that 5% of the power is taken to S5 for polarization spectroscopy [73, 74]; the other 95% goes to the double-pass AOM and the coupling to a PM-fiber. The power returning from the double passed AOM5 is completely reflected to AOM4 from PS11 due to the 90° polarization rotation at the $\lambda/4$-waveplate.

2.1.5 Complete system

The complete system with the laser beam configuration, the UHV chamber and the atom chip is shown in Fig. 2.6. The MOT, RP, and OP beams from the laser sources (Figs. 2.2, 2.3, 2.4) are taken out of the PM-fibers by collimators with respective optical powers of 200 mW, 11 mW and 3 mW. The imaging light of 1.6 mW power is taken directly from the fiber; the lens serves as an implicit beam expander and collimator with focal length chosen to produce a beam of diameter 8 mm for satisfactory coverage of the CCD-sensor area (see also Section 2.6.1). To create the mirror-MOT, the linearly polarized MOT light of power 200 mW is

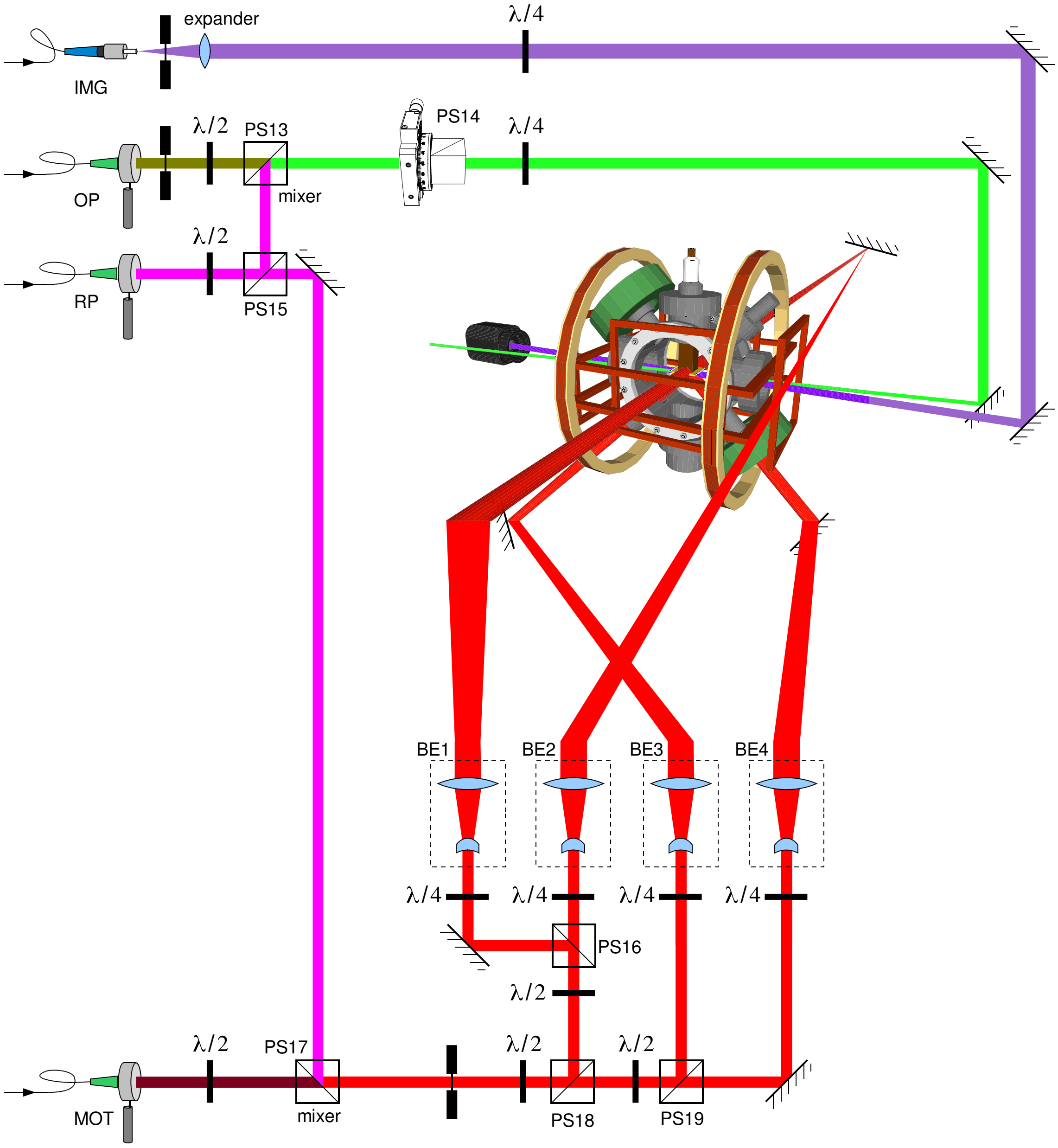

Figure 2.6: Vacuum chamber with atom chip mounted in it, surrounded by coils and the beams sourced from the PM-fibers. The experiment is mounted on a fixed-base optical table with no pneumatic damping to avoid spurious oscillations of cold atoms in the trap. PS14 is installed on a rotary mount to filter off linearly polarized light at different angles. The mirror-MOT is formed by uniformly overlapped 200 mW MOT and 7 mW RP beams after PS17. The IMG beam is set to σ^+ polarization by the $\lambda/4$-waveplate, has 1.6 mW of power, 8 mm diameter at the cloud location and is focused onto the CCD with an objective lens between the UHV chamber and the CCD (see Section 2.6.1). The OP beam of 6 mm diameter and power 2 mW is overlapped at the cloud with the RP beam of 0.1 mW, 3.5 mm in diameter, and is directed to the cloud at an angle of 15° with respect to the imaging axis to miss the CCD. After PS13 the OP and RP are overlapped orthogonally; after the successive PS14 and $\lambda/4$-waveplate their polarizations are coverted to mixtures of σ^- and π. A microwave antenna is abutted to the back 6-inch window of the vacuum chamber. Legend:
BE – beam expander with a miniscus and a biconvex lens outputing a beam of 3 cm in diameter;
PS – 50/50 polarizing beam splitter cubes;
MOT, **RP**, **OP** – collimated fiber output from a laser source;
IMG – fiber output with a consequential lens playing the roles of a beam expander and a collimator; output beam diameter is 8 mm.

uniformly overlapped with repump light of power 7 mW at PS17, passes through a computer controlled beam shutter, is split into four beams with variable attenuation via $\lambda/2$-waveplates and polarizing cubes, transformed into circularly polarized light by the $\lambda/4$-waveplates and is finally expanded through beam expanders BE1-4 to 3 cm in diameter. Two of the four beams are reflected from the gold film on the atomchip (Fig. 2.10) installed inside the vacuum chamber to form the six beams of the mirror-MOT. The MOT and repump beams are also used for polarization-gradient cooling in the counter-propagating σ^+–σ^--configuration [2] which works best in the absence of magnetic field [84].

The OP beam approaching the cloud is 6 mm in diameter and has a power of 2 mW. It is overlapped with a 0.1-mW RP beam, 3.5 mm in diameter, and is directed to the atoms at an angle of 15° with respect to the imaging axis to avoid hitting the CCD-sensor. PS13 overlaps the OP and RP beams. With orthogonal polarizations they are filtered by polarizer PS14 and their purely linear polarizations are converted to mixtures of σ^- and π on the successive $\lambda/4$-waveplate. There is no necessity to overlap the OP and RP beams, but within the limitations of the present vacuum chamber geometry, it simplifies the optical access of the three independent laser beams to the atoms, IMG, OP and RP.

2.1.6 Optical spectroscopy

The optically excited transitions of the fine-structure doublet D_2 line $5^2S_{1/2} \rightarrow 5^2P_{3/2}$ are used for locking of the MOT, RP and IMG lasers. The D_2 line transitions are scanned by the spectroscopy blocks of the IMG and RP lasers and are shown in Fig. 2.7 where all the transitions of the level diagram in Fig. 2.1 can be identified.

Six independent traces are shown in Fig. 2.7: an 11-GHz scan of the saturated-absorption spectrum with sub-Doppler structures resolved (a), Doppler-broadened 11-GHz scan of the absorption spectrum (b), an 11-GHz scan of the polarization spectrum with sub-Doppler features (c), the left-hand side inset of the zoomed-in polarization spectrum of ^{87}Rb $5^2S_{1/2}(F_g = 2) \rightarrow 5^2P_{3/2}(F_e = 1,2,3)$ transitions with cross-over resonances identified (faded color) on the overlapped and biased saturated-absorption spectrum (red faded line), and the saturated-absorption spectrum of the RP laser source vapour-cell containing ^{87}Rb $5^2S_{1/2}(F_g = 1) \rightarrow 5^2P_{3/2}(F_e = 0,1,2)$ lines. The fluorescent signals from the rubidium gas-cells were enhanced by Peltier ovens heating the cells to +60°C, amplified and averaged over 64 successive frames by the oscilloscope[18].

The Rb-gas cell of the imaging source was influenced by the inhomogeneous magnetic field from the closely placed optical isolator. The resulting spectra

---

[18] Tektronix TDS210; signals are read-out via the RF-232 interface and WaveStar software.

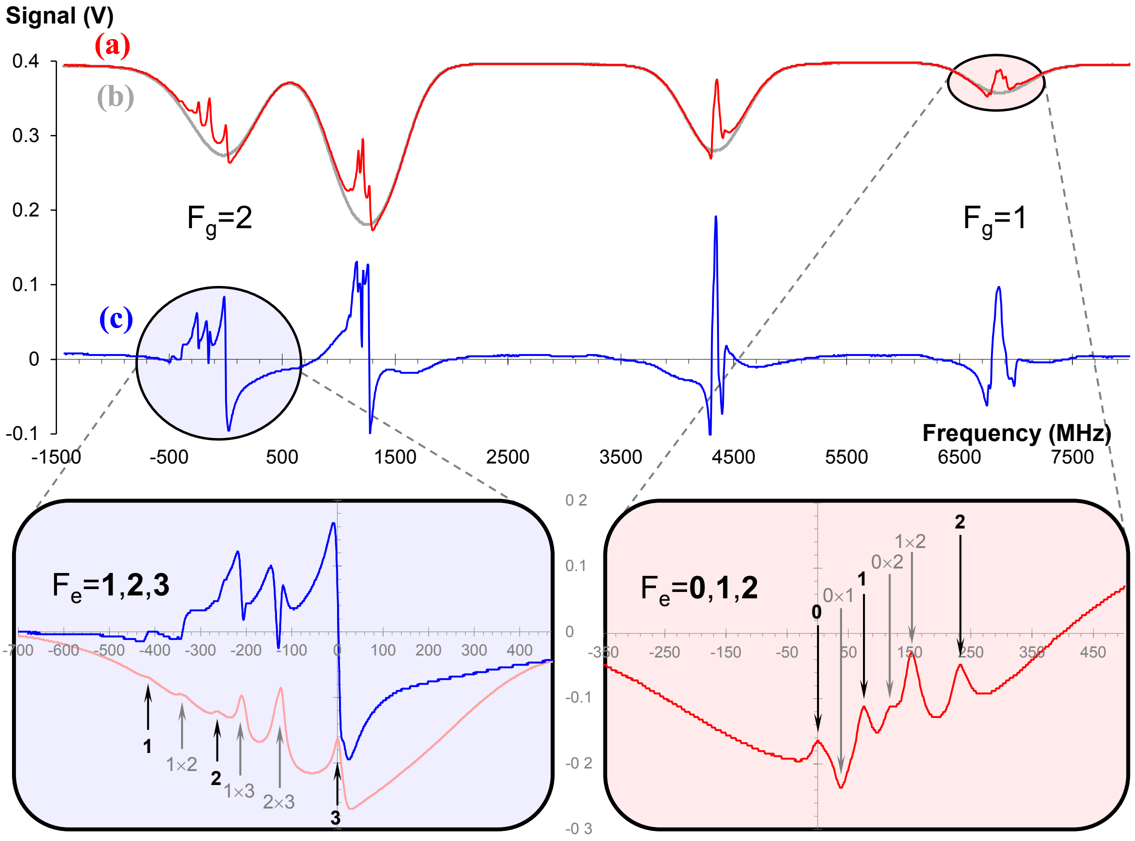

Figure 2.7: Optical spectra of a natural mixture of ^{85}Rb and ^{87}Rb synchronously measured in the polarization spectroscopy arrangement of the imaging laser (Fig. 2.5) and saturated-absorption spectroscopy block of the repump laser (Fig. 2.3). ^{87}Rb transitions are labeled and zoomed in to show $F_g \rightarrow F_e$ resonances:
(a) sub-Doppler saturated absorption spectrum;
(b) Doppler-broadened absorption spectrum;
(c) polarization spectrum; saturated absorption scan is not to scale in amplitude and is only added to accurately locate corresponding polarization resonances.
Optical pumping, imaging and MOT lasers are locked to the polarization resonance of the cycling transition $5^2\mathrm{S}_{1/2}(F_g = 2) \rightarrow 5^2\mathrm{P}_{3/2}(F_e = 3)$. Repump laser is locked to the saturated absorption resonance $5^2\mathrm{S}_{1/2}(F_g = 1) \rightarrow 5^2\mathrm{P}_{3/2}(F_e = 2)$.

Figs. 2.7 (a,c) are distorted compared to the ones expected for a homogeneous B-field. We are interested in two features of these spectra: RP saturated-absorption peak of the $5^2\mathrm{S}_{1/2}(F_g = 1) \rightarrow 5^2\mathrm{P}_{3/2}(F_e = 2)$ transition and the polarization spectral line to which the MOT, OP and IMG are locked $5^2\mathrm{S}_{1/2}(F_g = 2) \rightarrow 5^2\mathrm{P}_{3/2}(F_e = 3)$. These are used for error signal generation and laser diode stabilization.

2.2 Physical geometry

The physical geometry comprises the configuration of fields, positions and orientations of elements with respect to the atoms (Fig. 2.8). The cigar-shaped cloud of atoms with an aspect ratio of 1:10 is oriented along the Z-wire central seg-

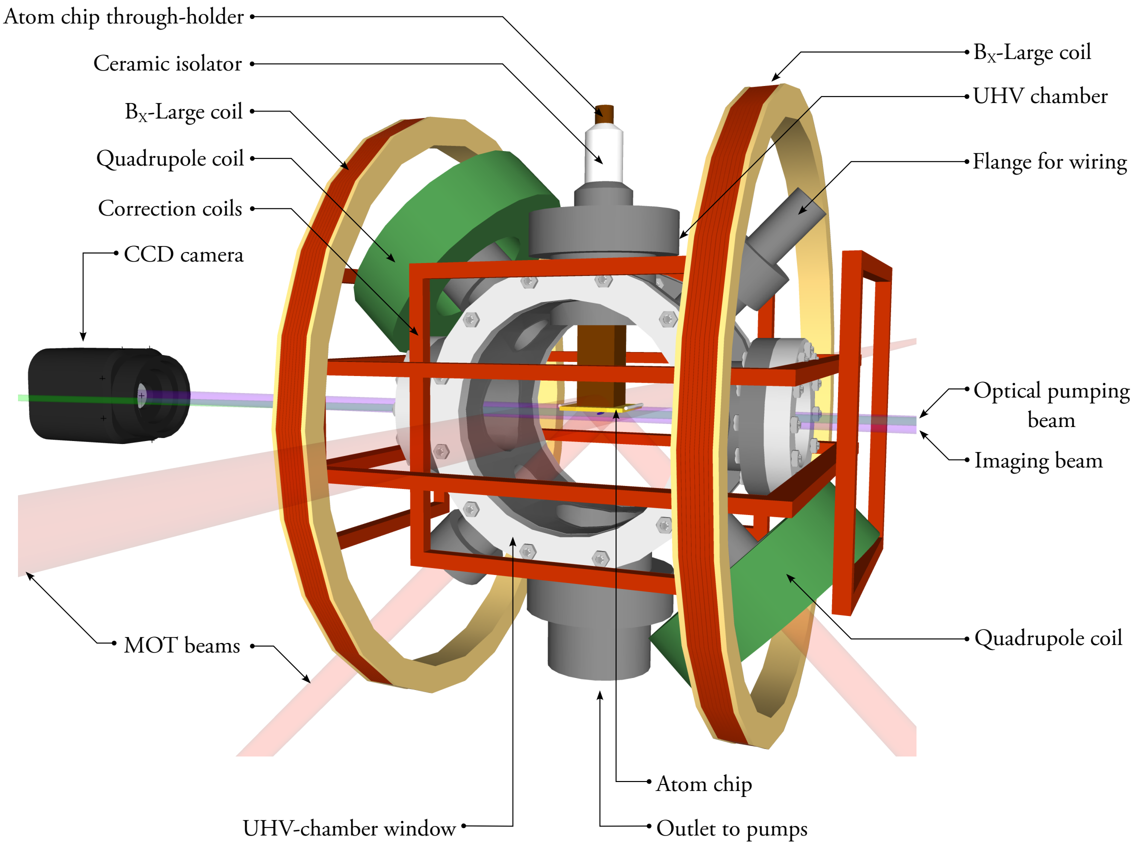

Figure 2.8: Physical geometry of the vacuum chamber with atom chip, laser beams, the coils and the imaging system. The objective abuts to the chamber window facing the CCD camera and is not seen. The atom cloud is depicted by the blue ellipsoid at the beam crossing underneath the atom chip. The MW-antenna is fixed on the glass of the back chamber window and is not seen in the front view. The ultra-high vacuum is supported by the pumps connected via the outlet at the bottom.

ment. The atom chip comprises all wire assemblies to implement necessary atom traps and provide transfers between them with the help of external fields. Even though it is a one-layer chip, both the U-wire trap (quadrupole trap) and the Ioffe-Pritchard trap (transversally biased Z-wire field forming a biased quadrupole trap) are implemented for low-field seeking atoms.

Vacuum chamber

The core of the system, the atom chip, is mounted inside an ultra-high vacuum (UHV) chamber, built of stainless steel with low relative permeability μ_r. Low μ_r is required to enable access of external magnetic fields to the atom chip and atoms nearby; when $\mu_r \approx 1$ the material is transparent to magnetic flux. In the static trapping applications the presence of the chamber can be ignored. However, it is not so for AC fields. Even at relatively low radiofrequencies, the *skin-effect* concentrates electromagnetic waves in a thin layer close to the metal surface. Via this mechanism, AC-excitation spatial modes are largely disturbed and the chamber with all the metallic constituents attached to it cannot be regarded as transparent. This situation is important when RF- and MW-signals are launched into the system, both via an irradiating antenna or feeding to atom chip conductors.

The pressure is monitored with an ion-counter which counts ionized atoms inside the chamber with electrodes installed in the vacuum. The ionic current is directed by the external permanent magnet. The pressure gauge is installed outside and provides high voltage to reach ionization threshold. After sealing the chamber the inner gas is removed by the pre-pump and the pressure is brought to 10^{-6} Torr. Then a turbo-pump pumps to a level of about 10^{-9} Torr. After this, the bakeout starts and runs for a week to obtain another two orders of magnitude pressure drop. After the bakeout, the all-metal valve is sealed to cut access of the mechanical pumps to the rest of the chamber, and the turbo-pump is turned off. Next, a *titanium sublimation pump* is employed: pre-installed in vacuum four Ti-filaments are heated by electrical pulses of up to 55 A and evaporate the metal (see Fig. B.2 in Appendix B). As a result, a thin film of Ti is deposited on the inner chamber surfaces. Titanium is reactive and gaseous substances are likely to be captured upon collisions with the Ti-coated walls and form a solid product. After a while, the Ti-surface will become contaminated and will not be reactive any longer. Then another sublimation and deposition may be needed. After a quick pressure spike due to the sublimation itself, the pressure goes below the level achieved by turbo-pumping and baking out, typically to 2×10^{-11} Torr. At this stage, the *ion pump* is turned on: its electrodes are installed in the chamber, they ionize gases and then remove them by directing in a field to an ion absorber. The ion pump is always on and the Ti sublimation pump is always present in the system, including during experimental cycles. If the ion pump is turned off, within minutes the pressure will rise by several orders of magnitude. This is due to inner wall outgassing and hydrogen atoms from the air outside the chamber percolating through the glass windows, before their partial pressure settles inside the chamber.

The chamber top is crested with a flange with a copper rod that holds the atom chip. All atom chip conductors are electrically isolated from the chamber metal, any external conductors and a common ground. The chamber is rigidly fixed to the optical table, i.e., with no mechanical or acoustic damping. The windows are antireflection coated and tolerate a maximum temperature change of 5° per minute. The bakeout schedule with the accompanying manipulations of the pumps is summarized on the pressure chart obtained from the gauge (see Appendix B).

Quadrupole coils

The pair of coaxial coils installed at an angle off the coordinate planes is the *quadrupole coils*. The current in one is oppositely directed to the current in the other while the magnitudes are kept equal. Due to the identical geometry the fields created by the coils compensate midway between them and form a point of zero field. [85, 86]. These coils have radius $R = 7.5$ cm, are separated by $d = 4R$, the number of turns $n = 400$ and they operate at 10 A. It is not the best ratio for the highest and most linear gradient of magnetic field at the centre of the geometry ($d = R$) but even far from the best ratio, the gradient is high enough and linear over a scale of millimeters. In [85] the magnetic field from an infinitely thin circular wire is decomposed into a series of multipoles to describe the field from a coil. Quadrupole is the lowest order which provides trapping of a magnetic dipole in a local $|\boldsymbol{B}|$-minimum. In Fig. 2.9 all orders are used to calculate the magnetic field potential $|\boldsymbol{B}|$ and the trapping minimum from the analytical expression is given by the formulæ 2.1:

$$\begin{aligned}
B_z &= \frac{\mu_0 I}{2\pi}\frac{1}{\sqrt{(R+\rho)^2+(z-A)^2}}\left(\frac{R^2-\rho^2-(z-A)^2}{(R-\rho)^2+(z-A)^2}E(k^2)+K(k^2)\right)\\
B_\rho &= \frac{\mu_0 I}{2\pi\rho}\frac{z-A}{\sqrt{(R+\rho)^2+(z-A)^2}}\left(\frac{R^2+\rho^2+(z-A)^2}{(R-\rho)^2+(z-A)^2}E(k^2)-K(k^2)\right)\\
k^2 &= \frac{4R\rho}{(R+\rho)^2+(z-A)^2},\ \text{and the field potential}\ |\boldsymbol{B}| = \sqrt{B_z^2+B_\rho^2},
\end{aligned} \tag{2.1}$$

where $E(k^2)$ and $K(k^2)$ are complete elliptic integrals, B_z and B_ρ are magnetic field projections onto cylindrical coordinates in Gauss, the Z-axis is coaxial with the coils, A is the coil distance from the origin and R is the coil radius. The vacuum permeability is defined as $\mu_0 = 4\pi \times 10^{-3}$ G·m/A[19].

In Fig. 2.9 (a) the potential map does not clearly reveal the trap, although on the smaller scale of Fig. 2.9 (b) the confining region is well distinguished. The quadrupole-field gradients produced by the coils and calculated from the spatial derivatives of equations 2.1 are 4.8 G/cm in the radial direction and 9.6 G/cm in the axial direction. An important hardware limitation of the coil geometry is the high-current source and high-current switch. The latter is an intricate problem: there is no low-noise technology for electronic switching. High currents are bound to large thermally induced noise and consequent trap instabilities. Our current reaches 10 A. The geometry could in principle be improved by either bringing the coils closer to each other to satisfy the optimal ratio of $d = R$ at the same currents, or to increase the coil radii and again meet the optimal ratio at the

---

[19] Here and for the other coils a mixed system of units is used for convenience: m, G, A.

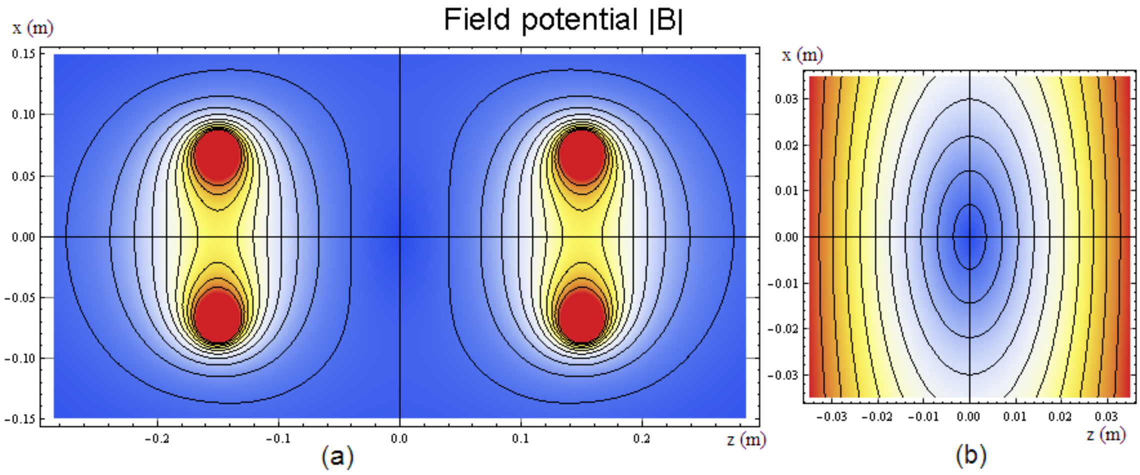

Figure 2.9: Quadrupole trap magnetic field potential $|\boldsymbol{B}|$:
(a) for a complete geometry of the pair of quadrupole coils;
(b) zoomed in and rescaled central region illuminated by MOT-beams (3 cm in diameter).
The configuration of coils is sub-optimal, but the potential is deep enough for the magneto-optical trapping of 4×10^8 atoms (see Section 2.4). Axes are only valid for this figure.

cost of increasing currents and heating issues. Both ways are inaccessible with the present vacuum chamber: the coils cannot be installed closes to the centre, and larger-R coils would require to scale up the other coils in the system. The quadrupole coils have inner water pipes and are cooled by a constant water flow during operation. Temperature fluctuations are monitored with a thermoresistive sensor (thermocouple). The cooling regime is chosen so that the coils return to the initial temperature before the new cycle starts.

Helmholtz coils

The pair of outer-most equally-sized coils is *Helmholtz coils*[20]. They create a large volume of uniform magnetic field in the vacuum. The distance between the coils is required to be equal to their radius $d = R$, and equal currents are required to flow in the same direction so that the fields produced by the coils add to the total axial field in the positive X-direction. The magnetic field in the coil centre is well approximated by the Biot-Savart result, derived from a single-loop on-axis field component of two coils with co-directed currents:

$$B_x = \frac{8\mu_0 n R^2}{\left(d^2 + 4R^2\right)^{3/2}} I$$

in Gauss. With a vacuum permeability $4\pi \times 10^{-3}$ G·m/A, the number of turns in each coil $n = 66$, total current I in A through the coils connected in series, radius

---

[20] Our coils are offset from the exact Helmholtz configuration $d = R$ being in reality $d = 1.2R$.

$R = 0.2$ m and distance between the coils $d = 0.24$ m, the field in the centre of the coils becomes $B_x = 2.615I$ G. The Biot-Savart result compares well with the calibration measurements and electromagnetic 3D-simulations ($\approx 3\%$ deviation).

Correction coils

The B_x-Large and quadrupole coils have large inductances; their transients are too slow to control sensitive trap transfers. For this purpose the system is equipped with a set of fast correction coils with low inductance, the rectangular coils in Fig. 2.8. The four pairs of coils in corresponding directions are B_y-Earth, B_y-Small, B_x-Small and B_z-Small. The pairs B_y-Earth and B_y-Small are wound around the same formers and are geometrically indistinguishable, although they are driven by individual current-switches. The B_y-pairs have the largest influence on the magnetic trapping potential bottom and thus its transients and mounting are particularly important for cold atom stability and BEC production.

2.3 Atom chip

An atom chip is an assembly of current carrying wires capable of creating magnetic-fields with well defined spatial distributions and high **B**-gradients. Atom chips have been used for over a decade for the creation of microtraps for neutral atoms [32, 33]. Our atom chip design is depicted in Fig. 2.10. The atom chip has a ceramic substrate with high thermal conductivity[21], electrically isolating the chip from the copper heat-sink installed on the top flange[22] of the vacuum chamber. The silver foil[23] is glued to the ceramic substrate with an epoxy[24] and cuts are milled in this structure to form current carrying wires with fixation holes near the chip circumference for the wires connecting the flange and the chip. A pair of 150 μm microscopic glass slides placed alongside each other with 100 nm gold film deposited on them (top most layer) faces the trapping beams. The milled silver foil glued on a ceramic plate is adhesively connected to the glass slides with the same epoxy. The estimated resistance of the Z- and U-wires from silver conductivity data and wire cross-sections is 1.7 mΩ[25]. This allows the maximal vacuum feedthrough current through the wires with a tolerable temperature rise, typically the currents are at the limit of 30 A associated with a 40°C change. Wires U2, Z2 and dispenser Rb1 are connected to high-current switches and used in the

---

[21] Square 54-mm side 2 mm thick machinable aluminium nitride ceramic Shapal-M, 90 W/mK.

[22] 12-pin Ceramaseal vacuum feedthrough rated 55 A.

[23] 5-cm side 0.5-mm thick square Ag foil Goodfellow AG000465, coated with Cr bonding layer.

[24] Two component, thermally conductive, electrically insulating epoxy EPO-TEK H77.

[25] Wire resistances are hard to measure for contacts of typically 10 times higher R.

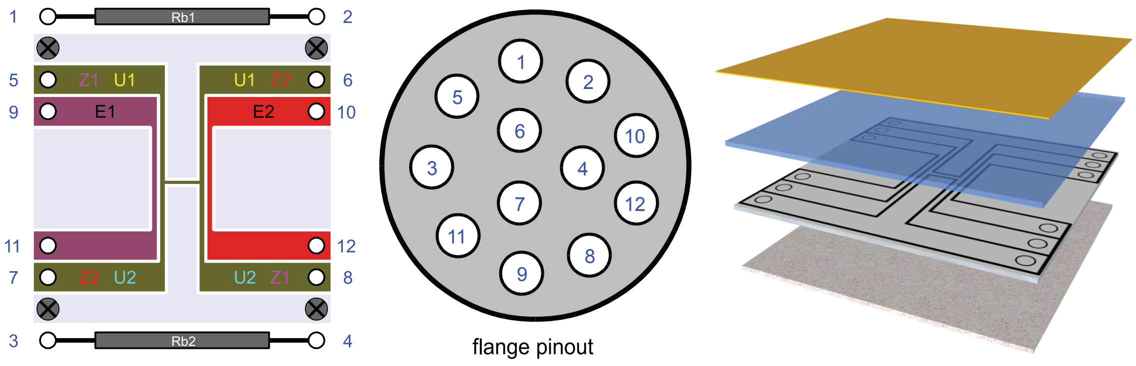

Figure 2.10: Atom chip wires: (on the **left**) H-, U1-, U2-, E1-, E2-, Z1-, Z2-, R1- and R2-wires. Rb-dispensers Rb1 and Rb2 are mounted on the side of the chip; it is convenient to include them in this drawing for completeness. The outer (blue) numbers are flange feedthrough (Fig. 2.8) indices showing all the electrodes wired outside the UHV chamber. An upside-down sandwich of the atom chip layers, as if the through-holder was underneath, is shown on the **right**. Vacuum chamber pins are single-wires fed through the flange, they are shown in the **middle**. The flange pinout corresponds to that on the atom chip.

experiment. The other structures are electrically floating.

The atom chip Z-wire (Z1 or Z2) in combination with the quantizing $\boldsymbol{B}_y$ and bias $\boldsymbol{B}_x$ fields forms an Ioffe-Pritchard trap with the quadrupole feature displayed in Fig. 2.11, where the results of the numerical 3D-simulations of Maxwell's equations in the retarded potential formulation are shown[26]. The effect of the anisotropic current distribution inside the conductor, as well as the rise of the *skin effect* in the AC-regime and the current coupling via the magnetic field induced by the current density in the wire, are taken into account. The latter is the reason for the transverse spatial mode distortion indicating the co-planar waveguide mode structure rather than a simplistic single-wire magnetic field distribution around the Z-wire.

The field at the cloud elevation of 1.24 mm in the magnetic trap (MT) is 3 times smaller in the AC regime at an RF-frequency $f_{RF} = 2.26$ MHz in the presence of the coplanar metal slabs filling the gaps of the H-wire structure Fig. 2.11(c), than without the slabs Fig. 2.11(d). A similar calculation for the RF-excitation from one of the end-wires (E1 or E2) gives a factor of 1.5 difference at the MT centre between the field magnitudes in the presence of all the other metal structures and in their absence, with only the end-wire inducing the field. The single-wire Biot-Savart formula, identical to the DC-case, $\boldsymbol{B}_{Zw} = 2\mu_0 \boldsymbol{I}_z / \boldsymbol{r}$ in G, where $\boldsymbol{I}_z$ is the Z-wire current in A, $\boldsymbol{r}$ is the distance from the wire in m and $\mu_0 = 4\pi \times 10^{-3}$ G·m/A, is not a good approximation for our geometry in either regime; this is seen in Fig. 2.11(d) where significant ellipticity of the magnetic field profile at the trap

---

[26] COMSOL Multiphysics v4.1 software was used. The spatial grid is relatively coarse, but for the purpose of practical estimates by the simplistic wire-models and within the other shortcomings this is an adequate resolution.

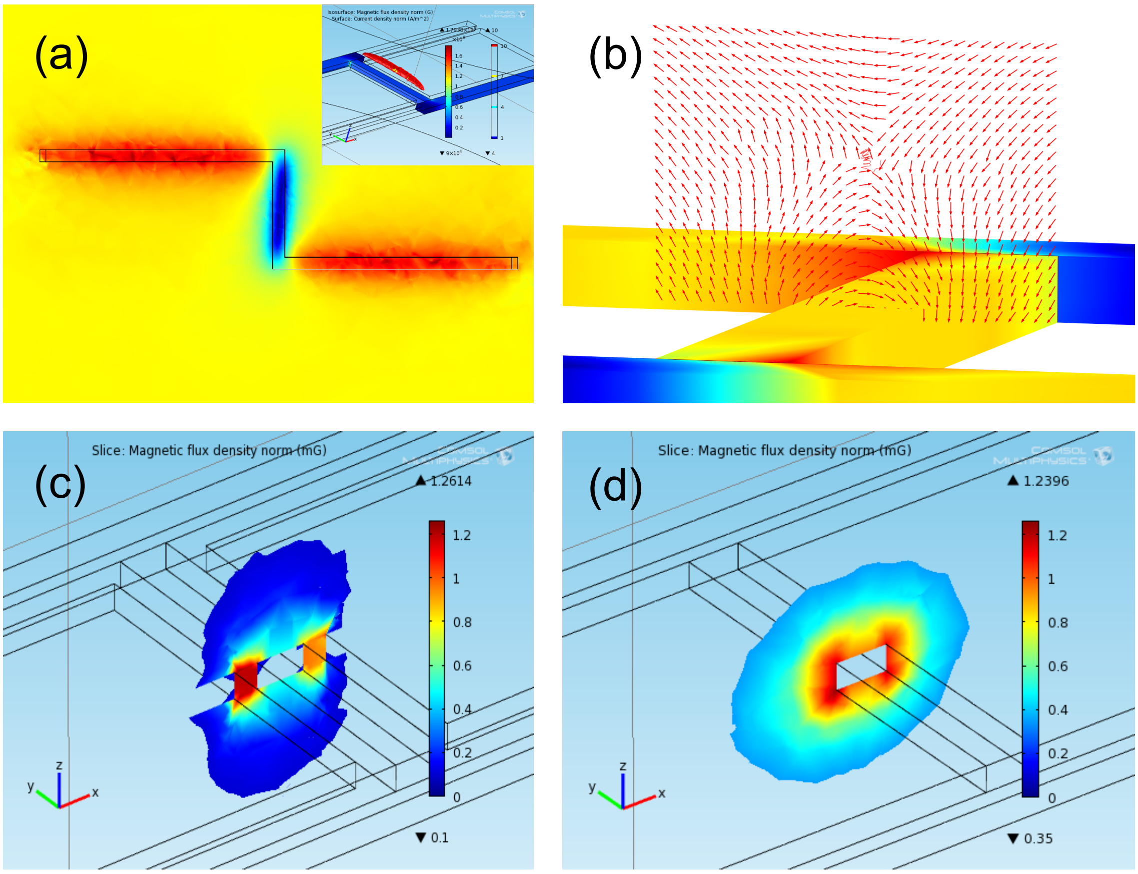

Figure 2.11: Atom chip field configurations numerically simulated from Maxwell's equations. Legend (colour scaling of $|\boldsymbol{B}|$ is identical for all subfigures):
(a) Z-wire trapping potential $|\boldsymbol{B}|$ and the corresponding equipotential volumic surface **(inset)**;
(b) a quadrupolar $\boldsymbol{B}$ feature of the Ioffe-Pritchard trap; quantization axis at the trap elevation is predominantly defined by $\boldsymbol{B}_y$ field and at the coalescence point is directed along Z-wire; a simulated trace of a test spin particle is shown magnetically trapped and oscillating around the trap centre;
(c) $|\boldsymbol{B}|$ distribution at $f_{RF} = 2.26$ MHz in the presence of the coplanar metal slabs at $\boldsymbol{B}_x = 0$; this corresponds to the RF-field excitation from the Z-wire (Z1 or Z2);
(d) $|\boldsymbol{B}|$ distribution at $f_{RF} = 2.26$ MHz in the absence of the coplanar metal slabs at $\boldsymbol{B}_x = 0$; this is given for the comparison of **(c)** with the Biot-Savart single-wire model and to derive the geometrical factor between the models.

elevation is seen. Practically the single-wire formula gives a 9% deviation from measurements of the distance from the chip $\boldsymbol{r}$ for different $\boldsymbol{I}_z$ by *in situ* absorption imaging.

Rubidium vapourization

Before getting to the coherent spin physics, a sequence of transformations is applied to prepare the ensemble in a well defined quantum state. In the presented experiments the atoms are initially prepared in spin state $\left|F = 1, m_F = -1\right\rangle$ and then superimposed by coherent population transfer with RF or MW radiation or their combination in the two-photon scheme.

Initially, rubidium is released from a 25 mm long *dispenser* [87], mounted on the atom chip in the vacuum chamber at 2×10^{-11} Torr, by resistively heating it to about +500°C by electrical current pulsing [88]. The powder of Rb_2CrO_4 salt is thermally activated to outgas rubidium through the microslits between the trapezoidal container and the sealing wire. The heavy particles of the chemicals are kept in the container while the gases are allowed to escape. Of those, hydrogen is the prevailing contaminant and it is absorbed by the titanium deposited on the vacuum chamber inner surfaces. The rest of the gaseous substance is Rb vapour at the natural abundance of isotopes ^{85}Rb (72.2%) and ^{87}Rb (27.8%).

The outgassing regime is set by the current amplitude and its pulse duration; it is chosen so that by the end of an experimental cycle of 1 to 2 minutes, the vacuum recovers from 2×10^{-10} to 2×10^{-11} Torr. It is essential to keep the rate of collisions with the background gas low, especially for BEC production.

At the stage of Rb vapourization, the gas uniformly spreads over the volume of the vacuum chamber: the most probable particle velocity at approximately +500°C according to the Maxwell-Boltzmann distribution

$$v_{th} = \sqrt{\frac{2k_B T}{m}}$$

is $\approx$ 400 m/s. At this speed the particles reach the most distant parts of the vacuum system (1 m) in 2.5 ms, a much longer time than that characteristic of the MOT-loading stage. In this respect, the dispenser location inside the chamber is unimportant.

A Rb-dispenser is connected to the current-supply line via two brass barrel connectors and two loose soft-copper strain-relief wires joining the barrel connectors and the supply line. Such an arrangement is necessary to prevent the contact pads from breakdown due to the cycling thermal expansion. Two dispensers are mounted near the atom chip (Fig. 2.6): one is regularly pulsed, the other is a backup.

2.4 BEC production sequence

We start the BEC production cycle from a well defined spin state $5^2S_{1/2}(F = 1, m_F = -1)$, further identified as $|1,-1\rangle$ in the $\{|F, m_F\rangle\}$ basis. The MOT-loading starts from 16.5 s of rubidium vapourization from the dispenser Rb1 by appying a current of 5.7 A to it and capturing atoms in the mirror-MOT formed by the quadrupole magnetic field and MOT-laser beams in the counter-propagating σ^+–σ^--configuration [2] mixed with RP-light (Fig. 2.6). The quadrupole-field gradients are 480 G/m in the radial and 960 G/m in the axial direction (from Eqs. 2.1), approximately constant across the volume illuminated by the trapping beams, 3 cm in diameter each, partly cropped by the atom chip surface. The MOT is formed 4 mm below the chip surface to avoid particle loss from touching the mirror and being accelerated by hot collisions with the +300°K atoms. A typical MOT-cloud geometry is roughly a sphere with a diameter of about 4 mm as viewed by a video camera[27] from the off-resonant fluorescence. By the end of the 16.5 s dispenser pulse the MOT captures 4×10^8 atoms at about the Doppler-limited temperature of 140 μK. The atom number is estimated from the MOT fluorescence captured by a calibrated photodiode with a 1-inch condenser lens [71, p. 50].

The MOT-loading stage is stopped at saturation observed in the photodiode signal. The UHV-chamber pressure increases to 2×10^{-10} Torr and the Doppler-cooled atoms are distributed over all eight magnetic substates of the ^{87}Rb ground states $5^2\mathrm{S}_{1/2}(F_g = 1, 2)$ (Fig. 2.1), predominanty occupying the cooling-cycle states $F_g = 2$ and $F_e = 3$. The ensemble is compressed and brought to a distance of 1.6 mm from the atom chip surface by passing a 5.4 A current through the U2-wire and ramping down the quadrupole magnetic field. Simultaneously with the B_x current, the U2-wire current is ramped for 110 ms to elevate (decrease the distance to the chip) and compress the cloud. The timing is chosen experimentally to achieve a maximal transfer to the compressed MOT (CMOT) based on the atom chip. The number of atoms is tracked by reverting the fields to the values they had in the MOT, re-capturing atoms and by observing spontaneous emission on the photodetector. The transferred population is estimated from the transfer coefficient, equal to the square root of the ratio of the re-captured atom number N_{recap} to the initial MOT atom number $k_{CMOT} \approx \sqrt{N_{recap}/N_{MOT}} = \sqrt{S_{recap}/S_{MOT}}$, where S_{recap} and S_{MOT} are amplified signals from the photodiode, observed on the oscilloscope during the MOT and re-capture periods correspondingly. It is easier to relate two time points on the oscilloscope to obtain k_{CMOT} than to measure the absolute numbers of atoms. Typically, k_{CMOT} is over 90%.

During the compression the cloud temperature increases. We use polarization-gradient cooling in a small magnetic field, where it performs best [84], to cool atoms below the Doppler limit. The U2-wire field is relaxed for a period of 13 ms, the MOT-laser detuning $\Delta_{MOT} = -18$ MHz is ramped over this period to $\Delta_{PGC} = -62$ MHz, and the RP light is turned on to keep the population trapped in the cooling cycle. After this stage the atoms are cooled down to 40 μK with a small atom number loss.

For optical pumping (OP) the field is kept relaxed at approximately $1 - 2$ G for another 1.6 ms and the OP-laser detuning is set to $\Delta_{OP} = +10$ MHz, providing optimal pumping for a narrow range of parameters [72]. OP operates at around the $5^2\mathrm{S}_{1/2}(F_g = 2) \rightarrow 5^2\mathrm{P}_{3/2}(F_e = 2)$ transition for the quick accumulation of atoms

---

[27] AvTech 1/3-inch AVC 301D B/W CCD camera.

in the $|2,-2\rangle$ state. The circularly polarized light is applied at a small angle to the $\boldsymbol{B}_x \approx 1-2$ G. This ensures a small fraction of π-polarization which pumps atoms to the $\boldsymbol{F}=1$ state. During this time the OP light mixed with the RP light is turned on and the population initially spread over all the magnetic sublevels accumulates in the $|1,-1\rangle$. The OP-stage is characterized by the CMOT-to-CMT (compressed magnetic trap) transfer efficiency where the atoms not transferred to $|1,-1\rangle$ by optical pumping are lost from the system. Typically, this stage has 40% efficiency as measured by the fluorescence from the population re-captured in CMOT.

The compressed magnetic trap (CMT) is formed by turning the U2-wire current and the lasers off, then substituting the CMOT with the Z2-wire trap with the characteristic frequencies $\omega_x = 2\pi \times 97.6$ Hz, $\omega_y = 2\pi \times 97.6$ Hz, $\omega_z = 2\pi \times 11.96$ Hz [72]. The CMOT-CMT transfer is accomplished by ramping the Z-wire current for 11-ms, a corresponding correction of the $\boldsymbol{B}_x$-current and enabling the $\boldsymbol{B}_y$ quantizing field to create the Ioffe-Pritchard trap. The atoms populate the trapped state $|1,-1\rangle$, and in practice there is a fraction occupying the $\boldsymbol{F}=2$ substates. To remove the latter, AOM1 (Fig. 2.2) is opened for 0.1 ms with the detuning set to $\Delta_{MOT} = -3$ MHz; this accelerates $\boldsymbol{F}_g = 2$ atoms which are lost in the subsequent 4-ms pause. Only the desired quantum spin-state $|1,-1\rangle$ is left trapped.

Prior to the forced radiofrequency (RF) evaporation the trap is decompressed by lowering the Z2-wire current from 10 A to 8.5 A. The evaporation is split into two stages. The first pre-cools atoms by a 9.1 s logarithmic ramp of radiofrequency from 25 MHz to 560 kHz, just above the Zeeman-split energy level defined by the $\boldsymbol{B}_y$-field; this stage is to maximize the population transferred to the magnetic trap (MT) and increase its lifetime. Atoms are transferred to a tighter trap by ramping fields for 100 ms for the second evaporation. The fields are set to the “magic” field $\boldsymbol{B}_y = 3.228$ G. The Bose-Einstein condensation (BEC) critical temperature $\boldsymbol{T}_c$ can be reached in both traps, but since BEC is a superfluid, it should be condensed in the last magnetic trap to avoid transfers which would inevitably bring the superfluid to a non-equilibrium state and cause sloshing. The second evaporation stage takes 2 s of the logarithmic RF-frequency ramp from 2.37 MHz to $f_{end2} = 2.27$ MHz which is 10 kHz above the trap bottom, being 2.26 MHz in the “magic” field, to produce $N_{BEC} = 30 \times 10^3$ atoms. The value of the second evaporation end-frequency f_{end2} is changed to prepare the necessary number of atoms as well as to regulate the ensemble temperature.

2.5 Microwave and radiofrequency feeding

The magnetically split hyperfine levels depicted in Fig. 2.1 for the ground state comprise MW and RF transitions routinely used in the experiments. The RF

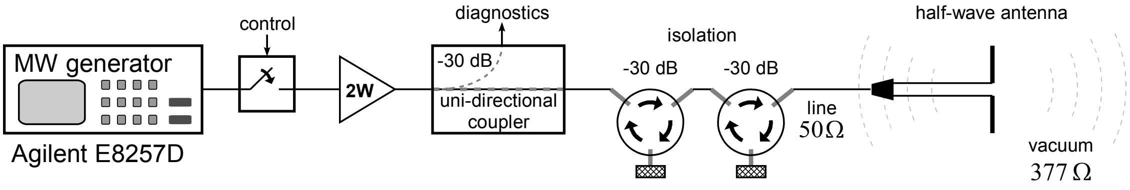

Figure 2.12: Microwave channel. The coaxial line and all the blocks have 50 Ω wave impedance. The line is coupled to vacuum with 377 Ω by a 23 mm long half-wave dipole antenna working near the MW-resonance of ^{87}Rb $5^2S_{1/2}$ hyperfine levels. Reflections from the antenna are suppressed by passive microwave circulators with absorbing plugs in the returning-wave ports. The control input of the MW-switch receives a TTL signal from LabView.

excitation is relatively simple to implement due to the characteristic dimensions of the apparatus being on the scale of meters whereas the highest RF-frequency used in the measurements is in the order of 3 MHz, yielding a 100-m wavelength. RF-evaporation that starts from 25 MHz does not influence the state preparation and its effect on measurements is neglected. However it does affect the atom number preparation because the corresponding smallest wavelength is 12 m, of the same scale as the apparatus dimensions, and coupling occurs to the unshielded circuit elements.

The signals from the RF-generators[28] pass through the computer-controlled RF-switches[29], are amplified[30] and fed to the atom chip end-wires E1, E2 (refer to Fig. 2.10 for atom chip labeling), separately or simultaneously. Since the RF-wavelength is large compared to the system size, wave impedance matching is not required.

The MW-generator[31] signal is fed via a separate channel ending with an antenna abutting to a vacuum chamber 6-inch viewport (Fig. 2.12). The output signal is controlled by a solid-state absorptive switch[32] installed after the generator, then amplified by a 2-W amplifier[33]. The high-power signal propagates along the 50 Ω coaxial line to a uni-directional coupler as a part of MW-diagnostics circuitry and proceeds to two successive MW-isolators, based on circulators with one absorbing port, with total extinction −60 dB. From the circulators the power reaches a resonant half-wavelength dipole antenna, 23 mm long to match the driving frequencies of the hyperfine transitions of ^{87}Rb ground state $5^2S_{1/2}$. Unlike in the RF-feeding, an antenna is required for MW, because the radiation condition is fulfilled and the media have mismatched wave impedances: a 50 Ω line would terminate with 377 Ω

---

[28] Stanford Research Systems DS345.

[29] Two models used: Minicircuits ZX90-DR230-S+ and ZASWA-2-50DR+.

[30] OPHIR 5303055 amplifier: 0.15-230 MHz, 25 W.

[31] Agilent Technologies E8257D with an oven-controlled quartz oscillator (OCXO). The relevant to our experiment OCXO specifications are given and discussed in Chapter 4.

[32] Agilent Technologies 9397A.

[33] Microwave Amplifiers Ltd AM53-6.6-7-40-40.

vacuum and reflect $\left(\frac{Z_2-Z_1}{Z_2+Z_1}\right)^2 = 59\%$ of power. The feed-point wave impedance of the dipole antenna working at the resonant frequency is lower, theoretically $72\,\Omega$, and the line-to-vacuum interface effectively transmits 97% of MW-power. The remaining 3% of the power returns to the circulators and is damped in absorbers. A half-wave dipole antenna has a toroidal radiation pattern, the only non-radiative direction is along the antenna arms. The antenna gain, reflected in higher directivity, forms a MW-beam in the vacuum chamber that is reflected by its metal. The complex interference pattern mixes σ^+, σ^-, π MW-polarizations and forms multiple closely spaced hills and dips, unlike in the toroidal pattern always having a smaller number of features over the same volume. This property makes it robust against position variations compared to directive antennas[34] it is easier to align for maximal coupling strength that we extract from Rabi oscillations on σ^+, σ^- and π MW-transitions.

2.5.1 MW transition strengths

The transitions strength is experimentally characterized by the Rabi frequency Ω (see Section 4.2.1). The Rabi frequency can be extracted from Rabi oscillations measured by exciting atoms from $F_g = 1$ to $F_g = 2$ by MW-radiation whose polarizations are anisotropic inside the vacuum chamber and can excite any of the transitions: σ^-, π or σ^+, selected only by the MW-frequency. The resultant two-level Rabi oscillations quickly lose contrast, because neither of the upper states are trappable. However, if the MW-radiation induces oscillations with Ω in the range of tens of kHz, the oscillations are quick and several Rabi periods can be observed on the millisecond scale (Fig. 2.13).

To obtain the data in Fig. 2.13 the thermal atoms are prepared in state $|1, -1\rangle$, then the three MW transitions σ^-, π and σ^+ are excited simultaneously (all polarizations are present in the radiation). The three upper states are lossy and the atoms leave the trap quickly. Nevertheless, the coupling with an Ω in the range of tens of kHz can still capture a few full oscillations before all the particles are lost. The oscillations in Figs. 2.13(b,c,d) are fitted with an exponentially decaying sinusoid to extract the values of the Rabi frequency Ω for the corresponding transitions.

We can conveniently relate these measurements and the radiofrequency Rabi frequencies to estimate the value of the two-photon Rabi frequency. The two-photon interrogation field is used in interferometry experiments; its Rabi frequency can be directly measured and related to the MW and RF Rabi frequencies, provided the intermediate state detuning is known. The two-photo Rabi frequency

---

[34] For example the directive spiral antenna with gain=16 that we have used in the past.

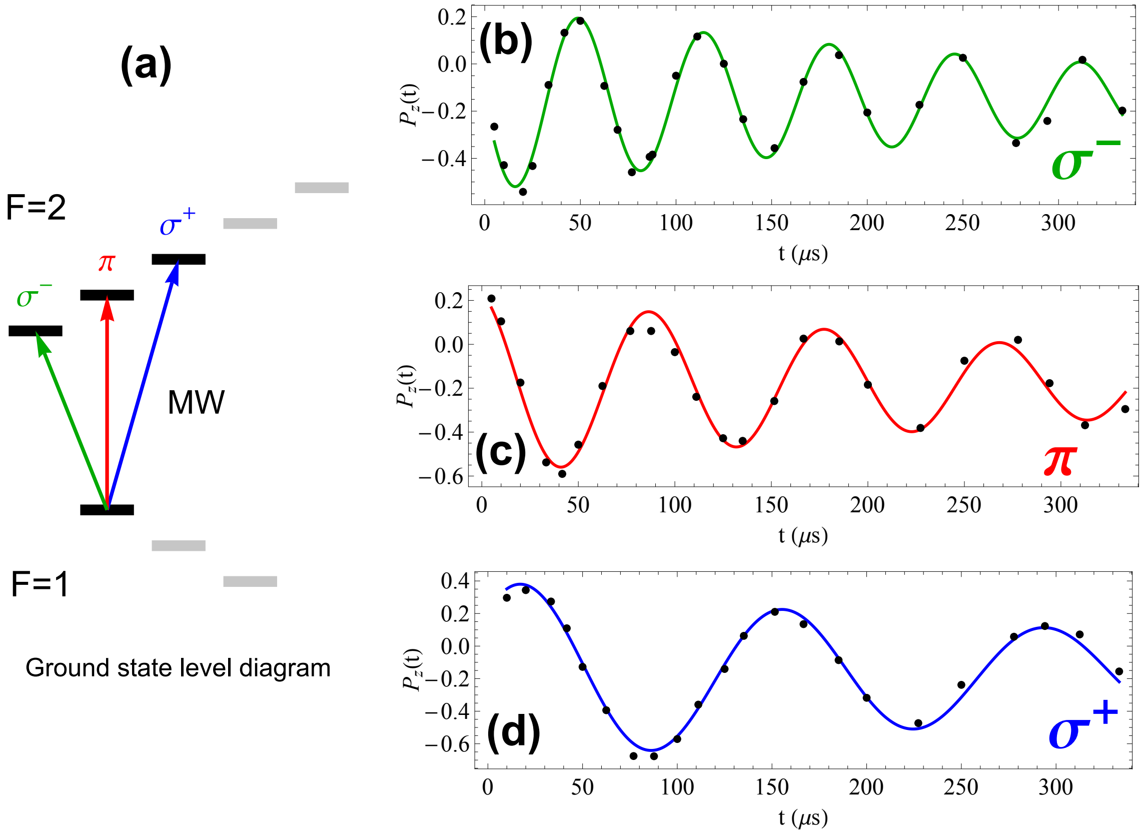

Figure 2.13: Microwave Rabi oscillations of $50{\times}10^3$ magnetically trapped condensed atoms with a trap bottom field of 3.228 G for σ^-, π, σ^+ polarizations excited by MW-radiation. MW-polarization is anisotropically distributed in the vacuum chamber and can excite any of the transitions; a particular transition is chosen by the frequency of MW-radiation. The Rabi frequency Ω fitted for each case with an exponentially decaying sinusoid is given in the legend below:
(a) – an excerpt from Fig. 2.1 for the $F = 1$ and $F = 2$ ground state magnetic sublevels;
(b) – Rabi oscillations on σ^--transition with $\Omega = 2\pi \times 15.23(3)$ kHz;
(c) – Rabi oscillations on π-transition with $\Omega = 2\pi \times 11.00(4)$ kHz;
(d) – Rabi oscillations on σ^+-transition with $\Omega = 2\pi \times 7.23(4)$ kHz.

formula is derived from the three-state model by the adiabatic elimination of the far detuned intermediate state and the results are summarized in Section 4.2.1.

2.5.2 Magnetic field calibration

To establish the “magic” field for two-state interferometry or an arbitrary magnetic field in the final magnetic trap (MT) microwave spectroscopy is used. The atoms are transferred to untrappable substates of the $F_g = 2$ state from where they leave the trap after several oscillations on the corresponding transition (Fig. 2.13). The MW Rabi pulse has a duration of 320 μs, during which time the Rabi oscillations almost vanish due to the high population loss from the untrapped states. The two-state MW spectroscopy can be described by the Schrödinger equation of the effective spin-$\frac{1}{2}$ system (Section 3.1.2). The MW pulse results in a power-broadened

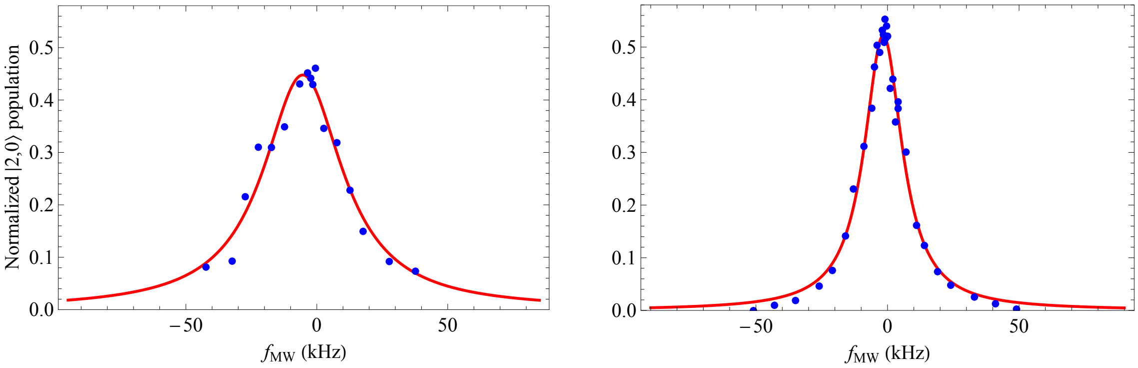

Figure 2.14: Microwave spectroscopy on the π transition corresponding to $|1,-1\rangle \rightarrow |2,-1\rangle$ (left) and on the σ^+ transition corresponding to $|1,-1\rangle \rightarrow |2,0\rangle$ (right). The fraction of atoms leaving the trap after the transfer to $|2,0\rangle$ is measured and normalized to the total population in both states. Red curves are Lorentzian fits. The origin is chosen at the resonance in the "magic" field 3.228 G; it is 6.830 160 324 GHz for the π-transition and 6.832 419 968 GHz for the σ^+-transition.

line with FWHM $= \Omega/\pi$ measured by the Lorentzian probability envelope. Additionally, the particles fall out of the trap and induce ensemble phase loss; the spectral line probing the ensemble averaged state broadens. The magnetic field value is extracted from the frequency of the resonance by the Breit-Rabi formula [89]. The MW spectra of the σ^+ and π transitions are given in Fig. 2.14.

There is a discrepancy in the Rabi frequency values extracted from the Rabi oscillation experiments and those extracted from the MW-spectoscopy measurements as FWHM $= \Omega/\pi$. This difference is attributed to the inhomogeneities of density and magnetic field across the cloud, due to motional effects [55] and gravitational sag [90, 91]. The rapid magnetic field variations while the atoms fall out of the trap and cross the regions with different local magnetic field also contribute to the line broadening through the Zeeman effect. The local spectral responses of atoms have to be spatially integrated; then multiple probability functions add up to approach the Lorentzian lineshape. In the calibration we are only interested in the peak position that gives the corresponding magnetic field values. The deviations from the expected lineshape are not critical. The measurement is done with 50×10^3 atoms of BEC to minimize the effects of the fall-out dephasing.

2.6 Detection methods

2.6.1 Absorption imaging

A simple absorption imaging scheme [92–95] with a magnification factor of 3 displayed in Fig. 2.15 is used. It projects four objects onto the imaging plane: a sharp image of a cloud placed in the lens focus, off-focal probe beam, off-focal scattered shadow and a spot from a fraction of the fluorescent light that impinges

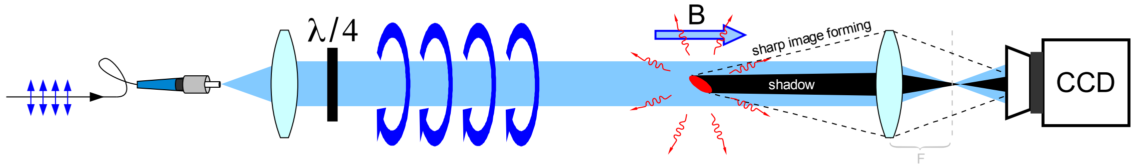

Figure 2.15: Two-state imaging with σ^+ light on $|2,+2\rangle \rightarrow |3,+3\rangle$ (an extended view of Fig. 2.8 for the imaging system). Imaging light is used in combination either with MW adiabatic passage and Stern-Gerlach state separation or with repump light. Imaging-pulse duration, chosen to let no cloud blurring due to photon recoils, is 100 μs. F is the imaging objective focal distance. CCD is a photocamera. The blue circular arrows show the light polarization. $\boldsymbol{B}$ is the magnetic field. The arrow underneath shows its direction at the cloud location.

on the lens aperture. The cloud image and its weak fluorescent trace are formed in the same place and cannot be distinguished. A slightly off-axial imaging, typical for the time-of-flight experiments, can separate the out-of-focus scattered shadow from the cloud in the CCD image plane. The off-focal probe beam forms a bright background on the CCD.

Since spontaneous emission is nearly isotropic, its contribution can be estimated by relating the full solid angle of the sphere 4π to the one associated with the lens. With a focal length of 15 cm and a physical aperture of 1 inch, the captured fraction is approximately 0.7%.

2.6.2 Scattering cross-section

A master equation can be developed for the two-state near-resonance fluorescence problem, giving a set of optical Bloch equations. The result of the population dynamics is well known under the electric dipole and rotating-wave approximations [96–99]: the radiative damping $\gamma = \Gamma/2$ counteracting the coherent excitation leads to a steady state that is reached in $\tau \approx 26$ ns. The steady-state population in the excited state is then

$$\rho_e(t \rightarrow \infty) = \frac{(\Omega/\Gamma)^2}{1 + 4\,(\Delta/\Gamma)^2 + 2\,(\Omega/\Gamma)^2}$$

from which the integral *photon scattering rate* over all directions $\boldsymbol{R}_{sc}$ can be written in terms of the *saturation parameter* defined via the identity

$$\begin{aligned} s &= \frac{I}{I_{sat}} = 2\left(\frac{\Omega}{\Gamma}\right)^2 \\ R_{sc} &= \Gamma \rho_e(t \rightarrow \infty) = \frac{\Gamma}{2} \cdot \frac{s}{1 + 4\,(\Delta/\Gamma)^2 + s} \end{aligned} \tag{2.2}$$

Imaging is sensitive to three parameters of the scattering cross-section σ that may vary from run to run: Δ, I and I_{sat}:

$$\begin{aligned}\sigma &= \frac{\sigma_0}{1+4\,(\Delta/\Gamma)^2+s}\\ \sigma_0 &= \frac{3\lambda^2}{2\pi} = \frac{\hbar\omega\Gamma}{2I_{sat}}\end{aligned}\tag{2.3}$$

The imaging system comprises an implicit beam expander consisting of a single-mode polarization maintaining fiber butt-end with a highly diverging beam that is allowed to reach 5 mm in diameter and is then collimated with a single lens placed exactly at the focal distance from the fiber. The light with a plane wavefront impinges on the atomic sample and resonantly excites the ^{87}Rb $F_g = 2 \to F_e = 3$ transition in a nearly zero magnetic field as depicted in Fig. 2.1. The excited optical levels have lifetimes $\tau = 26.2348(77)$ ns [97] and decay instantaneously via spontaneous emission compared to the 0.2 ms light pulse. The fluorescent photons almost isotropically scatter away[35], leaving a shadow behind the optically dense cloud in the direction of beam propagation. There is however a non-zero divergence angle due to the spherical nature of the scattering. The incident plane wave and the scattered spherical wave have different image planes.

For the intensities with saturation parameter $s \ll 1$ the atoms are mainly in the ground state. Due to the ensemble averaging in the scattering medium it is impossible to excite all atoms to the upper state. The absolute maximum is half of the total population which occurs when the ensemble equilibrates and the saturation parameter $s \gg 1$ [98].

With a 100 μs imaging pulse of 4 mW/cm^2 optical intensity, the sample absorbs light according to the saturation intensity and the on-resonance saturation parameter:

$$\begin{aligned}I_{sat} &= \frac{\pi hc}{3\lambda^3\tau} = 1.67\,\mathrm{mW/cm^2}\\ s_0 &= \frac{I}{I_{sat}} = 6.1\end{aligned}\tag{2.4}$$

The imaging transition $5^2\mathrm{S}_{1/2}(F_g = 2) \to 5^2\mathrm{P}_{3/2}(F_e = 3)$ is cycling for $\sigma^{\pm}$-polarized light. For this reason a quarter-wave plate is inserted in the beam path in Fig. 2.15 to convert linear polarization to circular. Illumination by σ^+ or σ^- light with $s_0 = 6.1 \geq 1$ collects all atoms in the upper state with the largest absolute spin projection value $m_F = +3$ or $m_F = -3$ correspondingly, where the sample equilibrates to half of the total population, the other half stays in the ground state[36]. To prevent population loss, repopulation light accompanies the imaging light. The

---

[35] The anisotropicity of scattering from magnetic sublevels in non-zero magnetic field is neglected.

[36] Magnetic field during imaging should be well controlled: if light is contaminated with π-polarization, the population will leak to the dark state $F_g = 1$. Saturation intensity of the π-transitions $I_{sat} = 2.5$ mW/cm^2 which is 1.5 times higher than that of $\sigma^{\pm}$.

lost population residing in $F_g = 1$ is transferred to $F_e = 2$, from where it decays to both $F_g = 1$ and $F_g = 2$. From the former it is returned back to the excited state $F_e = 2$; from the latter it comes back to the imaging cycle. One half of the total population equilibrates in $|F = 2, m_F = +2\rangle$ from where the atoms isotropically irradiate photons removing them from the coherent beam and forming a shadow. The second lens is an objective of two achromats that forms an image on a CCD sensor[37]. The scattered and the coherent rays can be distinguished since they focus at different distances from the lens: the paraxial beam focuses to a point at a focal length F from the lens where it can be spatially filtered out from the image by inserting a small opaque object in its focal plane. When all-optical imaging is performed, it is accompanied by repumping to compensate for atom losses due to π-polarization contamination which brings the population to the dark state. Another method of detection is described below, by the microwave adiabatic passage of the population with the consequential absorption imaging in the absence of repumping.

Absorption images are first processed by the Beer-Lambert particle counting, to obtain the number of atoms in the states, then by the method for strong saturation absorption imaging suggested in [100]. We do not account for the polarizing effect of a dense atomic cloud when the imaging beam passes through it and is “depolarized” [101]. After the saturation correction, the data is processed by the fringe-removal algorithm described in [102]. It has been known for almost a decade [102–106][38], but takes a new turn in the ultracold atom community, resulting in shot-noise limited statistics restored from the images full of optical fringes.

2.6.3 MW adiabatic population transfer

In the experiments, the Stern-Gerlach force [107] induced by the magnetic field gradient deflects the atomic beam. Then the number of atoms is counted by destructive absorption imaging after the state separation. We employ a multiple-state imaging technique, demonstrated in the case of two states in [70, 72]. State $|1, -1\rangle$, in which the atoms sit initially, is far off-resonant to the imaging light; they are transparent to absorption imaging. To detect the number of atoms in it, a microwave (MW) *adiabatic transfer* is used. The population is excited via the frequency selected π-polarized MW radiation; that transfers atoms into the $F = 2$ state of the same magnetic projection. In this manifold the Landé geometrical factor has opposite sign to that in $F = 1$ and the magnetic potential for low-field-seekers U_{lfs} flips sign too, leading to the opposite gradient and Stern-Gerlach force

---

[37] The photocamera is Princeton Instruments NTE/CCD-1024-EB.

[38] A comprehensive list of references on fringe-removal techniques in [102] is of particular interest.

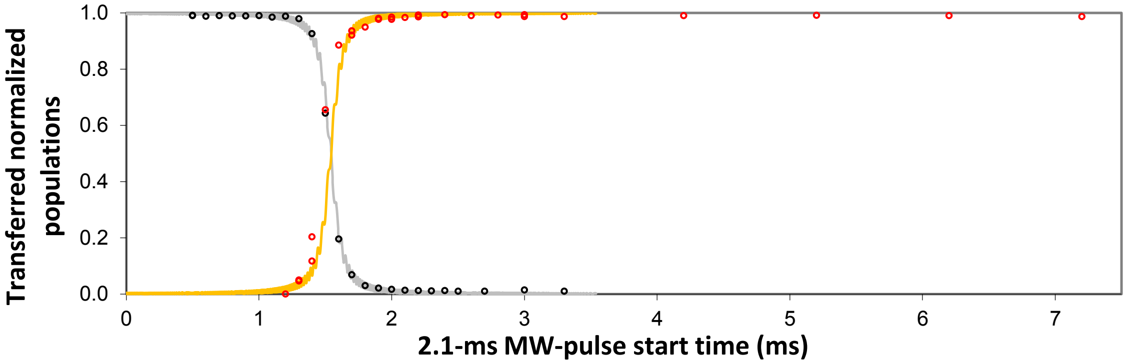

Figure 2.16: Adiabatic population transfer by a MW pulse of variable duration from $|1,-1\rangle$ to $|2,-1\rangle$: model (solid lines) and experiment (circles). All polarizations are present in MW-radiation and the transition selection is accomplished by setting MW frequency. The trap bottom is set to 3.228 G. The Rabi frequency of the π-transition is $\Omega = 2\pi \times 11.00(4)$ kHz, fitted transition rate $\lambda = 2\pi \times 250$ kHz/ms, total range covered by the optimal-duration MW pulse of 2.1 ms is ±262.5 kHz.

applied after the passage:

$$\begin{aligned} \boldsymbol{U}_{lfs} &= -\mu_B g_F \, |\boldsymbol{B}| \\ \boldsymbol{F} &= -\nabla \boldsymbol{U}_{lfs} \end{aligned} \tag{2.5}$$

The transfer is done adiabatically to make it robust to perturbations in the magnetic field transients, MW intensity and the uncertainty of pulse duration. The $\boldsymbol{B}_y$-Small coil pair sets up the quantizing field decaying after it is switched off to drive the Zeeman sweep across the $|1,-1\rangle \to |2,-1\rangle$ MW resonance. While the field relaxes, the constant initially blue-detuned MW frequency in 2.1 ms of MW pulse and field decay becomes red-detuned due to the DC Zeeman effect. This produces a sweep across the π-transition resonance. The MW pulse is on when the atomic frequency is sufficiently far from resonance and no population is transferred. It is off again when nearly all the popolation turns up in $|2,-1\rangle$. The MW pulse is optimized for maximal transfer by varying its start and duration, which indirectly chose the sweep rate λ to be different due to the field decay and approximately constant. A nearly ideal transfer found experimentally at a MW-pulse duration of 2.1 ms is demonstrated in Fig. 2.16.

The adiabatic transition model for a two-state system described by Schrödinger equations without approximations and under the assumption of the linear time-dependent detuning ramp $\Delta(t) = \lambda t$, where the transition rate λ is to be fitted by the model, can be written as:

$$\begin{aligned} i\hbar \frac{\partial S_1(t)}{\partial t} &= \Omega S_2(t) - \frac{1}{2}\Delta(t) S_1(t) \\ i\hbar \frac{\partial S_2(t)}{\partial t} &= \Omega S_1(t) + \frac{1}{2}\Delta(t) S_2(t) \end{aligned} \tag{2.6}$$

where $S_1(t)$ and $S_2(t)$ are the corresponding state probability amplitudes which take the values of 1 and 0, respectively, at the initial moment of time. A numerical solution is given by the solid lines in Fig. 2.16 overlapped with circled experimental data points. With the π-transition Rabi frequency $\Omega = 2\pi \times 11.00(4)$ kHz, measured independently (Fig. 2.13), the transition rate is numerically fitted to be $\lambda = 2\pi \times 250$ kHz/ms. Then the total detuning range for the maximal transfer given by λ and the 2.1-ms pulse duration spans from -262.5 kHz to $+262.5$ kHz.

2.7 Conclusion

We have presented the apparatus structure, its main technical characteristics and the measurements of the important physical parameters like Rabi frequency and the adiabatic passage transition rate λ well approximated by the theory. We demonstrated the apparatus performance by performing microwave spectroscopy on the transitions involving non-trappable states but oscillating long enough to measure the coupling strength. The coupling efficiency is estimated from the direct Rabi oscillation experiments set up on different MW transitions.

We also present the 3D-simulation analysis of the screening effect from the wire structures on the atom chip that distorts the excited RF magnetic field modes and makes uncertain the simplistic modelling with the Biot-Savart approximations for idealized wires [108, 109]. As a useful approximation, the Biot-Savart model can still be used with the geometrical factors derived from the 3D-simulations, showing that the RF-signal feeding through the Z-wire would result in a 3 times weaker magnetic field at the cloud position in the presence of the coplanar metal slabs (Fig. 2.11). If the feeding is done via the end-wires, E1 or E2, the surrounding wire structures reduce the field by a factor of 1.5.

Chapter 3

Ramsey interferometry: theory

3.1 Introduction

The most accurate experimental methods science has had are based on interferometers[1], first invented for the measurement of the velocity of light and subsequently extended to frequency standards [19–21, 110–115]. Looking down to the structure of matter, we find that the inherent behaviour of elementary particles is wave-like and is described by wavefunctions whereas the ensembles of particles are described by the statistical density matrix elements: populations and coherences.

In the present chapter we build a set of analytical models of various Ramsey-type interferometers, we investigate the models that allow one to account for the effects specific to the interferometry of magnetically trapped cold atoms, and we study the one-body and two-body collisional losses where the latter emerge from the high atomic density of the ensembles and the chances for a pair af atoms to collide and exchange enough kinetic energy and change the state via a spin flip are high enough to be observed in an experiment.

Another topic that is studied is a set of stochastic phenomena related to the motion of the atoms in a trapping potential and the phase destruction mechanisms resulting in quickly decaying envelopes of the interferometric fringe.

Atom number rate equations are solved, under an approximation, for inelastic collisional losses for the case of Ramsey evolution, which is of interest from a practical point of view. The approximation validity is discussed and a figure of merit is introduced to quantify the multiparametric unequal population decays of the two clock states.

The main results involve the derivation of the master equation with many-body losses and phenomenological dephasings derived from the *open systems* approach to the quantum system and including interactions with population and phase

---

[1] Interferometry milestones in time order [110]: Fizeau (1851) [111], Michelson (1881) [112], Rayleigh (1881) [113], Fabry and Pérot (1899), Rabi (1938) [114], Ramsey (1949) [20].

damping reservoirs, e.g. Eqs. 3.60. Along the way a set of the relevant population decay laws is derived for a comprehensive atom number relaxation analysis.

3.1.1 Measurable quantities

In all the experiments the measurable quantities, in terms of atom numbers N_j and density matrix elements ρ_{jj} with state index j, are:

$$\begin{aligned} N &= N_1 + N_2 \\ P_1 &= \frac{N_1}{N} = \frac{\rho_{11}}{\rho_{11} + \rho_{22}} \\ P_2 &= \frac{N_2}{N} = \frac{\rho_{22}}{\rho_{11} + \rho_{22}} \\ P_z &= P_1 - P_2 \end{aligned} \tag{3.1}$$

Normalization to the total number of atoms $N(T)$ (in contrast to $N(T = \text{const})$ is of benefit in thermal atom and BEC experiments for the following reasons. $N(T)$, with interferometry time T, fluctuates from shot to shot with a maximal value of the standard deviation $\text{STD}(N(T)) = 15\%$. Magnetic noise is the main source of the atom number fluctuations. Passive or active stabilization of the DC magnetic fields would be required to reduce the fluctuations to a negligible sub-percent level. Dividing the measured population by the total number suppresses the number noise resulting from the evaporative preparation by proportionally correcting the noise [95]. This correction proves effecient for thermal atoms but is more involved for a BEC, where the number dependence is stronger and nonlinear. This dependence can also be found and a correction made. In most experiments such a correction is not available because only one state can be measured at a time. However, we detect both states simultaneously and benefit from the accurate knowledge of the

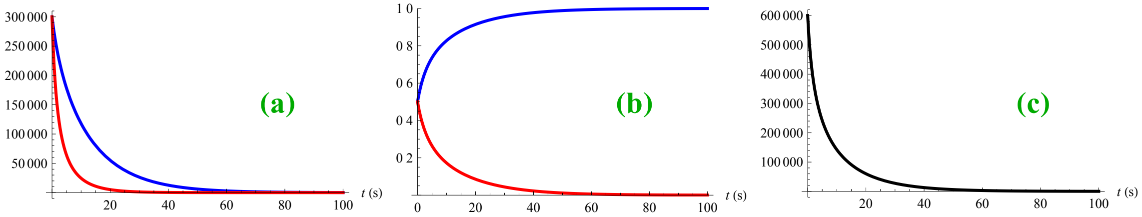

Figure 3.1: Symmetrization by normalizing measurable quantities on an example of state decays by the end of Ramsey evolution before the detecting $\pi/2$-pulse. Each state starts from 1/2 of the initial total population and evolves with different processes involved.
(a) Unnormalized populations: often inconvenient for analysis, sensitive to a number of parameters.
(b) Normalized populations: symmetrizes observables, but loses $N(t)$ information.
(c) The total number of atoms $N(t)$: needs to accompany normalized quantities.

total N in the described way.

The other reason to normalize measurables is to symmetrize such quantities with respect to a constant value of P_1, P_2 or P_z. The effect of unequal state decay is then eliminated. This effect is displayed in Fig. 3.1. It is not always beneficial, though; for example, such measurables lose information about the *population decay asymmetry*[2] and the total number N behaviour. Hence, N should also be recorded in a separate information channel and used in data fitting simultaneously with the populations, otherwise the fitted variables may be misinterpreted. A method of maximizing the P_z visibility by applying a non-$\pi/2$ Ramsey splitter pulse, based on the effect of measurable normalization, is devised in Section 3.2.6.

3.1.2 Rabi pulses and transition probability spectra

The detuning spectra of the lossless Rabi model [116] (Fig. 3.2) and the time-dependent state probability amplitudes of the two-level system [117–120] are found from the Schrödinger equations with the effective spin-$\frac{1}{2}$ Hamiltonian in the rotating wave approximation. For clarity, the solutions are split into time-dependent and time-independent parts where the Lorentzian spectral shapes become apparent. Starting from state $|1\rangle$ the equations for probability amplitudes with the resonant Rabi frequency Ω, detuning Δ, generalized Rabi frequency $\Omega_R = \sqrt{\Omega^2 + \Delta^2}$

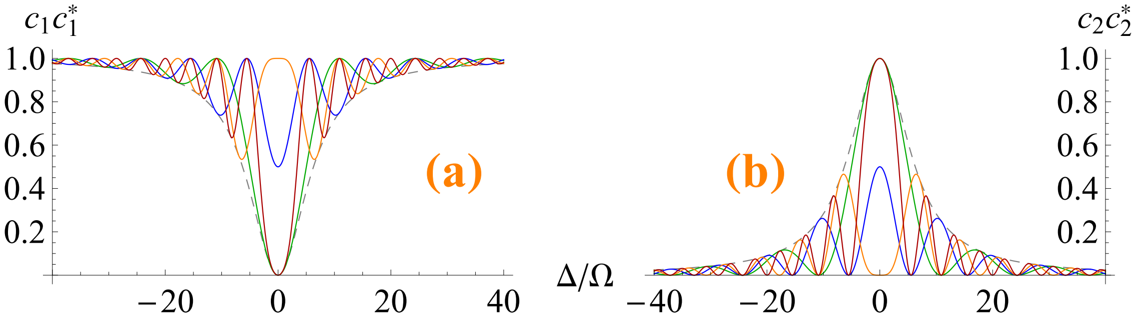

Figure 3.2: Spectra of transition probabilities $|c_1|^2$ and $|c_2|^2$ versus detuning Δ of the lossless Rabi model (Eqs. 3.3) for $\Omega = 2\pi \times 1$ and $t = \{0.5, 0.75, 1.0, 1.5\}$ (**green**, **blue**, **orange**, **brown**, respectively) and the Lorentzian envelopes (**dashed grey**). With the growth of t the spectral features (peaks) narrow down exposing Rabi interferometry spectrum behaviour.

(a) Transition probabilities $|c_1|^2$ for state $|1\rangle$ and the Lorentzian $\frac{\Delta^2}{\Delta^2+\Omega^2} = \left(\frac{\Delta}{\Omega_R}\right)^2$.

(b) Transition probabilities $|c_2|^2$ for state $|2\rangle$ and the Lorentzian $\frac{\Omega^2}{\Delta^2+\Omega^2} = \left(\frac{\Omega}{\Omega_R}\right)^2$.

---

[2] Loss *asymmetry* is discussed with respect to a constant value of a measurable: P_1, P_2, P_z. For example, in Fig. 3.1(b) this constant level is at $P_1(t) = P_2(t) = 0.5$.

and $\hbar = 1$ are:

$$\begin{aligned} 2i\frac{\partial c_1}{\partial t} &= -\Delta c_1 + \Omega c_2 \\ 2i\frac{\partial c_2}{\partial t} &= +\Omega c_1 + \Delta c_2 \end{aligned} \tag{3.2}$$

The transition probabilities are found as squares of the absolute values of the probability amplitudes:

$$\left|c_1\right|^2 = \frac{1}{2\Omega_R^2}\left(\Delta^2 + \Omega_R^2 + \Omega^2\cos\left(\Omega_R t\right)\right) \tag{3.3a}$$

$$\left|c_2\right|^2 = \frac{\Omega^2}{2\Omega_R^2}\left(1 - \cos\left(\Omega_R t\right)\right) \tag{3.3b}$$

This simplistic model is of practical importance for the interpretation of Rabi oscillation and spectroscopy experiments like the ones presented in Section 2.5.1. In the derivations below Ramsey interferometric sequences are considered, constituent parts of which are *Rabi pulses* evolving according to the presented equations which can be generalized to the *populations* of the density matrix by employing the equivalences $\left|c_1\right|^2 \equiv \rho_{11}$ and $\left|c_2\right|^2 \equiv \rho_{22}$ (see Fig. 3.2).

3.2 Interferometry with one-body losses

3.2.1 Bloch pseudo-spin vector representation

For the description of the ensemble state evolution in Ramsey interferometry the Bloch pseudo-spin vector $\boldsymbol{B}$ of the effective two-level system is introduced. It offers a particularly convenient representation of the state vector evolution in the absence of particle losses or phase damping. In a more comprehensive interferometry model, the population and phase losses will be considered in the density matrix framework. To establish a mapping between the representations the Bloch vector is defined in terms of the density matrix elements ρ_{nm} as:

$$\begin{aligned} \boldsymbol{B}_x &= \rho_{21} + \rho_{12} \\ \boldsymbol{B}_y &= \mathrm{Im}\left\{\rho_{21} - \rho_{12}\right\} \\ \boldsymbol{B}_z &= \rho_{11} - \rho_{22} \end{aligned} \tag{3.4}$$

Starting from the Liouville–von Neumann equation (refer to Section 3.2.3) for the resonant case without losses, we cast it in vector formulation, which is convenient for the qualitative analysis of the state evolutions presented in figures 3.3 and 3.4:

$$\frac{\partial \boldsymbol{B}}{\partial t} = \boldsymbol{\Omega} \times \boldsymbol{B} \tag{3.5}$$

where $\boldsymbol{B} = (B_x, B_y, B_z)^\top$ is the *pseudo-spin* vector and $\boldsymbol{\Omega} = (-\Omega, 0, \Delta)^\top$ acts on $\boldsymbol{B}$ as an *effective torque*. In terms of the matrix elements Eq. 3.5 reads:

$$\frac{\partial}{\partial t}\begin{bmatrix} B_x \\ B_y \\ B_z \end{bmatrix} = \begin{bmatrix} 0 & -\xi & 0 \\ \xi & 0 & \Omega \\ 0 & -\Omega & 0 \end{bmatrix}\begin{bmatrix} B_x \\ B_y \\ B_z \end{bmatrix} \tag{3.6}$$

We shall distinguish two regimes: during coupling pulses ($\xi = \Delta$) and during free evolution ($\xi = \varphi$). Eq. 3.6 is then explicitly expanded as the differential equations:

$$\begin{aligned} \frac{\partial B_x}{\partial t} &= -\xi B_y \\ \frac{\partial B_y}{\partial t} &= \xi B_x + \Omega B_z \\ \frac{\partial B_z}{\partial t} &= -\Omega B_y \end{aligned} \tag{3.7}$$

where the detuning from the atomic resonance has the conventional definition:

$$\Delta = \omega_{\text{atom}} - \omega_{\text{light}} \tag{3.8}$$

which is only defined during the coupling pulses. In the absence of coupling, during Ramsey free evolution, φ accumulates detuning or miscellaneous perturbations, e.g., collisional level shifts, radiation shifts, etc, taking the general form of a sum:

$$\varphi = \Delta + \Delta_{\text{collisions}} + \Delta_{\text{RF}} + \ldots \tag{3.9}$$

Decoupling of the detuning Δ and level shifts during the evolution φ makes the model capable of sensing perturbation normally considered as imperfections to a more simplistic model with φ always equal Δ. In the following chapters we routinely use this extra flexibility.

We shall refer to φ as the *Ramsey dephasing rate* measured in rad/s. The pulses nullify $\partial B_x / \partial t$ by setting $\varphi = 0$ and prohibiting phase evolution, whereas during the free evolution $\partial B_z / \partial t$ is nullified by setting $\Omega = 0$ allowing only phase evolution with no change in the transition probabilities.

This formalism is employed in the Ramsey sequence given in Fig. 3.3 and later on in the spin echo in Fig. 3.4. The Bloch vector $\boldsymbol{B}$ describes the evolution of state probabilities, unlike $\boldsymbol{P} = (P_x, P_y, P_z)^\top$ which reflects the normalized transition probabilities.

3.2.2 Ramsey interferometry in the time domain

The two-level system (Fig. 4.2) can be represented by a Bloch vector that reflects the evolution of the density operator during the Ramsey pulse sequence (Fig. 3.3) as given in Eq. 3.5. The ensemble is initially prepared in the state $|1\rangle$. A short $\pi/2$-long Rabi pulse equates the populations of both states bringing the vector to the plane where it can only undergo phase evolution[3], to the point of zero phase and zero population difference (*equatorial plane*) as shown in Fig. 3.3(b). The pulses in the method of separated oscillatory fields are considered instantaneous so that their imperfections can be neglected: no population losses, no dephasing. The criterion for no losses for a pulse duration d can be written as $1/\gamma_m \gg d$ with $m \in \{1,2\}$ and the criterion for the coupling is $\Omega \gg \Delta$. The pulses are made $\pi/2$-pulses at all Δ, that is instead of the usual duration $\pi \big/ (2\Omega)$, which leads to

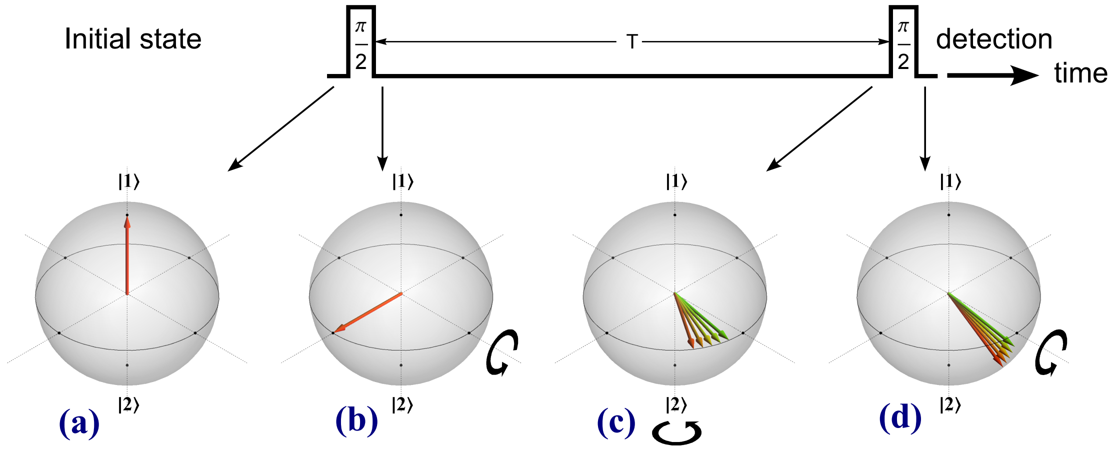

Figure 3.3: Ramsey interferometry and the state evolution represented by the Bloch (pseudo-spin) vector. The unitary vector illustrates lossless evolution; here it is used to display phase diffusion occuring during the evolution. The black circular arrows show the direction of rotation by the effective torque having acted on the vector and the Bloch-sphere diagram displays the resulting state. Colour gradation of the arrows encodes the phase difference between the corresponding Bloch vectors that is acquired in time as a consequence of phase destroying processes.
(a) Initially the atoms are in state $|1,-1\rangle \equiv |1\rangle$, the state $|2,+1\rangle \equiv |2\rangle$ is unpopulated.
(b) After the first $\pi/2$-pulse the effective torque brings the vector to the phase-plane where the population difference is zero and there is no degree of freedom to preserve unitarity other than the phase.
(c) Without interrogation the system relaxes, undergoing population loss and phase destruction, resulting in phase diffusion: the family of state vectors shows a phase-spread proportional to the free evolution time T.
(d) The detecting $\pi/2$-pulse applies a torque induced by the coupling field for yet another $\Omega_R T = \pi/2$ period which brings all the components of the diffused vector to the population difference axis; the detected projection onto the population difference axis (vertical) is modulated by letting the system evolve for a variable time T producing an interferometric signal (fringe) P_z. The fringe can be produced at a fixed T by varying the interrogating field phase of the second $\pi/2$-pulse; see Section 4.3.1 for discussion.

---

[3] For the principal Ramsey and spin-echo interferometry pictures of Figs. 3.3 and 3.4 we discuss the case of unitary evolution, i.e., without losses.

the non-$\pi/2$-pulse at $\Delta \neq 0$, their duration is computed as $\pi \big/ \left(2\Omega_R\right)$ to preserve the $\pi/2$-behaviour away from resonance. The spectra of such systems differ, see the discussion in Section 4.2.

This greatly simplifies the underlying formalism by cancelling the second summand on the right-hand side of Eq. 3.10. However, the effect of the off-resonant interrogation, defined by the two-photon detuning Δ, is in practice often significant and $\Delta \neq 0$ is assumed.

Once the coupling of the first $\pi/2$-pulse is off, the system is left to evolve for a time period $\boldsymbol{T}$. States $|1\rangle$ and $|2\rangle$ are *clock states* due to a “magic” field at which the atomic transition experiences only a small perturbation from the ambient magnetic noise. The phase difference between the two states starts growing in accordance with the instability of the two-photon driving frequency. Before the second $\pi/2$-pulse arrives, the ensemble phase will have dispersed due to the different atoms undergoing evolution in different local conditions.

The second $\pi/2$-pulse rotates the Bloch vector about the same axis to accomplish *projective detection* of the phase evolved after time $\boldsymbol{T}$. It brings the imprinted phase to the axis of the normalized population difference $\boldsymbol{P}_z$ being our measurable quantity. Locally dephased parts of the ensemble, schematically shown by a set of Bloch vectors in Fig. 3.3, result in a distribution of projections (blurring), the width of which defines the detection limit.

The analysis of the long Ramsey evolution of magnetically trapped atoms should include particle losses and ensemble effects like cold atomic collisions and dephasing due to field inhomogeneities as they become non-negligible.

3.2.3 Master equation with one-body losses

Particle loss, that causes dephasing, and the *pure dephasing* that only occurs between the states and is not associated with population loss, can be included in the Liouville–von Neumann equation [99, 121–123]. It is then generally written as:

$$\frac{\partial \rho}{\partial t} = \frac{1}{i\hbar}\left[\boldsymbol{H}, \rho\right] - \frac{1}{2}\left\{\hat{\Gamma}, \rho\right\} - \frac{1}{2}\hat{\Xi} \circ \rho \tag{3.10}$$

where $\hat{\Gamma}$ is the loss operator that sets up γ_1, the population loss rate of state $|1\rangle$, and γ_2, the population loss rate of state $|2\rangle$. ρ is the density operator, $[\bullet, \bullet]$ and $\{\bullet, \bullet\}$ are commutator and anticommutator brackets, respectively, and $\boldsymbol{H}$ is the effective Hamiltonian of a spin-$\frac{1}{2}$ system. In the interferometry discussions we shall consider $\boldsymbol{H}$ in the rotating wave approximation. The loss operator is defined as a matrix:

$$\hat{\Gamma} = \begin{bmatrix} \gamma_1 & 0 \\ 0 & \gamma_2 \end{bmatrix} \tag{3.11}$$

The Hadamard entrywise matrix product allows us to conveniently introduce the off-diagonal phase relaxation rates γ_d in the pure dephasing operator $\hat{\Xi}$ as a separate summand $\hat{\Xi} \circ \rho$ of Eq. 3.10 where $\hat{\Xi}$ takes the form of the following matrix:

$$\hat{\Xi} = \begin{bmatrix} 0 & \gamma_{12} \\ \gamma_{21} & 0 \end{bmatrix} \tag{3.12}$$

with equal pure dephasing rates[4] in the lower and upper parts of the operator matrix: $\gamma_{12} = \gamma_{21} = \gamma_d$. Eq. 3.10 can be written in the explicit form of the evolution differential equations as:

$$\frac{\partial \rho_{11}}{\partial t} = -\gamma_1 \rho_{11} - \frac{i}{2}\Omega\left(\rho_{21} - \rho_{12}\right) \tag{3.13a}$$

$$\frac{\partial \rho_{22}}{\partial t} = -\gamma_2 \rho_{22} + \frac{i}{2}\Omega\left(\rho_{21} - \rho_{12}\right) \tag{3.13b}$$

$$\frac{\partial \rho_{12}}{\partial t} = -\gamma_3 \rho_{12} + \frac{i}{2}\Omega\left(\rho_{11} - \rho_{22}\right) + i\Delta\rho_{12} \tag{3.13c}$$

$$\frac{\partial \rho_{21}}{\partial t} = -\gamma_3 \rho_{21} - \frac{i}{2}\Omega\left(\rho_{11} - \rho_{22}\right) - i\Delta\rho_{21} \tag{3.13d}$$

where an auxiliary relaxation constant including the pure dephasing rate γ_d is introduced:

$$\gamma_3 = \frac{\gamma_1 + \gamma_2 + \gamma_d}{2} \tag{3.14}$$

The Liouville–von Neumann equation (Eq. 3.10) is solved with non-zero loss terms included with the assumption of lossless interrogation pulses. The time sequence is split into regions, and the corresponding local solutions are made to satisfy the boundary conditions. The solution of Eq. 3.10 for the off-resonant Ramsey sequence where the losses are non-negligible and the Ramsey dephasing rate φ allows us to input various perturbations of the energy levels, reads:

$$\rho_{11} = \frac{1}{4\Omega_R^4}\left[\Omega^4 e^{-\gamma_2 T} + \left(\Delta^2 + \Omega_R^2\right)^2 e^{-\gamma_1 T} - k_1\right] \tag{3.15a}$$

$$\rho_{22} = \frac{1}{4\Omega_R^4}\left[\Omega^2\left(\Delta^2 + \Omega_R^2\right)\left(e^{-\gamma_1 T} + e^{-\gamma_2 T}\right) + k_1\right] \tag{3.15b}$$

$$P_z = \frac{\Delta^2\left(k_2 - k_3\right) - k_1 e^{(\gamma_1+\gamma_2)T}}{\Omega_R^2\left(k_2 + k_3\right)} \tag{3.15c}$$

---

[4] Strictly speaking γ_{12} and γ_{21} are only required to be complex conjugate. However in the frame of the discussed physics they are real and hence can be considered equal. The same argument is applied to $\Omega = \Omega^*$.

with the following auxiliary definitions:

$$
\begin{aligned}
k_1 &= 2\Omega^2 e^{-\gamma_3 T}(\Omega^2 \cos(\varphi T) - 2\Delta\Omega_R \sin(\varphi T)) \\
k_2 &= \left(\Delta^2 + \Omega_R^2\right) e^{\gamma_2 T} \\
k_3 &= \Omega^2 e^{\gamma_1 T} \\
\gamma_3 &= \frac{1}{2}\left(\gamma_1 + \gamma_2 + \gamma_d\right)
\end{aligned}
$$

The model is parametrized by the Ramsey evolution time T, the detuning Δ from the atomic resonance defined during interrogation, the cumulative Ramsey dephasing rate φ defined during free evolution, the resonant Rabi frequency Ω, the generalized Rabi frequency $\Omega_R = \sqrt{\Delta^2 + \Omega^2}$, the population loss rates for the states $|1\rangle$ and $|2\rangle$ – γ_1 and γ_2, respectively, and the phenomenological dephasing[5] rate γ_d.

It is often the case that the interrogation is made resonant with the atomic transition. Then Eqs. 3.15 simplify to[6]:

$$
\rho_{11} = \frac{1}{4}\left(e^{-\gamma_1 T} + e^{-\gamma_2 T} - 2e^{-\gamma_3 T}\cos(\varphi T)\right) \tag{3.17a}
$$

$$
\rho_{22} = \frac{1}{4}\left(e^{-\gamma_1 T} + e^{-\gamma_2 T} + 2e^{-\gamma_3 T}\cos(\varphi T)\right) \tag{3.17b}
$$

$$
P_z = -e^{-\frac{1}{2}\gamma_d T}\,\mathrm{sech}\left(\frac{\gamma_1 - \gamma_2}{2} T\right)\cos(\varphi T) \tag{3.17c}
$$

Equation 3.17c owes its simplicity to the inherent symmetry of P_z due to normalization to $N(t)$ (see Section 3.1.1). It is remarkable that at $\gamma_1 = \gamma_2$, which is the case in our experiment, $\mathrm{sech}\left((\gamma_1 - \gamma_2)T/2\right) = 1$ and the dephasing rate γ_d can be determined experimentally[7] by setting the Ramsey dephasing rate $\varphi = 0$.

3.2.4 Spin echo interferometry

As in time-domain Ramsey interferometry, the Bloch vector undergoes a number of successive rotations by an effective torque $\mathbf{\Omega}$ in the absence of losses (see Eqs. 3.5). In addition, in the middle of the Ramsey sequence a phase-reversal π-pulse flips the direction of the dephasing, the atoms start rephasing and at the instant of the arrival of the second $\pi/2$-pulse the dephased states are refocused, as schematically represented on the Bloch sphere in Fig. 3.4.

The solution of the above model (Eq. 3.10) for the off-resonant Ramsey sequence with spin echo, where the losses are non-negligible and Ramsey dephasing

---

[5] Hereinafter implying *pure* dephasing rate for γ_d.

[6] We provide ρ_{jj} elements as well to ease the construction of other observables upon necessity. The off-diagonal elements are of no interest for the phase cannot be measured; we omit ρ_{ij} elements.

[7] This is correct if the inhomogeneous phase distribution, e.g., due to trapping, is negligible.

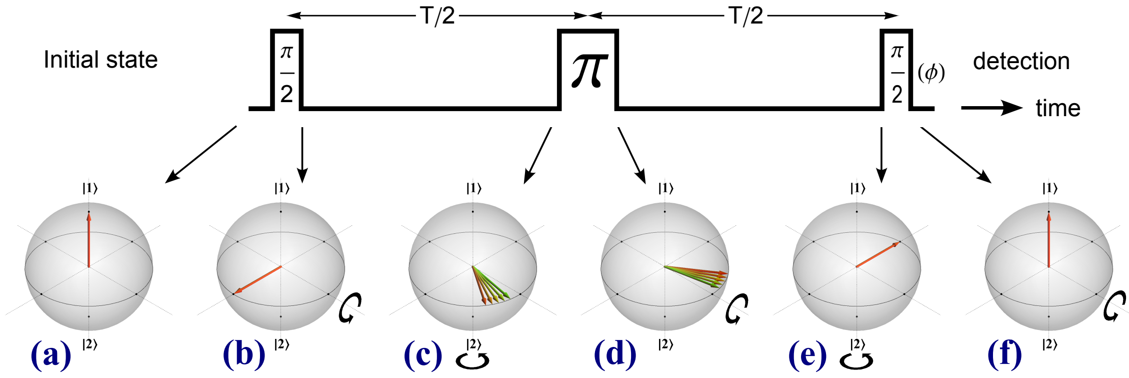

Figure 3.4: Spin echo interferometry and the state evolution represented by the Bloch vector. The unitary vector illustrates lossless evolution. Here it is used to display phase diffusion occurring during the evolution. The black circular arrows show the directions of rotation by the effective torque having acted on the vector and the Bloch-sphere diagram displays the resulting state. Colour gradation of the arrows displays the phase difference between them that is acquired in time as a consequence of phase destroying processes. ϕ is the phase of the second $\pi/2$-pulse. As in time-domain Ramsey interferometry, ϕ modulation can be used at a fixed T to record a P_z fringe; see Section 4.3.1 for discussion.
(a), (b), (c) The same processes as the correspondingly labelled ones in Fig. 3.3.
(d) Spin-echo pulse implements a complete phase reversal so that the phase dispersive behaviour starts acting in the opposite direction.
(e) By the arrival time of the last pulse all the phase-dispersed (diffused) components of the Bloch vector are completely refocused restoring the initial phase distribution of the Bloch vector (only the part that depends on atomic spins).
(f) The refocused pulse is subjected to torque by yet another coupling $\pi/2$-pulse that projects the vector onto the population axis only: there is no phase spread accumulated in the state vector during T. Upon modulation of either the Ramsey dephasing rate φ or the evolution time T or ϕ a full-period fringe can be mapped out on the population axis.

rates of the first arm of the interferometer φ_1 and of the second arm φ_2 allows the input of miscellaneous physical processes displacing the energy levels, that can be sensed by the interferometer, is parametrized by: the total sequence duration T from the first to the last pulse, and the cumulative Ramsey dephasing rates φ_1 and φ_2 in the first and second arms. Each arm is $T/2$ long as depicted in Fig. 3.4.

With the definitions

$$\begin{aligned}
&\gamma_3 = \frac{\gamma_1+\gamma_2+\gamma_d}{2}, \quad a_0 = e^{-\gamma_3 T}, \quad a_1 = e^{-\gamma_1 T}, \quad a_2 = e^{-\frac{\gamma_1+\gamma_3}{2}T}, \quad a_3 = e^{-\gamma_2 T},\\
&a_4 = e^{-\frac{\gamma_2+\gamma_3}{2}T}, \quad a_5 = e^{-\frac{\gamma_1+\gamma_2}{2}T}, \quad a_6 = \cos\left(\frac{\varphi_1}{2}T\right), \quad a_7 = \cos\left(\frac{\varphi_2}{2}T\right),\\
&a_8 = \sin\left(\frac{\varphi_1}{2}T\right), a_9 = \sin\left(\frac{\varphi_2}{2}T\right), b_0 = e^{\left(\gamma_1+\frac{\gamma_3}{2}\right)T}, b_1 = e^{\frac{1}{2}(\gamma_1+\gamma_2+\gamma_3)T},\\
&b_2 = e^{\left(\gamma_1+\frac{\gamma_2}{2}\right)T}, \quad b_3 = e^{\left(\gamma_2+\frac{\gamma_3}{2}\right)T}, \quad b_4 = e^{\left(\frac{\gamma_1}{2}+\gamma_2\right)T}, \quad b_5 = e^{\left(\gamma_1+\gamma_2-\frac{\gamma_3}{2}\right)T},\\
&k_0 = \Delta^2\Omega^2 b_0\Omega_R^3 + \Delta^4 b_3\Omega_R^3 - 2\Delta^2\Omega^2 b_2 a_6\Omega_R^3 + 2\Delta^2\Omega^2 b_4 a_6\Omega_R^3 - 2\Delta\Omega^2 b_2 a_8\Omega_R^4\\
&\qquad + 2\Delta\Omega^2 b_4 a_8\Omega_R^4 + 2\Omega^2 b_1\Omega_R^5 + \Delta^2 b_3\Omega_R^5
\end{aligned} \tag{3.18}$$

the Liouville–von Neumann equation yields the following solution for the populations ρ_{11}, ρ_{22} and the normalized population difference $\boldsymbol{P}_z$:

$$\begin{aligned}
\rho_{11}\cdot 4\Omega_R^7 = {} & \Delta^6 a_1 \Omega_R - 2\Delta^3\Omega^4 a_4 a_8 - 2\Delta\Omega^6 a_4 a_8 - 4\Delta^5\Omega^2 a_0 a_7 a_8 - 4\Delta^3\Omega^4 a_0 a_7 a_8 \\
& + \Delta^2\Omega^4 a_3 \Omega_R + 2\Delta^2\Omega^4 a_5 \Omega_R + 2\Delta^4\Omega^2 a_2 a_6 \Omega_R - 2\Delta^2\Omega^4 a_4 a_6 \Omega_R \\
& + 2\Delta^4\Omega^2 a_2 a_7 \Omega_R - 2\Delta^2\Omega^4 a_4 a_7 \Omega_R + 6\Delta^2\Omega^4 a_0 a_6 a_7 \Omega_R + 2\Omega^6 a_0 a_6 a_7 \Omega_R \\
& + 2\Delta^3\Omega^2 a_2 a_8 \Omega_R^2 + 2\Delta^3\Omega^2 a_2 a_9 \Omega_R^2 - 2\Delta\Omega^4 a_4 a_9 \Omega_R^2 - 4\Delta^3\Omega^2 a_0 a_6 a_9 \Omega_R^2 \\
& + 2\Delta^4 a_1 \Omega_R^3 + 2\Omega^4 a_5 \Omega_R^3 + 2\Delta^2\Omega^2 a_2 a_6 \Omega_R^3 + 2\Delta^2\Omega^2 a_2 a_7 \Omega_R^3 \\
& + 2\Omega^4 a_0 a_8 a_9 \Omega_R^3 + 2\Delta\Omega^2 a_2 a_8 \Omega_R^4 + 2\Delta\Omega^2 a_2 a_9 \Omega_R^4 + \Delta^2 a_1 \Omega_R^5
\end{aligned} \tag{3.19a}$$

$$\begin{aligned}
\rho_{22}\cdot 4\Omega_R^7 = {} & \Delta^4\Omega^2 a_1 \Omega_R + \Delta^4\Omega^2 a_3 \Omega_R - 4\Delta^5\Omega^2 a_4 a_8 - 6\Delta^3\Omega^4 a_4 a_8 - 2\Delta\Omega^6 a_4 a_8 \\
& + 4\Delta^3\Omega^4 a_0 a_7 a_8 + 4\Delta^5\Omega^2 a_0 a_7 a_8 + 4\Delta^4\Omega^2 a_5 \Omega_R + 4\Delta^2\Omega^4 a_5 \Omega_R - 2\Delta\Omega^2 a_2 a_9 \Omega_R^4 \\
& + 2\Omega^6 a_5 \Omega_R + 2\Delta^2\Omega^4 a_2 a_6 \Omega_R - 4\Delta^4\Omega^2 a_4 a_6 \Omega_R - 2\Delta^2\Omega^4 a_4 a_6 \Omega_R \\
& - 2\Delta^4\Omega^2 a_2 a_7 \Omega_R + 2\Delta^2\Omega^4 a_4 a_7 \Omega_R - 6\Delta^2\Omega^4 a_0 a_6 a_7 \Omega_R - 2\Omega^6 a_0 a_6 a_7 \Omega_R \\
& + 2\Delta\Omega^4 a_2 a_8 \Omega_R^2 - 2\Delta^3\Omega^2 a_2 a_9 \Omega_R^2 + 2\Delta\Omega^4 a_4 a_9 \Omega_R^2 + 4\Delta^3\Omega^2 a_0 a_6 a_9 \Omega_R^2 \\
& + \Delta^2\Omega^2 a_1 \Omega_R^3 + \Delta^2\Omega^2 a_3 \Omega_R^3 - 2\Delta^2\Omega^2 a_2 a_7 \Omega_R^3 - 2\Omega^4 a_0 a_8 a_9 \Omega_R^3
\end{aligned} \tag{3.19b}$$

$$\begin{aligned}
\boldsymbol{P}_z \cdot k_0 = {} & 2\Delta^5\Omega^2 b_2 a_8 + 2\Delta^3\Omega^4 b_2 a_8 + 2\Delta^5\Omega^2 b_4 a_8 + 2\Delta^3\Omega^4 b_4 a_8 - 4\Delta^5\Omega^2 b_5 a_7 a_8 \\
& - 4\Delta^3\Omega^4 b_5 a_7 a_8 - \Delta^4\Omega^2 b_0 \Omega_R - 2\Delta^4\Omega^2 b_1 \Omega_R + 2\Delta^6 b_3 \Omega_R + \Delta^4\Omega^2 b_3 \Omega_R \\
& + 2\Delta^4\Omega^2 b_2 a_6 \Omega_R + 2\Delta^4\Omega^2 b_4 a_6 \Omega_R - 2\Delta^2\Omega^4 b_2 a_7 \Omega_R + 4\Delta^4\Omega^2 b_4 a_7 \Omega_R \\
& + 2\Delta^2\Omega^4 b_4 a_7 \Omega_R + 6\Delta^2\Omega^4 b_5 a_6 a_7 \Omega_R + 2\Omega^6 b_5 a_6 a_7 \Omega_R - 2\Delta\Omega^4 b_2 a_9 \Omega_R^2 \\
& + 2\Delta^3\Omega^2 b_4 a_9 \Omega_R^2 - 4\Delta^3\Omega^2 b_5 a_6 a_9 \Omega_R^2 + 2\Omega^4 b_5 a_8 a_9 \Omega_R^3 + 2\Delta\Omega^2 b_4 a_9 \Omega_R^4
\end{aligned} \tag{3.19c}$$

Provided the detuning is zero in Eqs. 3.19, which is physically justified in the case of $\Delta \ll \Omega$, Eqs. 3.19 become:

$$\rho_{11} = \frac{1}{2} e^{-\gamma_3 T} \left[e^{\frac{\gamma_d}{2} T} + \cos\left(\frac{\varphi_1 - \varphi_2}{2} T \right) \right] \tag{3.20a}$$

$$\rho_{22} = \frac{1}{2} e^{-\gamma_3 T} \left[e^{\frac{\gamma_d}{2} T} - \cos\left(\frac{\varphi_1 - \varphi_2}{2} T \right) \right] \tag{3.20b}$$

$$\boldsymbol{P}_z = e^{-\frac{1}{2}\gamma_d T} \cos\left(\frac{\varphi_1 - \varphi_2}{2} T \right) \tag{3.20c}$$

It is easy to observe from Eqs. 3.20 that the phase acquired in the first arm of the spin-echo interferometer $\varphi_1 T / 2$ is completely eliminated by the same value of the phase in the second arm $\varphi_2 T / 2$ which is the expected behaviour of the spin echo interferometry. Since the sign of the dephasing is reversed by the π-pulse, the spin echo cancels out any perturbation that is persistent in the system between the $\pi/2$-pulses.

3.2.5 Interferometry with variable-duration pulses

As a useful extension to the standard Ramsey technique we present solutions for the interferometry method with variable durations of the splitting and detecting pulses. Similarly to the models above, we decouple the concepts of the detuning during interrogation Δ and its counterpart during evolution, the dephasing rate φ, that in the Ramsey method are equal $\varphi = \Delta$.

The Liouville–von Neumann Eq. 3.10 is parametrized appropriately in each period of the sequence and a solution for time-dependent variables is found, and then the boundary conditions are satisfied. The following assumptions are made in the model: the detuning of the interrogating field Δ is arbitrary, no losses during the interrogating pulses, no radiation during free evolution ($\Omega = 0$). The populations ρ_{11} and ρ_{22} at the interferometer output are give by:

$$
\begin{aligned}
\rho_{11} \cdot 4\Omega_R^4 e^{(\gamma_1+\gamma_2)T} &= k_3 k_4 e^{-\gamma_1 T} + 4\Omega^4 e^{\gamma_1 T} \sin^2\left(\frac{\Omega_R}{2}T_{p1}\right) \sin^2\left(\frac{\Omega_R}{2}T_{p2}\right) \\
&\quad - 2\Omega^2 e^{\frac{1}{2}(\gamma_1+\gamma_2-\gamma_d)T}(k_1 - k_2) \qquad (3.21\text{a}) \\
\rho_{22} \cdot 4\frac{\Omega_R^4}{\Omega^2} e^{(\gamma_1+\gamma_2)T} &= k_3 + k_4 - k_4 \cos(\Omega_R T_{p1}) - k_3 \cos(\Omega_R T_{p2}) \\
&\quad + 2e^{\frac{1}{2}(\gamma_1+\gamma_2-\gamma_d)T}(k_1 - k_2) \qquad (3.21\text{b})
\end{aligned}
$$

with auxiliary definitions for the sake of compactness:

$$
\begin{aligned}
k_1 &= \left[\Omega_R^2 \sin\left(\Omega_R T_{p1}\right) \sin\left(\Omega_R T_{p2}\right) - 4\Delta^2 \sin^2\left(\frac{\Omega_R}{2}T_{p1}\right) \sin^2\left(\frac{\Omega_R}{2}T_{p2}\right)\right] \cos(\varphi T) \\
k_2 &= \Omega_R \Delta \left[\sin\left(\Omega_R T_{p1}\right) + \sin\left(\Omega_R T_{p2}\right) - \sin\left(\Omega_R T_{p1} + \Omega_R T_{p2}\right)\right] \sin(\varphi T) \\
k_3 &= e^{\gamma_2 T} \left(\Delta^2 + \Omega_R^2 + \Omega^2 \cos\left(\Omega_R T_{p1}\right)\right) \qquad (3.22) \\
k_4 &= e^{\gamma_1 T} \left(\Delta^2 + \Omega_R^2 + \Omega^2 \cos\left(\Omega_R T_{p2}\right)\right) \\
k_5 &= e^{\gamma_1 T} \Omega^2 \left(1 - \cos\left(\Omega_R T_{p1}\right)\right)
\end{aligned}
$$

The normalized population difference is found from the definition of Eq. 3.1 to be:

$$
P_z = \frac{\Omega_R^{-2}}{k_3 + k_5} \left[\left(k_3 - k_5\right) \left[\Delta^2 + \Omega^2 \cos\left(\Omega_R T_{p2}\right)\right] - 2\Omega^2 \left(k_1 - k_2\right) e^{(\gamma_1+\gamma_2-\gamma_d)\frac{T}{2}}\right] \qquad (3.23)
$$

In the case when equal splitting is desired at arbitrary detuning Δ to obtain $P_z = 0$ the corresponding splitter pulse duration T_{p1} is obtained from the lossless Rabi model (Eqs. 3.3) by solving the equation $P_z(t) = 0$. The first pulse duration is then:

$$
t_{\pi/2} = T_{p1} = \arccos\left(-\frac{\Delta^2}{\Omega^2}\right) \Big/ \Omega_R^2 \qquad (3.24)
$$

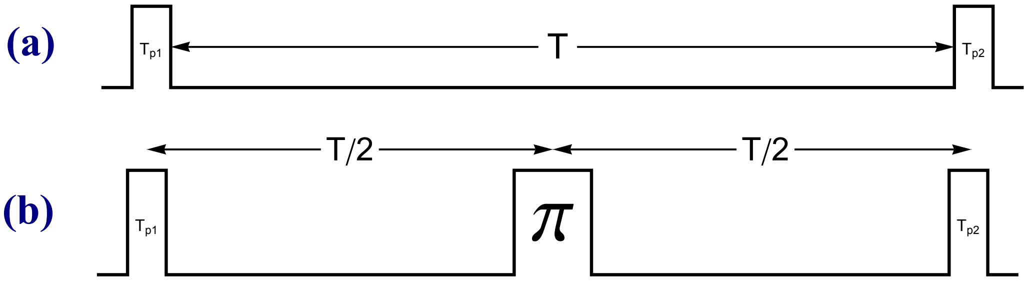

Figure 3.5: Ramsey interferometry with pulses of variable duration.
(a) Pulses have durations T_{p1} and T_{p2}, generally not equal to $\pi/2$.
(b) Modification of the spin echo sequence for the variable-duration pulses.

where the sequence can be closed by a $\pi/2$-pulse defining the duration $T_{p2} = \pi \big/ \left(2\Omega_R\right)$. The T_{p1} is limited by the detuning that is required to be not larger than the resonant Rabi frequency: $\Omega \geq \Delta$. If this condition is not satisfied, the equation $P_z(t) = 0$ gives an unphysical imaginary result. This is because the interferometric fringe detuned above $\Delta = \Omega$ raises the P_z minima above the zero line. The fringe never crosses zero and the solutions for $t_{\pi/2}$ become imaginary. The maximal possible off-resonant $\pi/2$-pulse duration that provides equal population splitting is then found to be:

$$t_{\pi/2} = \frac{\pi}{\Omega\sqrt{2}} \tag{3.25}$$

A straight-forward application of the T_{p2} variation is to include the experimental imperfections, associated with the second-pulse coupling, in the data fitting procedure. The T_{p1} variation is of a more subtle character: the splitter allows the initiation of free evolution with unequal populations that under one-body asymmetric losses may evolve into *equal* populations after some time. For this to happen the state with the higher loss rate needs to be loaded more at the beginning of the evolution. The point where the unequally split populations equalize gives the maximal normalized population value, e.g. $\max\left\{P_z\right\}$. Chasing the optimal value in T by accordingly correcting the splitter duration T_{p1} one can attain a perpetually maximal contrast of $P_z(T)$. This is of benefit for data fitting because the envelope function becomes constant and ceases to play a role. Of course, this method does not affect the signal-to-noise ratio defined by the fundamental limit, the Heisenberg uncertainty, assuming the absence of a super-Heisenberg number scaling [124–130].

It is tempting to develop an analogous model for the spin echo interferometry as shown in Fig. 3.5(b). However this is unnecessary for the purpose of the loss asymmetry cancellation discussed in Section 3.2.6, since the echo type sequence exactly compensates for the asymmetry by the end of the sequence. Including an additional mechanism of loss asymmetry correction would be overkill.

3.2.6 One-body loss asymmetry cancellation

The visibility in long Ramsey experiments decreases with loss asymmetry as has been discussed in the previous paragraphs. For analysis, though, it is desirable to have a constant visibility, i.e., independent of the loss asymmetry. A look at the population decays in Fig. 3.9 reveals that if the populations started from unequal values so that the faster decaying state is initially populated more highly, $N_2(T = 0) > N_1(T = 0)$, then $N_1(T)$ and $N_2(T)$ would cross. The normalized population difference P_z would turn out to have a maximum at this point with effectively *cancelled* loss asymmetry. One can tailor a time-domain Ramsey sequence to obtain a fringe with variable splitter $\pi/2$-pulse duration that gives unitary visibility at a desired location. The corresponding model of the interferometric sequence is given in Section 3.2.5.

To derive the expression for the optimal first-pulse duration, the density operator $\rho(t)$ is propagated till the end of free evolution, before the arrival of the second $\pi/2$-pulse, where the populations take the following values:

$$\rho_{11}(t) = \frac{1}{2\Omega_R^2} e^{-\gamma_1 t} \left(\Delta^2 + \Omega_R^2 + \Omega^2 \cos\left(\Omega_R T_{p1}\right)\right) \tag{3.26a}$$

$$\rho_{22}(t) = \frac{1}{2\Omega_R^2} e^{-\gamma_2 t} \Omega^2 \left(1 - \cos\left(\Omega_R T_{p1}\right)\right) \tag{3.26b}$$

The crossing of the populations is found by solving equation $\rho_{11}(t) = \rho_{22}(t)$ with respect to time t and discarding irrelevant solutions. The solution gives time where the maximum visibility of P_z occurs as a function of T_{p1}; we label this time $T_{optimal}$ further on:

$$T_{optimal} = \frac{1}{\gamma_1 - \gamma_2} \ln\left(\left[\frac{\Omega_R}{\Omega} \csc\left(\Omega_R T_{p1}/2\right)\right]^2 - 1\right) \tag{3.27}$$

In Fig. 3.6 the effect of loss compensation is shown with a set of test parameters. Fig. 3.6(a) shows the dynamics of the freely evolving populations following the application of the standard $\pi/2$ splitting pulse. The populations are plotted before the arrival of the detecting $\pi/2$-pulse. In contrast, Fig. 3.6(b) shows how the splitter can affect the populations and lead to their balance at an arbitrary time T. Figs. 3.6(c,d) show the populations and measurable P_z after the full interferometric sequence with a non-zero φ producing a fringe. In accordance with the expectations, Fig. 3.6(d) indicates an extremum in the visibility at $T = T_{optimal}$ that is defined by Eq. 3.27.

Equation 3.27 is only valid for one-body decay limited systems, i.e., under the assumption that γ_1 and γ_2 are much larger than the other characteristic decay rates in the system[8]. The many-body counterpart of this model can be obtained

---

[8] This condition holds, if the vacuum is low. See the next chapter for discussion.

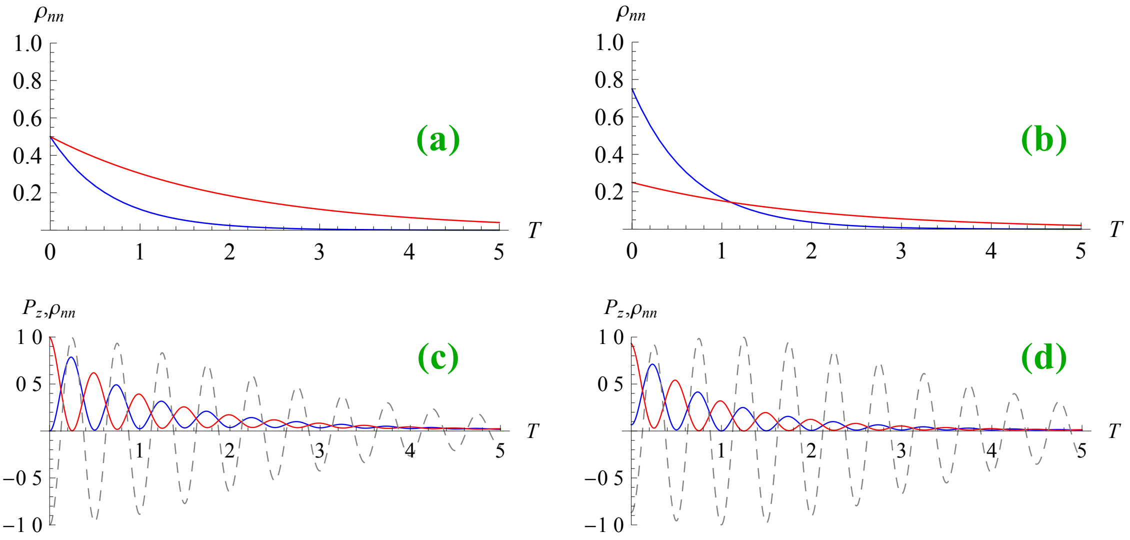

Figure 3.6: Equalizing the state $|1\rangle$ and $|2\rangle$ population decays by a variable-duration splitter pulse to enhance the observable P_z. The model is evaluated for the following set of parameters: $\Delta = 0$, $T_{p2} = \pi/2$, $\gamma_1 = 1.5$, $\gamma_2 = 0.5$, $\gamma_d = 0$, $\varphi = 2\pi \times 2$ and $\Omega > 0$. Populations ρ_{11} and ρ_{22} from Eqs. 3.26 are given in **blue** and **red**, respectively, P_z is given by Eq. 3.23 in **dashed grey**.
(a) $T_{p1} = \pi/2$: equally split populations ρ_{nn} at the end of free evolution, at T;
(b) $T_{p1} = \pi/3$: unequal splitting to produce a crossing of the population decay trajectories before the arrival of the second pulse;
(c) $T_{p1} = \pi/2$: after the complete sequence, P_z has a monotonic $\mathrm{sech}\left[(\gamma_1 - \gamma_2)T/2\right]$ envelope at $\gamma_1 \neq \gamma_2$ as follows from Eq. 3.17c;
(d) $T_{p1} = \pi/3$: after the complete sequence a peak of visibility is observed at $T = T_{optimal} \approx 1.1$ as expected from Eq. 3.27.

by applying the presented analysis, provided Eqs. 3.60 are used instead of Eq. 3.13. An approximate value of the many-body $T_{optimal}$ can be found by solving equation $N_1(t) = N_2(t)$ with respect to t with $N_1(t)$ and $N_2(t)$ taken from Eqs. 3.34. Such an approach suffers from the high nonlinearity of the resulting master equation which in practice implies numerical integration to search for the corresponding T_{optimal}. The two-level evolution with many-body processes is discussed in Section 3.3.5.

It should also be noted that such a technique does not improve the signal-to-noise ratio for the noise limit determined by the atomic flux with a Poissonian atom number distribution and Heisenberg uncertainty in the absence of spin squeezing. The attained effect helps to equalize the visibility for $P_z(\phi, T)$ and to facilitate fitting of the envelope function when only frequency or phase distribution is sought, as in the case of the atom clock stability experiments presented in the next chapter. The approach is equally valid for time- and phase-domain Ramsey experiments where a purely sinusoidal fit can be applied to the data sets. It makes it possible to use the time-Ramsey signal in phase characterization without going to the phase domain. The option of pulse phase modulation may not be available in the system whereas the visibility (fringe amplitude) decay be present.

3.3 Interferometry with many-body losses

3.3.1 Inelastic losses

In the most general form many-body losses can be included in the rate equation as a power series[9] where each order of a summand describes the atomic density $n_i(t)$ inelastic loss at the rate $\gamma_{i,ii,iii,...}$, i denotes the state $|i\rangle$ and the number of repeated indices reflects the number of simultaneously colliding particles in the states successively enumerated in the subscript. In this way γ_1 is the inelastic one-body loss rate of state $|1\rangle$ atoms without their collisional interaction with the other states included in the model[10], γ_{11} is the two-body decay rate for two colliding atoms in state $|1\rangle$, and so on.

$$\frac{\partial n_i}{\partial t} = -\gamma_i n_i - \gamma_{ii} n_i^2 - \gamma_{iii} n_i^3 - \ldots \tag{3.28}$$

When more than one state is involved, the interaction terms are added as shown later in this chapter. Then the two-body decay rate to account for the collisional interaction of the atoms in states $|1\rangle$ and $|2\rangle$ is denoted as γ_{12}.

If three-body losses cannot be neglected, the summand with γ_{111} would have a coefficient, analogous to k in Eqs. 3.33, defined as k_{111} below. The corresponding physical system can readily be implemented in spin-1 systems such as one of the stretched states of the ^{87}Rb $F = 1$ hyperfine ground state where two-body collisions are prohibited.

Since we measure atom numbers rather than atomic densities, to find N we perform integration over the thermal cloud density profile:

$$N = \int_{-\infty}^{+\infty} \int_{-\infty}^{+\infty} \int_{-\infty}^{+\infty} n(t)\,\mathrm{d}x\,\mathrm{d}y\,\mathrm{d}z \tag{3.29}$$

For a thermal cloud with quick re-thermalization we arrive at the rate equation for the number of atoms $N(t)$:

$$k_{111} = \frac{1}{\left(2\pi\sqrt{3}\right)^3 \left(\sigma_x \sigma_y \sigma_z\right)^2} \tag{3.30a}$$

$$\frac{\partial N}{\partial t} = -\gamma_1 N - \gamma_{111}\, k_{111}\, N^3 \tag{3.30b}$$

Integration with respect to t and the choice of a physically justfied solution gives

---

[9] Later in this chapter we shall derive the relevant rate equations; here they are introduced in a simpler form for transparency of the analysis.

[10] Such excluded atoms are collectively called a *background gas*.

the following exact solution:

$$N(t) = \left[\left(N_0^{-2} + k_{111} \frac{\gamma_{111}}{\gamma_1} \right) e^{2\gamma_1 t} - k_{111} \frac{\gamma_{111}}{\gamma_1} \right]^{-1/2} \tag{3.31}$$

where $N_0 \equiv N(0)$ is the initial population at $t = 0$. It is particularly interesting that in ^{133}Cs it is possible to find a pair of levels for two-state interferometry that both experience intra-state collisions, that is, the corresponding two-body decay processes should not differ as much as in a system of one stretched state and one unstretched state, and visibility is enhanced.

However, γ_{111} is very small[11], the values for BEC reported in [64, 65] are 5.4×10^{-30} cm^6/s and 5.8×10^{-30} cm^6/s. It follows from the analysis of Eq. 3.31 that for our typical experimental parameters the molecular formation due to three-body recombination is a negligible loss process which only becomes visible at temperatures close to T_{crit} for $N_0 > 10^6$ and pressures an order of magnitude lower than the lowest that can normally be achieved, that is, approximately 10^{-12} Torr[12], and magnetic trapping times over minutes, an order of magnitude longer than we can achieve. Alternatively, the stronger dependence on the initial atom number N_0 of Eq. 3.31 can be used. Then under the current experimental conditions N_0 should be of the order of 5×10^6 atoms for the molecular fraction to become distinct over a 10-s hold time and the available pressure of 2×10^{-11} Torr. Therefore, in most experiments with thermal atoms γ_{111} can safely be disregarded.

In a superposition of two states, when the total population is split into halves, the inter-state terms appear in the rate equations. The three-body recombination $\gamma_{111} n_1^3$ and two-body $\gamma_{22} n_1^2$ loss terms are excluded from the n_1 rate equation as they are irrelevant [132, 133]: γ_{111} has a notable contribution only below the critical temperature where the phase-space density drastically increases the probability of an atomic triplet to form; only state $|1,-1\rangle$ is occupied, the other state contributions nullify in the rate equation, and the intra-state collisions are prohibited by the selection rules in any stretched states. Owing to the latter, the experiment on the decay of the $|1,-1\rangle$ population results in a simple exponential law that can be readily fitted to the data points to extract γ_1. At the same time relying on the fact that the underlying process of losing atoms due to collisions with the background gas is state insensitive — an atom in either state will be immediately lost after momentum exchange with a room temperature atom — γ_2 can be equated to γ_1.

$$\frac{\partial n_1}{\partial t} = -\gamma_1 n_1 - \gamma_{12} n_1 n_2 \tag{3.32a}$$

---

[11] Note that the many-body loss rates measured in condensates need a correction if applied to thermal atoms as in the discussed case [65, 131]. See Section 3.3.6 for details.

[12] It also constitutes a problem to measure lower pressures than this value.

$$\frac{\partial n_2}{\partial t} = -\gamma_2 n_2 - \gamma_{12} n_1 n_2 - \gamma_{22} n_2^2 \tag{3.32b}$$

The above density rate equations need to be spatially integrated over the cloud density profile. Under the assumption of constant temperature, the number rate equations are found to be:

$$k = \frac{1}{8\pi^{3/2}\sigma_x\sigma_y\sigma_z}, \quad \sigma_p = \sqrt{\frac{k_B T}{m\omega_p^2}} \tag{3.33a}$$

$$\frac{\partial N_1}{\partial t} = -\gamma_1 N_1 - \gamma_{12}\, k\, N_1 N_2 \tag{3.33b}$$

$$\frac{\partial N_2}{\partial t} = -\gamma_2 N_2 - \gamma_{12}\, k\, N_1 N_2 - \gamma_{22}\, k\, N_2^2 \tag{3.33c}$$

where $p \in \{x, y, z\}$.

To solve Eqs. 3.33 we employ a perturbative approach under the feasible assumption that the decay of $N_1(t)$ is much slower than that of $N_2(t)$. First, Eq. 3.33c is solved for $N_2(t)$ assuming a constant N_1 equal to half of the initial total population, $N_0/2$. Then Eq. 3.33b is solved for $N_1(t)$ where the found solution for $N_2(t)$ is used. With the following substitutions:

$$a = \frac{N_0}{2} k\gamma_{12} + \gamma_2$$

$$b = \frac{N_0}{2} k\gamma_{22}$$

$$c = \frac{\gamma_{12}}{\gamma_{22}}$$

the approximate solution is then compactly expressed as:

$$N_1(t) = \frac{N_0}{2}\left(\frac{N_2(t)}{N_0/2}\right)^c \cdot e^{(ac-\gamma_1)t} \tag{3.34a}$$

$$N_2(t) = \frac{N_0}{2}\left(\frac{a}{(a+b)e^{at} - b}\right) \tag{3.34b}$$

The corresponding solutions for densities are algebraically equivalent to the atom number solutions of Eqs. 3.34, with the only difference that without the cloud profile integration the geometrical pre-factor k is identical to unity ($k = 1$):

$$n_1(t) = \frac{n_0}{2}\left(\frac{n_2(t)}{n_0/2}\right)^c \cdot e^{(ac-\gamma_1)t} \tag{3.35a}$$

$$n_2(t) = \frac{n_0}{2}\left(\frac{a}{(a+b)e^{at} - b}\right) \tag{3.35b}$$

where $\gamma_1 = \gamma_2 = \gamma = 1/\tau$. The model is conveniently parametrized with experimentally measurable quantities: cloud temperature T, trap frequencies ω_x, ω_y, ω_z, initial total atom number $N_0 = N_1(t=0) + N_2(t=0)$. The intermediate quantity σ_p (Eq. 3.33a) gives the Gaussian cloud width in the direction p. In practical situations the temperature, measured by cloud expansion in time-of-flight experiments, has unequal values in different directions. We consider the axial temperature measurement to give the value most consistent with the real ensemble temperature.

For a clean experiment, that is, with $N_1 = 0$, in a non-stretched state, for example $|2, +1\rangle$, the exact solution of Eq. 3.33c can be found:

$$N_2(t) = \frac{N_0 \gamma_2}{(2b + \gamma_2)e^{\gamma_2 t} - 2b} \tag{3.36}$$

Our approximate solution gives a slightly higher decay rate than the direct numerical integration of the rate equations, though producing a reasonably close result over broad ranges of the model parameters.

A smaller initial atom number N_0 gives better interferometric contrast as a result of the population dynamics governed by Eqs. 3.33. Strictly speaking, γ_{22} is solely responsible for the growing population asymmetry and the corresponding contrast loss, according to its role in the rate equations, because the other terms and the preparation conditions are such that otherwise the system behaves symmetrically (Eqs. 3.33): initial populations $N_1(0)$ and $N_2(0)$ are equal, loss rates due to the interaction with background gas for states $|1\rangle$ and $|2\rangle$ are equal, and the "combination" terms (with γ_{12}) are identical. These parts of the equations, provided $-\gamma_{22} k\, N_2^2$ is zero, lead to equal loss from both states and equal loss induced by $-\gamma_{12}\, k\, N_1 N_2$ at any given time, resulting in a symmetric population decay. Thus, only the $-\gamma_{22} k\, N_2^2$ term introduces asymmetry and ultimately degrades the interferometric contrast. Its effect can be minimized via its explicit dependence on the trap frequencies and ensemble temperature through the parameter k and the total number of atoms N_0 of Eq. 3.33a that affect the decay via the $-\gamma_{22} k\, N_2^2$ summand. The lower the temperature, the higher the asymmetry and the worse the contrast. The number of atoms in state $|2\rangle$ can be manipulated by changing the total population. The asymmetry and contrast decay will grow with the growth of N_0. Finally, trap frequencies can be chosen so that the asymmetry is tolerable; usually there is freedom in tailoring the trap parameters. The rule of thumb is that the tighter the trap, the higher the asymmetry, provided other relevant factors are kept constant. Since the trap frequencies algebraically oppose the temperatures as squares in the equations, it is easy to see that their effect on the asymmetry is stronger than that of the temperature T.

3.3.2 Optimizing asymmetric losses

It is tempting to exploit this multiparametric behaviour of interferometry contrast and find a way to predict optimal parameters at which the asymmetry would become minimal. It is possible to obtain a merit function for finding the parameters of an optimal interferometer by posing a minimization problem in the form:

$$\min\{LA\} \tag{3.37}$$

$$LA = \int_0^\infty \left(N_1 - N_2\right) \mathrm{d}t \tag{3.38}$$

where LA is the loss asymmetry merit function. The state populations N_1 and N_2 are functions of time t and of the experimentally variable parameters:
1) trap frequencies ω_x, ω_y, ω_z, that enter the equations as a geometrical average $\bar{\omega} = \sqrt[3]{\omega_x \omega_y \omega_z}$, because their individual contributions are indistinguishable;
2) ensemble temperature T;
3) decay constants γ_1, γ_2, γ_{12}, γ_{22}, γ_{111}: they are *not* all fixed in the experiment, e.g., the one-body loss rates γ_1 and γ_2 depend on the vacuum and are both time and background gas pressure dependent;
4) initial number of atoms N_0.

The integral of the optimization problem in Eq. 3.37 computes the area enclosed by the two state population decays in time as a measure of the loss asymmetry (Fig. 3.7). It is found in terms of an infinite series expansion expressed by the ordinary hypergeometric function ${}_2F_1(\bullet, \bullet; \bullet; \bullet)$:

$$LA = \underbrace{\frac{aN_0}{(a+b)2\gamma} \cdot {}_2F_1\left(1, \frac{\gamma}{a} - c + 1; \frac{\gamma}{a} + 1; \frac{b}{a+b}\right)}_{\text{from } N_1 \text{ integration}} + \underbrace{\frac{N_0}{2b} \ln\left(\frac{a}{a+b}\right)}_{\text{from } (-N_2) \text{ integration}} \tag{3.39}$$

This result can readily be evaluated analytically or numerically to minimize the integral of Eq. 3.38 for a given set of parameters. Below we shall investigate the cases relevant to our settings. Although the minimization integral is multivariate, it gives a monotonic function in a given one-dimensional projection (see Fig. 3.8), computed around typical experimental parameters slightly above the condensation temperature (Eq. 3.40) as a limiting case $T = T_{\text{crit}} + 15$ nK $= 100$ nK, $N_0 = 60\,000$ atoms, $\omega_x = 2\pi \times 97.6$ Hz, $\omega_y = 2\pi \times 97.6$ Hz, $\omega_z = 2\pi \times 11.96$ Hz, $\gamma_1 = \gamma_2 = \gamma = 1/13.64\ \text{s}^{-1}$, $\gamma_{12} = 3.0 \times 10^{-14}\ \text{cm}^3/\text{s}$, $\gamma_{22} = 16.2 \times 10^{-14}\ \text{cm}^3/\text{s}$ [134]. The condensed values were adapted to thermal atoms according to [65, 131]. The monotonicity does not take into account that the physics of losses changes when T falls below T_{crit} and this sets lower bounds on T, N_0 and $\bar{\omega}$ simultaneously, the relation between

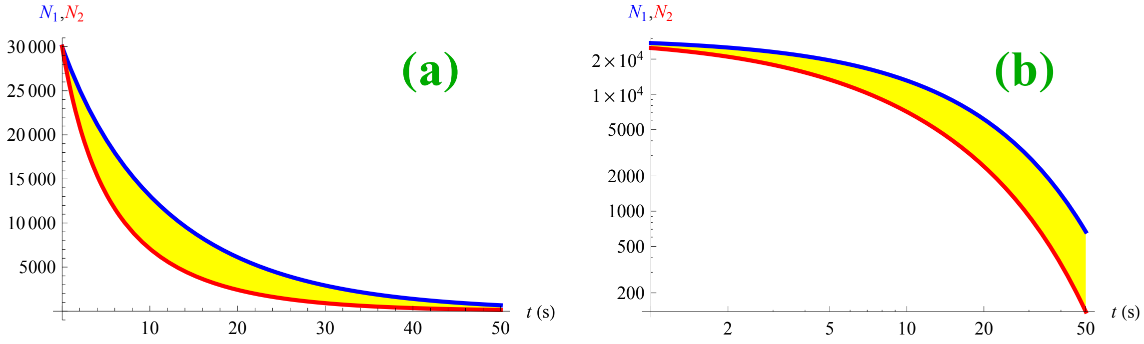

Figure 3.7: Decay of state populations and the area enclosed by the decay curves, expressing the merit function calculated in the asymmetric loss minimization problem. The decay curves are given for states $|1\rangle$ (**blue line**) and $|2\rangle$ (**red line**) in linear-linear **(a)** and log-log **(b)** scales. The minimization integral is the area enclosed by the decay curves (**yellow filling**).

which is established by the formulæ:

$$\bar{\omega} = 2\pi \bar{f} = 2\pi \sqrt[3]{f_x f_y f_z} \tag{3.40a}$$

$$T_{\text{crit}} = \frac{\hbar\bar{\omega}}{k_B} \sqrt[3]{\frac{N_0}{\zeta(3)}} \tag{3.40b}$$

where N_0 is the number of atoms, $\bar{\omega}$ is the average trap frequency, $\zeta(3) \approx 1.2$ is the Riemann zeta function and $k_B = 1.38065 \times 10^{-23}$ J/K is Boltzmann constant.

It is remarkable that lowering the temperature worsens the interferometric contrast via the growth of loss asymmetry: state $|2\rangle$ decays faster whilst $|1\rangle$ is limited only by the background collisions via γ and lives longer.

On log-log scales the optimization integral reveals a bend in each dimension that splits the domains of N_1 and N_2 domination, the *critical points*. It should be noted that some of the dimensions in this problem are dependent. If given experimental parameters deviate from the fixed LA variables used to compute a particular LA estimate[13] this can invalidate the result of minimization, especially if the critical points are shot over. In such a case a new multivariate slice for newly established parameters can be taken and the new critical points found.

The model has limitations. Since it has been derived on the assumption that $\gamma_{22} \gg \gamma_{12}$, it will fail to give accurate predictions otherwise. The temperature dependence does not assume a phase transition if the given T is below the condensation critical temperature T_{crit} which is usually kept in the range $160 - 300$ nK. The onset of Bose-Einstein condensation turns the ensemble into a superfluid. As a consequence, the drastically increased phase-space density results in a new loss

---

[13] E.g. f, γ and T are fixed while computing an LA for N_0. Having a different experimental value of f, for example, may result in inadequate LA predictions and require to recompute LA for the variables.

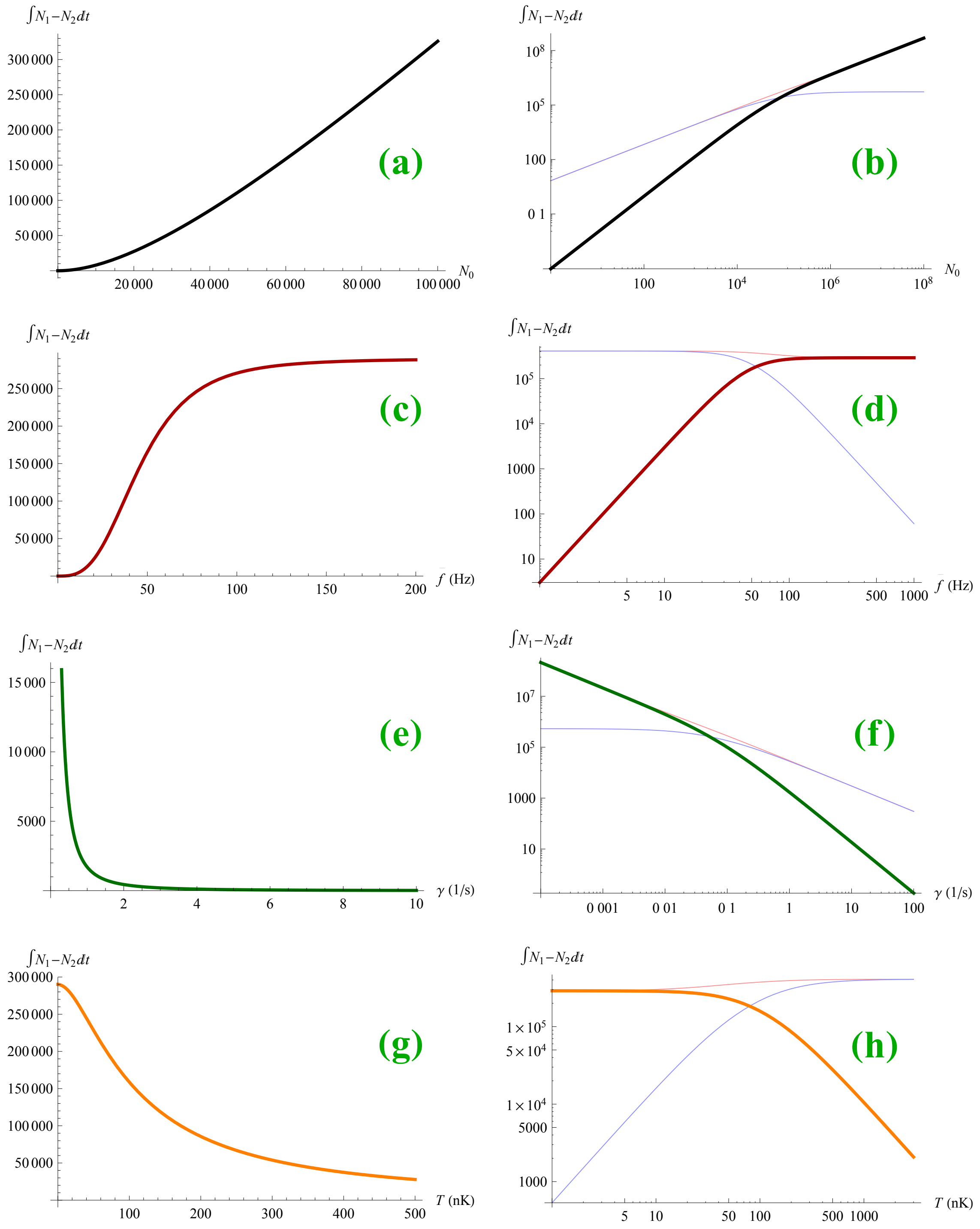

Figure 3.8: A set of cross-sections of the loss asymmetry merit function that quantifies the asymmetry of the population decays around typical experimental parameters slightly above the condensation temperature as a limiting case $T = T_{\mathrm{crit}} + 15$ nK $= 100$ nK, $N_0 = 60\,000$ atoms, $\omega_x = 2\pi \times 97.6$ Hz, $\omega_y = 2\pi \times 97.6$ Hz, $\omega_z = 2\pi \times 11.96$ Hz, $\gamma_1 = \gamma_2 = \gamma = 1/13.64$ s^{-1}, $\gamma_{12} = 3.0 \times 10^{-14}$ cm^3/s, $\gamma_{22} = 16.2 \times 10^{-14}$ cm^3/s. The integral values are given in linear-linear scale **(a,c,e,g)** in the range where the experiment is, and in log-log scale **(b,d,f,h)** to see the critical points where the integral over state $|1\rangle$ decay (**blue lines**) and the integral over state $|2\rangle$ decay (**red lines**) reveal their contributions to the total integral for:
(a,b) the total number of atoms N_0;
(c,d) average trap frequency $\bar{f} = \sqrt[3]{f_x f_y f_z}$;
(e,f) one-body decay rate $\gamma_1 = \gamma_2 = \gamma$;
(g,h) temperature T.

mechanism via three-body recombination and is accounted for with a non-zero γ_{111} term in the rate equations. Apart from this, the BEC Thomas-Fermi radius with non-negligible particle losses becomes dependent on time and instead of the presented rate equations the Gross-Pitaevskii equation [135–141] would need to be solved. This does not happen to the Gaussian profile, provided re-thermalization is much quicker that the other characteristic times defined by the inverse of the loss rates. This is the case for our system since re-thermalization occurs at a rate of 160 s^{-1} [71] and the thermal atom ensemble preserves a Gaussian profile during evolution with particle losses.

$\boldsymbol{LA}$ can be used to isolate the effect of loss asymmetry from other effects in the system and to choose a different set of parameters that evaluates to the same $\boldsymbol{LA}$ that may be desired when the configuration of one experiment is compared with or transfered to another one.

3.3.3 Approximation validity range

The worst practical case we can have is for the largest initial population $N_0 = 6 \times 10^5$ atoms and the lowest temperature just above the critical temperature $T = T_{\mathrm{crit}} + 15$ nK $= 200$ nK. The 15 nK above $T_{\mathrm{crit}} = 185$ nK is chosen from the residual magnetic field fluctuations that couple to the clock states in the "magic" field due to the residual differential Zeeman shift[14]. The cases of higher T or smaller N_0 produce smaller values of the minimization integral of Eq. 3.38 keeping the system further away from the worst case scenario. In Fig. 3.9 several ranges are shown where the approximate solutions are valid and where the deviation from the exact solution becomes intolerable: the experiment is held in the range of the Ramsey evolution time $T < 15$ s and $N_0 > 10^4$ where the approximation is very close to the exact solution over a broad range of parameter values. The middle range $N_0 = 200$ to 10^4 is usually hard to deal with in experiment due to optical fringing. The lowest sector of N_0 values below 200 atoms cannot be reliably detected in practice even with intricate data processing techniques. Also, CCD shot-noise sets in at low numbers of atoms. The range close to or below $N_0 = 10$ should involve a different type of analysis based on a quantum approach since single-particle effects cannot be neglected. The ranges of Ramsey evolution time above $T = 15$ s are limited by one-body collisions as a result of the finite vacuum reflected by γ in the formalism. Practically we also cannot access hold times beyond 15 s due to limitations of the electronics.

---

[14] Lower values are hard to control and condensation would set in. In practice it is often desirable to set $T = T_{\mathrm{crit}} + 100$ nK to absolutely avoid condensation that is likely from shot to shot due to the uncertainty of the atom number preparation amounting to $\mathrm{STD}(N_0) = 15\%$ and to the N_0-dependence of T_{crit}.

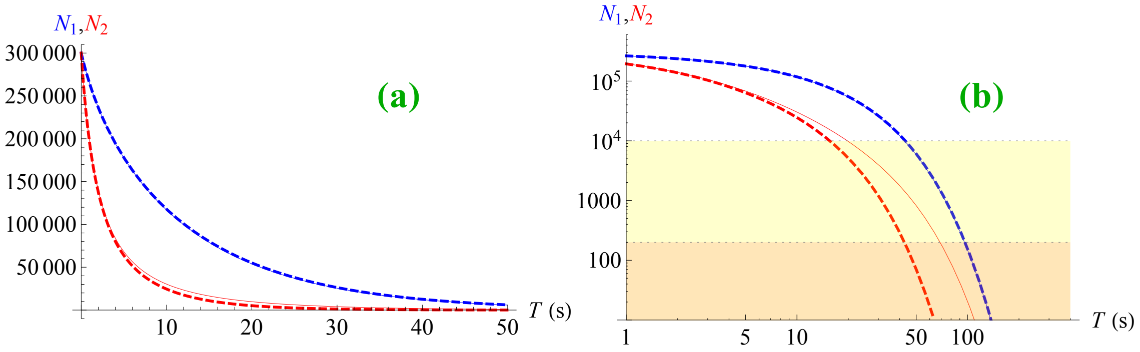

Figure 3.9: Approximation error analysis of the coupled loss rate equation solutions for Ramsey evolution (Eqs. 3.34): exact numerical solutions (**solid lines**) and approximate analytical solutions (**dashed lines**) for the decay of populations N_1 and N_2 starting from $N_1(T = 0) = N_0/2$ and $N_2(T = 0) = N_0/2$. The worst case scenario parameters are taken: $T = T_{\rm crit} + 15$ nK $= 200$ nK, $N_0 = 6 \times 10^5$ atoms, $\omega_x = 2\pi \times 97.6$ Hz, $\omega_y = 2\pi \times 97.6$ Hz, $\omega_z = 2\pi \times 11.96$ Hz, $\gamma_1 = \gamma_2 = \gamma = 1/13.64$ s^{-1}, $\gamma_{12} = 3.0 \times 10^{-14}$ cm^3/s, $\gamma_{22} = 16.2 \times 10^{-14}$ cm^3/s.
(a) loss asymmetry is shown on a linear-linear scale in the dominant range of the loss asymmetry influence;
(b) log-log scale reveals the ranges where the approximation is valid and where it breaks down: experiment is always held in the range of $T < 15$ s and N_0 above 10^4 where the approximation is very close to the exact solution over a broad range of parameter values; the middle (**beige**) area of $N_0 = 200$ to 10^4 is usually hard to deal with in an experiment due to optical fringing and Ramsey evolution times longer than ≈ 15 s are inaccessible due to the vacuum (one-body decay γ); the lowest sector (**pink**) below $N_0 = 200$ cannot be detected reliably enough for practical applications even with intricate data processing techniques employed; and the range close to or below $N_0 = 10$ should involve a different type of analysis based on a quantum approach since single-particle effects cannot be neglected.
Note: T is conventionally the Ramsey evolution time here, not to be confused with temperature.

As for the approximate result validity, the most influential range is in the initial part of the evolution and the asymmetry merit function LA expressed by the result of integration will always be steeply convergent in the long time limit for all the variables except N_0, for which it is always divergent. Direct numerical integration of Eqs. 3.34 of the minimization integral reproduces all the features of the analytical solution with negligible deviations.

3.3.4 Master equation with many-body losses

There is experimental evidence of the strong influence of two-body inelastic collisions on the decay of the populations. Until now only one-body interactions have been discussed in the context of Ramsey interferometry. The one-body processes are a sign of imperfect vacuum that allows collisions of hot background atoms with the cold trapped ensemble which provides enough momentum for the particle to escape. The master equation is parametrized in this case by the one-body decay rates γ_1 and γ_2 for the respective states. To incorporate many-body collisions into the model, the interaction of a quantum field of bosons with the damping reservoirs needs to be described. A suitable Markovian model setup is adopted from [142] and the ideas from [133, 143] are used in the following derivations.

The bosonic field operators are defined in the standard way for creation $\hat{\Psi}_j^\dagger(\boldsymbol{r})$ and annihilation $\hat{\Psi}_j(\boldsymbol{r})$ in state[15] $j \in \{1, 2, ..., S\}$ obeying the bosonic commutation relations:

$$[\hat{\Psi}_i(\boldsymbol{r}), \hat{\Psi}_j^\dagger(\boldsymbol{r}')] = \delta_{ij}\delta(\boldsymbol{r} - \boldsymbol{r}') \tag{3.41}$$

Most generally the system-bath interaction is described by a master equation which under the Born-Markov approximation describes a system that cannot develop memory over time and transforms into the Markovian master equation:

$$\frac{\partial \hat{\rho}}{\partial t} = \frac{1}{i\hbar}\left[\hat{\boldsymbol{H}}, \hat{\rho}\right] + \sum_{b \in \mathbb{B}} \mathcal{G}_b \int \hat{\mathcal{L}}_b\left[\hat{\rho}\right] \mathrm{d}^3\boldsymbol{r} \tag{3.42}$$

where $\hat{\boldsymbol{H}}$ is the system Hamiltonian in the interaction picture and the commutator part of the equation describes the coherent evolution of the system, $\mathbb{B} = \left\{\left(b_1, b_2, ..., b_S\right)\right\}$ is a set of tuples each with a number of elements corresponding to the number of states S interacting via simultaneous collisions where each element contains the number of colliding particles in the given state. Index $\boldsymbol{b}$ chooses one tuple $\left(b_1, b_2, ..., b_j, ..., b_S\right)$ that describes all particles in all states interacting with the tuple loss channel characterized by the constant $\mathcal{G}_b$. The set element b_j is the number of colliding particles in state j. The cardinality of the set $|\mathbb{B}|$ equals the number of loss channels. Interaction with reservoirs via loss channel $\boldsymbol{b}$ is found by applying the Lindblad superoperator to the density operator:

$$\hat{\mathcal{L}}_b\left[\hat{\rho}\right] = 2\hat{O}_b\hat{\rho}\hat{O}_b^\dagger - \hat{O}_b^\dagger\hat{O}_b\hat{\rho} - \hat{\rho}\hat{O}_b^\dagger\hat{O}_b \tag{3.43}$$

The operators $\hat{O}_b$ define the local collision of all of the particles in all of the states defined by the corresponding tuple in terms of the field operators:

$$\hat{O}_b = \prod_{j=1}^{S} \hat{\Psi}_j^{b_j}(\boldsymbol{r}) \tag{3.44}$$

The field operators are expanded in momentum space in terms of wavefunctions and single-mode boson operators as:

$$\hat{\Psi}_j(\boldsymbol{r}) = \sum_k \hat{a}_{jk}\psi_{jk}(\boldsymbol{r}) \tag{3.45}$$

where $\hat{a}_{jk}$ is the bosonic operator that creates a particle in state j, momentum mode k, at location $\boldsymbol{r}$ and obeys bosonic commutation relations. The arguments $\boldsymbol{r}$

---

[15] Called interchangeably *mode* or *component*.

will be omitted hereafter for compactness of notation: $\hat{\Psi}_j \equiv \hat{\Psi}_j(\boldsymbol{r})$ and $\hat{\Psi}'_j \equiv \hat{\Psi}_j(\boldsymbol{r}')$.

Measurables are averages of quantum operators. To compute the average of an operator element, the following trace should be evaluated [144–148]:

$$\frac{\partial}{\partial t}\langle\hat{\Psi}_i^\dagger\hat{\Psi}_j\rangle = \mathrm{Tr}\left[\left(\frac{\partial\hat{\rho}}{\partial t}\right)_{\mathrm{loss}}\hat{\Psi}_i^\dagger\hat{\Psi}_j\right] \tag{3.46}$$

The particles that experience inelastic collisions are assumed to immediately leave the trap without interaction with the rest of the ensemble. By calculating the expectation values of the $\hat{\rho}$ elements from Eq. 3.46 we arrive at:

$$\frac{\partial}{\partial t}\langle\hat{\Psi}_1^\dagger\hat{\Psi}_1\rangle = -2\mathcal{G}_{(1,0)}\langle\hat{\Psi}_1^\dagger\hat{\Psi}_1\rangle - 2\mathcal{G}_{(1,1)}\langle\hat{\Psi}_1^\dagger\hat{\Psi}_1\hat{\Psi}_2^\dagger\hat{\Psi}_2\rangle - 4\mathcal{G}_{(2,0)}\langle\hat{\Psi}_1^{\dagger 2}\hat{\Psi}_1^2\rangle \tag{3.47a}$$

$$\frac{\partial}{\partial t}\langle\hat{\Psi}_2^\dagger\hat{\Psi}_2\rangle = -2\mathcal{G}_{(0,1)}\langle\hat{\Psi}_2^\dagger\hat{\Psi}_2\rangle - 2\mathcal{G}_{(1,1)}\langle\hat{\Psi}_1^\dagger\hat{\Psi}_1\hat{\Psi}_2^\dagger\hat{\Psi}_2\rangle - 4\mathcal{G}_{(0,2)}\langle\hat{\Psi}_2^{\dagger 2}\hat{\Psi}_2^2\rangle \tag{3.47b}$$

$$\frac{\partial}{\partial t}\langle\hat{\Psi}_1^\dagger\hat{\Psi}_2\rangle = -\mathcal{K}_1\langle\hat{\Psi}_1^\dagger\hat{\Psi}_2\rangle - \mathcal{K}_2\langle\hat{\Psi}_1^\dagger\hat{\Psi}_2\hat{\Psi}_1^\dagger\hat{\Psi}_1\rangle - \mathcal{K}_3\langle\hat{\Psi}_2^\dagger\hat{\Psi}_2\hat{\Psi}_1^\dagger\hat{\Psi}_2\rangle \tag{3.47c}$$

$$\frac{\partial}{\partial t}\langle\hat{\Psi}_2^\dagger\hat{\Psi}_1\rangle = -\mathcal{K}_1\langle\hat{\Psi}_2^\dagger\hat{\Psi}_1\rangle - \mathcal{K}_2\langle\hat{\Psi}_1^\dagger\hat{\Psi}_1\hat{\Psi}_2^\dagger\hat{\Psi}_1\rangle - \mathcal{K}_3\langle\hat{\Psi}_2^\dagger\hat{\Psi}_1\hat{\Psi}_2^\dagger\hat{\Psi}_2\rangle \tag{3.47d}$$

where the reservoir constants are absorbed in the following scalars for compactness:

$$\begin{aligned}\mathcal{K}_1 &= \mathcal{G}_{(1,0)} + \mathcal{G}_{(0,1)}\\ \mathcal{K}_2 &= 2\mathcal{G}_{(2,0)} + \mathcal{G}_{(1,1)}\\ \mathcal{K}_3 &= 2\mathcal{G}_{(0,2)} + \mathcal{G}_{(1,1)}\end{aligned} \tag{3.48}$$

The field operators are ordered suitably for the physical interpretation: the operator average $\langle\hat{\Psi}_j^\dagger\hat{\Psi}_j\rangle$ corresponds to the density of particles in state j at the position defined by the coordinate vector $\boldsymbol{r}$. The products $\langle\hat{\Psi}_i^\dagger\hat{\Psi}_j\rangle$ with $i \neq j$ carry the phase difference information between the operators of states i and j.

Now that we see the identification of the involved processes, it is clear from the structure of the equations, for example, from the coherence between states $j = 1$ and $j = 2$ associated with Eq. 3.47c, that there are three independent terms $\langle\hat{\Psi}_1^\dagger\hat{\Psi}_2\rangle$, $\langle\hat{\Psi}_1^\dagger\hat{\Psi}_2\hat{\Psi}_1^\dagger\hat{\Psi}_1\rangle$, $\langle\hat{\Psi}_2^\dagger\hat{\Psi}_2\hat{\Psi}_1^\dagger\hat{\Psi}_2\rangle$ responsible for damping to the reservoirs associated with the involved states. Each of the prefactors to the operator averages on the right-hand side has a clear physical meaning as a decay rate. We can establish a convenient identification of $\mathcal{G}_b$ to the corresponding decay rates by letting:

$$\begin{aligned}2\mathcal{G}_{(1,0)} &\longrightarrow \gamma_1\\ 2\mathcal{G}_{(0,1)} &\longrightarrow \gamma_2\\ 2\mathcal{G}_{(1,1)} &\longrightarrow \gamma_{12}\\ 4\mathcal{G}_{(2,0)} &\longrightarrow \gamma_{11}\\ 4\mathcal{G}_{(0,2)} &\longrightarrow \gamma_{22}\end{aligned} \tag{3.49}$$

where on the right-hand side we have decay rates for thermal atoms. For the distinction from the BEC decay rates the thermal atom decay rates are superscripted with th later in the text: $\gamma_\ell^{th} \equiv \gamma_\ell$.

In terms of the atomic densities the loss part $\left(\partial\rho/\partial t\right)_{\text{loss}}$ of the master equation simplifies to the equations:

$$\frac{\partial n_1}{\partial t} = -\gamma_1 n_1 - \gamma_{12} n_1 n_2 - \gamma_{11} n_1^2 \tag{3.50a}$$

$$\frac{\partial n_2}{\partial t} = -\gamma_2 n_2 - \gamma_{12} n_1 n_2 - \gamma_{22} n_2^2 \tag{3.50b}$$

$$\frac{\partial n_{12}}{\partial t} = -\kappa_1 n_{12} - \kappa_2 n_1 n_{12} - \kappa_3 n_2 n_{12} \tag{3.50c}$$

$$\frac{\partial n_{21}}{\partial t} = -\kappa_1 n_{21} - \kappa_2 n_1 n_{21} - \kappa_3 n_2 n_{21} \tag{3.50d}$$

with the following constants defined for convenience:

$$\kappa_1 = \frac{\gamma_1 + \gamma_2}{2}, \qquad \kappa_2 = \frac{\gamma_{11} + \gamma_{12}}{2}, \qquad \kappa_3 = \frac{\gamma_{22} + \gamma_{12}}{2} \tag{3.51}$$

The relaxation constants that enter these equations are defined in terms of the experimentally observed quantities in the discussion below.

3.3.5 Two-level pure phenomenological dephasing

Collisional dephasing caused by population loss appears in the off-diagonal density operator elements naturally while accounting for inelastic collisions between particles in the relevant states. However, there are other mechanisms of dephasing not related to population loss, e.g., elastic collisions and inhomogeneity of the trapping field. Such *pure dephasing* can be introduced *phenomenologically* by adding other reservoirs for phase damping of state-1 $\boldsymbol{R}_{ph1}$, state-2 $\boldsymbol{R}_{ph2}$ etc to the total Hilbert space by combining the subspaces of the system $\boldsymbol{S}$, particle damping $\boldsymbol{R}$ and phase damping reservoirs as well as the coupling degrees of freedom that describe interactions between them as $\boldsymbol{S} \oplus \boldsymbol{R} \oplus \boldsymbol{SR} \oplus \boldsymbol{R}_{ph1} \oplus \boldsymbol{R}_{ph2} \oplus \boldsymbol{SR}_{ph1} \oplus \boldsymbol{SR}_{ph2}$. The Lindblad operator should then only couple the states, since they are *phase sources*, to $\boldsymbol{R}_{phj}$ where j is the state index. A suitable choice would be:

$$\hat{A}_j = \hat{\Psi}_j^\dagger(\boldsymbol{r})\hat{\Psi}_j(\boldsymbol{r}) \tag{3.52}$$

with the associated system-bath interaction superoperator[16]:

$$\hat{\mathcal{L}}_j\left[\hat{\rho}\right] = 2\hat{A}_j\hat{\rho}\hat{A}_j^\dagger - \hat{A}_j^\dagger\hat{A}_j\hat{\rho} - \hat{\rho}\hat{A}_j^\dagger\hat{A}_j \tag{3.53}$$

---

[16] We distinguish the superoperators defined for different indices: $\hat{\mathcal{L}}_b\left[\hat{\rho}\right]$ and $\hat{\mathcal{L}}_j\left[\hat{\rho}\right]$.

Owing to the fact that the reservoirs are statistically independent, the master equation can be re-written by adding an independent dephasing summand:

$$\frac{\partial \hat{\rho}}{\partial t} = \frac{1}{i\hbar}\left[\hat{\boldsymbol{H}}, \hat{\rho}\right] + \sum_{b \in \mathbb{B}} \mathcal{G}_b \int \hat{\mathcal{L}}_b\left[\hat{\rho}\right] \mathrm{d}^3\boldsymbol{r} + \sum_{j}^{S} \mathcal{X}_j \int \hat{\mathcal{L}}_j\left[\hat{\rho}\right] \mathrm{d}^3\boldsymbol{r} \tag{3.54}$$

where $\boldsymbol{S}$ is the number of states. The last summation is over the set of reservoirs each damping the phase of a dedicated state j and characterized by a reservoir constant $\mathcal{X}_j$. Omitting the intermediate steps, the resulting equations for loss take the same algebraic form as Eqs. 3.50 except that the scalar κ_1 given by Eq. 3.51 absorbs the pure phenomenological dephasing rate γ_d:

$$\kappa_1 = \frac{\gamma_1 + \gamma_2 + \gamma_d}{2} \tag{3.55}$$

The fact that γ_d appears as a scaling factor to $\hat{\rho}_{ij}$ with $i \neq j$ only is physically justified: the states can only destroy phase by coupling to the degrees of freedom included in $\boldsymbol{R}_{ph1} \oplus \boldsymbol{R}_{ph2}$. The dephasing process can only affect the phase difference between the states which is described by $\hat{\rho}_{ij}$. The two reservoir constants have been absorbed into the pure dephasing rate by applying a rule analogous to Eqs. 3.49:

$$2(\mathcal{X}_1 + \mathcal{X}_2) \longrightarrow \gamma_d \tag{3.56}$$

This result suggests that the relative phase between $|1\rangle$ and $|2\rangle$ is defined by γ_d.

3.3.6 Conversion of population relaxation rates

Unlike in the equations above, many-body relaxation rates are usually not available in 1/s units, because the numbers of atoms are counted in experiments rather than atomic densities, resulting in density units, e.g., cm^3/s for two-body losses, etc. A more practical version of equations Eqs. 3.60 should then be found. The preferred form is where ρ_{ii} are normalized populations. To convert to ρ_{ij} one needs to first integrate each density equation over the density profile by employing the integral of Eq. 3.29, then establish conversion rules for the relaxation constants [133]. The following factors valid for thermal ensembles should be taken into account to write down the number equations: the geometrical factor k for many-body decay rates, the multiplicity $M!$ of the colliding particles and the normalization to the initial particle number N_0 to limit the range of ρ values to the one from 0 to 1 appropriate to obtain normalized populations.

The resulting equations for N or ρ lose explicit spatial dependence describing the ensemble as a whole. The equations for N allow to directly use the two-body decay rates in units cm^3/s. To obtain them, as before, the density profile is integrated. Under the assumptions of quick re-thermalization the cloud does not change its shape and the Gaussian functions on the right and left sides of the equations cancel out leaving only geometrical factors k, k_{111}. The factors k, k_{111}, and the ones for a larger number of colliding particles can be found from the density profile integration. The ones we use here are taken from Eq. 3.33 and Eq. 3.30. Equations 3.50 after the integration become:

$$\frac{\partial N_1}{\partial t} = -\gamma_1^{th} N_1 - k\gamma_{12}^{th} N_1 N_2 - k\gamma_{11}^{th} N_1^2 \tag{3.57a}$$

$$\frac{\partial N_2}{\partial t} = -\gamma_2^{th} N_2 - k\gamma_{12}^{th} N_1 N_2 - k\gamma_{22}^{th} N_2^2 \tag{3.57b}$$

$$\frac{\partial N_{12}}{\partial t} = -\kappa_1 N_{12} - \kappa_2 N_1 N_{12} - \kappa_3 N_2 N_{12} \tag{3.57c}$$

$$\frac{\partial N_{21}}{\partial t} = -\kappa_1 N_{21} - \kappa_2 N_1 N_{21} - \kappa_3 N_2 N_{21} \tag{3.57d}$$

with $\gamma_\ell^{th} \equiv \gamma_\ell$ and with the auxiliary constants where we include γ_d too:

$$\kappa_1 = \frac{\gamma_1^{th} + \gamma_2^{th} + \gamma_d}{2}, \qquad \kappa_2 = k\frac{\gamma_{11}^{th} + \gamma_{12}^{th}}{2}, \qquad \kappa_3 = k\frac{\gamma_{22}^{th} + \gamma_{12}^{th}}{2} \tag{3.58}$$

Evolution of the density matrix is governed by the equation:

$$\frac{\partial \rho}{\partial t} = \frac{1}{i\hbar}[\boldsymbol{H}, \rho] + \left(\frac{\partial \rho}{\partial t}\right)_{\text{loss}} \tag{3.59}$$

where $\left(\partial\rho/\partial t\right)_{\text{loss}}$ describes the evolution of the collisional losses[17].

After the normalization of equations 3.57 to N_0 the final equations with the unitary part of the master equation Eq. 3.59 constructed from the two-level Hamiltonian in the rotating wave approximation with one-body and two-body losses and pure phenomenological dephasing become ($\hbar = 1$):

$$\frac{\partial \rho_{11}}{\partial t} = -\Gamma_1\rho_{11} - \Gamma_{12}\rho_{11}\rho_{22} - \Gamma_{11}\rho_{11}^2 + \frac{i}{2}\Omega\left(\rho_{12} - \rho_{21}\right) \tag{3.60a}$$

$$\frac{\partial \rho_{22}}{\partial t} = -\Gamma_2\rho_{22} - \Gamma_{12}\rho_{11}\rho_{22} - \Gamma_{22}\rho_{22}^2 - \frac{i}{2}\Omega\left(\rho_{12} - \rho_{21}\right) \tag{3.60b}$$

$$\frac{\partial \rho_{12}}{\partial t} = -\mathrm{K}_1\rho_{12} - \mathrm{K}_2\rho_{11}\rho_{12} - \mathrm{K}_3\rho_{22}\rho_{12} + \frac{i}{2}\Omega\left(\rho_{11} - \rho_{22}\right) + i\Delta\rho_{12} \tag{3.60c}$$

$$\frac{\partial \rho_{21}}{\partial t} = -\mathrm{K}_1\rho_{21} - \mathrm{K}_2\rho_{11}\rho_{21} - \mathrm{K}_3\rho_{22}\rho_{21} - \frac{i}{2}\Omega\left(\rho_{11} - \rho_{22}\right) - i\Delta\rho_{21} \tag{3.60d}$$

with the corresponding constants where Γ_d is the counterpart of γ_d:

$$\mathrm{K}_1 = \frac{\Gamma_1 + \Gamma_2 + \Gamma_d}{2}, \qquad \mathrm{K}_2 = \frac{\Gamma_{11} + \Gamma_{12}}{2}, \qquad \mathrm{K}_3 = \frac{\Gamma_{22} + \Gamma_{12}}{2} \tag{3.61}$$

---

[17] $\gamma_{11} = 0$ in this system, but is kept non-zero to show the symmetry of the equations.

The decay constants are obtained from the conversion, where $N_0 \equiv N(t=0)$:

$$\begin{aligned}
\Gamma_1 &= \gamma_1^{th} \\
\Gamma_{11} &= kN_0\gamma_{11}^{th} \\
\Gamma_{12} &= kN_0\gamma_{12}^{th} \\
\Gamma_{22} &= kN_0\gamma_{22}^{th} \\
\Gamma_{111} &= k_{111}N_0^2\gamma_{111}^{th}
\end{aligned} \tag{3.62}$$

and to account for the multiplicity of the colliding particles [65, 131] we define:

$$\gamma_\ell^{th} = M!\,\gamma_\ell^{BEC} \tag{3.63}$$

where the superscripts th and BEC are assigned to the decay rates measured with thermal atoms and BEC, correspondingly, ℓ is the γ-constant subscript, for which $M!$ is also computed, e.g., $\ell = 1$ or $\ell = 2$ produce $M! = 1! = 1$, $\ell = 11$ or $\ell = 12$ or $\ell = 22$ produce $M! = 2! = 2$, $\ell = 111$ produces $M! = 3! = 6$. Note, that the one-body coefficients are the same in either representation, i.e. $\Gamma_1 = \gamma_1^{th} = \gamma_1^{BEC}$ and $\Gamma_2 = \gamma_2^{th} = \gamma_2^{BEC}$. Note also, that decay rates reported for condensed atoms are $M!$ smaller than for thermal atoms, where M is the number of participating bodies (the number of the γ subscripts). This is attributed to the fact that at the collision point the condensed particle wavefunctions overlap resulting in unitary probability, because they have the same wavefunction overlapped macroscopically [65, 131]. Thermal atom wavefunctions, by contrast, are not the same and in the collision point the probability is a factorial of the number of colliding particles. This probability enhancement effect is called *bunching* [149].

The solutions of Eqs. 3.57 can be sought separately from the master equation Eq. 3.59, if the population dynamics is of interest. Then $\left(\partial\rho_{nm}\middle/\partial t\right)_{\text{loss}}$ should simply be replaced with $\partial\rho_{nm}\big/\partial t$ on the left-hand side of the corresponding equation.

Using the relations of Eq. 3.62 and Eq. 3.63 the rates reported for thermal atoms, condensate or in 1/s units can readily be inserted in the model. The master equation with the non-linear coupled loss terms, Eq. 3.60, is difficult to solve in an exact analytical form. In practice, Monte-Carlo methods can be applied to solving the master equation instead, or the problem can be rendered in a probabilistic form to model the Itō phase-diffusion process which is usually of interest: the phase distribution, that forms the Ramsey fringe envelope function, is discussed in Section 3.4 and emerges from the Itō drift-diffusion process. When the Itō stochastic differential equation is transformed to the deterministic Fokker-Planck equation[18], the solution is found to be this envelope function.

---

[18] The problem is often formulated as the less general Langevin stochastic equation [150, 151].

3.3.7 Third-level extension for the loss term

In the $F = 1 \oplus 2$ system of a ^{87}Rb clock there are three trapped magnetic sublevels[19]. The two are routinely used in Ramsey interferometry and a third state $|2,+2\rangle$ can eventually acquire population due to two-body decays from the $|2,+1\rangle$ state. This may become significant at ultralong evolution times, when the presence of the non-negligible fraction of third-state atoms should be considered[20].

Spin-1 and spin-2 subsystems produce pairs with a total spin of 1 or 3 upon collisions. Apart from the already included loss channels, the two-body collisions between $|1,-1\rangle$ and $|2,+2\rangle$ particles with their consequential loss will also occur. The collision of states $|2,+1\rangle$ and $|2,+2\rangle$ is forbidden since for all the allowed channels $\langle F_1\, m_{F_1}\, F_2\, m_{F_2}|\mathcal{F}\mathcal{M}\rangle = \langle 2\,1\,2\,2|\mathcal{F}\mathcal{M}\rangle \equiv 0$, where $\mathcal{F}$ and $\mathcal{M}$ are the total spin and projection of the colliding pair. Same-state $|1,-1\rangle$ collisions are excluded from the loss channels for the same reason: $\langle 1\ -1\,1\ -1|\mathcal{F}\mathcal{M}\rangle \equiv 0$. The exclusion of states $|F,\pm F\rangle$ in the $\{|F,m_F\rangle\}$ basis can be briefly expressed thus: stretched states do not experience collisions.

The only way for the $|2,+2\rangle$ atoms to leave the trap is via one-body collisions with the background gas, because they do not experience same-state two-body collisions that would let them change their orientation or flip the spin and migrate to another state. The effect of the presence of the state $|2,+2\rangle$ on Ramsey interferometry will be greater, the better the vacuum in the UHV chamber and the longer the hold time. Hence, the only loss channel that should be added to the model is $|1,-1\rangle \leftrightarrow |2,+2\rangle$.

To construct a model appropriate for this case, the master equation needs to be extended: the coherent coupling hidden in the commutator $[H,\rho]$ would take the form of the corresponding unitary evolution problem in a known way; the loss part would need to be derived from the Markovian master equation. If strong-coupling-field effects are neglected, e.g., the Bloch–Siegert shift, the commutator part $[H,\rho]$ can be written in a classical form as it appears in the optical Bloch equations with *general* coupling amplitudes[21], otherwise the coupling field should be quantized. Therefore, we concentrate on the population and phase loss parts

---

[19] This section is specific to the mixed system of spin-1 and spin-2 particles. To generalize it to other cases, e.g. a Caesium clock, a dedicated analysis of the collisional physics would need to be made for a multiplet of the spurious trapped sublevel unintensionally participating in Ramsey interferometry.

[20] If the atoms in the third state experience a different trapping potential, e.g., in magnetic traps for hyperfine magnetic sublevel of alkali, they may form a cloud of different geometry. Then the non-uniform overlap should be taken into account. Here we assume that the spatial profiles of the clouds in all the states overlap.

[21] By saying *general* we mean that the spin-$1 \oplus 2$ system requires to take into account atomic orientations that would have resulted in the Clebsch-Gordan coefficients at the coupling amplitudes: $\mathrm{const}\cdot\Omega$, – and would include a single Rabi frequency Ω for all the transitions as a benefit. Instead, the coupling amplitudes of the less specific form Ω_{ij} can be employed for the sake of generality.

of the master equation Eq. 3.42 and evaluate the trace of Eq. 3.46 to obtain the following solutions:

$$\left(\frac{\partial \rho_{11}}{\partial t}\right)_{\text{loss}} = -\gamma_1\rho_{11} - \gamma_{12}\rho_{11}\rho_{22} - \gamma_{13}\rho_{11}\rho_{33} \tag{3.64a}$$

$$\left(\frac{\partial \rho_{22}}{\partial t}\right)_{\text{loss}} = -\gamma_2\rho_{22} - \gamma_{12}\rho_{11}\rho_{22} - \gamma_{22}\rho_{22}^2 \tag{3.64b}$$

$$\left(\frac{\partial \rho_{33}}{\partial t}\right)_{\text{loss}} = -\gamma_{13}\rho_{11}\rho_{33} \tag{3.64c}$$

$$\left(\frac{\partial \rho_{12}}{\partial t}\right)_{\text{loss}} = -\kappa_1\rho_{12} - \kappa_2\rho_{11}\rho_{12} - \kappa_3\rho_{22}\rho_{12} - \kappa_4\rho_{33}\rho_{12} \tag{3.64d}$$

$$\left(\frac{\partial \rho_{21}}{\partial t}\right)_{\text{loss}} = -\kappa_1\rho_{21} - \kappa_2\rho_{11}\rho_{21} - \kappa_3\rho_{22}\rho_{21} - \kappa_4\rho_{33}\rho_{21} \tag{3.64e}$$

$$\left(\frac{\partial \rho_{13}}{\partial t}\right)_{\text{loss}} = -\kappa_5\rho_{13} - \kappa_2\rho_{12}\rho_{23} - \kappa_4\rho_{11}\rho_{13} - \kappa_4\rho_{33}\rho_{13} \tag{3.64f}$$

$$\left(\frac{\partial \rho_{31}}{\partial t}\right)_{\text{loss}} = -\kappa_5\rho_{31} - \kappa_2\rho_{21}\rho_{32} - \kappa_4\rho_{11}\rho_{31} - \kappa_4\rho_{33}\rho_{31} \tag{3.64g}$$

$$\left(\frac{\partial \rho_{23}}{\partial t}\right)_{\text{loss}} = -\kappa_6\rho_{23} - \kappa_7\rho_{22}\rho_{23} - \kappa_8\rho_{11}\rho_{23} \tag{3.64h}$$

$$\left(\frac{\partial \rho_{32}}{\partial t}\right)_{\text{loss}} = -\kappa_6\rho_{32} - \kappa_7\rho_{22}\rho_{32} - \kappa_8\rho_{11}\rho_{32} \tag{3.64i}$$

with the corresponding constants:

$$\begin{gathered}\kappa_1 = \frac{\gamma_1+\gamma_2}{2}, \quad \kappa_2 = \frac{\gamma_{12}}{2}, \quad \kappa_3 = \frac{\gamma_{22}+\gamma_{12}}{2}, \quad \kappa_4 = \frac{\gamma_{13}}{2} \\ \kappa_5 = \frac{\gamma_1}{2}, \quad \kappa_6 = \frac{\gamma_2}{2}, \quad \kappa_7 = \frac{\gamma_{22}}{2}, \quad \kappa_8 = \frac{\gamma_{12}+\gamma_{13}}{2}\end{gathered} \tag{3.65}$$

As before, one can make use of the substitution $\left(\partial\rho_{ij}/\partial t\right)_{\text{loss}} \longrightarrow \partial\rho_{ij}/\partial t$ to treat Eqs. 3.64 separately from the unitary part of the master equation for the purpose of population relaxation analysis.

3.3.8 Three-level pure phenomenological dephasing

The same formalism is employed as above, only in the three-level system the number of phase damping reservoirs should increase by one in order to let the third level have a statistically independent way of losing phase via system-to-reservoir interactions. The latter will also need a new independent space SR_{ph3} to couple R_{ph3} and S. The set of loss equations, Eqs. 3.64, will preserve their algebraic form, but some of the constants in Eq. 3.65 will change value to absorb the pure dephasing rates:

$$\begin{aligned}\kappa_1 &= \frac{\gamma_1+\gamma_2+\gamma_{d12}}{2},\\ \kappa_5 &= \frac{\gamma_1+\gamma_{d13}}{2},\\ \kappa_6 &= \frac{\gamma_2+\gamma_{d23}}{2}\end{aligned} \tag{3.66}$$

where the following rules have been used to transform reservoir constants to decay rates:

$$\begin{aligned}2(\mathcal{X}_1+\mathcal{X}_2) &\longrightarrow \gamma_{d12}\\ 2(\mathcal{X}_1+\mathcal{X}_3) &\longrightarrow \gamma_{d13}\\ 2(\mathcal{X}_2+\mathcal{X}_3) &\longrightarrow \gamma_{d23}\end{aligned} \tag{3.67}$$

Again, *pure dephasing* is only relevant to the *state-relating* density operator elements responsible for state superpositions, i.e., ρ_{ij} with $i \neq j$, and cannot occur in the other terms. There are three distinct pure dephasing rates that quantify the phase relations between all the combinations of states: $1 \leftrightarrow 2$, $1 \leftrightarrow 3$, $2 \leftrightarrow 3$.

By examining the structure of the obtained equations one can develop an *informal* procedure to construct the loss part of the master equation for arbitrarily many participating bodies with appropriate pure phenomenological dephasing terms under the same approximations and thus avoid the direct invocation of quantum field theory, because the solutions above represent all the essential features.

3.4 Trap effects

3.4.1 Trap-induced dephasing

A spin echo cancels out atomic phase diffusion over the sequence duration along with other factors perturbing the atomic transition equally in the interferometer arms. If a constant local oscillator frequency drift is present, it is also nullified. However, local oscillator instability causing $\boldsymbol{P}_z$ phase dispersion is left imprinted on the state phase difference by the end of the sequence and is detected by projecting the state onto the population axis $\boldsymbol{P}_z$.

There is a number of effects that define the form of the Ramsey contrast decay, we shall investigate a method of separate treatment of the dominant ones: ensemble *phase dispersion* caused by complete motional averaging, magnetic-field fluctuations and local oscillator instability [55, 152, 153]. In the model presented in [55] a magnetic trap with a harmonic potential is considered, where an atom with an average position in the Maxwell-Boltzmann distribution is taken to find the standard deviation of the transition frequency that is averaged due to the harmonic motion of atoms in the trap. Inserting the standard deviation in the expression for the resonant lossless Ramsey interferometry, allows the dephasing time τ_{deph} to be obtained. Another interferometry model can be used as well.

It can be shown that the special case of the *Itō drift-diffusion process*, described by the Itō stochastic differential equation, converted to the deterministic Fokker-Planck equation with nonzero diffusion coefficient α gives the *diffusion equation* [154, 155]:

$$\frac{\partial p}{\partial t} = \alpha\, \nabla^2 p \tag{3.68}$$

To solve this equation, we assume that the initial phase $\Delta\varphi_0$ is well defined for all particles in the ensemble[22]. This corresponds to the Dirac δ-function distribution at $T = 0$ in Fig. 3.10(a) and is formally written as $p(\Delta\varphi, T = 0, \ldots) = \delta(\Delta\varphi - \Delta\varphi_0)$.

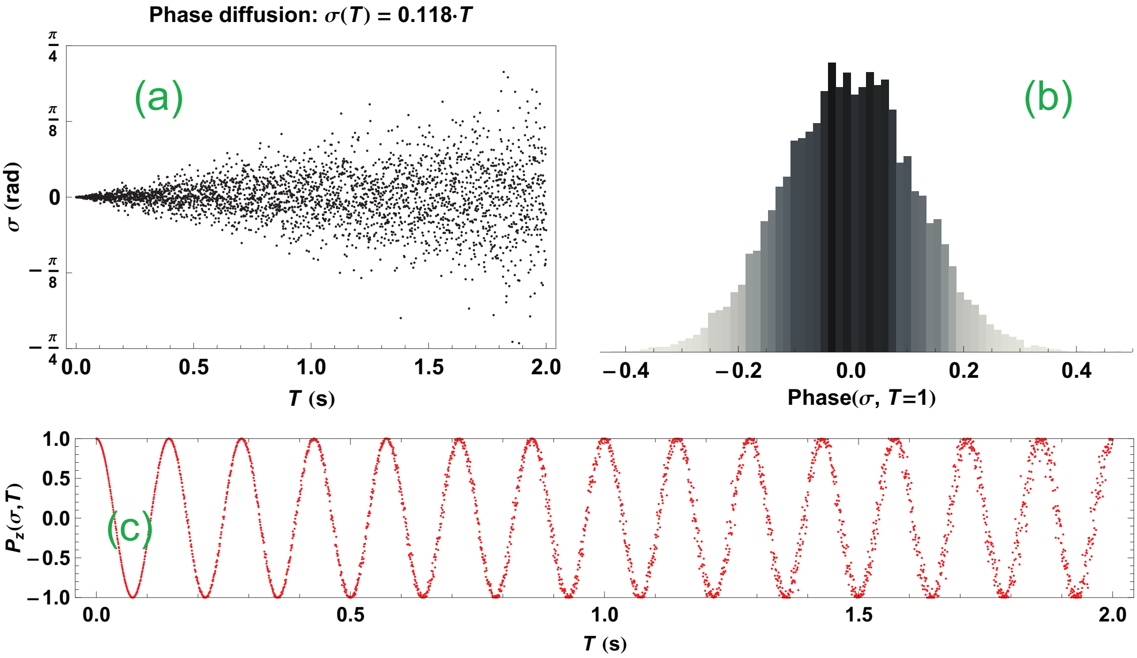

Figure 3.10: Phase diffusion. Spin echo time-domain interferometry with variable evolution time T. The $\sigma = 0.118 \cdot T$ rad dependence is taken from the experiment analysis of the next chapter for *phase*-domain spin echo interferometry with 3×10^4 thermal atoms at 160 nK with $T_{\text{crit}} = 90$ nK. **(a)** The simulated phase vs. time T shows the linear growth of the phase standard deviation σ. **(b)** The histogram of the simulated normal phase distribution **(a)** at $T = 1$ s; phase is in radians. **(c)** Simulated $P_z(\sigma, T)$ from Eq. 3.68 with a normal phase distribution and a linear growth of σ in *time*-domain spin echo interferometry.

The solution of this equation [156] for the phase distribution function p is then found to be Gaussian [155]:

$$p = \frac{1}{\sqrt{4\pi\alpha T}}\, e^{-\frac{\Delta\varphi^2}{4\alpha T}} \tag{3.69}$$

where the spatial dependence is absorbed in $\Delta\varphi$. The infinite integral of the probability density $\int_{-\infty}^{\infty} p\, \mathrm{d}\Delta\varphi$ is equal to unity. By identifying that the diffusion

---

[22] In this section Δ denotes an infinitesimally small quantity, not detuning.

coefficient $\alpha = \frac{v_\sigma^2}{2T}$, where v_σ is the phase uncertainty growth rate in rad/s, and finding the average phasor for the off-diagonal *statistical* density matrix element, the coherence ρ_{nm}, we arrive at the integration of Eq. 3.69:

$$\begin{aligned} \rho_{nm} &= \overline{C_n C_m^*} = \overline{\left|C_n C_m\right| e^{i\Delta\varphi}} \\ &= \int_{-\infty}^{+\infty} p\, e^{i\Delta\varphi}\, \mathrm{d}\Delta\varphi \\ &= e^{-\frac{1}{2}v_\sigma^2 T^2} \end{aligned} \tag{3.70}$$

with the substitution $\Delta\varphi_n - \Delta\varphi_m \mapsto \Delta\varphi$, the complex amplitudes C_n and C_m of the eigenstates labelled by indices n and m, and the averaging operator over all particles in the ensemble $\overline{(\bullet)}$ that maps into the integration over the phase distribution function p with respect to the phase difference between the two states $\Delta\varphi$. The result is identical to the visibility function V obtained below (Eq. 3.75). It is possible to quantify phase diffusion by measuring the phase uncertainty in radians:

$$\sigma = v_\sigma \cdot T \tag{3.71}$$

that enters the visibility formulæ above, with v_σ slope measured in rad/s. The experimental results are presented in the next chapter.

3.4.2 Visibility and dephasing time

The normalized population difference P_z in the case of Ramsey interferometry without losses and resonant interrogation pulses can be re-written with the random variable $\Delta\varphi$ as:

$$P_z = -\cos\left[\left(\varphi + \underbrace{\Delta\varphi}_{\text{noise}}\right)T\right] \tag{3.72}$$

Employing the standard statistical averaging procedure [152], the effect of phase noise on the observable is modeled by finding the statistical average over the obtained Gaussian probability density function p of the Wiener process with the random variable $\Delta\varphi$. In the resonant case of Eq. 3.13 the average becomes:

$$\begin{aligned} \langle P_z \rangle = \int_{-\infty}^{+\infty} p P_z(\Delta\varphi)\, \mathrm{d}\Delta\varphi = \\ -e^{-\frac{1}{2}v_\sigma^2 T^2} \cos(\varphi T) \end{aligned} \tag{3.73}$$

where φT is the phase acquired during free evolution. From Eq. 3.73 the *dephasing time* at a contrast amplitude decay level of $1/e$ can readily be obtained by setting

$\varphi = 0$ and solving the equation with respect to T:

$$\tau_{deph} = \frac{\sqrt{2}}{v_\sigma} \tag{3.74}$$

It is also useful to split off a relation between the fringe visibility V and the phase noise distribution parametrized by v_σ from the results above:

$$V = e^{-\frac{1}{2} v_\sigma^2 T^2} \tag{3.75}$$

There are other models for the phase dispersion, but the complete motional averaging of the most probable atom by the Maxwell-Boltzmann law gives the best comparison with the experiment up to now [55].

3.4.3 Stochastic dephasing mechanisms

For the reason that the many-body losses lead to a highly-nonlinear master equation, it is difficult to obtain a solution of the Ramsey interferometry model in an exact analytical form. Numerical integration, though, represents no issues. The interferometry model should include envelope functions that degrade the contrast in a way suitable for analysis, e.g., factored out to the visibility term [153, p. 114]. There are several contributions to the P_z fringe envelope: local oscillator instability, ambient magnetic field noise and atomic motion in the trap potential.

$$\begin{aligned} \langle P_z \rangle &= \int f\,(T)\; p_1\, p_2 \cdot \ldots \cdot \cos\left[\left(\varphi + \Delta\varphi_1 + \Delta\varphi_2 + \ldots\right) T\right]\; \mathrm{d}\Delta\varphi_1 \mathrm{d}\Delta\varphi_2 \cdot \ldots \\ &= f(T) e^{-\frac{1}{2}\left(v_{\sigma 1}^2 + v_{\sigma 2}^2 + \ldots\right) T^2} \cos\left(\varphi T\right) \end{aligned} \tag{3.76}$$

where the probability distributions are given in short-hand notation by the equivalence $p_n \equiv p(\Delta\varphi_n, v_{\sigma n}, \ldots)$ with $n \in \mathbb{N}$.

This result allows to factor out the cosine Ramsey projection function from the arbitrary decay envelope function $f(T)$ and the Wiener processes characterized by the respective $v_{\sigma n}$ with $n \in \mathbb{N}$ responsible for random contributions from the local oscillator instability, atomic motional averaging, etc. This result is of great importance in the context of the highly nonlinear interferometry model and the associated many-body loss master equation (Eqs. 3.60) that can practically be integrated only numerically whereas the inclusion of stochastic processes in the numeric computation to account for the Wiener processes would require a substantial complication of the computational method. With the factorized contributions resulting from Eq. 3.76 the envelope function $f(T)$ can be computed separately by direct numerical integration of the master equation, and the stochastic

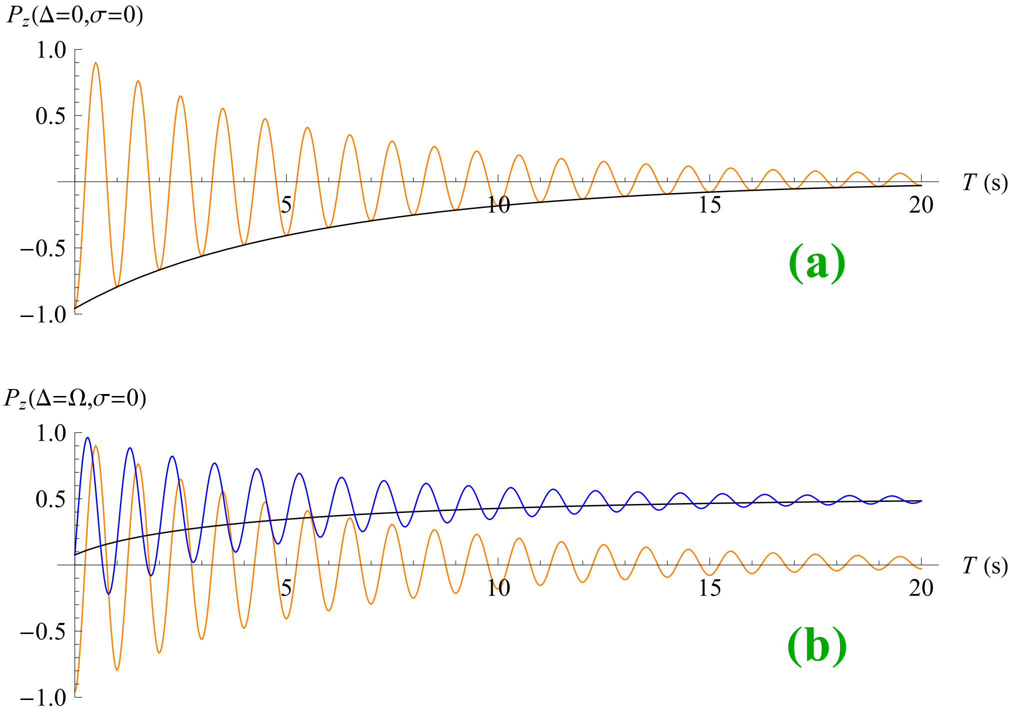

Figure 3.11: Numerically integrated Ramsey interferometry model of Eqs. 3.60 illustrating the factorizability of the envelope functions from the interference cosine term, with the following set of test parameters: $\Gamma_1 = 0.1$, $\Gamma_2 = 0.2$, $\Gamma_{11} = 0.7$, $\Gamma_{12} = 1$, $\Gamma_{22} = 3$, $\Gamma_d = 0.2$, $\Omega = 2\pi \times 1$. Initially only state $|1\rangle$ is populated. The relaxation constants are chosen to be distinct to produce an envelope function of the highest loss-dependent complexity: its shape departs from the exponent or the one-body sech. The pulses are real (lossy), their durations are made $\pi \big/ (2\Omega_R)$ long. Stochastic processes are not included for they play no role in the present analysis. To indicate this explicitly the plots are labeled with $\sigma = 0$.
(a) Envelope function coincides with the oscillating part at $\Delta = 0$; a test value of $\varphi = 2\pi \times 1$ Hz produces a fringe (**orange**) and $\varphi = 0$ gives the envelope (**black**).
(b) If $\Delta \neq 0$, the fringe acquires a certain bias function in addition to the envelope given in **black**, but the frequency of the phase-shifted oscillation (**blue**) is purely defined by $\varphi = 2\pi \times 1$ Hz revealing the underlying cosine of the same argument φT as in lossless Ramsey interferometry; the fringe from **(a)** is given for comparison in **orange**.

part found from measurements of the standard deviation growth constants $\{\upsilon_{\sigma n}\}$ of the corresponding processes. The cosine function is a result of the unitary coupling part of the master equation and, independently of the loss part, can only be (co-)sinusoidal. The latter implies that even the numerically obtained $f(T)\cos\left[(\varphi + \Delta\varphi_1 + \Delta\varphi_2 + \ldots)T\right]$ would have factored out the same envelope functions due to the noise variables if solved analytically[23]. The envelope can be found by numerical integration of Eqs. 3.60 with $\varphi = 0$, producing a pure P_z envelope function $f(T)$, and the same integration with $\varphi \neq 0$, as shown in Fig. 3.11, which gives a sinusoidal oscillation with the envelope $f(T)$. If $\Delta \neq 0$, the observables acquire a bias function as well and the obtained $P_z(T, \varphi = 0)$ does not reproduce the fringe $P_z(T, \varphi \neq 0)$ shape (see Fig. 3.11(b)). The pulse durations are chosen to

---

[23] There is no general method of solution for nonlinear differential equations.

be $\pi \big/ \left(2\Omega_R\right)$ long. A closer examination shows that the fringe has a shifted phase, but apart from the bias and envelope functions it follows a cosine law of exactly the same argument φT that defines the oscillation frequency.

From these observations we can conclude that the cosine and other relaxation contributions are independent and the $e^{-\frac{1}{2}(v_{\sigma 1}^2+v_{\sigma 2}^2+\ldots)T^2}$ envelope, as well as other noise envelopes, can be *phenomenologically* included in the visibility as an extra factor, whilst the rest of the visibility with the cosine term can be computed numerically.

It is essential to include random processes because otherwise P_z may have nonzero visibility for times much longer than observed. In an experiment random processes severely limit the coherence time since the $v_\sigma^2 T^2$ component in the power of the exponent in the envelope quickly degrades the visibility in T.

A spin echo reverses the atomic phases which leads to an ensemble spin reversal and consequential refocusing, cancelling out the part of the decay envelope caused by the dephasing of the atomic spins, e.g., due to the motional averaging [55]. However, the local oscillator instability, the variance of which adds up to the total variance of the involved random processes in Eq. 3.76, is not cancelled because this type of phase destruction is not refocussed by a spin echo: clock phase uncertainty continues to grow with time T and with the arrival of subsequent pulses the oscillating field is progressively more dephased with respect to the Larmor precession phase. In this way we can associate the atomic phase diffusion with the constant $v_{\sigma 1}$ and the clock instability, measured in a spin echo experiment, with the constant $v_{\sigma 2}$ in Eq. 3.76. The constant $v_{\sigma 1}$ can be measured in a Ramsey experiment: the measured uncertainty growth rates will then be the sum of the local oscillator instability and the atomic spin dephasing contributions, i.e., $v_{\sigma \exp}^2 = v_{\sigma 1}^2 + v_{\sigma 2}^2$. Ambient magnetic noise is largely rejected by operating at the "magic" field, although it residually affects the atom via the higher orders of the Zeeman effect nonlinearity which are not compensated by the "magic" field. Magnetic field fluctuations induce spatially inhomogeneous level shifts, but since we are unable to distinguish them in an experiment from the local oscillator instabilities, we think of them as a whole. Both constants are determined experimentally in the next chapter.

3.4.4 Ensemble spin self-rephasing

In addition to the effects we have discussed, there is an important aspect of the collective spin dynamics that allows the system to preserve ensemble spin and dramatically increase its coherence time. The rephasing phenomenon acting on the atomic ensemble as a built-in spin echo has recently been revived in the ultracold bosonic community as the *identical spin rotation effect* (ISRE) [56–58], however it was introduced decades ago [157] and extensively studied in fermionic gases [158–160].

The ISRE-effect is based on the following mechanism. The ensemble spins are split into two velocity classes, *fast* and *slow*, depending on the inhomogeneous shift $\Delta(\boldsymbol{r})$. Whether an atom belongs to a fast or slow class is defined by the relation of the characteristic inhomogeneity Δ_0, being the standard deviation of the inhomogeneous shift due to the magnetic field inhomogeneity and the collisional shifts spatially averaged over the atomic cloud [56], to the class exchange rate (ISRE rate) ω_{ex}. If $\omega_{\mathrm{ex}} > \gamma_c$, the atom rarely changes its class and the two classes can experience dephasing with respect to each other. The dephasing is broken if this condition is not fulfiled: then the quick class exchange results in the atoms leaving the class and mixing up the phase, resulting in phase averaging and evanescent relative class dephasing. The average class-spins have different precession speeds since atoms with higher velocities collide more often and dephase faster. At certain moments of time the class spins temporally synchronize in free evolution and, owing to their inherent property of angular momenta, start rotating around their total angular momentum. After time π/ω_{ex} both class spins reverse their phases so that the one that was ahead now lags behind: the class spins have *rephased*. Continuing to precess in the same direction at the same speeds, the spins may become locked in a continuous spin rephasing, alternately flipping the phase of each other in a synchronous motion around the total spin moving in the phase plane. The overall ensemble polarization in this case becomes more localized around the total than without ISRE, or the *polarization is preserved* and the Ramsey contrast improved. Of course, the improvement is subject to conditions: if the rephasing is not sufficient to keep the class spins locked in mutual precession, they would relatively dephase; this would degrade the ensemble spin and, as a consequence, the Ramsey contrast. In the worst case the dephasing is accelerated. The self-rephasing must complete the phase reversal before the atoms have a chance to change the class, i. e.

$$\frac{\omega_{\mathrm{ex}}}{\pi} > \gamma_c \tag{3.77}$$

and earlier than the average dephasing approaches π, i. e.

$$\omega_{\mathrm{ex}} > \Delta_0 \tag{3.78}$$

If the latter does not hold, the dephasing accelerates. Under the assumption of equal scattering lengths $a_{11} = a_{22} = a_{12}$, which is true within a 5% accuracy, the lateral elastic collisional rate γ_c is defined as [56]:

$$\gamma_c = \frac{16}{3}\sqrt{2\pi}\, a_{12}^2 v\, \bar{n} \tag{3.79}$$

and the ISRE spin exchange rate ω_{ex} as:

$$\omega_{\text{ex}} = 2\pi \times 2\hbar \frac{|a_{12}|}{m} \bar{n} \tag{3.80}$$

where $\bar{n}$ is the average atomic density, $v = \sqrt{2k_B T/m}$ is the most probable velocity in the Maxwell-Boltzmann distribution, a_{ij} is the scattering length for states i and j taken from [59] to be $a_{11} = 100.44a_0$, $a_{22} = 95.47a_0$, $a_{12} = 98.09a_0$ and the Bohr radius $a_0 = 0.529$ Å.

The relation of the average dephasing Δ_0 and the ISRE exchange rate ω_{ex} can be visualized on the Bloch sphere as the radius of the circle that is plotted out by the precessing spin tips on the Bloch sphere surface. If $\omega_{\text{ex}} \gg \Delta_0$, the radius is very small and the rephasing is immediate; the so called *spin locking* takes place and dephasing of the class spins with respect to each other is suppressed by instant refocusing. In practice it is possible to achieve conditions where ω_{ex} is moderately larger than Δ_0 and ISRE still takes place.

We can quantitatively assess the role of the effect in our experiments. ISRE self-rephasing is defined by the average atomic density $\bar{n}$: the higher the density, the more pronounced the self-rephasing. The atomic density at the centre of the Gaussian cloud is found as $n_0 \equiv n(x=0, y=0, z=0)$ from [161, 162] and the cloud widths σ_x, σ_y, σ_z from Eq. 3.33:

$$n(x,y,z) = \left(\frac{1}{\sqrt{2\pi}}\right)^3 \frac{N_0}{\sigma_x \sigma_y \sigma_z} e^{-\left(\frac{x^2}{2\sigma_x^2} + \frac{y^2}{2\sigma_y^2} + \frac{z^2}{2\sigma_z^2}\right)} \tag{3.81}$$

There are two dominant contributions to the ensemble dephasing. The first is the magnetic field inhomogeneity due to the local Zeeman effect which for a magnetic field $\boldsymbol{B}$ close to $\boldsymbol{B}_{\text{magic}} = 3.228$ G gives the detuning:

$$\Delta_Z(\boldsymbol{r}) = q(\boldsymbol{B} - \boldsymbol{B}_{\text{magic}})^2 \tag{3.82}$$

as a result of the power series expansion of the Breit-Rabi formula and elimination of the zeroth and first orders, where $q = 2\pi \times 431.35\ \text{Hz/G}^2$. The second contribution is the effect of *cold atomic collisions* [59] producing a shift across the cloud Δ_{mf} due to different scattering lengths of the involved hyperfine states averaged in the mean-field approximation. With this in mind the quadratic Zeeman contribution can be added to the collisional contribution to obtain:

$$\Delta(\boldsymbol{r}) = \Delta_Z(\boldsymbol{r}) + \Delta_{mf}(\boldsymbol{r}) \tag{3.83}$$

The mean-field dephasing is density dependent and after the splitting Ramsey pulse it can conveniently be expressed as [56]:

$$\Delta_{mf}(\boldsymbol{r}) = -2\pi \times 0.4\, n(\boldsymbol{r}) \times 10^{-12}\,\mathrm{Hz} \cdot \mathrm{cm}^3 \tag{3.84}$$

It is shown in [55] that the field may be set away from $\boldsymbol{B}_{\mathrm{magic}}$ to partially compensate for the collisional shift so that Δ_0 is minimized: $\Delta_Z(\boldsymbol{r})$ can only give a positive value due to the quadratic dependence on $\boldsymbol{B}$ whereas $\Delta_{mf}(\boldsymbol{r})$ is always negative. Consequently, the spatial dependencies of $\boldsymbol{B}(\boldsymbol{r})$ and $n(\boldsymbol{r})$ define Δ_0.

At a typical thermal cloud temperature, measured in the axial direction, of $T = 250$ nK, trap frequencies $\omega_x = 2\pi \times 97.6$ Hz, $\omega_y = 2\pi \times 97.6$ Hz, $\omega_z = 2\pi \times 11.96$ Hz, initial total atom number $N_0 = 150\,000$, the average atomic density is $n_0 = 2.3 \times 10^{12}$ cm^{-3}, which is close to the maximal predicted fringe contrast in [56] and the optimal value reported in [55]. The ISRE rate $\omega_{\mathrm{ex}} = 2\pi \times 109.7$ Hz and $\gamma_c = 5.7$ Hz. For the other set of typical values used in our experiments, $N_0 = 60\,000$ and temperature $T = 225$ nK, the density $n_0 = 1.1 \times 10^{12}$ cm^{-3}, $\omega_{\mathrm{ex}} = 2\pi \times 51.4$ Hz and $\gamma_c = 2.5$ Hz. The cloud widths σ_x, σ_y and σ_z can be fitted from the captured absorption images, but here they are calculated from the trap frequencies and measured temperatures found from the relation of Eq. 3.33. For either of the combination of T and N_0 the ratio $\omega_{\mathrm{ex}}/\gamma_c \approx 3$, satisfying the ISRE condition of Eq. 3.77. The only condition left to fulfil is Eq. 3.78. Typically the dephasing at $\boldsymbol{B}_{\mathrm{magic}}$ and the given experimental parameters is at the sub-Hz level. We have not investigated the $\boldsymbol{B}$-dependence away from the “magic” field, as was done in [56], where the temperature was also controlled within the limits of ±50 nK. Even so, the numbers above at the exact $\boldsymbol{B}_{\mathrm{magic}}$ suggest that ISRE must be present with negligible visibility oscillations.

3.5 Conclusion

The presented one-body model is of general interest; it can be used in other experiments where many-body physics is absent or sufficiently small. The model is parametrized with an interrogation field detuning from the clock transition and with variable pulse durations to model more realistic pulses. The latter allows an optimal splitter-pulse duration to be found to alleviate the asymmetric one-body loss effect on $\boldsymbol{P}_z$ by tailoring the Ramsey sequence to maximize the fringe contrast. It turns out that the expression for the optimal time has a simple analytical form. The one-body model should be considered obsolete since it has been shown that two-body processes have a strong influence on the trapped atom clock, but it is still routinely used in the community for its simplicity in analysis [163].

The more subtle two-body phenomena enter the model with non-linear terms in the master equation that couple all of the elements of the density operator and severely complicate the solution. The interferometric fringe envelope significantly deviates from the exponent with any power law in T or the hyperbolic secant (sech) functions, where the latter is expected from the one-body model (Eqs. 3.17). Although the analytical solutions are difficult to obtain in this case, a *semi-analytical* approach allows us to combine the analytical model of the phase averaging due to the atomic thermal motion in the harmonic trap — complete motional averaging by [55] — and other stochastic dephasing mechanisms like the local oscillator instability and the numerical integration that provides the value of P_z. Such method mixing is possible because the Ramsey fringe can always be seen as a cosine with accompanying envelopes. This suggests that P_z must have an arbitrary envelope function that factors out from P_z and isolates the cosine. As a consequence, the factored envelope can be obtained numerically and combined with the fringe cosine.

It is remarkable that such an approach is equally applicable to either method including phase evolution and projective detection, be it the Ramsey method, spin echo or composite pulses for the dynamic decoupling of the clock states from the bath, because the underlying detection principle is the same and the interferometric outcome is of the form $\cos(\varphi T)$ which immediately leads to the analysis of stochastic dephasing presented in this chapter.

The till-now reported ISRE model [56–58] has been used with two correction factors to the two of the three model parameters: 1.6 to Δ_0, 0.6 to ω_{ex}. The lateral elastic collisional rate γ_c has been left uncorrected. The high data and data fitting accuracies [56, 58] with yet very large correction factors suggest there should be some additional decoherence mechanism missing in the ISRE model. The many-body collisional Ramsey model governed by Eqs. 3.60 may be able to fill in the gap by including all the relevant collisions in the system. Together with the ISRE model it may provide a comprehensive understanding of ensemble coherent dynamics over long evolution times in a trapped atom clock.

The availability of spin-1 and spin-2 subsystems allows us to distinguish the population decay rates by experimental means and to cancel out individual terms in the rate equations so that the formally non-linearly coupled systems of equations can be accurately characterized by decay rates. In the next chapter we provide measurements of γ_1, γ_2 as they are specific to the UHV-system and latest bakeout conditions. These rates are solely defined by the pressure in the vacuum-chamber which may vary by orders of magnitude. The other decay rates are universal and obtained from elsewhere.

In the models presented the shot-noise limit is considered unachievable, relying on the number of atoms prepared in experiments and the Poissonian number counting statistics (see Section 3.3.3). However, it should be kept in mind that the normalization of measurables hides the growing noise component that would translate into white noise ranging in $\boldsymbol{P}_z$ from −1 to +1 in the limiting case. The assumption of negligible noise is justified in experiments with the parameters given above.

Chapter 4

Trapped atom clock performance

4.1 Introduction

Along with the developed models, the phase diffusion process is experimentally studied in the present chapter. It is crucial to distinguish a multiplicity of population and phase loss phenomena that are encountered in experiments on the ^{87}Rb trapped atom clock. Their appropriate inclusion in the models allows us to extract the ensemble lifetime, the coherence time, the phase diffusion constant (or phase uncertainty growth rate) and other characteristic quantities.

A set of Ramsey and spin echo experiments is performed to separate the contributions from the losses caused by cold atomic collisions and energy level fluctuations due to the magnetic field instability, the local oscillator frequency noise and the frequency averaging to the atomic motion in a harmonic trap. According to the Ramsey model that is based on Eqs. 3.60 to include all the relevant inter- and intra-state one-body and two-body collisional losses, the population relaxation caused by two-body collisions in the system of ^{87}Rb clock states forms a highly asymmetric[1] population decay behaviour of states $|1\rangle \equiv |1, -1\rangle$ and $|2\rangle \equiv |2, +1\rangle$. Whilst the many-body relaxation constants are transferable between the systems, the one-body rates are apparatus-dependent and the corresponding measurements are reported.

The main result of this chapter is the presentation of experimental evidence of the linear growth of the phase standard deviation σ which agrees well with the phase diffusion model discussed in Chapter 3 in both Ramsey and spin echo interferometers. As a direct benefit, it allows the fringe envelope functions responsible for the motional averaging and the local oscillator frequency instability to be separated. Assuming a negligible ISRE envelope, since the experiments are operated at $\boldsymbol{B}_{\text{magic}}$, the presented interpretation can be considered to be comprehensive.

---

[1] We use the *asymmetry* term in the same sense as in Chapter 3: the asymmetry of the state population decays with respect to a constant $\boldsymbol{P}_z$ level.

4.2 Atom clock operation

An atom clock is a device stabilized via a feedback loop that keeps the oscillation frequency of an atomic transition at around the lock point chosen at one of the zero-crossings (see Fig. 4.1). To achieve the best accuracy the error signal of the feedback loop should be generated from the steepest slope of the interferometer signal which occurs at a near resonant zero-crossing ($P_z = 0$). At this point the fringe visibility is maximal. For these reasons it is chosen to be the *clock operating point*. From the one-body Ramsey interferometry model of Eqs. 3.15 one can obtain the clock spectral behaviour, which is most interesting at around the resonance[2].

The Ramsey resonance of an atom interferometer [164] with an experimentally determined value of the Rabi frequency of $\Omega = 2\pi \times 510$ Hz (see Section 4.2.2) takes the shape of Fig. 4.1. This figure assumes no losses, a free evolution time of $T = 5$ ms and a phase growth rate $\varphi = \Delta$ corresponding to the standard Ramsey

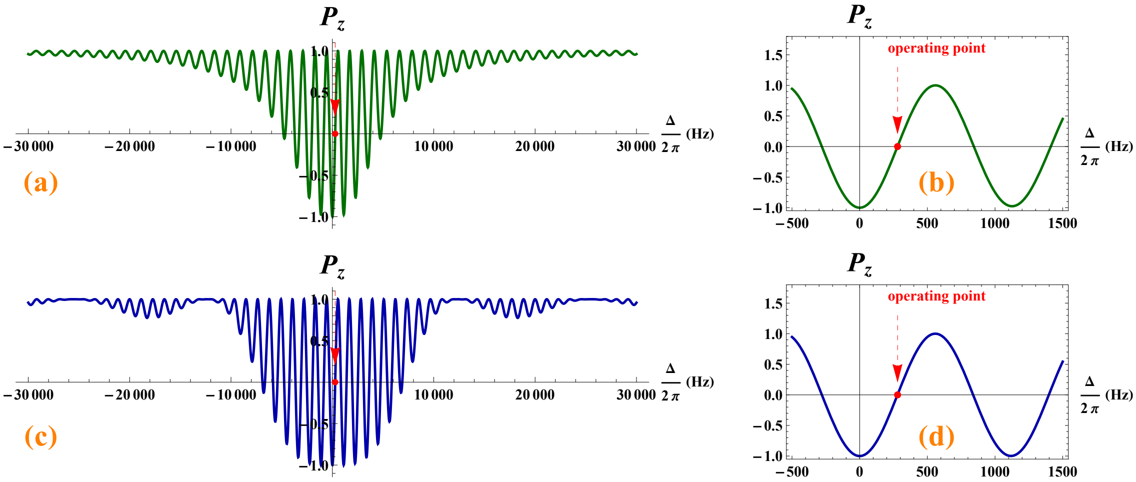

Figure 4.1: Ramsey interferometric resonance and the operating point of an atom clock in the frequency domain. The following values are used: $\Omega = 2\pi \times 510$ Hz, $T = 5$ ms. The measurable $P_z(\Delta, T)$ with the Ramsey condition $\varphi = \Delta$ (the one-body model of Eqs. 3.15) is plotted in **(a)** zoomed at around one of the operating points (**red** dot) in **(b)**. All losses are neglected. Frequency fluctuations convert to P_z fluctuations which is used to generate an error signal for active clock stabilization. The Rabi pedestal in **(a)** has a Lorentzian line shape at $T = 0$ and keeps holding the single-peak form over all T. This is a property of the Eq. 3.23 model where the pulses are assumed to always be $\pi/2$ for all Δ. Whereas in **(c)**, corresponding to the model of Eqs. 3.15, the pulses are $\pi/2$ only at resonance and at $\Delta \neq 0$ become non-$\pi/2$-pulses distorting the spectrum. **(b)** is the magnified central Ramsey fringe of **(a)** that reveals the operating point, usually chosen at the first zero-crossing. **(d)** is a zoom of **(c)** indicating an operating point indistinguishable from **(b)**. The Ramsey interference pattern shifts inside the Rabi pedestal if a phase difference is acquired during free evolution. In clocks this is considered as an imperfection, but is routinely used in sensing applications.

---

[2] If desired, the many-body model of Eqs. 3.60 can be used instead. However in the present discussion we take the analytical one-body model to demonstrate the principle of operation.

free (unperturbed) evolution. As in the case of the Rabi model (Eqs. 3.3, Fig. 3.2), the Ramsey spectrum has a comb of resonances at around $\Delta = 0$ (Fig. 4.1) that narrow down with increasing evolution time T. The Ramsey peaks[3] at around $\Delta = 0$ have maximal visibility. The clock spectrum features multiple zero-crossings in P_z. At resonance the visibility is highest and the slope is steepest, which is ultimately converted to the best clock accuracy: the slope translates frequency fluctuations to P_z fluctuations which can be employed to generate an error signal for active frequency stabilization with the highest signal-to-noise ratio.

The so called *Rabi pedestal*, the broad spectral feature caused by the $\pi/2$-pulses, is sensitive to detuning and perturbations and can shift the spectrum from its central position to affect the clock operation. In practice, it is only worth considering with the state-of-the-art precision demonstrated by the primary frequency standards [165–167] as the ^{133}Cs clock at NIST [164], whereas the ^{87}Rb clock is a secondary frequency standard [168, 169], currently with a worse fractional frequency and poorer stability [170–172]. However, the fundamental limits have not been reached yet: the future stability of ^{87}Rb clocks is expected to be $10^{-14}\ \tau^{-1/2}$ and the fractional frequency to be 10^{-17}. ^{87}Rb clocks may be expected to surpass the ^{133}Cs standards [173–175].

In the model of Eqs. 3.15 the $\pi/2$-pulses split the populations of the two states 50:50, even off resonance with $\Omega \neq \Omega_R$. This is different from the standard $\pi/2$-pulse whose duration is adjusted at resonance and kept constant while the detuning Δ is changed. Such pulses of a Δ-dependent duration produce a Lorentzian Rabi pedestal which has a single broad peak as shown in Fig. 4.1(a) where the Ramsey interferometry spectral features modulate the broad Rabi pedestal. In the standard Ramsey approach to keep $\pi/2$-pulse durations constant one can employ the model of Eq. 3.23 and use the definition that matches the standard Ramsey technique by setting $T_{p1} = T_{p2} = \pi/2 \big/ \Omega$. In this case the pulses split the populations 50:50 at resonance, but provide an unequal splitting away from resonance. The corresponding Ramsey spectrum has an infinite multiplet of peaks that form ripples in the Rabi interferometry spectrum in Fig. 4.1(c). Losses in Fig. 4.1 are neglected, but in a more realistic model the effects of the Maxwell-Boltzmann velocity distribution, atomic motion and field inhomogenieties would suppress and distort the Ramsey features away from $\Delta = 0$.

These two models (Fig. 4.1) have different assumptions about how the $\pi/2$-pulse duration is measured in experiment. Typically in applications, near resonant operation is desirable to benefit from high visibility; hence in the present discussion we shall neglect the contrast loss away from $\Delta = 0$, the envelope shift away from

---

[3] Hereafter in the clock spectra discussion the *peak* and the *Rabi pedestal* refer to the *inverted* peak and Rabi pedestal, respectively, in order to preserve the original terminology.

$\Delta = 0$ and limit ourselves to the dominant effect of Ω_R solely forming the broad spectral feature in Fig. 4.1. Either interferometer suffers from miscellaneous spatial inhomogenieties and *in situ* motional effects [55] resulting in a spectrally more localized envelope [176, 177]. Individual features of the spectral comb are also affected by the collisional shift [59] and the effects of the trap [55] e.g., phase difference acquired during the evolution, if any, shifts the interference pattern. In clock applications this effect is undesirable, but it is routinely used in sensing applications.

4.2.1 Two-state magnetically trapped clock

The two-state interferometer is implemented using a pair of ^{87}Rb hyperfine levels $|1,-1\rangle$ and $|2,+1\rangle$ in the $\left\{\big|F, m_F\rangle\right\}$ basis with a far detuned intermediate $|2,0\rangle$ level with the detuning Δ_{int} being typically -1 MHz (see Fig. 4.2 for the level diagram) to avoid population leakage from the clock states to the untrappable intermediate state. The level splitting diagram in the intermediate-field Zeeman effect given by the Breit-Rabi formula [89] is shown in Fig. 4.2. The system of levels experiences magnetic field shifts allowing magnetic dipole transitions in the hyperfine manifolds $F = 1$ and $F = 2$ to be induced by MHz radiofrequency radiation and GHz microwave radiation. The magnetic states $|1,-1\rangle$, $|2,+1\rangle$ and $|2,+2\rangle$ form a set of *low-field seekers* that are trapped in a magnetic potential

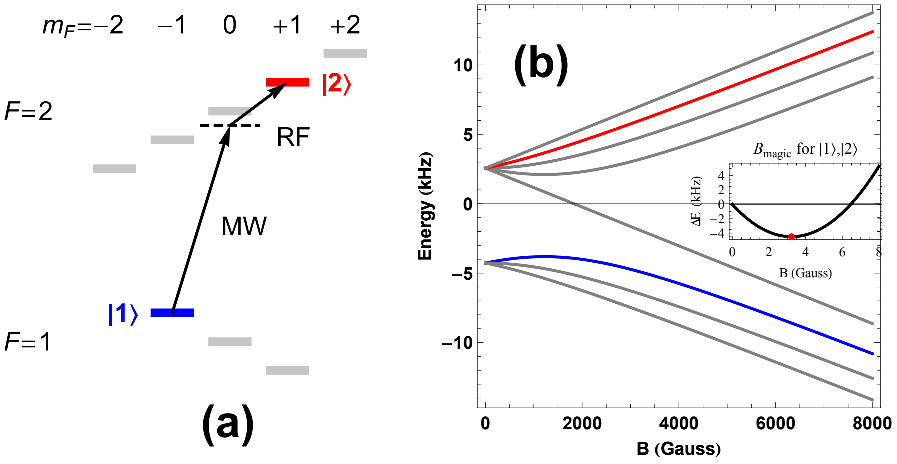

Figure 4.2: Two-photon coupling scheme for the $\pi/2$ splitting pulses in effective two-state interferometry and the level diagram of the nonlinear DC Zeeman effect. The colour-coding and order of energy levels in **(a)** match those in **(b)**.
(a) ^{87}Rb hyperfine ground state magnetic sublevels; the intermediate state detuning of the MW field from the $|2,0\rangle$ state $\Delta_{int}/(2\pi)$ spans from -1 MHz to $+1$ MHz;
(b) the nonlinear DC Zeeman effect from the Breit-Rabi formula: energy level dependence on magnetic field and the minimum (inset) of the energy difference ΔE between states $|1\rangle \equiv |1,-1\rangle$ and $|2\rangle \equiv |2,+1\rangle$ giving the "magic" field $B_{\rm magic} = 3.228$ G marked by the red dot; numerical values of energies and energy differences for $B_{\rm magic}$ are given in Appendix A. The parabolic B-field dependence in the inset is given by Eq. 3.82.

minimum.

The three-level system (Fig. 4.2) is reduced to an effective two-level system by the adiabatic elimination of the intermediate level. The resulting two-level system with a trap bottom $B_{\text{magic}} = 3.228$ G, the "magic" field, defining the Zeeman level splitting of 2.2596 MHz is coupled by MW and RF radiations via a two-photon transition with the intermediate state detuning $\Delta_{int} = -2\pi \times 1$ MHz keeping the single-photon resonances far away from the allowed transitions to avoid population leakage to untrapped states.

Placing atoms in the "magic" field eliminates the sensitivity of the energy level difference between the states $|1\rangle$ and $|2\rangle$ to magnetic field fluctuations, up to the first order. The atoms are still sensitive to second order perturbations of the magnetic field. Albeit, the usual ambient magnetic noise is measured in the order of circa 10 mG inducing a negligible level difference perturbation relative to the other sources of noise in the system (see discussion of the miscellaneous noise contributions to ΔP_z in Section 4.4.2).

The two-photon coupling amplitude Ω_{2ph} can then be expressed in terms of Ω_1 and Ω_2 by applying adiabatic elimination to the three-state model resulting in [72, 120]:

$$\Omega \equiv \Omega_{2ph} = \frac{\Omega_1 \Omega_2}{2\Delta_{int}} \tag{4.1}$$

with Ω_1 and Ω_2 defined as:

$$\begin{aligned} \Omega_1 &= \Omega_{MW}\sqrt{2} \qquad & \Omega_{MW} &= \frac{\mu_B g_F B_{MW}}{2\hbar} \\ \Omega_2 &= \Omega_{RF}\sqrt{6} \qquad & \Omega_{RF} &= \frac{\mu_B g_F B_{RF}}{2\hbar} \end{aligned} \tag{4.2}$$

where Ω_{MW} and Ω_{RF} are the angular Rabi frequencies of the microwave and radiofrequency transitions measured in experiments and Ω, B_{RF} and B_{MW} are linearly polarized microwave and radiofrequency magnetic fields.

4.2.2 Two-photon Rabi oscillations

The coupling strength needs to be measured to determine the Rabi oscillation period and to choose the $\pi/2$-pulse duration for Ramsey interferometry as well as to make sure there is no population leakage to the intermediate state and no visible losses present.

After the atom preparation sequence described in Chapter 2 an ensemble of $N = 30\,000$ non-condensed atoms is in the stretched state $|1, -1\rangle$. The two-photon pulse results in Rabi oscillations observed in P_z with phase $\Omega_R t$, where t is the two-photon pulse duration, and an amplitude equal to one following the general

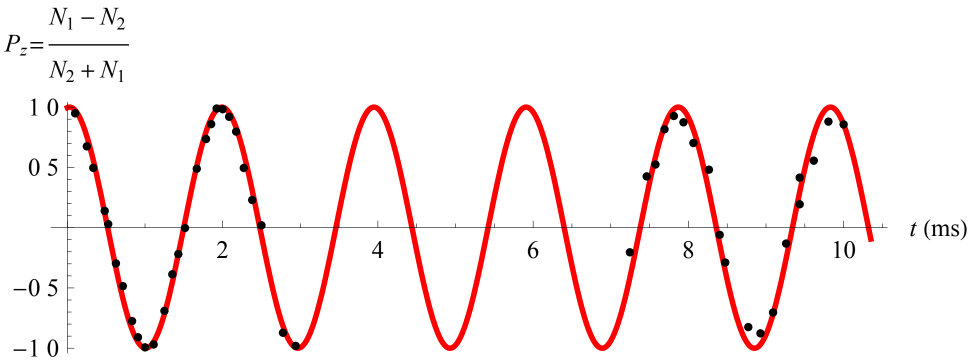

Figure 4.3: Two-photon Rabi oscillations in the normalized population difference P_z excited by MW and RF fields at $B_{\mathrm{magic}} = 3.228$ G with the intermediate state detuning $\Delta_{int} = -1$ MHz, and total number of non-condensed atoms $N = N_1 + N_2 = 30\,000$. The model (Eqs. 3.3) fit for the resonant case ($\Delta = 0$) gives a Rabi frequency $\Omega = 2\pi \times (510 \pm 6)$ Hz. In the $t > 6$ ms range there is some loss of contrast observed, but in experiments the two-photon interrogating field is used for no longer than 2 ms per pulse where the losses contribute a smaller amplitude decay than the noise level.

two-state evolution described in the previous chapter (see Eqs. 3.3). The cloud temperature is approximately 200 nK, being far above the critical temperature of the BEC transition T_{crit} for our trap frequencies and 3×10^4 atoms. The pulse duration is varied from 0 to t to obtain several cycles of P_z oscillations. The coupling field is applied to the atoms both from the microwave dipole antenna abutting a vacuum chamber window 12 cm away from the atoms and from feeding the radiofrequency to one of the end-wires: E1 or E2 – the effect from either wire is identical due to the end-wire symmetry with respect to the cloud position (Fig. 2.10). In the measurements presented in Fig. 4.3 the RF frequency is 2.44808 MHz and the MW frequency is chosen to maximize the number of atoms in state $|2\rangle$ halfway through the cycle. In the ideal case there is no P_z phase shift or amplitude decay and the cosine approximation is sufficiently accurate. MW and RF generators are clocked from the same oscillator to eliminate possible phase mismatch between the fields which would lead to additional noise in the data.

The oscillations in Fig. 4.3 have the highest strength achievable in our system[4] expressed in terms of the resonant Rabi frequency as $\Omega = 2\pi \times (510 \pm 6)$ Hz. The Ramsey $\pi/2$-pulse is then 0.49-ms in duration. Since the LabView control software has a coarse discretization step of 100 μs, the pulse duration is further tuned by changing the RF- or MW-field amplitudes that give a smaller effective time step.

In Fig. 4.3 the data set is fitted with the resonant cosine model of Eqs. 3.3 or Eqs. 3.15 with neglected losses: two-photon Rabi oscillations in the context of this work are always a quick measurement, limited to a few milliseconds where the present losses are negligible as indicated by Fig. 4.3.

---

[4] Mainly limited by the set of MW and RF generating equipment; refer to Chapter 2 to find out the specific model identifiers. Higher Rabi frequencies would not only require more powerful amplifiers, their excitation may cause a larger atom number instability during preparation.

4.2.3 Inelastic collisional losses

The lifetime of state $|1,-1\rangle$ limited by background collisions is determined from fitting data in Fig. 4.4 and relation $\tau = 1/\gamma_1$. The measurements of γ_1 performed by observing atomic loss in MT and the results are presented in Fig. 4.4. From the fit of Fig. 4.4(a) we obtain $\gamma_1 = 1/\tau = 1/13.64$ s^{-1}. The model is parametrized with the cloud temperature $T = 160$ nK, the trap frequencies $\omega_x = 2\pi \times 97.6$ Hz, $\omega_y = 2\pi \times 97.6$ Hz, $\omega_z = 2\pi \times 11.96$ Hz, and the initial total atom number $N_0 = 6 \times 10^4$. An intermediate quantity $\sigma_{\{x,y,z\}}$ gives a Gaussian cloud width in a chosen direction. In practical situations temperature, measured by cloud expansion in the time-of-flight experiments, has unequal values.

It should be kept in mind that the γ_1 term acquires a time dependence in measurements over long periods of time, because the pressure drops by an order of magnitude from the end of MOT-load to the end of the experimental sequence. Using the cold cathode vacuum gauge we measure the background-gas pressure by the end of the MOT-stage to be 2×10^{-10} Torr. By the end of the experimental sequence it drops to 2×10^{-11} Torr. The lifetime, measured when the pressure of the MOT-loading stage is 2×10^{-10} Torr, is $\tau = 13.64$ s, whereas at a pressure of 4×10^{-9} Torr the lifetime constitutes only 4.63 s. In the analysis done in this work we neglect the time-dependence of the background collision loss rate γ_1. This can be verified by integrating Eqs. 3.32 with $\gamma_1 = 0$ or seeking its steady-state

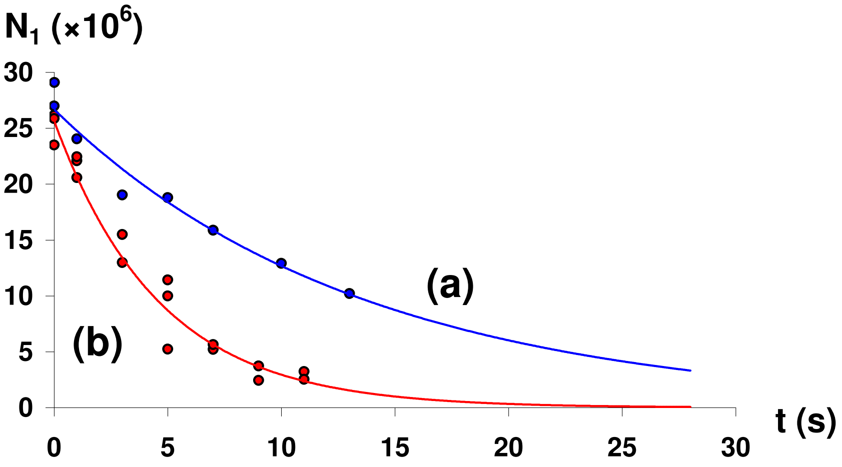

Figure 4.4: Ensemble lifetime measurements in the magnetic trap for the stretched state $|1,-1\rangle$ with 3×10^7 thermal atoms. In this state the dominant population loss mechanisms are one-body background collisions and three-body recombination (Eq. 3.31). However the three-body loss at a temperature 50 μK in the magnetic trap is negligibly small. It allows to determine γ_1 from a purely exponential fit and, since the same process leads to a loss in $|2,+1\rangle$, it also allows to determine $\gamma_2 = \gamma_1$. The decay at different pressures is considered to indicate the importance of paying special attention to designing an interferometry pulse sequence to minimize the time-dependence of one-body loss rates. The model is also given by Eqs. 3.34 as a special case.
(a) $\tau = 13.64$ s is the fitted decay time at a pressure of 2×10^{-10} Torr after the MOT-loading stage;
(b) $\tau = 4.63$ s is measured at a higher a pressure of 4×10^{-9} Torr after the MOT-loading stage.

solutions. It would immediately become clear that there is a nonzero steady-state solution in the absence of collisions with background gas.

The data collection consists of two stages. In the first, the atoms are prepared in $|1,-1\rangle$. After transfer to the the magnetic trap they are released by instantaneously relaxing the Z-wire field. In the second, an absorption image is taken in time-of-flight. Our magnification factor of 3 does not allow us to observe the whole cloud at the approximate temperature of 50 μK, since the cloud is large. However, we can observe most of the atoms. Thus, the atom number in Fig. 4.4 is acceptably underestimated: the non-exponential behaviour in $N_1(t)$ only appears at either a much lower temperature or with many more atoms or with a better vacuum resulting in lower one-body decay rates (consider the model of Eq. 3.31). This allows us to experimentally isolate γ_1 from the three-body loss and to determine its value in a simple experiment. The data is then fitted with a pure exponent.

4.2.4 On the accuracy of the many-body loss rates

The two-body inelastic loss constants employed in the present work are measured on our system at Swinburne [134]. Previously the values were experimentally determined in [64], although in both works and in [133] the data fitting was performed by neglecting the one-body losses that are induced by the interaction of the trapped atoms in both states with background gas. This is an apparatus-specific loss and fitting the data without it will lead to discrepancies in data interpretation (see Fig. 4.5) if the pressures in the UHV chambers of the experiments being interpreted were different[5]. Another important factor is that the rate equations (Eqs. 3.32 or Eqs. 3.33) with neglected one-body losses have non-zero steady-state solutions testifying that in general they cannot be used to accurately extract the decay rates since the $|1,-1\rangle$ population virtually never decays in perfect vacuum (see $n_1(t)$ in Fig. 4.5(a)). Neglecting this mechanism of population relaxation would lead to additional uncertainties in the extracted relaxation rates.

The measurement should also be done at a constant pressure to avoid spurious time-dependencies in the many-body relaxation rates: the pressure by the end of a minute-long cycle varies by an order of magnitude, from 2×10^{-11} Torr to 2×10^{-10} Torr. In Fig. 4.4 we determine the one-body decay rate for two pressure values to demonstrate the importance of the pressure influence. Since the one-body decays cannot be neglected while measuring both one-body and two-body decays, the influence of the one-body decay rate time dependence on the extracted values

---

[5] We provide a detailed bakeout log and a titanium sublimation pump activation sequence that result in the high vacuum. See Appendix B.

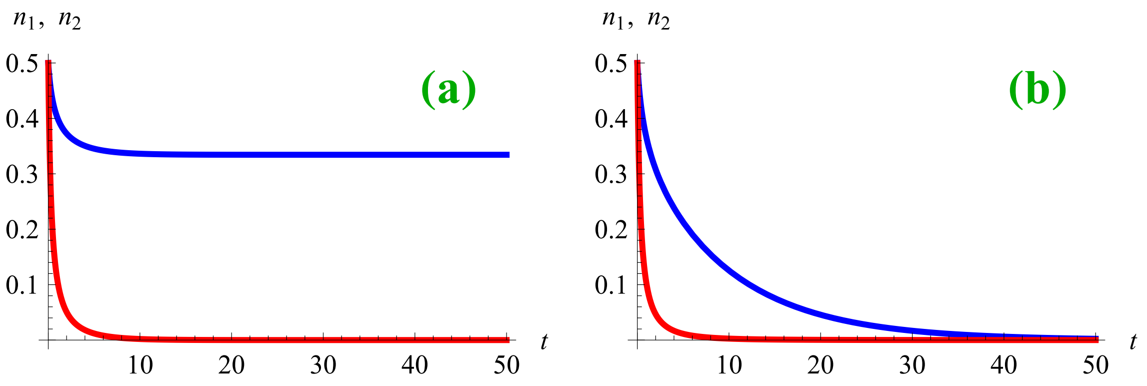

Figure 4.5: Numerical integration of the rate equations Eqs. 3.32 for the case of Ramsey evolution: state $|1,-1\rangle$ is shown in **blue**, state $|2,+1\rangle$ in **red**. The following sets of test parameters are used:
(a) $\gamma_{12} = 1$, $\gamma_{22} = 5$, $\gamma_1 = 0$, $\gamma_2 = 0$: $n_1(t)$ does not decay, $n_2(t)$ does;
(b) $\gamma_{12} = 1$, $\gamma_{22} = 5$, $\gamma_1 = 0.1$, $\gamma_2 = 0.1$: both $n_1(t)$ and $n_2(t)$ relax to zero.

of γ_{11}, γ_{12} and γ_{22} will be significant.

The pressure can be stabilized by loading atoms with the rubidium dispensers kept constantly on throughout the experimental cycle so that the atom loading and pumping[6] rates in the vacuum chamber equilibrate and keep the pressure constant. This would raise the one-body rate $\gamma = \gamma_1 = \gamma_2$, but will allow a more accurate determination of the two-body rates.

Integration of Eqs. 3.32 for the case of Ramsey evolution with $\gamma = 0$ results in the plots of Fig. 4.5(a) under the initial conditions that the number densities are initially set equal to $n_0/2$ which is equivalent to the beginning of the Ramsey free evolution. Alternatively to the density equations Eqs. 3.32, the atom number equations Eqs. 3.33 can be solved, if the parameters of the experiment are known. We also provide an approximate analytical solution in Eqs. 3.34. If at least one of the one-body decay constants is not equal to 0, the steady-state solution for $|1,-1\rangle$ will go to zero at $t \to \infty$. Since in our system $\gamma_1 = \gamma_2$, both relaxation constants should be larger than zero for the system to have temporal convergence. In fact, the one-body losses have been often neglected [64, 133, 134], but such an assumption should contextually be re-considered. We use the currently available many-body relaxation constants with compromised accuracy, leaving space for future experimental efforts.

---

[6] Here we mean the background gas pumping in the UHV chamber.

4.3 Phase stability with thermal atoms

4.3.1 Interferometry in the phase domain

The phase of the detecting $\pi/2$-pulse in Ramsey or spin echo sequences can be changed to acquire data points corresponding to a range of phases. The total phase can be modified by either the RF-phase or the MW-phase; here we employ the latter. The RF- and MW-generators are clocked from the same oscillator [95], be it the Rb clock or the oven-controlled quartz oscillator (OCXO) in different experiments, to avoid an asynchronous MW- and RF-field overlap drastically influencing the interferometry signal and making stability analysis difficult.

After the first $\pi/2$-pulse the atomic spins start an evolution from zero relative phase (Fig. 3.3). In general, the relative phase can change during the evolution. Upon arrival of the projecting $\pi/2$-pulse the Larmor precessed atomic spins interfere with the variable phase of the two-photon field. At a fixed evolution time T the phase can scan a full 2π range to obtain a complete fringe in the phase domain. With this method the radiation phase is changed rather than the atomic precession phase. This results in the same projection effect, but has the advantage of keeping T constant: the time-domain Ramsey signal accumulates phase noise during evolution and has limitations related to the dependence on T.

We use two methods to analyze the phase-domain measurements. The first method involves the direct fit of Eq. 3.15c where the visibility V below replaces the respective envelope function of Eq. 3.15c:

$$P_z = V\cos\left(k\left(\phi + \phi_0\right)\right) \tag{4.3}$$

where k is a phase calibration factor, ϕ_0 is the phase of the two-photon field defined in experiment by the MW phase. The phase standard deviation σ (Eq. 3.71) is extracted from the fit standard error (SE) provided by a fitting function. Assuming Poissonian statistics, the error bars have lengths covering the range of $\pm SE$ and are calculated as:

$$SE = \frac{\sigma}{\sqrt{N_{pts}}} \tag{4.4}$$

where N_{pts} is the number of points in the data set, $\sigma = v_\sigma \cdot T$ and v_σ is the phase uncertainty growth rate in rad/s and determined experimentally.

In the second method, the zero-crossing experiments, we employ the simplistic one-body model of Eq. 3.15c. One would then arrive at the phase deviation associated with P_z fluctuations:

$$\phi\left(P_z\right) = \frac{1}{k}\arccos\left(\frac{P_z}{V}\right) - \phi_0 \tag{4.5}$$

from which we define the phase standard deviation as $\sigma = \mathrm{STD}(\phi(P_z))$. We measure a number of the P_z data points for different values of ϕ_0. The visibility V incorporates τ_{deph} and can be expressed as[7]:

$$V = e^{-\frac{1}{2}v_\sigma^2 T^2} = e^{-\left(\frac{T}{\tau_{deph}}\right)^2} \tag{4.6}$$

For the purpose of the clock stability and $\Delta f/f$ analysis the exact form of V is not important. V is fitted in either of two ways. If the data contains a full interferometric fringe, the visibility is obtained by fitting Eq. 3.15c. The phase standard deviation is then extracted from the fitting routine. Otherwise the visibility is found by a measurement separate from the collection of the zero-crossing P_z data points (see below). In the latter case Eq. 4.5 is used to find the phase uncertainty. With equal decay rates $\gamma_1 = \gamma_2$ there is no imbalance in the state population decays that would degrade the P_z visibility (see Eq. 3.15c). In either case the clock stability analysis does not require knowledge of the particular visibility decay contributions.

Equation 4.5 has a limitation: the real argument of arccos in the range from -1 to $+1$ results in a range of real phases from π to 0 respectively. Larger phase sweeps cannot be adequately represented by the model. This leads to an important conclusion: such a method of the phase standard deviation determination from P_z is only valid for relatively small data fluctuations around $P_z = 0$, the "zero-crossing", which is the atom clock operating point [178]. This suggests that if the measurements are accomplished at around $P_z = 0$, the result can be interpreted without fitting, by the direct computation of σ from the formulæ above. However, if Eq. 4.3 is fitted, there is no such limitation, and one can achieve accuracy from fitting a complete 2π fringe period which does not imply a dedicated zero-crossing experiment.

The phase calibration to determine k is made by running a separate Ramsey experiment in the phase domain over a full-period 2π-scan at a minimal evolution time to obtain a fringe with negligible noise and fitting the cosine argument. A sufficiently good data set is given in Fig. 4.9(a). In practice the MW-source phase modulation over 2π may result in a $k \cdot 2\pi$ fringe with $k = 0.95$. Such calibration is made before each measurement.

If the many-body model is chosen, the semi-analytical approach described in Chapter 3 can be used: the visibility is replaced with the general envelope function $f(T)$ modeled numerically. From there we borrow the dephasing time definition

---

[7] Note that in the case of another measurable, e.g., P_1 or P_2, there will be dependence on γ_1 and γ_2, even if they are equal (see Section 3.1.1). Equation 3.15c shows that only P_z has no dependence on the one-body decays, if $\gamma_1 = \gamma_2$.

in terms of υ_σ (Eq. 3.74): $\tau_{deph} = \sqrt{2}\big/\upsilon_\sigma$. The following is a summary of the dephasing times for a variety of Ramsey and spin echo experiments done with pulse field synchronization from the oven-stabilized quartz oscillator built into the MW-generator[8] and from the commercial Rb clock[9].

4.3.2 Stability of on-chip Ramsey interferometry

There are two aspects of the clock or interferometer stability that are of our concern: the fractional frequency $\Delta f\big/f$ that reflects the phase fluctuations $\Delta\phi$, and the frequency stability measured by the overlapped Allan deviation. In the present section we study the former which is defined as $y = \Delta f\big/f$ and is collected with periods T_{cycle}. The clock transition frequency variations Δf are extracted from the measured phase variations $\Delta\phi$ at a fixed evolution time T through the correspondence obtained from $P_z = V\cos(\Delta\phi)$, yielding $\Delta\phi = 2\pi TV\Delta f = \arcsin\left(P_z\big/V\right)$, where V is the visibility (the fringe amplitude). The cosine has changed to a sine since the data points are at around $P_z = 0$, leading to an additional phase shift by a multiple of $-\pi/2$. The y data is obtained on the assumption of zero bias and the exact calibration ($k = 1$ from Eq. 4.5) as:

$$y_j \equiv y\left(jT_{cycle}\right) = \frac{\Delta f}{f} = \frac{1}{2\pi Tf}\arcsin\left(\frac{P_z\left(jT_{cycle}\right)}{V}\right) \tag{4.7}$$

where the continuous experimental time runs with integer steps as jT_{cycle}, $j \in \mathbb{N}_0$.

To collect a single data point in Fig. 4.6 an ensemble of 30 000 non-condensed atoms is prepared in the $|1,-1\rangle$ state, each with $T_{cycle} = 83$ s. The ensemble temperature is approximately 250 nK, while the atoms are kept in our usual trap configuration at B_{magic}. The clock transition frequency is set to the two-photon resonance at $f \approx 6.834$ GHz. The first $\pi/2$-pulse of 1.0-ms duration prepares an equal population splitting. After an evolution time T, the second $\pi/2$-pulse projects the populations to obtain $P_z(T)$. To obtain an interferometric fringe, the phase of the second pulse is changed between data points. For each cycle a new phase is randomly chosen over a range of ϕ equal 2π. Once the fringe acquires enough points to reliably fit a sinusoidal function, the fitting function extracts the standard deviation value σ of the phase uncertainty for a given T. To collect another data point the value of T is changed and the ϕ scanning is done over again.

Figures 4.6(a,b) presents two such phase scans: for $T = 100$ ms (a) and $T =$

---

[8] Agilent Technologies E8257D with an oven-stabilized quartz oscillator. The oscillator is superseded by an external 10 MHz signal from a Rb clock in the corresponding experiments.

[9] Stanford Research Systems FS725 Rubidium Frequency Standard.

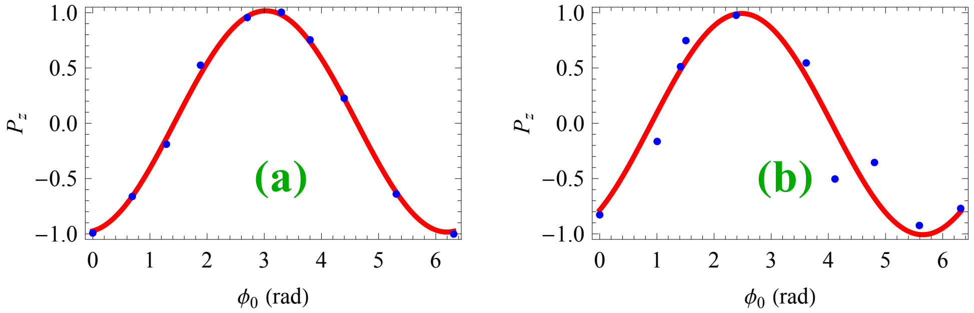

Figure 4.6: Ramsey interferometry in the phase domain with the Agilent MW generator with a built-in oven-controlled quartz oscillator. The phase ϕ_0 scans (**blue** data points) are done for evolution times $T = 100$ ms **(a)** and $T = 500$ ms **(b)**. The ensemble spin dephasing and the oscillator frequency instability leads to a noticeable dephasing shown in the data spread around the sinusoidal fit function (**red** line) in **(b)**. The phase uncertainty in **(a)** is $\sigma = 21.3$ mrad and 116.6 mrad in **(b)**. The extracted phase uncertainty growth rate $\upsilon_\sigma = 734.9$ mrad/s and the dephasing time $\tau_{deph} = 1.92$ s are summarized in Table 4.1.

500 ms (b). The data point distribution at $T = 100$ ms almost ideally fits a sine function with an amplitude equal to one revealing a $\sigma = 21.3$ mrad phase uncertainty. However, at $T = 500$ ms the dephasing and the oscillator instability markedly destroy the phase showing a $\sigma = 116.6$ mrad uncertainty. The fitted phase uncertainty growth rate becomes $\upsilon_\sigma = 734.9$ mrad/s and the respective $\tau_{deph} = 1.92$ s. In Ramsey interferometry with non-condensed atoms the phase uncertainty υ_σ grows linearly with time. This is due to the fact that the cloud profile does not experience reshaping over the evolution: re-thermalization is fast, of the order of 1/160 s^{-1}, the states experience the same trapping potential, and the ensemble temperature is kept nearly constant. The dephasing is attributed to OCXO instability and ensemble spin dephasing.

4.3.3 Correction for atom number fluctuations

As a way to enhance data accuracy, the dependence of P_z on the total number of atoms N can be taken into account before obtaining υ_σ from the fit. Otherwise the phase standard deviation will be overestimated and not all related to the phase diffusion process or the OCXO instability. In the zero-crossing experiments the $P_z(N)$ dependence is linear for non-condensed atoms. In Fig. 4.7 the results of a Ramsey interferometry experiment at zero-crossings are shown. By subtracting this function from the data we remove the irrelevant contribution to the phase spread. We shall call this procedure the *number correction* or N-correction.

The interferometer is loaded with $N_0 = 5 \times 10^4$ thermal atoms in state $|1, -1\rangle$ at 250 ± 50 nK. The $P_z(N)$ slope is experimentally determined for each point in T. After putting the interferometer in the clock regime ($P_z = 0$) the data points are collected successively with the time periods $T_{cycle} = 83$ s. Experimental

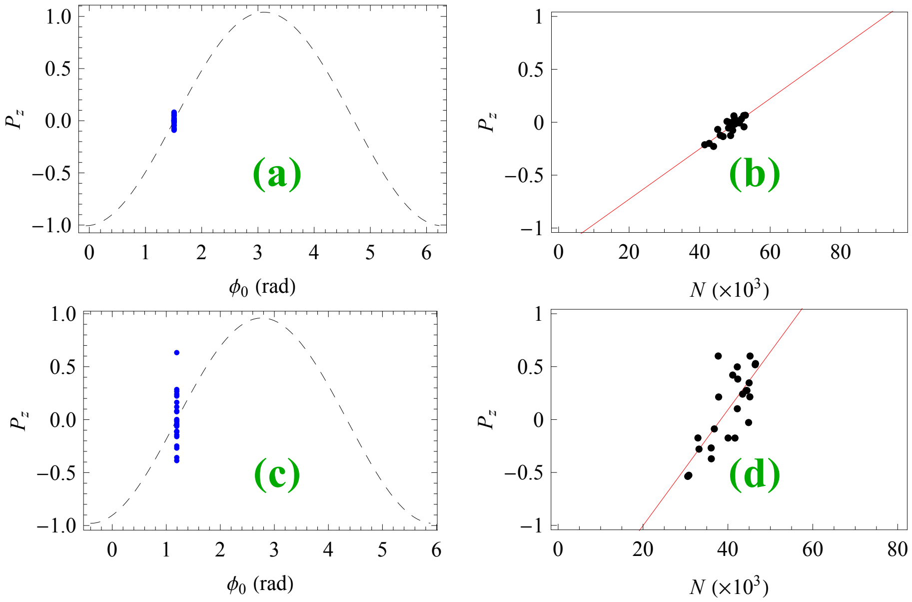

Figure 4.7: Zero-crossing Ramsey interferometry in the phase **(a,c)** and atom number **(b,d)** domains with and initial number $N_0 = 5\times10^4$ of non-condensed atoms at 250 ± 50 nK, with an oven-stabilized quartz oscillator clocking the two-photon field, installed in the MW-generator. Plots **(a,c)** correspond to measurements at evolution times $T = \{100, 500\}$ ms with the atom number correction (N-corr.). Experimental data points (**blue**) are corrected for the $P_z(N)$ fluctuations having an approximately linear dependence (**red** in **(b,d)**) with a slope of 2.38×10^{-5} for **(b)** and 5.47×10^{-5} for **(d)**. The fitted linear function is subtracted from $P_z(N)$ before extracting υ_σ. The $P_z(\phi)$ cosine (**grey dashed**) is fitted to show where the zero-crossing $P_z = 0$ occurs. The fitted σ values after the number correction are $\{47.6, 239.4\}$ mrad for **(a)** and **(c)**, respectively, resulting in a linearly fitted $\sigma = 478.7\cdot T$ mrad. Without N-corr. the phase uncertainty values are $\sigma = \{89.3, 374.7\}$ mrad and $\sigma = 754.9\cdot T$ mrad. The extracted phase uncertainty growth rates are included in Table 4.1.

data points in Fig. 4.7(a,c) are corrected for the $P_z(N)$ fluctuations having an approximately linear dependence in Fig. 4.7(b,d). The fitted linear function is subtracted from $P_z(N)$ before extracting υ_σ. At a Ramsey time of $T = 0$ the phase is well defined, its uncertainty is zero. The times $T = \{100, 500\}$ ms result in $\sigma = \{47.6, 239.4\}$ mrad, respectively. After the $P_z(N)$ fluctuation correction these values fitted with a linear law give $\sigma = 478.7\cdot T$ mrad. If no number correction is made, the phase uncertainty values are $\sigma = \{89.3, 374.7\}$ mrad and the linear law becomes $\sigma = 754.9\cdot T$ mrad. The two slopes in the number corrected and the uncorrected fits indicate a clear difference that cannot be attributed to the dephasing physics or the OCXO instability, but rather is a signature of the imperfect number preparation.

Different realizations of P_z lead to the scattered data points in Fig. 4.7. There is an obvious linear dependence of $P_z(N)$ shown in Fig. 4.7(b,d). By the linear fitting of the $P_z(N)$ points we obtain a slope of 2.38×10^{-5} for Fig. 4.7(b) and 5.47×10^{-5} for Fig. 4.7(d).

Figure 4.8 shows the phase-domain Ramsey measurements with thermal atoms (**red**) and a BEC (**black**). In the BEC case a condensed sample of $N_0 = 5.5\times10^4$

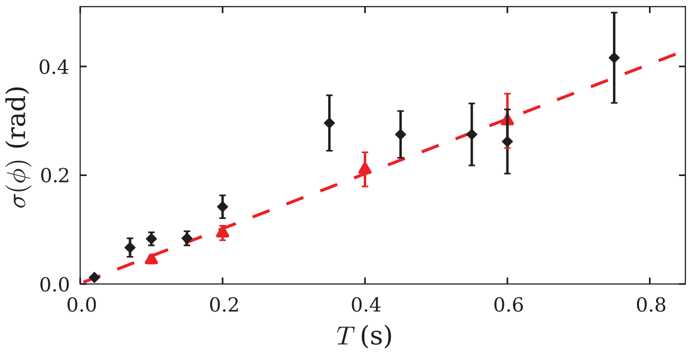

Figure 4.8: Phase uncertainty growth with evolution time T in the phase-domain Ramsey sequence for 5.5×10^4 thermal atoms (at a temperature of 160 nK, **red**) and a two-component BEC of 5.5×10^4 atoms (**black**). The phase uncertainty of a non-condensed ensemble clearly has linear temporal growth and is fitted with a straight line (**red** dashed) with a slope of 0.50(8) rad/s and $\Delta f / f = 1.16 \times 10^{-11}$. Published in [179].

atoms with a peak density $n_0 = 7.4{\times}10^{13}$ cm^{-3} is measured repeatedly with intervals of 120 s to collect points in Fig. 4.8. Such a high density system, approximately 50 times higher than that in the thermal atoms, has higher rates of collisional interactions being one of the dominant phase destruction mechanisms [175, 180].

A two-component condensate is formed by the splitting $\pi/2$-pulse and an equal superposition of the two states $|1,-1\rangle$ and $|2,+1\rangle$ is obtained. After the pulse the condensate is in a non-equilibrium energy state. Since the scattering lengths of the two states, a_{11} and a_{22}, are slightly different, they cause the superimposed superfluids to experience a quantum pressure which causes collective oscillations in the condensate. The components are then spatially repelled from each other and visibly separate in a few ms [179], completing the separation in approximately 220 ms. The collective oscillations repeat periodically and by approximately 440 ms the two component reunite again with a little imperfection in the overlap.

Despite the fifty times higher density of the condensate than that of the thermal cloud, the phase uncertainty growth is nearly the same for both systems: the fit of the non-condensed experimental data points in Fig. 4.8 gives a $\sigma(\phi, T)$ amounting to 0.50(8) rad/s and $\Delta f / f = 1.16{\times}10^{-11}$. Due to the identical spin rotation effect (ISRE) the collisional dephasing of the thermal ensemble is strongly suppressed as shown in [56]. The phase uncertainty is determined by the fractional frequency of the oscillator as demonstrated in the following sections by the different υ_σ rates of the ensemble interrogated by the two different oscillators: OCXO and a Rb frequency standard. See our collaborative work [179] for the condensate dynamics details.

The condensate phase diffusion is discussed here in the context of atomic interactions [181], it should not be confused with the spatially dependent relative phase of a condensate.

4.3.4 Stability of the spin echo interferometer

In analogy to Ramsey interferometry, we investigate the stability figures of spin echo interferometry. The sequence starts from the loading of state $|1\rangle$ and splitting the populations by a $\pi/2$-pulse of 1-ms duration in the same way as in the Ramsey sequence. Then the atoms are left unperturbed for the first evolution period of duration $T/2$. By the end of it, the dephasing amounts to the same magnitude as by the end of the Ramsey evolution for the same duration, denoted by φ_1 in the models (Eq. 3.19 or Eq. 3.20 for the $\Delta = 0$ case). At this moment phase reversal is performed by the application of a 2-ms spin echo pulse. As described in Section 3.2.4, the echo starts spin rephasing that completes the ensemble spin refocusing at the moment of the arrival of the detecting $\pi/2$-pulse after another $T/2$. The phase acquired in the second evolution amounts to φ_2.

Over the free evolution periods the clock transition is subjected to a number of unintentional perturbing processes that influence the phases during the evolution. However, at the end of the sequence φ_1 is subtracted from φ_2, according to the models. Those contributions that were not exerted by the driving field are cancelled out and the fringe cosine argument is only dependent on the difference $\varphi_1 - \varphi_2$. This largely eliminates most of the perturbations that were affecting the Ramsey interferometer performance.

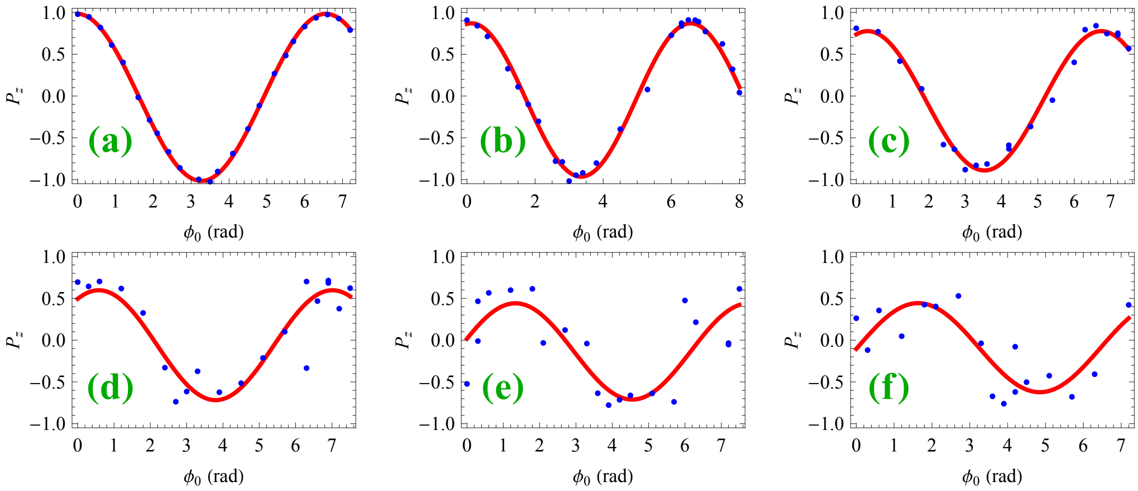

Figure 4.9: Spin echo experiment in the phase domain synchronized by the quartz oscillator with fixed free evolution times $T = \{0.2, 1, 2, 4, 6, 8\}$ s corresponding to plots **(a,b,c,d,e,f)** in the respective order. $N_0 = 3 \times 10^4$ thermal atoms in B_{magic} were employed at a temperature of 250 ± 50 nK. The spin echo drastically reduces the phase uncertainty growth over the evolution compared to the analogous Ramsey experiment: at $T = 8$ s the fringe still clearly follows a cosine function whereas in the Ramsey experiment a comparable clarity is possible at evolution times $T \lesssim 1.6$ s (with the number correction). The extracted σ values are included in Fig. 4.12. The $v_\sigma = 124.7$ mrad/s rate is extracted from the fitting of Eq. 4.3 to each of the ϕ_0 scans, then performing a linear fit of the obtained σ values (shown in Fig. 4.12). The result is included in Table 4.1.

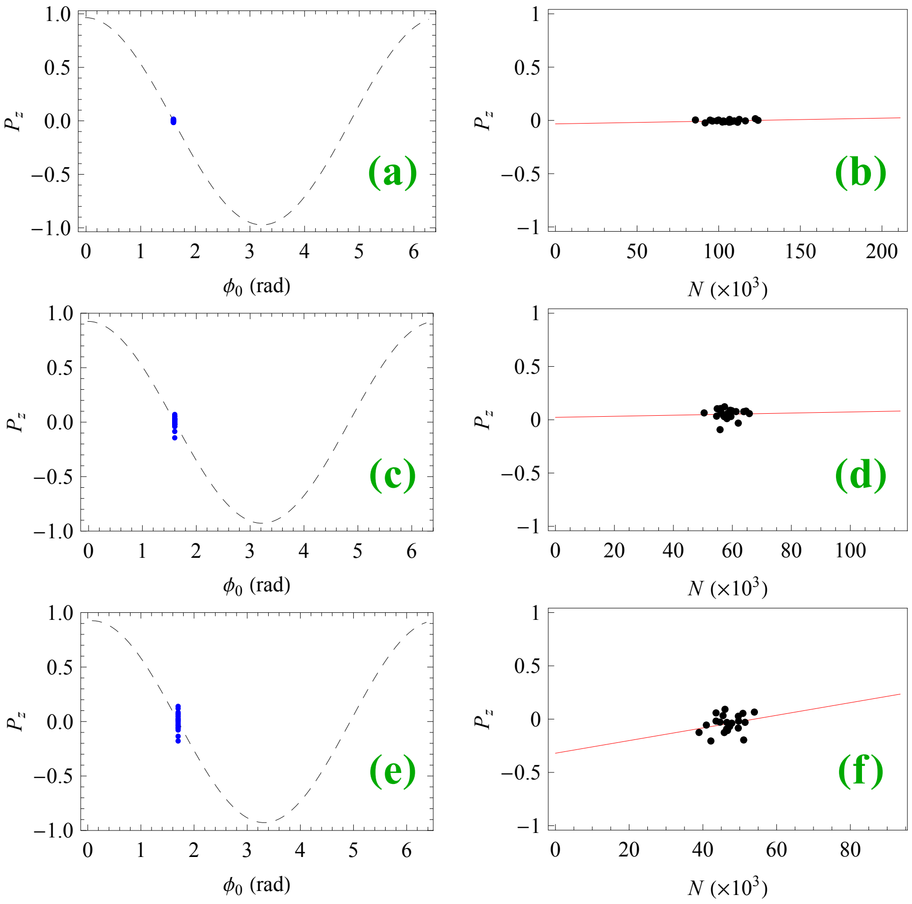

Figure 4.10: Zero-crossing spin echo interferometry in the phase **(a,c,e)** and the atom number domains **(b,d,f)** with an initial number of $N_0 = 1.1 \times 10^5$ trapped non-condensed atoms, with an oven-stabilized quartz oscillator clocking the two-photon field. Plots **(a,b)**, **(c,d)** and **(e,f)** correspond to the measurements at evolution times $T = \{100, 500, 1000\}$ ms, respectively, with the atom number correction (N-corr.) performed before extracting the v_σ values. Experimental data points (**blue** dots) are corrected for the $P_z(N)$ fluctuations (**black** dots) having an approximately linear dependence (**red** lines). The linear fit gives a slope of 2.7×10^{-7} for **(b)**, 5.05×10^{-7} for **(d)** and 5.93×10^{-6} for **(f)**. The $P_z(\phi)$ cosine curve (**grey dashed**) is fitted to indicate the zero-crossing $P_z = 0$. The values $\sigma = \{10.3, 54.2, 87.8\}$ mrad for the evolution times $T = \{100, 500, 1000\}$ ms, respectively, give a linear fit of $\sigma = 92.0 \cdot T$ mrad. The extracted $v_\sigma = 92.0$ mrad/s with and without the number correction is included in Table 4.1.

A set of the phase-domain spin echo measurements for evolution times $T = \{0.2, 1, 2, 4, 6, 8\}$ s is given in Figs. 4.9(a,b,c,d,e,f) in the corresponding order. A thermal ensemble of $N_0 = 3 \times 10^4$ atoms was prepared at a repetition rate of 1/120 s^{-1} in our usual experimental conditions: trap frequencies $\omega_x = 2\pi \times 97.6$ Hz, $\omega_y = 2\pi \times 97.6$ Hz, $\omega_z = 2\pi \times 11.96$ Hz, trap bottom at B_{magic}. The ensemble temperature is kept at 250 ± 50 nK. The RF and MW field synchronization is performed by the quartz oscillator[10]. It is immediately observed in Fig. 4.9 that the phase randomness has no noticeable dependence on ϕ_0, the data points are distributed around the fit function (Eq. 4.3), where ϕ accounts for the time T dependent phase, with a comparable spread in all the argument ϕ_0 sub-ranges

---

[10] The relevant specifications are given in the Allan deviation analysis, see Section 4.4.1.

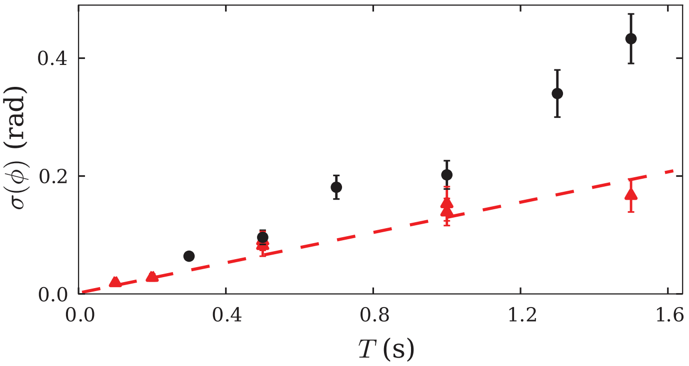

Figure 4.11: Phase uncertainty spin echo experiment in the phase domain with a quartz oscillator. 5.5×10^4 thermal atoms (**red**) at 160 nK give the phase uncertainty growth rate of 125(20) mrad/s (the fit shown by the **red dashed** line) and $\Delta f / f = 2.9 \times 10^{-11}$. A BEC sample of 5.5×10^4 atoms at an initial peak density of 7.4×10^{13} cm^{-3} (**black**) shows, on average, a steeper trend which becomes non-linear due to the spatially oscillating characters of the two constituent superfluids in a superposition of states $|1, -1\rangle$ and $|2, +1\rangle$. The BEC has higher collisional interactions compared to a thermal atom system; it destroys ensemble phase faster. Published in [179].

(ϕ_0-bins, if the data were binned).

In Fig. 4.10 we present the zero-crossing experimental results under the same conditions but only for short evolution times of $T = \{100, 500, 1000\}$ ms. Identically to the previous analysis of the phase-domain Ramsey interferometry, we employ the number correction to eliminate irrelevant atom preparation errors from the phase uncertainty. The data points in Figs. 4.10(a,c,e) are corrected for the $P_z(N)$ fluctuations having a linear dependence at around $P_z = 0$ shown by the solid lines in Figs. 4.10(b,d,f). The linear fit gives a slope of 2.7×10^{-7} for Fig. 4.10(b), 5.05×10^{-7} for Fig. 4.10(d) and 5.93×10^{-6} for Fig. 4.10(f). The v_σ rate is initially extracted as 94.8 mrad/s. However, after employing the number-correction procedure this gowth rate is evaluated to be 92.0 mrad/s (Table 4.1).

In the pursuit to investigate a highly interacting condensate in interferometry, we set up two experiments similar to the ones presented for the Ramsey sequence in Fig. 4.8. In the thermal atom experiments 5.5×10^4 atoms were prepared for each data point at a temperature of 160 nK in the trap with trap frequencies $\omega_x = 2\pi \times 97.0$ Hz, $\omega_y = 2\pi \times 97.0$ Hz, $\omega_z = 2\pi \times 11.69$ Hz. The slope of the noncondensed $\sigma(\phi, T)$ in Fig. 4.11 is measured to be 125(20) mrad/s. The other contributions are largely compensated by the spin echo. The dependence of the condensate case cannot be well approximated by a linear function since it has a repeatable nonlinear structure caused by the strong interactions of the two condensate components during the evolution that is not well compensated by spin echo. It is shown in our collaborative paper that the numerical quantum simulations also reproduce the curvature [179]. However, a linear estimate has obviously a higher phase uncertainty growth rate in the case of the condensate than in the thermal atoms. This dependence is attributed to the 50 times higher densities and,

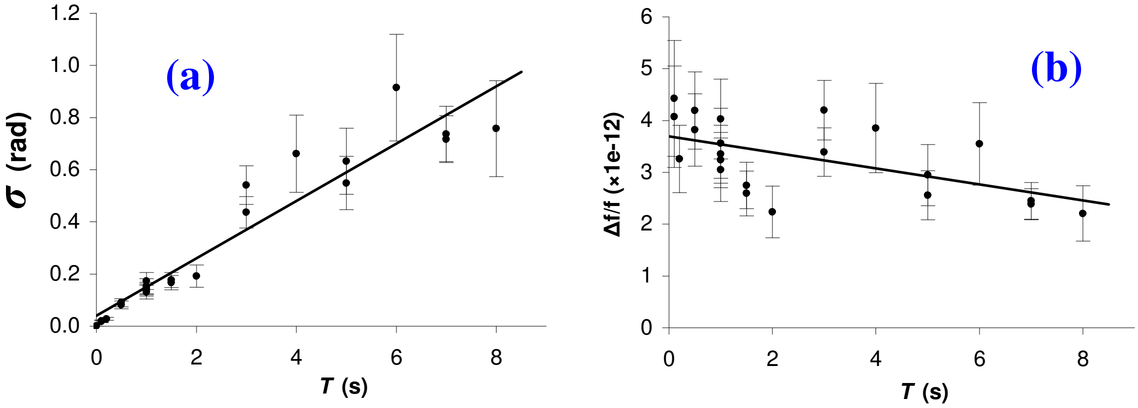

Figure 4.12: Phase diffusion measured with spin echo interferometry in the phase domain synchronized by the quartz oscillator. The points with $T \leq 2$ s are measured in zero-crossing experiments and estimated by the approximate formulæ (Eq. 4.5). The points with $T > 2$ s are values of the phase standard deviation obtained by fitting a full fringe, since at large evolution times the phase spread results in the P_z spread far away from $P_z = 0$ and the approximations break down (see Fig. 4.9). The error bars are estimated from the number of data points assuming Poissonian statistics.
(a) Phase standard deviation legitimate for the preceding Allan deviation analysis have revealed only phase noise limiting current experiments; the growth rate extracted from the linear fit (solid line) is $\upsilon_\sigma = 0.118$ rad/s fitted from **(a)**;
(b) Corresponding instantaneous values of the fractional frequency fitted linearly (solid line): $\Delta f / f = 2.75 \cdot 10^{-12} \pm 21\%$.

as a consequence, a stronger interacting system. There is also a contribution from the imperfect secondary overlap of the two BEC components that occurs after a period of repulsion [179, Fig. 1].

In the experiment of Fig. 4.11, a $\pi/2$-pulse of duration of 0.7 ms is obtained from the two-photon Rabi frequency $\Omega = 2\pi \times 350$ Hz and the two-photon detuning $\Delta = -2\pi \times 37$ Hz. The MW is radiated from a half-wave dipole antenna at a frequency of ≈ 6.8 GHz and the RF is fed to the on-chip end-wire E1 at a frequency of ≈ 3.2 MHz. This gives an intermediate state detuning of 1 MHz. Placing the atoms in B_{magic} protects the clock transition from ambient magnetic noise (see Section 4.4.2 for discussion). For the experiment a condensate of $N_0 = 5.5 \times 10^4$ atoms with a negligible thermal fraction at an initial peak density of 7.4×10^{13} cm^{-3} was studied when a π-pulse was applied at half the collective oscillation period, that is, when the BEC density waves of the two components maximally overlap again after a period of repulsive interaction, the π-pulse gives the maximal visibility revival by the end of the spin echo sequence.

In Fig. 4.12 we study the phase uncertainty of the best obtained result[11] more accurately with two techniques. The first is to use P_z zero-crossings as in the normal clock operation, then to extract the phase ϕ values by the simple linear

---

[11] See Table 4.1 for the summary of the experiments.

approximation of Eq. 4.5. This method has a limitation: if the phase uncertainty spreads the points far away from $P_z = 0$, the approximation breaks down. The results of the experiments with an evolution time T of up to 2 s are analyzed with Eq. 4.5 and presented in Fig. 4.12(a). To avoid further error growth at $T > 2$ s, when the spread of the P_z data points at a fixed T becomes noticeable, we scan a full 2π period instead, by changing the last $\pi/2$-pulse phase, then fit a cosine with the phase as a fit parameter and extract the phase standard deviation from the fitting routine. A larger sampling keeps the accuracy of the determination of the phase uncertainty constant irrespective of the position in the fringe. This approach is used to collect the rest of the points in Fig. 4.12. In order to estimate $\Delta f / f$ with fitted v_σ we use Eq. 4.9 below, the instantaneous values of $\Delta f / f$ are found from:

$$\frac{\Delta f}{f} = \frac{\sigma}{2\pi f T} \tag{4.8}$$

The results are displayed in Fig. 4.12(b).

4.3.5 Miscellaneous clock configurations

When the phase standard deviation growth rate v_σ is known, the fractional frequency can be obtained from:

$$\frac{\Delta f}{f} = \frac{v_\sigma}{2\pi f} \tag{4.9}$$

Table 4.1 summarizes the experiments comparing different methods of phase uncertainty characterization. In this set a relatively small number of points in T is used. This facilitated the determination of the most accurate technique. In principle, a phase uncertainty measurement can be accomplished if only one point of evolution time $T \neq 0$ is measured in Fig. 4.12(a). The phase uncertainty is known to be zero at $T = 0$; it gives a second data point, enough to fit a linear function. However, to reduce the confidence band we depart from such an ultimate case and demonstrate the phase uncertainty dynamics over a range of evolution times, relevant to all our experiments, with better sampling.

In addition to the OCXO-clocked experiments we also used a Rb frequency standard (Rb clock) to synchronize the driving two-photon field in a separate set of experiments reported in Table 4.1. Our MW-generator allows to use an external 10 MHz reference signal provided by the Rb-standard. Both RF and MW generators are clocked from the same source to avoid additional frequency deviations between the interferometric pulses. Analogously to the OCXO experiments the experiments are performed for a range of evolution times up to 1 s to reliably determine the phase uncertainty growth v_σ. All the data is collected in the

Table 4.1: Summary on the phase uncertainty experiments on thermal atoms in the phase domain with the data taken at the clock operating point ($P_z = 0$) and small sampling in T. The data is linearly fitted (including the origin which adds an extra point). The two methods are compared: the zero-crossing (№1-8 and partly №10) and the full 2π phase scan (partly №10 and №11). The abbreviation N/A indicates the N-correction is inapplicable.
*measured by fitting Eq. 4.3.
**a more accurate experiment compared to №7 and №8; measured by fitting Eq. 4.3.

№	type	oscillator	N-corr.	υ_σ (mrad/s)	τ_{deph} (s)	$\frac{\Delta f}{f}$ ($\times 10^{-12}$)
1	Ramsey	Rb clock		875.0	1.62	20.4
2	Ramsey	Rb clock	✓	842.9	1.68	19.6
3	Ramsey	OCXO		754.9	1.78	17.6
4	Ramsey	OCXO	✓	478.7	2.95	11.1
5	spin echo	Rb clock		888.9	1.59	20.7
6	spin echo	Rb clock	✓	868.1	1.63	20.2
7	spin echo	OCXO		94.8	14.91	2.21
8	spin echo	OCXO	✓	92.0	15.37	2.14
9	spin echo*	OCXO	N/A	124.7	11.34	2.90
10	spin echo**	OCXO	N/A	118.0	11.98	2.75
11	Ramsey*	OCXO	N/A	734.9	1.92	17.1

zero-crossing experiments and υ_σ is extracted via Eq. 4.5.

The set of different types of stability experiments with the results presented in Table 4.1 can now be compared. The spin echo experiments, as expected from theory (see Chapter 3), outperform the Ramsey interferometry by suppressing the phase diffusion by approximately a factor of 5. In the hope of achieving a better short-time stability we utilized a rubidium standard. However, its stability is compromised in the measured time range (refer to Table 4.1) compared to the OCXO stability. For this reason we stick to the OCXO. In the data processing we employ the linear number dependence of $P_z(N)$ clearly observed in experiments to correct the $P_z(T)$ data before extracting the υ_σ rates. At around the zero-crossing the linear fit of the cosine P_z is an adequate approximation regardless of what physical process is responsible for the number fluctuations. The υ_σ value with the number correction may be noticeably smaller than υ_σ without it. In Table 4.1 we report both values for each zero-crossing experiment. Despite the larger $\tau_{deph} = 15.37$ s, the statistically more reliable result is 11.98 s, supported by Fig. 4.12.

The low-sampled results reported in Table 4.1 were re-measured with a larger number of data points for the configuration with the highest τ_{deph}: spin echo with the quartz OCXO and are reported in Fig. 4.12. As the re-measured data analysis indicates, our clock stability gives the following figure for the thermal atom spin echo interferometry in the phase domain synchronized by the quartz oscillator without the number correction:

$$\boxed{\frac{\Delta f}{f} = 2.75 \cdot 10^{-12} \pm 21\%} \tag{4.10}$$

This number comes from $v_\sigma = 118$ mrad/s extracted from the fitting of Fig. 4.12(a). The corresponding expected dephasing time is:

$$\boxed{\tau_{deph} = 11.98 \ s} \tag{4.11}$$

4.4 Frequency stability and Allan deviation

The main characteristic of a clock is its frequency stability. We dedicated the previous section to the $\Delta f / f$ and here we discuss the frequency stability, directly related to phase stability, measured in terms of the fractional frequency $y = \Delta f / f$ and the Allan deviation conventionally denoted by $\sigma_y(\tau)$. The function y is defined by Eq. 4.7. It is essential that the data points are collected successively without interruptions. The stability depends on the types of noise present in the system that differently influence the clock operation.

The commonly accepted tool to assess both the frequency stability and the types of noise is the *Allan deviation* [95, 170, 182–187]. From a plot of the Allan deviation [188, 189] versus integration time τ figure[12] the different types of noise are classified as follows, in order of the τ growth: phase noise ($\mu = -2$), white frequency noise ($\mu = -1$), flicker frequency noise ($\mu = 0$), random walk frequency noise ($\mu = 1$), drift ($\mu = 2$), – where μ is the characteristic slope of the Allan variance $\sigma_y^2(\tau)$ on a log-log scale in the τ-region of the corresponding noise type domination (convenient diagrams can be found in [178, 190]). The Allan deviation $\sigma_y(\tau)$ slopes are $\mu/2$ [190]. Once the noise types are identified, the clock stability can be quantitatively characterized in each τ range.

There exist "smooth" versions of the Allan deviation[13], based on the moving average (with overlapped samples) [182, 183], circular sequence representation [191], etc. The advantage of such methods is that they add new degrees of freedom by producing a number of packets of the existing data. Although there is no new information added, because the new degrees of freedom are correlated, the confidence interval of the Allan deviation is drastically improved. It is crucial to use one such "filtering" algorithm to extract all noise types that are present in the system. In the original Allan deviation the outcome typically has poor

---

[12] Integration time τ is sometimes referred to as averaging time.

[13] The significance of the difference between the original Allan deviation and its smoother counterparts can be confirmed, e.g., by the figures in [183] and the description in [190].

confidence making it practically impossible to distinguish fine noise patterns in the sigma-tau plots with limited-size data sets[14] [190]. The latter is possible, if the $\sigma_y(\tau)$ features are larger than the confidence interval. In the analysis presented below we employ the *overlapped Allan deviation* [190] abundantly elucidated in the literature referred to in this section. The Allan deviation algorithm and its overlapped version have been verified against the known 1000-point data set [182, 183, 190] obtained from a "good" random generator [192].

4.4.1 Experimental determination of the types of noise

In an effort to determine the types of noise in the clock signal (a set of data points at $P_z = 0$) we set up experiments that complement the previously described systems of non-condensed atoms, a two-component BEC and Rabi interferometry. Since the $\Delta f \big/ f$ figure was best for the quartz oscillator (OCXO), the experiments are carried out in the phase domain with the quartz OCXO. To eliminate the irrelevant perturbations we employ spin echo.

The experiment of Fig. 4.13 is performed with 3×10^4 non-condensed atoms in B_{magic} with trap frequencies $\omega_x = 2\pi{\times}97.6$ Hz, $\omega_y = 2\pi{\times}97.6$ Hz, $\omega_z = 2\pi{\times}11.96$ Hz. The data points are collected repeatedly with an interval of $T_{cycle} = 83$ s and an evolution time of $T = 200$ ms. Following the classification of the noise types in

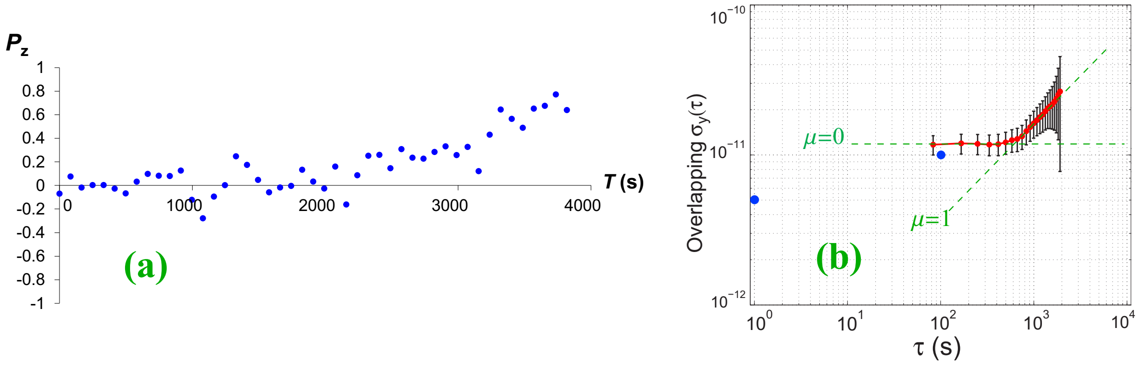

Figure 4.13: The clock zero-crossing signal (**blue dots** in **(a)**) and its overlapping Allan deviation $\sigma_y(\tau)$ in **(b)** of 3×10^4 non-condensed atoms in the phase-domain spin echo experiment with an oven-controlled quartz oscillator at evolution time $T = 200$ ms. According to the classification of noise types [190] we observe a flicker frequency noise plateau ($\mu = 0$) in $\sigma_y(\tau)$ (**red dots**), and a random walk frequency noise ($\mu = 1$) with practically no other contributions. The $\sigma_y(\tau)$ confidence band shows that the OCXO specifications (**blue dots** in **(b)**) allow to conclude that the atom clock stability is limited by the OCXO frequency instability in the range $\tau \gtrsim 7{\times}10^2$ s. The minimal stability achieved is $\min\{\sigma_y(\tau)\} = 1.18 \times 10^{-11} \pm 15\%$. The error bars are estimated as $\pm\sigma_y \big/ \sqrt{Y}$, where Y is the number of τ-bins used by the $\sigma_y(\tau)$ algorithm. The solid interconnecting lines are guides to the eye.

---

[14] We have compared the analysis performed with the original Allan deviation and the overlapped version. The conclusion about the impossibility to distinguish noise types is made on this ground.

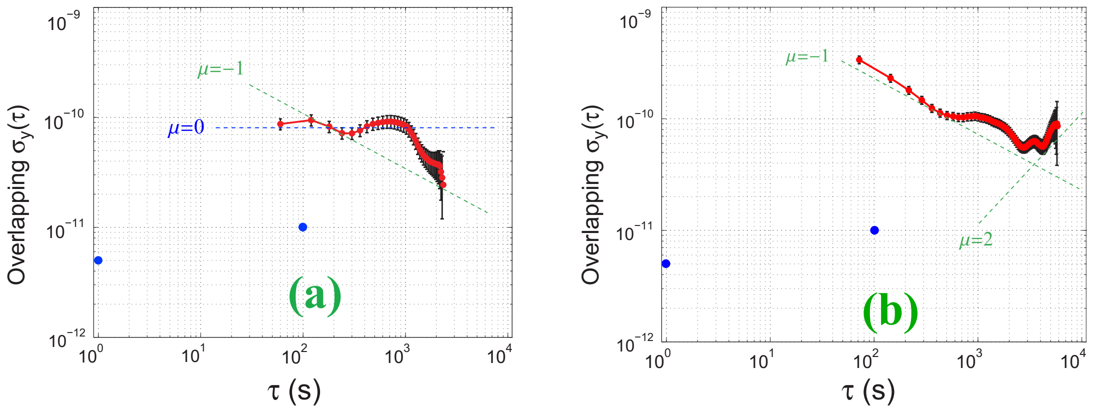

Figure 4.14: Overlapping Allan deviations $\sigma_y(\tau)$ of experiments with an oven-controlled quartz oscillator. The $\sigma_y(\tau)$ plot is given by the **red dots** with the interconnecting guides to the eye (**red solid** lines) with the error bars defined as $\pm\sigma_y \Big/ \sqrt{Y}$, where Y is the number of τ-bins used by the $\sigma_y(\tau)$ algorithm. The quartz oscillator specifications (**blue dots**).
(a) The phase-domain spin echo experiment: 1.5×10^5 *condensed* atoms are loaded at $T = 0$ and interrogated after $T = 20$ ms, and the data points are collected with a sampling period of $T_{cycle} = 60$ s. The $\sigma_y(\tau)$ reveals two contributions: white frequency noise with $\mu = -1$ (it cannot be $\mu = 0$ given by the **blue dashed** line because this level does not limit $\sigma_y(\tau)$) enveloped by the wavy vibrational modulation pattern [190] where the vibrations are circa in the mHz range. The OCXO frequency instability is below the minimum of $\sigma_y(\tau)$ implying that this experimental data does not reveal the atom clock limitations by the OCXO. The reliable minimum of $\sigma_y(\tau)$ amounts to $3.6 \times 10^{-11} \pm 38\%$ lying at the crossing with the extrapolated OCXO instability.
(b) Rabi oscillations: 3×10^4 *thermal* atoms are loaded at $T = 0$, and the data points are collected with a sampling period of $T_{cycle} = 72$ s after a single Rabi-pulse of $T = 1.6$-ms duration (this is approximately a $\pi/2$-pulse that sets P_z near the first zero-crossing). The $\sigma_y(\tau)$ reveals three contributions: white frequency noise with $\mu = -1$, frequency drift ($\mu = 2$), and the wavy vibrational modulation envelope [190] where the vibrations are circa in the mHz range. The minimum of $\sigma_y(\tau)$ amounts to $5.5 \times 10^{-11} \pm 11\%$. The OCXO limited stability is slightly worse than that of **(a)**.

[190], two slopes can be identified in the Fig. 4.13(b) analysis. At low τ, below $\approx 5 \times 10^2$ s, the plateau ($\mu = 0$) and the confidence band imply a flicker frequency noise. Above this range of τ the $\sigma_y^2(\tau)$ slope changes steeply to $\mu = 1$ indicating the dominance of random walk frequency noise. Comparing the overlapped OCXO specifications (blue dots in Fig. 4.13(b)) with the sigma-tau plot we may conclude that in the range $\tau > 7\times10^2$ s the atom clock is limited by instability of the OCXO. The standard errors for the error bars are computed from Poissonian statistics as $\pm\sigma_y \Big/ \sqrt{Y}$, where Y is the number of τ-bins obtained in the $\sigma_y(\tau)$ evaluation. The minimal absolute stability value obtained is $\min\{\sigma_y(\tau)\} = 1.18\times10^{-11} \pm 15\%$ which stays constant over a large range of τ.

Figure 4.14(a) is an example of a condensate system of initially 1.5×10^5 atoms with a negligible amount of thermal fraction, of the order of a few percent. The atoms are detected after an evolution time of $T = 20$ ms with a sampling period of $T_{cycle} = 60$ s. In this fast evolution in the unchanged trap configuration the condensate dynamics lead to a spatial separation of the condensate components $|1,-1\rangle$ and $|2,+1\rangle$. The phase destroying collisions are higher in the regions where the profile overlap is larger, but they are taken care of by the spin echo rephasing mechanism. However, condensation results in a more complex dependence of the phase uncertainty growth, resulting in a change of slope of the phase uncertainty graph, shown in Fig. 4.11 at $T = 1$ s, which also well fits the result of the Monte Carlo simulation [179]. There are two types of noise observed in the $\sigma_y(\tau)$ plot: the wavy vibrational modulation envelope [190] and white frequency noise with $\mu = -1$. The vibrations are in the mHz range. However tempting it may be to recognize a $\mu = 0$ given by the blue dashed line in Fig. 4.14(a), it is not correct because this level does not limit $\sigma_y(\tau)$ and the data points go well below this value for longer integration times. This is however consistent with the vibrational modulation pattern [190].

The Allan deviation analysis of Fig. 4.14(a) suggests that the clock stability $\sigma_y(\tau)$ is largely affected by condensation. This leaves the condensate clock with a minimal $\sigma_y(\tau) = 3.6 \times 10^{-11} \pm 38\%$, slightly above the non-condensed clock stability of Fig. 4.13 amounting to $1.18 \times 10^{-11} \pm 15\%$. In principle, it is possible to find some chemical species or their combinations which have a pair of hyperfine levels whose scattering lengths are more equal than in ^{87}Rb to avoid the appearance of the collective oscillations in the interferometry and alleviate the phase diffusion related to them. The reliable minimum of $\sigma_y(\tau) = 3.6 \times 10^{-11} \pm 38\%$ lies at the crossing with the extrapolated OCXO instability. To obtain this minimum the integration should be performed for an order of magnitude longer time than in the experiment of Fig. 4.13 with yet worse stability. In fact, the drift in Fig. 4.13(a) can be efficiently removed by subtracting the result of Savitzky-Golay filtering [193] from the P_z data points [128, 194]. However, this would not characterize the raw clock performance, but rather give an additional means of extracting data with better stability.

In Fig. 4.14(b) the Allan deviation analysis of the Rabi oscillations is presented. It is important to characterize this type of stability for either type of separated oscillatory field experiment, because the broadest spectral feature, the *Rabi pedestal*, has a different stability than that of the Ramsey spectral features modulating the Rabi pedestal (as shown in Fig. 4.1, see accompanying discussion).

Each data point in Fig. 4.14(b) is collected after a single $\pi/2$-pulse of 1.6-ms duration. The $\pi/2$-pulse sets P_z to the first zero-crossing. At $T = 0$ the number of thermal atoms in state $|1, -1\rangle$ is 3×10^4. The sampling period $T_{cycle} = 72$ s. The $\sigma_y(\tau)$ plot indicates three instability contributions: white frequency noise with the $\mu = -1$, frequency drift with $\sigma_y^2(\tau)$ slope $\mu = 2$, and the wavy vibrational modulation envelope [190]. The vibrations are estimated to be in the mHz range. The minimum of $\sigma_y(\tau)$ amounts to $5.5 \times 10^{-11} \pm 11\%$. The stability limited by the oven-controlled quartz oscillator is slightly worse than that of Fig. 4.14(a).

We do not know the origin of the vibrational modulation instability found in Fig. 4.13 and Fig. 4.14.

4.4.2 Miscellaneous instability contributions

Projective detection fundamentally limits the fractional frequency via the quantum projection noise as:

$$\left(\frac{\Delta f}{f}\right)_N = \frac{1}{2\pi T f V\sqrt{N}} \tag{4.12}$$

Apart from this, there is a contribution from magnetic field fluctuations that maximally amounts to a standard deviation of 15 mG as measured by a calibrated fluxgate magnetometer at the vacuum chamber along the quantization axis. Ambient magnetic noise is coupled to the clock transition via the residual second-order differential Zeeman shift (see Fig. 4.2(b) inset and Eq. 3.82) and is estimated as:

$$\Delta f_Z = 431.35 \cdot 0.015^2 = 97 \text{ mHz} \tag{4.13}$$

Atom number fluctuations translate into frequency fluctuations. The standard deviation σ_N amounting to 3% to 15% is then contributing to $\Delta f/f$ via the collisional shift [59, 95]:

$$\Delta f_c = \frac{2\hbar}{m}\left(a_{22} - a_{11}\right) \cdot \sigma_N n_0 \tag{4.14}$$

yielding from −27 mHz to −133 mHz at the maximal density used in experiments, where $n_0 = 2.3 \times 10^{12}$ cm^{-3} is the peak atomic density (maximal used).

Fluctuations in the total atom number N also contribute to $\Delta f/f$ directly via the change of a normalized observable quantity, e.g. P_z. It is estimated as [95]:

$$\Delta f_N = \frac{\sigma_N}{2\pi T V} \tag{4.15}$$

amounting to minimally 0.3 mHz at $T = 15$ s, $\sigma_N = 3\%$, and maximally to 2.38 Hz at $T = 10$ ms, $\sigma_N = 15\%$.

As another contribution to the Allan deviation we should assume that the quantizing field B_y can drift with time resulting in deviations indistinguishable from the oscillator instability in the Allan deviation plots. Since the drifts occur at very long integration times, it is important to understand that when both drifts, of the OCXO and of the magnetic field, are in the same direction for the duration of the data collection (all the points for a $\sigma_y(\tau)$ plot), they worsen the stability figure by shifting the $\sigma_y(\tau)$ plot above the limiting OCXO line. It is even more remarkable, that if the OCXO and magnetic field drifts are in opposite directions, the $\sigma_y(\tau)$ will lie *below* the OCXO figure (extrapolated to higher τ). Such behaviour is observed in Fig. 4.13(b) in a negligible form, but can often go well below the OCXO specifications. Of course, this is not a real stability. In this case the experimentally uncompensated magnetic field drift and the OCXO drift make the data set less representative, because the data is collected in a relatively short time. Sampling would need to be done that covers the characteristic times of such drifts.

4.5 Conclusion

In this chapter we have studied important aspects of the atom clock operation: the fractional frequency $\Delta f / f$, the phase stability expressed by the Allan deviation versus integration time $\sigma_y(\tau)$, miscellaneous contributions to the the fractional frequency (proportional to the phase uncertainty), $\Delta f / f$ in the condensate regime of operation with a two-component BEC and in the thermal atom regime showing both higher fractional frequency and higher stability. The experiments were conducted with Ramsey and spin echo sequences in the phase-domain.

The fractional frequency in the Ramsey interferometry on thermal atoms is shown to be $\Delta f / f = 1.16 \times 10^{-11}$, markedly different from the value for spin echo of 2.75×10^{-12}. In contrast, interferometry based on condensate atoms has on average a higher phase diffusion rate. Condensate produces a non-linear phase uncertainty growth compared to the linear dependence of the thermal ensemble. The condensate ^{87}Rb ground state system is perhaps not apt for clock applications because of its inherent highly-interacting nature and unequal scattering lengths $a_{11} \neq a_{22}$ giving rise to collective oscillations resulting in the modulation of the phase diffusion and the higher average phase uncertainty growth rate. This is confirmed by the spin echo experiment where the ensemble phase diffusion is removed by the spin echo phase reversal. In our trap configuration the latter leads to significant spatial cloud separation in less than 5 ms of Ramsey evolution. Also, our particular system of hyperfine levels results in highly unequal decays of the states because state $|2, +1\rangle$ has a significantly larger two-body decay. This leads to a lower visibility of Ramsey fringes which can be seen by solving Eqs. 3.60 or from an analysis of the loss dynamics (see Eqs. 3.33 and their solutions).

The *overlapped Allan deviation* analysis is accomplished for three cases: the spin echo interferometry with thermal atoms, with a condensate and for the Rabi oscillations of thermal atoms. The Rabi oscillations analysis gives a figure on how stable the *Rabi pedestal* in the Ramsey spectrum is: the Rabi pedestal has different stability to that of the Ramsey spectral features and should be characterized separately. We observe a comparable stability, attaining $\sigma_y(\tau) =$

$1.18 \times 10^{-11} \pm 15\%$, in thermal atoms with that of a condensate system amounting to $\sigma_y(\tau) = 3.6{\times}10^{-11}{\pm}38\%$, but the latter requires an approximately 25 times longer integration time. The Rabi oscillations show a minimal stability of $5.5{\times}10^{-11}{\pm}11\%$.

Along with the determination of the lowest $\sigma_y(\tau)$ values, the overlapped Allan deviation offers the possibility to identify the types of noise present in the atom clock. This is a virtue of the *overlapped* version that results in a narrow confidence band for relatively small data sets. The identified noise types are different for the three experiments. The spin echo interferometry on thermal atoms (Fig. 4.13) shows a $\sigma_y^2(\tau)$ slope of zero and a slope of one in the $\sigma_y(\tau)$ graph, testifying to the presence of flicker frequency noise and random walk frequency noise, coinciding with the trajectory of the extrapolated OCXO specifications. The spin echo interferometry with condensate atoms (Fig. 4.14(a)) shows white frequency noise ($\sigma_y^2(\tau)$ slope of -1) and the wavy vibrational modulation pattern with frequency in the mHz range. It also does not continue decreasing below the extrapolated OCXO specifications line. In the experiment with the Rabi pulse (Fig. 4.14(b)), the Allan variance $\sigma_y^2(\tau)$ has a slope of -1 (white frequency noise), $\mu = 2$ (frequency drift) and vibrational modulation envelope with vibrations in the mHz range.

Chapter 5

Conclusions and future directions

In this thesis we have presented a number of analytical means for the analysis of the evolution of trapped cold-atom interferometry, encompassing in the models the off-resonant and on-resonant regimes of operation and treating separately the case of one-body losses and many-body losses. We phenomenologically included pure dephasing rates for the analysis of cumulative dephasing processes not related to population loss. Emphasis was placed on many-body population losses and the ensuing dephasings, since they play an increasing role in the area of atom clocks.

The trapped ground states involved in the interferometry of ^{87}Rb atoms have a large inequality in the population decays resulting in the loss of interferometric contrast. We introduced a merit function for such a type of contrast loss. Within the framework of the recent experiments where a long coherence time on the scale of a minute has been demonstrated in a trapped atom clock [56], at least two-body processes should be included in the interferometry model to appropriately account for corresponding visibility loss. Interferometry with such losses leads to a more complex envelope function of the fringe visibility than in the case of one-body losses. We have also discussed the possibility of mixing the numerical computation of the many-body fringe envelope function and the analytical envelope induced by trapping effects.

In the experimental discussions we have presented the atom clock performance figures in all the relevant regimes of operation: with condensate and thermal cloud ensembles, in phase-domain Ramsey and spin echo interferometries, with synchronization from a rubidium frequency standard and from an oven-controlled quartz oscillator, and with and without the number fluctuation correction. These results allowed us to identify the types of noise present in the system by performing an Allan deviation analysis. A comparison of the condensate and thermal cloud experiments has revealed that the difference in stability is reasonably small despite the 50 times different cloud densities.

It was identified that the atom clock stability is limited by the oven-controlled quartz oscillator (OCXO), the best reference we have had. A better stability can be achieved by replacing it with an oscillator with better stability in terms of both the Allan deviation $\sigma_y(\tau)$ and the fractional frequency $\Delta f / f$.

There are more advanced techniques than the Hahn spin echo that we have been using. Instead, dynamic decoupling pulse sequences can be used to substantially suppress the effect of ensemble dephasing [67, 68] mainly caused by cold atomic collisions. A limiting case of such sequences is the so called *spin locking* which is implemented with ultra-short pulses that rephase the ensemble spin so quickly that it virtually stops rephasing. Almost an order of magnitude of improvement in coherence time has been demonstrated by the application of the spin locking technique and the maximum possible coherence time was achieved [69].

Combined with the radiofrequency shift measurements, carried out by the author but not included in the thesis, additional experiments can be set up to demonstrate the possibility of accessing σ^+ or σ^- polarizations of the radiofrequency interrogation field by measuring the Bloch-Siegert shift sensitive to the sign of the detuning.

The accuracy of experiments conducted on an atom chip crucially depend on the wave matching of radiofrequency and microwave signals to it. A new atom chip can be developed that delivers AC power to the atom chip without reflections and with accurate control over spatial modes of the guided AC fields.

Bibliography

[1] T. W. Hänsch. Nobel Lecture: Passion for precision. *Reviews of Modern Physics* **78**(4), 1297–1309 (2006) (cited on p. 15).
doi: `10.1103/RevModPhys.78.1297`

[2] J. Dalibard and C. Cohen-Tannoudji. Laser cooling below the Doppler limit by polarization gradients: simple theoretical models. *Journal of the Optical Society of America B* **6**(11), 2023 (1989) (cited on pp. 15, 30, 39, 151, 152).
doi: `10.1364/JOSAB.6.002023`

[3] S. Chu. Nobel Lecture: The manipulation of neutral particles. *Reviews of Modern Physics* **70**(3), 685–706 (1998) (cited on p. 15).
doi: `10.1103/RevModPhys.70.685`

[4] C. Cohen-Tannoudji. Nobel Lecture: Manipulating atoms with photons. *Reviews of Modern Physics* **70**(3), 707–719 (1998) (cited on p. 15).
doi: `10.1103/RevModPhys.70.707`

[5] W. D. Phillips. Nobel Lecture: Laser cooling and trapping of neutral atoms. *Reviews of Modern Physics* **70**(3), 721–741 (1998) (cited on pp. 15, 151).
doi: `10.1103/RevModPhys.70.721`

[6] T. W. Hänsch and A. L. Schawlow. Cooling of gases by laser radiation. *Optics Communications* **13**(1), 68–69 (1975) (cited on p. 15).
doi: `10.1016/0030-4018(75)90159-5`

[7] W. D. Phillips, P. L. Gould, and P. D. Lett. Cooling, stopping, and trapping atoms. *Science (New York, N.Y.)* **239**(4842), 877–883 (1988) (cited on pp. 15, 151).
doi: `10.1126/science.239.4842.877`

[8] W. Ketterle. Nobel lecture: When atoms behave as waves: Bose-Einstein condensation and the atom laser. *Reviews of Modern Physics* **74**(4), 1131–1151 (2002) (cited on p. 15).
doi: `10.1103/RevModPhys.74.1131`

[9] E. A. Cornell and C. E. Wieman. Nobel Lecture: Bose-Einstein condensation in a dilute gas, the first 70 years and some recent experiments. *Reviews of Modern Physics* **74**(3), 875–893 (2002) (cited on p. 15).
doi: `10.1103/RevModPhys.74.875`

[10] S. N. Bose. Plancks Gesetz und Lichtquantenhypothese. *Zeitschrift für Physik A Hadrons and Nuclei* **26**(1), 178–181 (1924) (cited on p. 15).
doi: `10.1007/BF01327326`

[11] S. N. Bose. The beginning of quantum statistics: A translation of "Planck's law and the light quantum hypothesis". *American Journal of Physics* **44**(11), 1056 (1976) (cited on p. 15).
doi: `10.1119/1.10584`

[12] A. Einstein. Quantentheorie des einatomigen idealen Gases. In: *Sitzungsberichte der Preußischen Akademie der Wissenschaften (Berlin), Physikalisch-mathematische Klasse*. 1924, pp. 261–267 (cited on p. 15).
doi: `10.1002/3527608958.ch27`

[13] A. Einstein. Zur Quantentheorie des idealen Gases. In: *Sitzungsberichte der Preußischen Akademie der Wissenschaften (Berlin), Physikalisch-mathematische Klasse*. 1925, pp. 18–25 (cited on p. 15).
doi: `10.1002/3527608958.ch29`

[14] A. Einstein. Quantentheorie des einatomigen idealen Gases. Zweite Abhandlung. In: *Sitzungsberichte der Preußischen Akademie der Wissenschaften (Berlin), Physikalisch-mathematische Klasse*. 1925, pp. 3–14 (cited on p. 15).
doi: `10.1002/3527608958.ch28`

[15] D. Simon, ed. Albert Einstein: Akademie-Vorträge: Sitzungsberichte der Preußischen Akademie der Wissenschaften 1914-1932. Wiley-VCH Verlag GmbH & Co. KGaA, Weinheim, 2006. isbn: 9783527608959 (cited on p. 15).
doi: `10.1002/3527608958`

[16] T. W. Hänsch, I. S. Shahin, and A. L. Schawlow. Optical Resolution of the Lamb Shift in Atomic Hydrogen by Laser Saturation Spectroscopy. *Nature Physical Science* **235**, 63–65 (1972) (cited on p. 15).
doi: `10.1038/physci235063a0`

[17] A. L. Schawlow. Lasers, light, and matter. *Journal of the Optical Society of America* **67**(2), 140 (1977) (cited on pp. 15, 23).
doi: `10.1364/JOSA.67.000140`

[18] A. L. Schawlow. Spectroscopy in a new light. *Reviews of Modern Physics* **54**(3), 697–707 (1982) (cited on pp. 15, 23).
doi: `10.1103/RevModPhys.54.697`

[19] I. I. Rabi, S. Millman, P. Kusch, and J. R. Zacharias. The Molecular Beam Resonance Method for Measuring Nuclear Magnetic Moments. The Magnetic Moments of ${}_3\mathrm{Li}^6$, ${}_3\mathrm{Li}^7$ and ${}_9\mathrm{F}^{19*}$. *Physical Review* **55**(6), 526–535 (1939) (cited on pp. 15, 51).
doi: `10.1103/PhysRev.55.526`

[20] N. F. Ramsey. A New Molecular Beam Resonance Method. *Physical Review* **76**(7), 996 (1949) (cited on pp. 15, 16, 51).
doi: `10.1103/PhysRev.76.996`

[21] N. F. Ramsey. Experiments with separated oscillatory fields and hydrogen masers. *Reviews of Modern Physics* **62**(3), 541–552 (1990) (cited on pp. 15, 51).
doi: `10.1103/RevModPhys.62.541`

[22] H. Lyons. Spectral lines as frequency standards. *Annals of the New York Academy of Sciences* **55**, 831–871 (1952) (cited on p. 15).
doi: `10.1111/j.1749-6632.1952.tb26600.x`

[23] L. Essen and J. V. L. Parry. An Atomic Standard of Frequency and Time Interval: A Cæsium Resonator. *Nature* **176**(4476), 280–282 (1955) (cited on p. 15).
doi: `10.1038/176280a0`

[24] N. F. Ramsey. History of atomic clocks. *Journal of Research of the National Bureau of Standards* **88**(5), 301–320 (1983) (cited on p. 15).

[25] M. Vengalattore, J. M. Higbie, S. R. Leslie, J. Guzman, L. E. Sadler, and D. M. Stamper-Kurn. High-Resolution Magnetometry with a Spinor Bose-Einstein Condensate. *Physical Review Letters* **98**(20), 200801 (2007) (cited on p. 15).
doi: `10.1103/PhysRevLett.98.200801`

[26] D. E. Pritchard. Cooling Neutral Atoms in a Magnetic Trap for Precision Spectroscopy. *Physical Review Letters* **51**(15), 1336–1339 (1983) (cited on p. 15).
doi: `10.1103/PhysRevLett.51.1336`

[27] A. Peters, K. Y. Chung, and S. Chu. High-precision gravity measurements using atom interferometry. *Metrologia* **38**(1), 25–61 (2001) (cited on p. 15).
doi: `10.1088/0026-1394/38/1/4`

[28] M. Snadden, J. M. McGuirk, P. Bouyer, K. Haritos, and M. A. Kasevich. Measurement of the Earth's Gravity Gradient with an Atom Interferometer-Based Gravity Gradiometer. *Physical Review Letters* **81**(5), 971–974 (1998) (cited on p. 15).
doi: `10.1103/PhysRevLett.81.971`

[29] T. L. Gustavson, P. Bouyer, and M. A. Kasevich. Precision Rotation Measurements with an Atom Interferometer Gyroscope. *Physical Review Letters* **78**(11), 2046–2049 (1997) (cited on p. 15).
doi: `10.1103/PhysRevLett.78.2046`

[30] J. M. Hensley, A. Wicht, B. C. Young, and S. Chu. Progress towards a measurement of $\hbar/M_{\mathrm{Cs}}$. In: *AIP Conference Proceedings, Volume 551*. Vol. 551. AIP, 2001, pp. 43–57 (cited on p. 15).
doi: `10.1063/1.1354338`

[31] S. Chu. Cold atoms and quantum control. *Nature* **416**(6877), 206–210 (2002) (cited on p. 15).
doi: `10.1038/416206a`

[32] D. Lau, A. I. Sidorov, G. Opat, R. McLean, W. Rowlands, and P. Hannaford. Reflection of cold atoms from an array of current-carrying wires. *The European Physical Journal D - Atomic, Molecular and Optical Physics* **5**(2), 193–199 (1999) (cited on pp. 15, 36).
doi: `10.1007/s100530050244`

[33] M. Drndić, G. Zabow, C. Lee, J. Thywissen, K. Johnson, M. Prentiss, R. Westervelt, P. Featonby, V. Savalli, L. Cognet, K. Helmerson, N. Westbrook, C. I. Westbrook, W. D. Phillips, and A. Aspect. Properties of microelectromagnet mirrors as reflectors of cold Rb atoms. *Physical Review A* **60**(5), 4012–4015 (1999) (cited on pp. 15, 36).
doi: `10.1103/PhysRevA.60.4012`

[34] J. Fortágh and C. Zimmermann. Magnetic microtraps for ultracold atoms. *Reviews of Modern Physics* **79**(1), 235–289 (2007) (cited on p. 15).
doi: `10.1103/RevModPhys.79.235`

[35] S. Hofferberth, B. Fischer, T. Schumm, J. Schmiedmayer, and I. Lesanovsky. Ultracold atoms in radio-frequency dressed potentials beyond the rotating-wave approximation. *Physical Review A* **76**(1), 013401 (2007) (cited on p. 15).
doi: `10.1103/PhysRevA.76.013401`
arXiv: `quant-ph/0611240`

[36] J. Reichel. Microchip traps and Bose-Einstein condensation. *Applied Physics B: Lasers and Optics* **74**(6), 469–487 (2002) (cited on p. 15).
doi: `10.1007/s003400200861`

[37] B. Lev. Fabrication of micro-magnetic traps for cold neutral atoms. *Quantum Information & Computation* **3**(5), 450–464 (2003) (cited on p. 15).
arXiv: `quant-ph/0305067`

[38] P. Treutlein, T. Steinmetz, Y. Colombe, B. Lev, P. Hommelhoff, J. Reichel, M. Greiner, O. Mandel, A. Widera, T. Rom, I. Bloch, and T. W. Hänsch. Quantum information processing in optical lattices and magnetic microtraps. *Fortschritte der Physik* **54**(8-10), 702–718 (2006) (cited on p. 15).
doi: `10.1002/prop.200610325`
arXiv: `quant-ph/0605163`

[39] G.-B. Jo, Y. Shin, S. Will, T. Pasquini, M. Saba, W. Ketterle, D. E. Pritchard, M. Vengalattore, and M. Prentiss. Long Phase Coherence Time and Number Squeezing of Two Bose-Einstein Condensates on an Atom Chip. *Physical Review Letters* **98**(3), 98–101 (2007) (cited on p. 15).
doi: `10.1103/PhysRevLett.98.030407`

[40] T. Schumm, S. Hofferberth, L. M. Andersson, S. Wildermuth, S. Groth, I. Bar-Joseph, J. Schmiedmayer, and P. Krüger. Matter-wave interferometry in a double well on an atom chip. *Nature Physics* **1**(1), 57–62 (2005) (cited on p. 15).
doi: `10.1038/nphys125`

[41] T. V. Tscherbul, T. Calarco, I. Lesanovsky, R. V. Krems, A. Dalgarno, and J. Schmiedmayer. rf-field-induced Feshbach resonances. *Physical Review A* **81**(5), 050701 (2010) (cited on p. 15).
doi: `10.1103/PhysRevA.81.050701`
arXiv: `1001.1004v2`

[42] J. Grond, U. Hohenester, I. Mazets, and J. Schmiedmayer. Atom interferometry with trapped Bose–Einstein condensates: impact of atom–atom interactions. *New Journal of Physics* **12**(6), 065036 (2010) (cited on p. 15).
doi: `10.1088/1367-2630/12/6/065036`
arXiv: `1002.0265`

[43] T. van Zoest et al. Bose-Einstein condensation in microgravity. *Science (New York, N.Y.)* **328**(5985), 1540 (2010) (cited on p. 15).
doi: `10.1126/science.1189164`

[44] M. Jones, C. J. Vale, D. Sahagun, B. V. Hall, and E. Hinds. Spin Coupling between Cold Atoms and the Thermal Fluctuations of a Metal Surface. *Physical Review Letters* **91**(8), 080401 (2003) (cited on p. 15).
doi: `10.1103/PhysRevLett.91.080401`

[45] D. Gallego, S. Hofferberth, T. Schumm, P. Krüger, and J. Schmiedmayer. Optical lattice on an atom chip. *Optics letters* **34**(22), 3463 (2009) (cited on p. 15).
doi: `10.1364/OL.34.003463`
arXiv: `0905.2207`

[46] I. Teper, Y.-J. Lin, and V. Vuletić. Resonator-Aided Single-Atom Detection on a Microfabricated Chip. *Physical Review Letters* **97**(2), 023002 (2006) (cited on p. 15).
doi: `10.1103/PhysRevLett.97.023002`
arXiv: `cond-mat/0603675`

[47] P. Böhi, M. F. Riedel, J. Hoffrogge, J. Reichel, T. W. Hänsch, and P. Treutlein. Coherent manipulation of Bose–Einstein condensates with state-dependent microwave potentials on an atom chip. *Nature Physics* **5**(8), 592–597 (2009) (cited on p. 15).
doi: `10.1038/nphys1329`
arXiv: `0904.4837`

[48] Y. Colombe, T. Steinmetz, G. Dubois, F. Linke, D. Hunger, and J. Reichel. Strong atom-field coupling for Bose-Einstein condensates in an optical cavity on a chip. *Nature* **450**(7167), 272–277 (2007) (cited on p. 15).
doi: `10.1038/nature06331`

[49] S. Pollock, J. P. Cotter, A. Laliotis, and E. A. Hinds. Integrated magneto-optical traps on a chip using silicon pyramid structures. *Optics Express* **17**(16), 14109 (2009) (cited on p. 15).
doi: `10.1364/OE.17.014109`

[50] T. Steinmetz, Y. Colombe, D. Hunger, T. W. Hänsch, A. Balocchi, R. J. Warburton, and J. Reichel. Stable fiber-based Fabry-Pérot cavity. *Applied Physics Letters* **89**(11), 111110 (2006) (cited on p. 15).
doi: `10.1063/1.2347892`

[51] I. Lesanovsky, T. Schumm, S. Hofferberth, L. Andersson, P. Krüger, and J. Schmiedmayer. Adiabatic radio-frequency potentials for the coherent ma-

nipulation of matter waves. *Physical Review A* **73**(3), 033619 (2006) (cited on p. 15).
doi: `10.1103/PhysRevA.73.033619`
arXiv: `physics/0510076`

[52] P. Böhi, M. F. Riedel, T. W. Hänsch, and P. Treutlein. Imaging of microwave fields using ultracold atoms. *Applied Physics Letters* **97**(5), 051101 (2010) (cited on p. 15).
doi: `10.1063/1.3470591`
arXiv: `1009.4651`

[53] I. Herrera, J. Petrovic, P. Lombardi, L. Consolino, S. Bartallini, and F. S. Cataliotti. Degenerate quantum gases manipulation on AtomChips. *Physica Scripta* **T149**, 014002 (2012) (cited on p. 15).
doi: `10.1088/0031-8949/2012/T149/014002`

[54] J. Grond, U. Hohenester, J. Schmiedmayer, and A. Smerzi. Mach-Zehnder interferometry with interacting trapped Bose-Einstein condensates. *Physical Review A* **84**(2), 023619 (2011) (cited on p. 15).
doi: `10.1103/PhysRevA.84.023619`
arXiv: `1010.3273`

[55] P. Rosenbusch. Magnetically trapped atoms for compact atomic clocks. *Applied Physics B* **95**(2), 227–235 (2009) (cited on pp. 15, 45, 83, 86, 88, 91, 92, 98).
doi: `10.1007/s00340-009-3451-x`

[56] C. Deutsch, F. Ramírez-Martínez, C. Lacroûte, F. Reinhard, T. Schneider, J.-N. Fuchs, F. Piéchon, F. Laloë, J. Reichel, and P. Rosenbusch. Spin Self-Rephasing and Very Long Coherence Times in a Trapped Atomic Ensemble. *Physical Review Letters* **105**(2), 020401 (2010) (cited on pp. 16, 88, 89, 91, 92, 109, 123).
doi: `10.1103/PhysRevLett.105.020401`
arXiv: `1003.5925`

[57] W. Maineult, C. Deutsch, K. Gibble, J. Reichel, and P. Rosenbusch. Spin Waves and Collisional Frequency Shifts of a Trapped-Atom Clock. *Physical Review Letters* **109**(2), 020407 (2012) (cited on pp. 16, 88, 92).
doi: `10.1103/PhysRevLett.109.020407`
arXiv: `1204.1150`

[58] G. Kleine Büning, J. Will, W. Ertmer, E. Rasel, J. Arlt, C. Klempt, F. Ramírez-Martínez, F. Piéchon, and P. Rosenbusch. Extended Coherence

Time on the Clock Transition of Optically Trapped Rubidium. *Physical Review Letters* **106**(24), 240801 (2011) (cited on pp. 16, 88, 92).
doi: `10.1103/PhysRevLett.106.240801`
arXiv: `1103.2283`

[59] D. M. Harber, H. J. Lewandowski, J. M. McGuirk, and E. A. Cornell. Effect of cold collisions on spin coherence and resonance shifts in a magnetically trapped ultracold gas. *Physical Review A* **66**(5), 053616 (2002) (cited on pp. 16, 90, 98, 120).
doi: `10.1103/PhysRevA.66.053616`

[60] M. Jack. Decoherence due to Three-Body Loss and its Effect on the State of a Bose-Einstein Condensate. *Physical Review Letters* **89**(14), 140402 (2002) (cited on p. 17).
doi: `10.1103/PhysRevLett.89.140402`
arXiv: `cond-mat/0208319`

[61] M. Jack and M. Yamashita. Signatures of the quantum fluctuations of cold atoms in an optical lattice in the three-body loss rate. *Physical Review A* **67**(3), 033605 (2003) (cited on p. 17).
doi: `10.1103/PhysRevA.67.033605`

[62] J. Söding, D. Guéry-Odelin, P. Desbiolles, F. Chevy, H. Inamori, and J. Dalibard. Three-body decay of a rubidium Bose-Einstein condensate. *Applied Physics B: Lasers and Optics* **69**(4), 257–261 (1999) (cited on p. 17).
doi: `10.1007/s003400050805`

[63] S. Whitlock, C. F. Ockeloen, and R. J. C. Spreeuw. Sub-Poissonian Atom-Number Fluctuations by Three-Body Loss in Mesoscopic Ensembles. *Physical Review Letters* **104**(12), 120402 (2010) (cited on p. 17).
doi: `10.1103/PhysRevLett.104.120402`
arXiv: `0911.4420`

[64] K. Mertes, J. Merrill, R. Carretero-González, D. Frantzeskakis, P. Kevrekidis, and D. S. Hall. Nonequilibrium Dynamics and Superfluid Ring Excitations in Binary Bose-Einstein Condensates. *Physical Review Letters* **99**(19), 190402 (2007) (cited on pp. 17, 67, 102, 103).
doi: `10.1103/PhysRevLett.99.190402`

[65] E. Burt, R. Ghrist, C. Myatt, M. Holland, E. A. Cornell, and C. E. Wieman. Coherence, Correlations, and Collisions: What One Learns about Bose-Einstein Condensates from Their Decay. *Physical Review Letters* **79**(3), 337–340 (1997) (cited on pp. 17, 67, 70, 80).
doi: `10.1103/PhysRevLett.79.337`

[66] E. L. Hahn. Spin Echoes. *Physical Review* **80**(4), 580–594 (1950) (cited on p. 17).
doi: `10.1103/PhysRev.80.580`

[67] G. S. Uhrig. Keeping a Quantum Bit Alive by Optimized π-Pulse Sequences. *Physical Review Letters* **98**(10), 100504 (2007) (cited on pp. 17, 124).
doi: `10.1103/PhysRevLett.98.100504`

[68] Y. Sagi, I. Almog, and N. Davidson. Process Tomography of Dynamical Decoupling in a Dense Cold Atomic Ensemble. *Physical Review Letters* **105**(5), 053201 (2010) (cited on pp. 17, 124).
doi: `10.1103/PhysRevLett.105.053201`
arXiv: `1004.1011`

[69] B. Naydenov, F. Dolde, L. Hall, C. Shin, H. Fedder, L. Hollenberg, F. Jelezko, and J. Wrachtrup. Dynamical decoupling of a single-electron spin at room temperature. *Physical Review B* **83**(8), 081201 (2011) (cited on pp. 17, 124).
doi: `10.1103/PhysRevB.83.081201`

[70] R. P. Anderson, C. Ticknor, A. I. Sidorov, and B. V. Hall. Spatially inhomogeneous phase evolution of a two-component Bose-Einstein condensate. *Physical Review A* **80**(2), 023603 (2009) (cited on pp. 17, 48).
doi: `10.1103/PhysRevA.80.023603`

[71] S. Whitlock. Bose-Einstein condensates on a magnetic film atom chip. PhD Thesis. Swinburne University of Technology, 2007 (cited on pp. 19, 40, 73).

[72] R. P. Anderson. Nonequilibrium dynamics and relative phase evolution of two-component Bose-Einstein condensates. PhD Thesis. Swinburne University of Technology, 2009 (cited on pp. 19, 25, 40, 41, 48, 99).

[73] C. E. Wieman and T. W. Hänsch. Doppler-Free Laser Polarization Spectroscopy. *Physical Review Letters* **36**(20), 1170–1173 (1976) (cited on pp. 22, 25, 28).
doi: `10.1103/PhysRevLett.36.1170`

[74] M. Harris, C. S. Adams, S. L. Cornish, I. McLeod, E. Tarleton, and I. G. Hughes. Polarization spectroscopy in rubidium and cesium. *Physical Review A* **73**(6), 062509 (2006) (cited on pp. 22, 25, 28).
doi: `10.1103/PhysRevA.73.062509`

[75] J. Guéna, P. Jacquier, M. Lintz, L. Pottier, M. A. Bouchiat, and A. Hrisoho. Reaching the shot noise limit in the polarization measurement of individual nanosecond light pulses. *Optics Communications* **71**(1-2), 6–10 (1989) (cited on p. 22).
doi: `10.1016/0030-4018(89)90293-9`

[76] Y. Yoshikawa, T. Umeki, T. Mukae, Y. Torii, and T. Kuga. Frequency Stabilization of a Laser Diode with Use of Light-Induced Birefringence in an Atomic Vapor. *Applied Optics* **42**(33), 6645 (2003) (cited on p. 23).
doi: `10.1364/AO.42.006645`

[77] C. P. Pearman, C. S. Adams, S. G. Cox, P. F. Griffin, D. A. Smith, and I. G. Hughes. Polarization spectroscopy of a closed atomic transition: applications to laser frequency locking. *Journal of Physics B: Atomic, Molecular and Optical Physics* **35**(24), 5141–5151 (2002) (cited on p. 23).
doi: `10.1088/0953-4075/35/24/315`

[78] K. B. MacAdam. A narrow-band tunable diode laser system with grating feedback, and a saturated absorption spectrometer for Cs and Rb. *American Journal of Physics* **60**(12), 1098 (1992) (cited on p. 23).
doi: `10.1119/1.16955`

[79] C. J. Hawthorn, K. P. Weber, and R. E. Scholten. Littrow configuration tunable external cavity diode laser with fixed direction output beam. *Review of Scientific Instruments* **72**(12), 4477 (2001) (cited on p. 24).
doi: `10.1063/1.1419217`

[80] A. Kastler. Quelques suggestions concernant la production optique et la détection optique d'une inégalité de population des niveaux de quantifigation spatiale des atomes. Application à l'expérience de Stern et Gerlach et à la résonance magnétique. *Journal de Physique et le Radium* **11**(6), 255–265 (1950) (cited on p. 25).
doi: `10.1051/jphysrad:01950001106025500`

[81] C. Cohen-Tannoudji and A. Kastler. Optical pumping. In: *Progress in Optics, Volume V*. Ed. by E. Wolf. Amsterdam: North-Holland, 1966 (cited on p. 25).

[82] D. Suter. The Physics of Laser-Atom Interactions. Cambridge University Press, 2005. isbn: 9780521017916 (cited on p. 25).

[83] A. Kastler. Optical methods for studying hertzian resonances. *Science (New York, N.Y.)* **158**(3798), 214–221 (1967) (cited on p. 25).
doi: `10.1126/science.158.3798.214`

[84] P. D. Lett, R. N. Watts, C. I. Westbrook, W. D. Phillips, P. L. Gould, and H. J. Metcalf. Observation of atoms laser cooled below the doppler limit. *Physical Review Letters* **61**(2), 169–172 (1988) (cited on pp. 30, 40, 152).
doi: `10.1103/PhysRevLett.61.169`

[85] T. Bergeman, G. Erez, and H. J. Metcalf. Magnetostatic trapping fields for neutral atoms. *Physical Review A* **35**(4), 1535–1546 (1987) (cited on p. 34).
doi: `10.1103/PhysRevA.35.1535`

[86] A. Migdall, J. Prodan, W. D. Phillips, T. Bergeman, and H. J. Metcalf. First Observation of Magnetically Trapped Neutral Atoms. *Physical Review Letters* **54**(24), 2596–2599 (1985) (cited on p. 34).
doi: `10.1103/PhysRevLett.54.2596`

[87] S. J. Hellier. Alkali metal vapor generator. United States Patent 4195891. 1980 (cited on p. 38).

[88] J. Fortágh, A. Grossmann, T. W. Hänsch, and C. Zimmermann. Fast loading of a magneto-optical trap from a pulsed thermal source. *Journal of Applied Physics* **84**(12), 6499 (1998) (cited on p. 39).
doi: `10.1063/1.369018`

[89] G. Breit and I. I. Rabi. Measurement of Nuclear Spin. *Physical Review* **38**(11), 2082–2083 (1931) (cited on pp. 45, 98).
doi: `10.1103/PhysRev.38.2082.2`

[90] F. Gerbier, P. Bouyer, and A. Aspect. Quasicontinuous Atom Laser in the Presence of Gravity. *Physical Review Letters* **86**(21), 4729–4732 (2001) (cited on p. 45).
doi: `10.1103/PhysRevLett.86.4729`

[91] R. Gerritsma. Permanent magnetic atom chips and Bose-Einstein condensation. PhD Thesis. University of Amsterdam, 2007 (cited on p. 45).

[92] W. Ketterle, D. S. Durfee, and D. M. Stamper-Kurn. Making, probing and understanding Bose-Einstein condensates. In: *Bose-Einstein condensation in atomic gases, Proceedings of the International School of Physics "Enrico Fermi", Course CXL*. Ed. by M. Inguscio, S. Stringari, and C. E. Wieman. IOS Press, Amsterdam, 1999, pp. 67–176 (cited on p. 45).
arXiv: `cond-mat/9904034`

[93] D. S. Durfee. Dynamic Properties of Dilute Bose-Einstein Condensates. PhD Thesis. Massachusetts Institute of Technology, 1999 (cited on p. 45).

[94] D. A. Smith, S. Aigner, S. Hofferberth, M. Gring, M. Andersson, S. Wildermuth, P. Krüger, S. Schneider, T. Schumm, and J. Schmiedmayer. Absorption imaging of ultracold atoms on atom chips. *Optics express* **19**(9), 8471–8485 (2011) (cited on p. 45).
doi: `10.1364/OE.19.008471`
arXiv: `1101.4206`

[95] P. Treutlein. Coherent manipulation of ultracold atoms on atom chips. PhD Thesis. Ludwig-Maximilians-Universität München, 2008 (cited on pp. 45, 52, 104, 116, 120).

[96] R. Loudon. The Quantum Theory of Light. 3rd ed. Oxford Science Publications. Oxford University Press, USA, 2000. isbn: 9780198501763 (cited on p. 46).

[97] D. A. Steck. Rubidium 87 D Line Data. Tech. rep. Oregon Center for Optics and Department of Physics, University of Oregon, 2010 (cited on pp. 46, 47).

[98] H. J. Metcalf and P. van der Straten. Laser cooling and trapping. Graduate Texts in Contemporary Physics. Springer, 1999. isbn: 9780387987286 (cited on pp. 46, 47).

[99] K. Blum. Density Matrix Theory and Applications. 2nd ed. Physics of Atoms and Molecules. Springer, 1996. isbn: 9780306453410 (cited on pp. 46, 57).

[100] G. Reinaudi, T. Lahaye, Z. Wang, and D. Guéry-Odelin. Strong saturation absorption imaging of dense clouds of ultracold atoms. *Optics Letters* **32**(21), 3143 (2007) (cited on p. 48).
doi: `10.1364/OL.32.003143`
arXiv: `0707.2930`

[101] J. M. Kinast. Thermodynamics and Superfluidity of a Strongly Interacting Fermi gas. PhD Thesis. Duke University, 2006 (cited on p. 48).

[102] C. F. Ockeloen, A. Tauschinsky, R. J. C. Spreeuw, and S. Whitlock. Detection of small atom numbers through image processing. *Physical Review A* **82**(6), 061606 (2010) (cited on p. 48).
doi: `10.1103/PhysRevA.82.061606`
arXiv: `1007.2136`

[103] M. Erhard. Experimente mit mehrkomponentigen Bose-Einstein-Kondensaten. PhD thesis. Universität Hamburg, 2004 (cited on p. 48).

[104] J. Kronjäger. Coherent Dynamics of Spinor Bose-Einstein Condensates. PhD Thesis. Hamburg University, 2007 (cited on p. 48).

[105] A. R. Griesmaier. Dipole-dipole interaction in a degenerate quantum gas Bose-Einstein condensation of chromium atoms. PhD thesis. Universität Stuttgart, 2007 (cited on p. 48).

[106] X. Li, M. Ke, B. Yan, and Y. Wang. Reduction of interference fringes in absorption imaging of cold atom cloud using eigenface method. *Chinese Optics Letters* **5**(3), 128–130 (2007) (cited on p. 48).

[107] W. Gerlach and O. Stern. Das magnetische Moment des Silberatoms. *Zeitschrift für Physik A Hadrons and Nuclei* **9**(1), 353–355 (1922) (cited on p. 48).
doi: `10.1007/BF01326984`

[108] M. H. T. Extavour. Fermions and bosons on an atom chip. PhD Thesis. University of Toronto (Canada), 2009. isbn: 9780494609507 (cited on p. 50).

[109] S. Hofferberth. Coherent manipulation of Bose-Einstein condensates with radio-frequency adiabatic potentials on atom chips. PhD Thesis. Ruperto-Carola University of Heidelberg, 2007 (cited on p. 50).

[110] A. Cronin, J. Schmiedmayer, and D. E. Pritchard. Optics and interferometry with atoms and molecules. *Reviews of Modern Physics* **81**(3), 1051–1129 (2009) (cited on p. 51).
doi: `10.1103/RevModPhys.81.1051`

[111] H. Fizeau. Sur les hypothèses relatives à l'éther lumineux, et sur une expérience qui paraît démontrer que le mouvement des corps change la vitesse avec laquelle la lumière se propage dans leur intérieur. *Comptes rendus hebdomadaires des séances de l'Académie des sciences* **33**, 349–355 (1851) (cited on p. 51).

[112] A. A. Michelson. The Relative Motion of the Earth and the Luminiferous Ether. *The American Journal of Science* **22**, 120–129 (1881) (cited on p. 51).

[113] J. W. S. Rayleigh. XXV. On copying diffraction-gratings, and on some phenomena connected therewith. *Philosophical Magazine Series 5* **11**(67), 196–205 (1881) (cited on p. 51).
doi: `10.1080/14786448108626995`

[114] I. I. Rabi, J. R. Zacharias, S. Millman, and P. Kusch. A New Method of Measuring Nuclear Magnetic Moment. *Physical Review* **53**(4), 318 (1938) (cited on p. 51).
doi: `10.1103/PhysRev.53.318`

[115] A. A. Michelson. Recent advances in spectroscopy. In: *Nobel Lectures in Physics (1901-1921)*. Singapore: World Scientific, 1998, p. 166. isbn: 9789810234010 (cited on p. 51).

[116] I. I. Rabi. Space Quantization in a Gyrating Magnetic Field. *Physical Review* **51**(8), 652–654 (1937) (cited on p. 53).
doi: `10.1103/PhysRev.51.652`

[117] P. K. Aravind and J. O. Hirschfelder. Two-state systems in semiclassical and quantized fields. *The Journal of Physical Chemistry* **88**(21), 4788–4801 (1984) (cited on p. 53).
doi: `10.1021/j150665a002`

[118] J. H. Shirley. Interaction of a quantum system with a strong oscillating field. PhD thesis. California Institute of Technology, 1963 (cited on p. 53).

[119] J. H. Shirley. Solution of the Schrödinger Equation with a Hamiltonian Periodic in Time. *Physical Review* **138**(4B), B979–B987 (1965) (cited on p. 53).
doi: `10.1103/PhysRev.138.B979`

[120] B. W. Shore. Coherent manipulation of atoms using laser light. *Acta Physica Slovaca* **58**(3), 243–486 (2008) (cited on pp. 53, 99).

[121] M. Zhang, J. Han, P. Liu, D. Muller, and H.-l. Dai. Collision Induced Dephasing in Fluorescence Quantum Beat of $SO_2(\tilde{C}^1B_2)^\dagger$. *The Journal of Physical Chemistry A* **107**(49), 10845–10850 (2003) (cited on p. 57).
doi: `10.1021/jp030957z`

[122] B. W. Shore. The Theory of Coherent Atomic Excitation, 2 Volume Set. The Theory of Coherent Atomic Excitation. John Wiley & Sons, 1990. isbn: 9780471524175 (cited on p. 57).

[123] M. Auzinsh, D. Budker, and S. M. Rochester. Optically Polarized Atoms: Understanding Light-Atom Interactions. Oxford University Press, 2010. isbn: 9780199565122 (cited on p. 57).

[124] M. Napolitano, M. Koschorreck, B. Dubost, N. Behbood, R. J. Sewell, and M. W. Mitchell. Interaction-based quantum metrology showing scaling beyond the Heisenberg limit. *Nature* **471**(7339), 486–9 (2011) (cited on p. 63).
doi: `10.1038/nature09778`

[125] Y. Li, Y. Castin, and A. Sinatra. Optimum Spin Squeezing in Bose-Einstein Condensates with Particle Losses. *Physical Review Letters* **100**(21), 210401 (2008) (cited on p. 63).
doi: `10.1103/PhysRevLett.100.210401`

[126] M. Kitagawa and M. Ueda. Squeezed spin states. *Physical Review A* **47**(6), 5138 (1993) (cited on p. 63).
doi: `10.1103/PhysRevA.47.5138`

[127] Y. Li, P. Treutlein, J. Reichel, and A. Sinatra. Spin squeezing in a bimodal condensate: spatial dynamics and particle losses. *The European Physical Journal B* **68**(3), 365–381 (2009) (cited on p. 63).
doi: `10.1140/epjb/e2008-00472-6`

[128] M. F. Riedel, P. Böhi, Y. Li, T. W. Hänsch, A. Sinatra, and P. Treutlein. Atom-chip-based generation of entanglement for quantum metrology. *Nature* **464**(April), 1170–1173 (2010) (cited on pp. 63, 119).
doi: `10.1038/nature08988`

[129] C. Gross, T. Zibold, E. Nicklas, J. Estève, and M. K. Oberthaler. Nonlinear atom interferometer surpasses classical precision limit. *Nature* **464**(April), 1165–1169 (2010) (cited on p. 63).
doi: `10.1038/nature08919`

[130] I. Bloch, J. Dalibard, and W. Zwerger. Many-body physics with ultracold gases. *Reviews of Modern Physics* **80**(3), 885–964 (2008) (cited on p. 63).
doi: `10.1103/RevModPhys.80.885`
arXiv: `0704.3011`

[131] Y. Kagan, B. V. Svistunov, and G. V. Shlyapnikov. Effect of Bose condensation on inelastic processes in gases. *JETP Letters* **42**(4), 209 () (cited on pp. 67, 70, 80).

[132] F. Dalfovo, S. Giorgini, L. P. Pitaevskii, and S. Stringari. Theory of Bose-Einstein condensation in trapped gases. *Reviews of Modern Physics* **71**(3), 463–512 (1999) (cited on p. 67).
doi: `10.1103/RevModPhys.71.463`

[133] S. Tojo, T. Hayashi, T. Tanabe, T. Hirano, Y. Kawaguchi, H. Saito, and M. Ueda. Spin-dependent inelastic collisions in spin-2 Bose-Einstein condensates. *Physical Review A* **80**(4), 042704 (2009) (cited on pp. 67, 75, 78, 102, 103).
doi: `10.1103/PhysRevA.80.042704`

[134] M. Egorov, B. Opanchuk, P. D. Drummond, B. V. Hall, P. Hannaford, and A. I. Sidorov. Precision measurements of s-wave scattering lengths in a two-component Bose-Einstein condensate (2012) (cited on pp. 70, 102, 103).
arXiv: `1204.1591`

[135] L. P. Pitaevskii. Bose–Einstein condensation in magnetic traps. Introduction to the theory. *Physics-Uspekhi* **41**(6), 569–580 (1998) (cited on p. 73).
doi: `10.1070/PU1998v041n06ABEH000407`

[136] E. P. Gross. Structure of a quantized vortex in boson systems. *Il Nuovo Cimento* **20**(3), 454–477 (1961) (cited on p. 73).
doi: `10.1007/BF02731494`

[137] E. P. Gross. Hydrodynamics of a Superfluid Condensate. *Journal of Mathematical Physics* **4**(2), 195 (1963) (cited on p. 73).
doi: `10.1063/1.1703944`

[138] L. P. Pitaevskii and S. Stringari. Bose-Einstein condensation. The International Series of Monographs on Physics. Oxford University Press, USA, 2003. isbn: 9780198507192 (cited on p. 73).

[139] C. J. Pethick and H. Smith. Bose-Einstein condensation in dilute gases. 2nd ed. Cambridge University Press, 2008. isbn: 9780521846516 (cited on p. 73).

[140] M. Ueda and Y. Kawaguchi. Spinor Bose-Einstein condensates (2010) (cited on p. 73).
arXiv: `1001.2072`

[141] A. Leggett. Bose-Einstein condensation in the alkali gases: Some fundamental concepts. *Reviews of Modern Physics* **73**(2), 307–356 (2001) (cited on p. 73).
doi: `10.1103/RevModPhys.73.307`

[142] B. Opanchuk and P. D. Drummond. Functional Wigner representation of BEC quantum dynamics (2012) (cited on p. 75).
arXiv: `1210.1302`

[143] H. J. Carmichael. An open systems approach to quantum optics. Lecture Notes in Physics. Springer-Verlag Berlin and Heidelberg GmbH & Co. K, 1993. isbn: 9783540566342 (cited on p. 75).

[144] J. J. Sakurai. Modern quantum mechanics. Ed. by S. F. Tuan. Addison-Wesley, 1993. isbn: 9780201539295 (cited on p. 76).

[145] A. Messiah. Quantum Mechanics. Vol. 1. North-Holland Publishing Company, 1961 (cited on p. 76).

[146] A. Messiah. Quantum Mechanics. Vol. 2. North-Holland Publishing Company, 1962 (cited on p. 76).

[147] W. H. Louisell. Quantum statistical properties of radiation. Wiley Classics Library. John Wiley & Sons, 1990. isbn: 0471523658,9780471523659 (cited on p. 76).

[148] D. J. Griffiths. Introduction to quantum mechanics. 2nd ed. Pearson Prentice Hall, 2005. isbn: 9780131118928 (cited on p. 76).

[149] R. Hanbury Brown and R. Q. Twiss. Correlation between Photons in two Coherent Beams of Light. *Nature* **177**(4497), 27–29 (1956) (cited on p. 80). doi: `10.1038/177027a0`

[150] P. Langevin. Sur la théorie du mouvement brownien. *Comptes Rendus de l'Académie des Sciences* **146**, 530–532 (1908) (cited on p. 80).

[151] D. S. Lemons and A. Gythiel. Paul Langevin's 1908 paper "On the Theory of Brownian Motion" ["Sur la théorie du mouvement brownien," C. R. Acad. Sci. (Paris) 146, 530–533 (1908)]. *American Journal of Physics* **65**(11), 1079 (1997) (cited on p. 80).
doi: `10.1119/1.18725`

[152] J. Minář, H. de Riedmatten, C. Simon, H. Zbinden, and N. Gisin. Phase-noise measurements in long-fiber interferometers for quantum-repeater applications. *Physical Review A* **77**(5), 052325 (2008) (cited on pp. 83, 85).
doi: `10.1103/PhysRevA.77.052325`

[153] A. Widera. Constructing correlated spin states with neutral atoms in optical lattices. PhD Thesis. Johannes-Gutenberg-Universität Mainz, 2007 (cited on pp. 83, 86).

[154] S. Stenholm. Foundations of laser spectroscopy. Wiley series in pure and applied optics. Wiley, 1984. isbn: 9780471059998 (cited on p. 84).

[155] M. Weissbluth. Photon-Atom Iteractions. Academic Press, Inc., 1989. isbn: 9780127436609 (cited on p. 84).

[156] A. D. Polyanin. Handbook of linear partial differential equations for engineers and scientists. Chapman & Hall/CRC, 2002. isbn: 9781584882992 (cited on p. 84).

[157] E. P. Bashkin. Spin waves in polarized paramagnetic gases. *JETP Letters* **33**(1), 8 (1981) (cited on p. 89).

[158] C. C. Lhuillier and F. Laloë. Transport properties in a spin polarized gas, II. *Journal de Physique* **43**(2), 225–241 (1982) (cited on p. 89).
doi: `10.1051/jphys:01982004302022500`

[159] C. C. Lhuillier and F. Laloë. Transport properties in a spin polarized gas, I. *Journal de Physique* **43**(2), 197–224 (1982) (cited on p. 89).
doi: `10.1051/jphys:01982004302019700`

[160] C. C. Lhuillier and F. Laloë. Addendum - Transport properties in a spin polarized gas, I and II. *Journal de Physique* **43**(5), 833 (1982) (cited on p. 89).
doi: `10.1051/jphys:01982004305083300`

[161] A. S. Arnold. Preparation and manipulation of an ^{87}Rb Bose-Einstein Condensate. PhD Thesis. University of Sussex, 1999 (cited on p. 90).

[162] H. J. Lewandowski. Coherences and correlations in an ultracold Bose gas. PhD Thesis. University of Colorado, 2002 (cited on p. 90).

[163] C. Lacroûte. Développement d'une horloge atomique sur puce à atomes: optimisation de la durée de cohérence et caractérisation préliminaire. PhD thesis. Université Pierre et Marie Curie, 2010 (cited on p. 91).

[164] D. B. Sullivan, J. C. Bergquist, J. J. Bollinger, R. E. Drullinger, W. M. Itano, S. R. Jefferts, W. D. Lee, D. Meekhof, T. E. Parker, F. L. Walls, and D. J. Wineland. Primary atomic frequency standards at NIST. *Journal of Research of the National Institute of Standards and Technology* **106**(1), 47–63 (2001) (cited on pp. 96, 97).
doi: `10.6028/jres.106.004`

[165] A. Bebeachibuli, M. S. Santos, D. V. Magalhães, S. T. Müller, and V. S. Bagnato. Characterization of the main frequency shifts for the brazilian ^{133}Cs atomic beam frequency standard. *Brazilian Journal of Physics* **35**(4a), 1010–1015 (2005) (cited on p. 97).
doi: `10.1590/S0103-97332005000600017`

[166] F. Teles, D. V. Magalhães, M. S. Santos, A. Bebeachibuli, and V. S. Bagnato. Characterization of the Brazilian Cs atomic-frequency standard: evaluation of major shifts. *Metrologia* **39**(2), 135–141 (2002) (cited on p. 97).
doi: `10.1088/0026-1394/39/2/3`

[167] J. H. Shirley, W. D. Lee, G. D. Rovera, and R. E. Drullinger. Rabi pedestal shifts as a diagnostic tool in primary frequency standards. *IEEE Transactions on Instrumentation and Measurement* **44**(2), 136–139 (1995) (cited on p. 97).
doi: `10.1109/19.377792`

[168] V. V. Flambaum, V. A. Dzuba, and A. Derevianko. Magic Frequencies for Cesium Primary-Frequency Standard. *Physical Review Letters* **101**(22), 220801 (2008) (cited on p. 97).
doi: `10.1103/PhysRevLett.101.220801`
arXiv: `0809.2825`

[169] A. Derevianko. "Doubly Magic" Conditions in Magic-Wavelength Trapping of Ultracold Alkali-Metal Atoms. *Physical Review Letters* **105**(3), 033002 (2010) (cited on p. 97).
doi: `10.1103/PhysRevLett.105.033002`
arXiv: `1004.2941`

[170] Y. Ovchinnikov and G. Marra. Accurate rubidium atomic fountain frequency standard. *Metrologia* **48**(3), 87–100 (2011) (cited on pp. 97, 116).
doi: `10.1088/0026-1394/48/3/003`

[171] R. Li and K. Gibble. Comment on 'Accurate rubidium atomic fountain frequency standard'. *Metrologia* **48**(5), 446–447 (2011) (cited on p. 97).
doi: `10.1088/0026-1394/48/5/N03`

[172] Y. Ovchinnikov and G. Marra. Reply to comment on 'Accurate rubidium atomic fountain frequency standard'. *Metrologia* **48**(5), 448–449 (2011) (cited on p. 97).
doi: `10.1088/0026-1394/48/5/N04`

[173] Y. Sortais, S. Bize, C. Nicolas, A. Clairon, C. Salomon, and C. Williams. Cold collision frequency shifts in a 87Rb atomic fountain. *Physical review letters* **85**(15), 3117–3120 (2000) (cited on p. 97).
doi: `10.1103/PhysRevLett.85.3117`

[174] S. Bize, Y. Sortais, M. S. Santos, C. Mandache, A. Clairon, and C. Salomon. High-accuracy measurement of the ^{87}Rb ground-state hyperfine splitting in an atomic fountain. *Europhysics Letters (EPL)* **45**(5), 558–564 (1999) (cited on p. 97).
doi: `10.1209/epl/i1999-00203-9`

[175] S. J. J. M. F. Kokkelmans, B. Verhaar, K. Gibble, and D. Heinzen. Predictions for laser-cooled Rb clocks. *Physical Review A* **56**(6), R4389–R4392 (1997) (cited on pp. 97, 109).
doi: `10.1103/PhysRevA.56.R4389`

[176] N. F. Ramsey. Molecular Beams. International Series of Monographs on Physics. Oxford University Press, 1956. isbn: 9780198520214 (cited on p. 98).

[177] G. Xu and D. Heinzen. State-selective Rabi and Ramsey magnetic resonance line shapes. *Physical Review A* **59**(2), R922–R925 (1999) (cited on p. 98).
doi: `10.1103/PhysRevA.59.R922`

[178] F. Reinhard. Design and construction of an atomic clock on an atom chip. PhD Thesis. Université Pierre et Marie Curie, 2009 (cited on pp. 105, 116).

[179] M. Egorov, R. P. Anderson, V. Ivannikov, B. Opanchuk, P. D. Drummond, B. V. Hall, and A. I. Sidorov. Long-lived periodic revivals of coherence in an interacting Bose-Einstein condensate. *Physical Review A* **84**(2), 021605 (2011) (cited on pp. 109, 112, 113, 119).
doi: `10.1103/PhysRevA.84.021605`
arXiv: `1012.3813`

[180] K. Gibble and S. Chu. Future Slow-atom Frequency Standards. *Metrologia* **29**(2), 201–212 (1992) (cited on p. 109).
doi: `10.1088/0026-1394/29/2/008`

[181] J. Javanainen and M. Wilkens. Phase and Phase Diffusion of a Split Bose-Einstein Condensate. *Physical Review Letters* **78**(25), 4675–4678 (1997) (cited on p. 109).
doi: `10.1103/PhysRevLett.78.4675`

[182] W. J. Riley. A test suite for the calculation of time domain frequency stability. In: *Proceedings of the 1995 IEEE International Frequency Control Symposium (49th Annual Symposium)*. IEEE, 1995, pp. 360–366. isbn: 0-7803-2500-1 (cited on pp. 116, 117).
doi: `10.1109/FREQ.1995.483922`

[183] W. J. Riley. Addendum to a test suite for the calculation of time domain frequency stability. In: *Proceedings of 1996 IEEE International Frequency Control Symposium*. June 1995. IEEE, 1996, pp. 880–882. isbn: 0-7803-3309-8 (cited on pp. 116, 117).
doi: `10.1109/FREQ.1996.560270`

[184] F. Riehle. Frequency Standards: Basics and Applications. John Wiley and Sons, 2009. isbn: 9783527402304 (cited on p. 116).

[185] F. Ramírez-Martínez, C. Lacroûte, P. Rosenbusch, F. Reinhard, C. Deutsch, T. Schneider, and J. Reichel. Compact frequency standard using atoms trapped on a chip. *Advances in Space Research* **47**(2), 247–252 (2011) (cited on p. 116).
doi: `10.1016/j.asr.2010.04.014`

[186] P. Treutlein, P. Hommelhoff, T. Steinmetz, T. W. Hänsch, and J. Reichel. Coherence in Microchip Traps. *Physical Review Letters* **92**(20), 203005 (2004) (cited on p. 116).
doi: `10.1103/PhysRevLett.92.203005`
arXiv: `quant-ph/0311197`

[187] R. Wynands and S. Weyers. Atomic fountain clocks. *Metrologia* **42**(3), S64–S79 (2005) (cited on p. 116).
doi: `10.1088/0026-1394/42/3/S08`

[188] D. W. Allan. Statistics of atomic frequency standards. *Proceedings of the IEEE* **54**(2), 221–230 (1966) (cited on p. 116).
doi: `10.1109/PROC.1966.4634`

[189] B. E. Blair, ed. Time and Frequency: Theory and Fundamentals. Boulder: U. S. Department of Commerce and National Bureau of Standards, 1974 (cited on p. 116).

[190] W. J. Riley. NIST Special Publication 1065: Handbook of frequency stability analysis. Tech. rep. National Institute of Standards and Technology, 2008 (cited on pp. 116, 117, 118, 119).

[191] D. A. Howe. Circular representation of infinitely extended sequences. In: *Proceedings of the 1995 IEEE International Frequency Control Symposium (49th Annual Symposium)*. IEEE, 1995, pp. 337–345. isbn: 0-7803-2500-1 (cited on p. 116).
doi: `10.1109/FREQ.1995.483919`

[192] S. K. Park and K. W. Miller. Random number generators: good ones are hard to find. *Communications of the ACM* **31**(10), 1192–1201 (1988) (cited on p. 117).
doi: `10.1145/63039.63042`

[193] A. Savitzky and M. J. E. Golay. Smoothing and Differentiation of Data by Simplified Least Squares Procedures. *Analytical Chemistry* **36**(8), 1627–1639 (1964) (cited on p. 119).
doi: `10.1021/ac60214a047`

[194] S. Stoll and A. Schweiger. EasySpin, a comprehensive software package for spectral simulation and analysis in EPR. *Journal of magnetic resonance (San Diego, Calif. : 1997)* **178**(1), 42–55 (2006) (cited on p. 119).
doi: `10.1016/j.jmr.2005.08.013`

[195] C. J. Foot. Atomic physics. Oxford Master Series in Atomic, Optical and Laser Physics. Oxford University Press, USA, 2005. isbn: 9781435609679 (cited on p. 151).

[196] Y. Castin, H. Wallis, and J. Dalibard. Limit of Doppler cooling. *Journal of the Optical Society of America B* **6**(11), 2046 (1989) (cited on p. 151).
doi: `10.1364/JOSAB.6.002046`

[197] E. Raab, M. Prentiss, A. Cable, S. Chu, and D. E. Pritchard. Trapping of Neutral Sodium Atoms with Radiation Pressure. *Physical Review Letters* **59**(23), 2631–2634 (1987) (cited on p. 151).
doi: `10.1103/PhysRevLett.59.2631`

[198] W. Ketterle and N. J. Van Druten. Evaporative cooling of trapped atoms. *Advances In Atomic, Molecular, and Optical Physics* **37**, 181–236 (1996) (cited on p. 153).
doi: `10.1016/S1049-250X(08)60101-9`

[199] N. Masuhara, J. Doyle, J. Sandberg, D. Kleppner, T. Greytak, H. Hess, and G. Kochanski. Evaporative Cooling of Spin-Polarized Atomic Hydrogen. *Physical Review Letters* **61**(8), 935–938 (1988) (cited on p. 153).
doi: `10.1103/PhysRevLett.61.935`

[200] W. Petrich, M. Anderson, J. Ensher, and E. A. Cornell. Stable, Tightly Confining Magnetic Trap for Evaporative Cooling of Neutral Atoms. *Physical Review Letters* **74**(17), 3352–3355 (1995) (cited on p. 153).
doi: `10.1103/PhysRevLett.74.3352`

[201] K. B. Davis, M.-O. Mewes, M. A. Joffe, M. R. Andrews, and W. Ketterle. Evaporative cooling of sodium atoms. *Physical review letters* **74**(26), 5202–5205 (1995) (cited on p. 153).
doi: `10.1103/PhysRevLett.74.5202`

[202] N. Newbury, C. Myatt, and C. E. Wieman. s-wave elastic collisions between cold ground-state ^{87}Rb atoms. *Physical Review A* **51**(4), R2680–R2683 (1995) (cited on p. 153).
doi: `10.1103/PhysRevA.51.R2680`

Appendix A

MW and RF transitions

- **σ^+, π, σ^- MW-transition frequencies, 2-photon transition in B_{magic}**

f_{σ^+} (F=1, mF=-1 to F=2 mF=0) = 6.832 419 968 GHz

f_{π} (F=1, mF=-1 to F=2 mF=-1) = 6.830 160 324 GHz

f_{σ^-} (F=1, mF=-1 to F=2 mF=-2) = 6.827 899 177 GHz

$f_{2\,\text{ph}}$ (F=1, mF=-1 to F=2 mF=+1) = 6.834 678 114 GHz

- **Two-photon frequency (with ~1 MHz detuning)**

$f_{2\,\text{ph transition}}$ = 6.834 678 114 GHz

Δ = 989 848. Hz

$f_{2\,\text{ph, RF-generator}}$ = 3.247 993 MHz [set to give ~1 MHz detuning]

$f_{2\,\text{ph, MW-generator}}$ = 6.831 430 121 GHz [set to match RF-generator and 2-photon transition]

- **RF-transition frequencies for F=2 and differences between them**

f_1 (F=2, mF=-2 to F=2, mF=-1) = 2.261 147 MHz

f_2 (F=2, mF=-1 to F=2, mF=0) = 2.259 644 MHz

f_3 (F=2, mF=0 to F=2, mF=+1) = 2.258 145 MHz

f_4 (F=2, mF=+1 to F=2, mF=+2) = 2.256 649 MHz

$\delta_1 = |f_1 - f_2|$ = 1 502.1 Hz

$\delta_2 = |f_2 - f_3|$ = 1 499.1 Hz

$\delta_3 = |f_3 - f_4|$ = 1 496.1 Hz

- **RF frequencies for F=1**

f_5 (F=1, mF=-1 to F=1, mF=0) = 2.268 639 MHz

f_6 (F=1, mF=0 to F=1, mF=+1) = 2.267 14 MHz

$\delta_4 = |f_5 - f_6|$ = 1 499.1 Hz

- **Differential <u>nonlinear</u> Zeeman between clock states 1,-1 and 2,+1 (is non-zero!)**

$\delta_{\text{clk}} = |f_5 - f_3|$ = 10 494. Hz

Appendix B

UHV-chamber bakeout

One of the key ingredients of the BEC-producing system is ultra-high vacuum. Vacuum defines the collision rate of the cold atomic ensemble with the hot background gas and, from practice, if it drops to 10^{-9} Torr the BEC lifetime will suffer, and in a few hours of apparatus operation BEC production may cease. In this section we provide detailed logs of the bakeout and the subsequent Ti sublimation pump activation that gives us a typical level of 2×10^{-11} Torr.

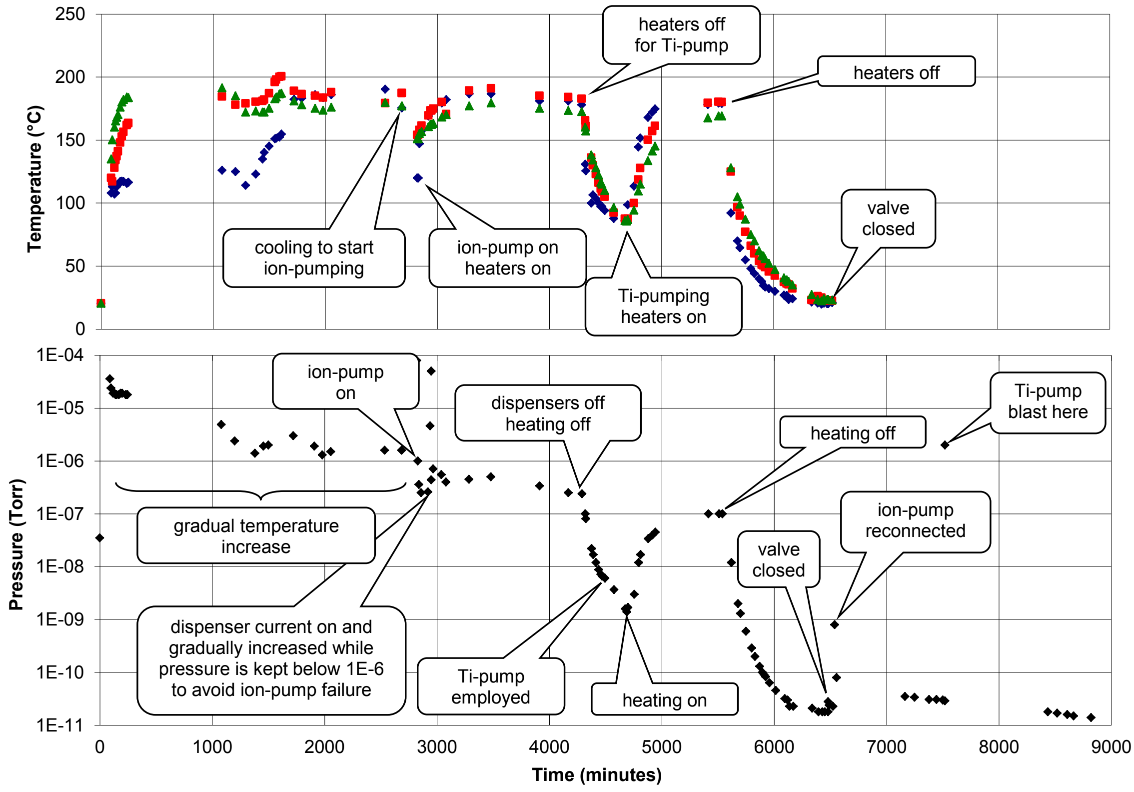

Figure B.1: Bakeout schedule with annotations. The three colours correspond to the three independent temperature sensors inserted under the Al-foil thermal isolation of the vacuum system to track the warming of different parts of the vacuum system. The pressure is measured by a cold cathode gauge.

time (min)	stimulus	Ti-filament number			
		1	2	3	4
0	I = 25 A Δt = 30 s	$P_{peak} = 2\cdot10^{-7}$ Torr $P_{\Delta t+60s} = 5\cdot10^{-9}$ Torr	$P_{peak} = 5\cdot10^{-7}$ Torr $P_{\Delta t+60s} = 6.6\cdot10^{-9}$ Torr	$P_{peak} = 2\cdot10^{-6}$ Torr $P_{\Delta t+60s} = 9\cdot10^{-9}$ Torr	$P_{peak} = 1\cdot10^{-6}$ Torr $P_{\Delta t+60s} = 1\cdot10^{-8}$ Torr
12	I = 35 A Δt = 20 s	$P_{peak} = 4\cdot10^{-7}$ Torr $P_{\Delta t+60s} = 3.5\cdot10^{-8}$ Torr	$P_{peak} = 5\cdot10^{-7}$ Torr $P_{\Delta t+60s} = 4\cdot10^{-8}$ Torr	$P_{peak} = 5\cdot10^{-7}$ Torr $P_{\Delta t+60s} = 4\cdot10^{-8}$ Torr	$P_{peak} = 7\cdot10^{-7}$ Torr $P_{\Delta t+60s} = 1\cdot10^{-8}$ Torr
22	I = 45 A Δt = 15 s	$P_{peak} = 1\cdot10^{-6}$ Torr $P_{\Delta t+60s} = 5\cdot10^{-8}$ Torr	$P_{peak} = 1\cdot10^{-6}$ Torr $P_{\Delta t+60s} = 4\cdot10^{-8}$ Torr	$P_{peak} = 4\cdot10^{-7}$ Torr $P_{\Delta t+60s} = 4\cdot10^{-8}$ Torr	$P_{peak} = 3\cdot10^{-6}$ Torr $P_{\Delta t+60s} = 5\cdot10^{-8}$ Torr
29	I = 55 A Δt = 30 s	$P_{peak} = 2\cdot10^{-6}$ Torr $P_{\Delta t+60s} = 4\cdot10^{-8}$ Torr	$P_{peak} = 1.2\cdot10^{-6}$ Torr $P_{\Delta t+60s} = 3\cdot10^{-8}$ Torr	$P_{peak} = 2.4\cdot10^{-7}$ Torr $P_{\Delta t+60s} = 1\cdot10^{-8}$ Torr	$P_{peak} = 3.3\cdot10^{-7}$ Torr $P_{\Delta t+60s} = 3\cdot10^{-8}$ Torr

Figure B.2: Titanium sublimation pump activation sequence. The filaments are initially oxidized and should be heated with small currents for cleaning. Gradually, the sublimation current is reached and Ti released. Peak pressure values are registered during the current pulse of duration Δt. At 60 s after the pulse the value is also recorded to ensure that Ti has precipitated onto the walls and decreased the pressure. The pressure settles at even a lower level hours after the sublimation.

Appendix C

Notes on laser cooling

C.1 Doppler cooling and trapping

Doppler cooling sets a lower limit to the achievable temperature for a two-level atom: the Doppler force is proportional to the friction coefficient which is proportional to the laser power [2]. If only two levels in an atom participate in the cooling cycle, the lowest temperature limit is given by [195], under the assumption that the energy width of excited state $\hbar\Gamma$ is much larger than the recoil energy $E_{rec} = \hbar^2 k^2 \big/ (2m)$:

$$T_{Doppler} = \frac{h\gamma}{2k_B}$$

for the two-level atom, which is an adequate model for this case. If this assumption breaks down — the width $\hbar\Gamma$ is narrow compared to E_{rec} — this semiclassical result is invalid and a proper quantum treatment is needed; the limit becomes comparable with the recoil limit [196] like in the case of sub-Doppler cooling.

An increase of phase-space density is the primary goal of cooling: cloud dimensions and the particle velocities need to be reduced. Magneto-optical trapping (MOT) does both: the atoms are *trapped* and *cooled* simultaneously [5, 7].

The magneto-optical trapping, repumping lasers and the quadrupole magnetic field are turned on to create a magnetic field potential minimum to trap low-field seeking atoms at the crossing of the laser beams, approximately 4 mm below the atom chip surface[1]. The phase-space density increases at the molasses centre by capturing atoms from the isotropic background gas according to the 3D magneto-optical trapping mechanism [197]. MOT-loading is monitored via a photodiode, installed outside the chamber with a lens capturing residual fluorescence from the rare events of the off-resonant scattering in the cooling cycle.

---

[1] Distances *from atom chip* are counted from the centre of the current carrying film that forms the chip wires, i.e., the vertical axis origin is taken at half the film thickness inside the film.

C.2 Sub-Doppler cooling

In Fig. 2.6 the $\lambda/4$-plates immediately preceding the atom chip along the optical path set up $\sigma^{\pm}$ polarizations for the trapping beams. A three-dimensional MOT itself is insensitive to the polarization chosen because its detuning $\Delta = 50$ MHz is a much larger than the distance between the magnetic sublevels induced by the σ^{+} and σ^{-} light in a magnetic field of a few Gauss, and because the inhomogeneous broadening amounts approximately to 600 MHz, which defines the capture velocity range.

The MOT beams are also used for the polarization-gradient cooling (PGC) [2], a type of sub-Doppler cooling which has cooling features on the profile of Doppler force versus momentum. In the counter-propagating σ^{+}–σ^{-}-configuration of the PGC beams, used in our experiments, the resulting polarization at the atom location is always linear and rotates along the direction of propagation. The radiation that reaches the atoms has an equal light-shifted potential everywhere and loses momentum because of the distinct coupling strengths for the σ^{+} and σ^{-} transitions induced by the counter-propagating beams. PGC overcomes the Doppler cooling limit because its friction coefficient is independent of laser power unlike in Doppler cooling. The optical power in PGC is proportional to the velocity range captured in the molasses.

The polarization-gradient cooling only takes place in the atoms with more than two levels. It works best in the absence of magnetic fields [84]. We cannot completely satisfy this condition since the atoms are magnetically trapped, resulting in a finite magnetic potential, but our trap operates at a weak magnetic field of approximately 1 G at the trap centre which is satisfactory for both cooling and trapping.

Sub-Doppler cooling has a lower temperature limit. The cooling light spontaneously emits photons that kick atoms and transfer momentum to them. The temperature limit is then the recoil limit [2]:

$$T_{rec} = \frac{\hbar^2 k^2}{2 k_B m}$$

With the Boltzmann constant $k_B = 1.38065 \times 10^{-23}$ J/K, ^{87}Rb atomic mass 1.44316×10^{-25} kg, $k = 2\pi/\lambda$, $\lambda = 780$ nm, the T_{rec} limit becomes 180 nK. This value is lower than the one achieved in the lin $\perp$ lin configuration with the same experimental arrangement. This limit cannot be reached in practical situations because atoms are trapped with non-zero magnetic field during the polarization-gradient cooling stage.

C.3 Forced evaporative cooling

There are only two fundamental physical principles of heat transfer: radiational, by photon recoils, and kinetic, by particle collisions. Hence, cooling methods based on light-atom interactions are fundamentally limited by photon recoils. Once T_{rec} is reached, other processes must be employed to further reduce the temperature and they must be of a collisional nature. A lossy, yet effective, cooling technique is the *evaporative cooling* of neutral atoms[2] first reported in [199]. This follows a simple principle: in a long evaporation the ensemble re-thermalizes and the most energetic atoms escape from the trap by spilling over the trapping potential. A much faster evaporation method is *forced evaporative cooling* [200, 201], when the atoms are coupled to an untrappable state by radiation of a frequency that decreases with time, approaching the trap bottom. In this way the atoms with higher energies undergo a spin flip transition to an untrappable state and leave the system. The ensemble temperature decreases by having evaporated the hottest particles. With the frequency reduction the system allows only lower lying energy states, lower temperatures.

The forced evaporation is driven by *elastic*, or “good”, collisions. There is another type of collisions, *inelastic* or “bad” collisions, that are inevitable and influence the cooling process unfavourably. The end temperature is defined by the balance of the two mechanisms.

Forced evaporative cooling has a theoretical lower temperature bound amounting to $\pi m G_{dip}^2 \big/ \left(16 k_B \sigma^2\right)$, but for a three-dimensional harmonic trap the value is three times larger and the smallest experimental achievable temperature by this method is considered to be 2000 times larger [198]. The resulting temperature limit is thus:

$$T_{evap} \approx \frac{m G_{dip}^2}{k_B \sigma^2} \times 10^3$$

With a rate coefficient of the dipolar relaxation $G_{dip} = 10^{-15}$ cm^{3}s^{-1} and the elastic collisional cross-section $\sigma = 5.4 \times 10^{-12}$ cm^2 [202] forced evaporation is limited to a temperature of $T_{evap} = 36$ pK.

It is useful to relate $T_{Doppler}$, T_{rec} and T_{evap} with the Bose-Einstein condensation transition temperature T_{crit} dependent on the trap frequencies to estimate if a further cooling is required. With the typical parameters of our experiments the forced evaporation limit T_{evap} is orders of magnitude lower than the critical temperature T_{crit}.

---

[2] See a comprehensive review by Ketterle [198].

Publications of the author

During the thesis I have been a co-author of the following works:

[1] A. M. Akulshin, B. V. Hall, V. Ivannikov, A. A. Orel, and A. I. Sidorov. Doppler-free Two-photon Resonances for Atom Detection and Sum Frequency Stabilization. *Journal of Physics B: Atomic, Molecular and Optical Physics* **44**(21), 215401 (2011).
doi: 10.1088/0953-4075/44/21/215401

[2] M. Egorov, R. P. Anderson, V. Ivannikov, B. Opanchuk, P. D. Drummond, B. V. Hall, and A. I. Sidorov. Long-lived Periodic Revivals of Coherence in an Interacting Bose-Einstein Condensate. *Physical Review A* **84**(2), 021605 (2011).
doi: 10.1103/PhysRevA.84.021605
arXiv: 1012.3813